ABSTRACT

Title of Document:	PLASMA-SURFACE INTERACTION AT ATMOSPHERIC PRESSURE: FROM MECHANISMS WITH MODEL POLYMERS TO APPLICATIONS FOR STERILIZATION
	Pingshan Luan, Doctor of Philosophy, 2018
Directed By:	Professor Gottlieb S. Oehrlein Department of Materials Science and Engineering and Institute for Research in Electronics and Applied Physics

Cold temperature atmospheric pressure plasma (APP) produces many types of chemically reactive species and is capable of modifying materials at atmospheric pressure. Studying plasma-surface interaction (PSI) at such pressure has been challenging due to the small mean-free-path (< 100 nm) which prohibits the conventional method of using independently controlled beams of ions/neutrals to isolate the role of each species. In this dissertation, we developed an alternative approach of studying PSI at atmospheric pressure using well-controlled source-ambient-sample systems and comprehensive surface/gas phase characterization techniques. In this new approach, we emphasize the controlled generation of reactive species from the plasma source, the regulated transportation of reactive species to the target surfaces, as well as the simplified material structure subjected to plasma treatment. To isolate and identify the role of certain reactive species on materials, a

plasma source is selected with its operating conditions carefully tuned for the delivery of such species to target surface. Plasma-induced effects on model polymers and biomolecules were characterized and then quantitatively correlated to the gas phase species. Due to the multi-phase nature of PSI, many characterization techniques, including that of plasma/gas phases such as optical emission spectroscopy (OES), Fourier transform infrared spectroscopy (FTIR) and UV absorption, and that of material surfaces such as X-ray photoelectron spectroscopy (XPS), attenuated total reflection (ATR) FTIR and Ellipsometry were adopted. Using this approach, we were able to evaluate the effect of both short- and long-lived reactive neutrals on many types of surface moieties. For example, we find that atomic O and OH radicals are able to cause fast material removal but moderate oxidation on the etched surface. We also find that O_3 can participate in the chemical modification of aromatic rings, i.e. cleavage and their conversion into ether, ester carbonyls and surface organic nitrate groups, both on surface and in the polymer bulk. We also find evidence for (1) the competition between etching and surface modification processes when a high density of short-lived reactive species is involved, and (2) three polymer transformation stages when large fluxes of long-lived reactive species are interacting with styrene-based polymers. Lastly, we extended our work to explore the potential application of APP reactors for disinfecting raw foods and evaluated bacterial inactivation mechanisms.

PLASMA-SURFACE INTERACTION AT ATMOSPHERIC PRESSURE: FROM MECHANISMS WITH MODEL POLYMERS TO APPLICATIONS FOR STERILIZATION

By

Pingshan Luan

Dissertation submitted to the Faculty of the Graduate School of the
University of Maryland, College Park, in partial fulfillment
of the requirements for the degree of
Doctor of Philosophy

2018

Advisory Committee:
Prof. Gottlieb S. Oehrlein, Department of Materials Science & Engineering, Chair
Prof. Robert M. Briber, Department of Materials Science & Engineering
Prof. Raymond J. Phaneuf, Department of Materials Science & Engineering
Prof. Raymond J. Sedwick, Department of Aerospace Engineering
Prof. Peter J. Bruggeman, Department of Mechanical Engineering, University of Minnesota

Acknowledgements

I have been very fortunate to have learned from and collaborated with many excellent scholars since I started my pursuit of a Ph.D. degree. Among these accomplished people, the most influential individual to me is my Ph.D. advisor Prof. Gottlieb S. Oehrlein. Through 5 years of his rigorous training, the way how I think, plan and execute has been fundamentally changed. After answering whether I have an established approach for solving problems in a recent interview, I started realizing that what he taught me is far beyond the knowledge contained in this dissertation. I will never forget the high moral standard, great social responsibility and constant pursuit to excellence that a qualified researcher should possess as he has been showing me on daily basis.

I would like to thank my dissertation committee for taking the time to examine my work. I hope you find it worthwhile. Thank you Prof. Briber, Prof. Phaneuf, Prof. Sedwick, and Prof. Bruggeman.

I would like to thank the U.S. National Science Foundation and the U.S. Department of Energy for financial support over the years.

I want to thank my collaborators - the UMN team: Prof. Peter Bruggeman and V. S. Santosh K. Kondeti; the UCB team: Prof. David Graves and Carly Anderson; the UMD team: Prof. Rohan Tikekar, Dr. Luis Bastarrachea and Andrea Gilbert - for their expertise and support on various research projects related to this thesis. Your input and feedback provided a fresh perspective which I found particularly inspiring.

Thank you to all my colleagues in Prof. Oehrlein's lab who have become close friends of mine over the years. I appreciate the help, support and fun you have been giving me. Your accompany has made me feel right at home in Maryland. Thank you Dr. Elliot

Bartis who helped me on not only starting my career but also overcoming the culture shock during my first year at UMD - I really appreciate your effort on training me as the manager of the XPS which was not an easy job. Thank you Dr. Andrew Knoll – I enjoyed working closely with you for 5 years and also all the fun we had outside the lab. Thank you Dr. Dominik Metzler, Chen Li, Adam Pranda, Kang-yi Lin and Dr. Shiqiang Zhang. It made me smile just to think about all the good times. I hope I can work with you again in future!

I am also grateful to the help and contribution from the undergraduate students and interns who have worked with me, including Connor Hart, Haotian Wang, Cristina Tous, Wei-lee Wu, Marcel Kleinkonradt, Martin Lai and Sinan Telli.

Thank you to the staff of IREAP and the Department of MSE. Your generous support has made the daily maintenance and occasional upgrade of the lab a breeze. Thank you Brian Quinn, Nolan Ballew, Jay Pyle, William Schuster, Thomas Weimar, Kathryn Tracey Metzler, Kay Morris, Jenna Bishop and Ginette Villeneuve.

I would like to thank all the friends that I made on and off campus in the past few years, especially the graduate students in the MSE department and all my roommates.

Last, I would like to say thank you to my parents who have encouraged me to do a Ph.D. since I was a kid. Thank you Dad for teaching me to study and work for passion rather than fortune or fame. Thank you Mom for guiding me to pursue happiness and a balanced life.

Table of Contents

List of Figures

Chapter 3:

Chapter 7:

Chapter 8:

List of Tables

Chapter 1: Introduction

This dissertation is concerned with the mechanisms of plasma-surface interaction (PSI) at atmospheric pressure, especially for carbon-based compounds. We seek to understand why materials respond in a certain way, such as etching, oxidation, nitritation, or a combination of the above, under the exposure of atmospheric pressure plasma (APP). We seek to establish correlations between plasma generated reactive species and their effect on material surfaces at atmospheric pressure. With the knowledge of these fundamental mechanisms of PSI, we seek to establish controlled APP treatments that can produce desired surface effects suitable for applications such as surface functionalization, etching as well as the sterilization of microbes, etc.

1.1 The challenge of studying plasma-surface interaction at atmospheric pressure

The challenge of studying PSI comes from the complexity of chemical reactions on the interface between material and plasma/gas phase.[2] While many types of plasma generated reactive species simultaneously bombard the material surface, the classic approach of studying PSI is by isolating individual elementary processes under well-controlled conditions, for example the interaction of one type of reactive species (controlled beam) with a well-defined material surface. This method can be effective for understanding PSI at low pressure; however when it comes to APP, high gas density reduces the mean free path of particles to sub-100 nm level which prohibits the adoption of such controlled beam approach. Besides, the synergistic effects of plasma treatment[3]

suggest that material surfaces may respond very differently when they are exposed to many plasma species in parallel.

Despite the lack of sufficient reports of PSI at atmospheric pressure, many studies on the interaction of materials with APP related reactive species do exist, even though some of these works may have been performed by scientists from various research communities using different experimental approaches. For example, the properties of atomic O, OH and NO_x have been widely discussed in articles focused on atmospheric chemistry.[4] Furthermore, the previously accumulated knowledge of PSI in low pressure may still apply for APP, such as the effect of ions and UV photons.[5, 6]

In this dissertation, we will discuss the development of our approach on studying PSI at atmospheric pressure aside from the controlled beam method. We will compare the mechanisms of PSI studied at atmospheric pressure with those learned from low pressure plasma systems. For the target materials of PSI, we choose polymers as the main subject due to its simplicity, importance in applications and close resemblance to biomolecules. Besides, the vast existing knowledge of polymer interaction with reactive species - which we provide a detailed overview in this chapter - makes it ideal for exploring the basic principles of PSI.

1.2 Fundamentals of polymer modification and etching

Depending on treatment conditions, polymers may experience three types of changes under the exposure of APP as shown in figure 1.1: (1) irreversible modification to the polymer surface and/or sub-surface, (2) etching, and (3) deposition. Such classification is based on the dominant effect seen on polymers upon plasma treatment: modification specifies the change of composition and/or structure of the polymer, whereas etching and

deposition refers to the removal and addition of substances to the original material. As we will show later in this chapter, the composition and/or structure of etched and deposited polymer surfaces are often irreversibly modified.[1] Other terms such as surface activation, chemical functionalization, and surface cleaning are also frequently used in plasma processing. They usually denote special changes in surface conditions which may include one or combinations of the above three types of surface processes.

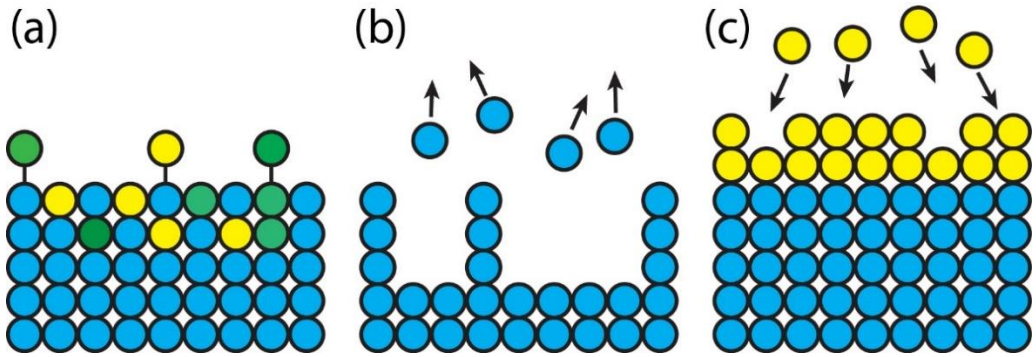

Figure 1.1 Simplified view of three types of changes that polymers may experience under plasma treatment: (1) chemical modification, (2) etching/ablation, (3) deposition

1.2.1 Chemical reactions of polymers

The chemical reactions of polymers can be classified into two main categories: (1) with polymer chain scission in which the polymer chain is split into smaller parts, and (2) without polymer chain scission where the side groups are usually modified.[7] For chain scission related reactions, two subclasses, namely chain-end scission (or unzipping) and random chain scission, can be separated. For reactions without chain scission, cross-linking and cyclization of the main chain or stripping/substitution/modification of the side groups may occur.[7]

When polymers are exposed to an APP source, many of the above reactions can happen simultaneously. Polymer etching is closely related to the chain scission reactions since dry etching relies on the formation of small molecular weight volatile products, such as CO and CO_2 at room conditions. All chemical reactions with the polymer will cause modification to a certain degree, whereas the special case of cross-linking may cause the densification of polymers which is very different from the other types of reactions.

Since plasma processing of polymers usually is performed without the presence of solvent, the reaction mechanism is rarely ionic but mainly radical. Similar to and inspired by free-radical reactions, previous researchers have proposed a universal Plasma Polymer Interaction (PPI) mechanisms for both low pressure plasma (LPP)[8] and APP,[9, 10] as discussed below.

1.2.2 Radical reaction mechanism of PPI

The chemical reaction process during PPI can be conveniently divided into four stages, although in reality this separation may not be realistic: (1) radical site creation, (2) radical site propagation, (3) chain cleavage/scission and (4) radical site termination. The process of radical site creation by surface reaction with plasma species is fast, while the rest of the three processes is usually slow and might still be happening after plasma exposure is complete.

Radical site creation

In the first stage, free-radical sites can be created on polymer surfaces by plasma treatment. Since the bond-dissociation energy of common covalent bonds in polymers is in the range of 2 – 5 eV (1 eV = 96.49 kJ/mol),[11] one could expect that when interacting with plasma species with high potential or kinetic energy, polymers may experience bond

cleavages which results in the formation of unsaturated molecular fragments (moieties with an unpaired electron). The unsaturated sites, often called radical sites, are highly reactive and can be responsible for further chemical transformation of the polymer.

The most abundant covalent bond in common polymers is C-H whose dissociation energy depends on its chemical environment.[12] The dissociation of C-H bond in polymers by plasma species, sometimes called H-abstraction, can be the most important channel of radical site creation. The strength of the C-H bond is the weakest on tertiary carbon site and strongest on primary carbon site. Take C_3H_8 as an example:

$$CH_3CH_2CH_2 - H \rightarrow CH_3CH_2CH_2 \bullet + H \qquad \Delta H^{\ominus} = 4.25\ eV \quad (1.1)$$

$$(CH_3)_2CH - H \rightarrow (CH_3)_2CH \bullet + H \qquad \Delta H^{\ominus} = 4.12\ eV \quad (1.2)$$

$$(CH_3)_3C - H \rightarrow (CH_3)_2C \bullet + H \qquad \Delta H^{\ominus} = 4.03\ eV \quad (1.3)$$

Therefore it would be easier to abstract the hydrogen on tertiary carbon sites than on secondary or primary sites.

Polymer radical sites can be created by heat, bombardment of UV photons, electrons, ions,[13] or via chemical reactions with neutral species such as atomic oxygen, hydroxyl radicals (OH)[9] and NO_x (x = 2,3, detail see section 1.3.5):[4]

$$R - H \xrightarrow{kT,h\nu,ion,e^-} R \bullet + H \bullet \qquad p\ depends\ on\ the\ energy \quad (1.4)$$

$$R - H + O \rightarrow R \bullet + OH \qquad p = 10^{-3}, 10^{-4}, 10^{-5} \quad (1.5)$$

$$R - H + OH \rightarrow R \bullet + H_2O \qquad p = 10^{-1}, 5 \times 10^{-2}, 12 \times 10^{-3} \quad (1.6)$$

where p is the estimated reaction probability for the tertiary, secondary and primary site provided by Bhoj and Kushner.[9] It can be seen that the tertiary H always has the highest H-abstraction reaction probability regardless of the attacking species. Upon the creation of

alkyl radicals (R•), these fragmented sites serve as reactive centers for the next step of polymer transformation.

Free radical sites can also be created by the homolysis of unstable chemical bonds, such as peroxides, hydroperoxides, carbonyls, disulfides and azo compounds, especially under UV exposure (photo-initiation).[14] For example, the photolysis of peroxide bond -O-O-:

$$R - O - O - R \xrightarrow{h\nu} 2R - O \bullet \quad (1.7)$$

$$R - O - OH \xrightarrow{h\nu} R - O \bullet + OH \quad (1.8)$$

Radical site propagation

The second stage of PPI is radical site propagation. The alkyl radicals created in the first step may further react with other gas phase species. For instance, interaction with oxygen leads to the formation of alkoxy (R-O•) and peroxide (R-OO•) groups:

$$R \bullet + O \rightarrow R - O \bullet \qquad p = 0.1 \quad (1.9)$$

$$R \bullet + O_3 \rightarrow R - O \bullet + O_2 \qquad p = 1.0 \quad (1.10)$$

$$R \bullet + O_2 \rightarrow R - OO \bullet \qquad p = 10^{-3} \quad (1.11)$$

Reaction of radical sites with other surface moieties may also occur. For example, H abstraction by alkoxy and peroxide radicals from its neighboring tertiary R-H bond:

$$R - O \bullet + RH \rightarrow R - OH + R \bullet \qquad k = 8 \times 10^{-14}\ cm^2\ s^{-1} \quad (1.12)$$

$$R - OO \bullet + RH \rightarrow R - OOH + R \bullet \qquad k = 5.5 \times 10^{-16}\ cm^2\ s^{-1} \quad (1.13)$$

Both of the gas-solid phase and solid-solid phase reactions contribute to the propagation of radical sites from one part of the polymer chain to the other. The formation of peroxides and hydroperoxides is also important for the polymer autoxidation and aging process in natural or O_3 environments.[7]

Chain scission/cleavage

The third stage of chain scission/cleavage plays an essential role for the degradation and etching of polymers. Some of the radical fragments created above are not stable, for example the C-C bond at alkoxy and peroxy radical sites may break through β-scission[15] which leads to the formation of carbonyl (C=O) groups and new alkyl radical sites:

$$R - O \bullet \xrightarrow{\beta-scission} R'C = O + R'' \bullet \qquad k = 10^3\ s^{-1} \quad (1.14)$$

Here k is the reaction rate coefficient. If this bond cleavage happens on tertiary carbon sites, it results in the formation of ketones (RC=OR) whereas that on secondary carbon sites leads to aldehydes (RHC=O). The aldehyde groups can further undergo H abstraction by atomic oxygen or hydroxyl radicals to produce carbonyl radicals (•R=O):

$$RHC = O + O \rightarrow \bullet R = O + OH \qquad p = 0.04 \quad (1.15)$$

$$RHC = O + OH \rightarrow \bullet R = O + H_2O \qquad p = 0.4 \quad (1.16)$$

The carbonyl radicals can experience chain cleavage which leads to the formation of CO, or react with O atoms to produce CO_2, both of these processes cause the ablation of polymers by producing volatile products:

$$\bullet R = O \rightarrow R' \bullet + CO \qquad p = 0.4 \quad (1.17)$$

$$\bullet R = O + O \rightarrow R'H + CO_2 \qquad p = 0.1 \quad (1.18)$$

Besides, the homolysis of peroxides (reaction 1.7) is also an important chain scission process, especially for the photo-degradation of polymers.

Radical site termination and cross-linking of polymers

The last stage is radical site termination where the free-radical sites on polymers recombine with gas phase species or other polymer radical sites to form relatively stable moieties. In the case of termination by gas phase species:

$$R\bullet + H \rightarrow RH \qquad p = 0.2 \quad (1.19)$$

$$R\bullet + OH \rightarrow ROH \qquad p = 0.2 \quad (1.20)$$

$$\bullet R = O + OH \rightarrow OH - R = O \qquad p = 0.12 \quad (1.21)$$

More importantly, the recombination between two radical sites may lead to the cross-linking of polymer chains,[7] which is well-studied for electron and high-energy photon (VUV, X-ray) treated polymers.[16] This type of cross-linking mechanism also plays a significant role for the plasma treated polymers,[17, 18] especially for rare gas discharges[19] in which the flux of neutral reactive gas species is low. Two types of cross-linking processes exist, i.e. intramolecular and intermolecular cross-linking. As suggested by its name, intramolecular cross-linking can connect multiple individual polymer chains together. Due to the long length of polymer chains, usually a small amount of intramolecular cross-links are sufficient to connect the whole system.

$$R\bullet + R'\bullet \rightarrow R - R' \qquad k = 10^{-15}\ cm^2\ s^{-1} \quad (1.22)$$

$$ROO\bullet + R'\bullet \rightarrow ROOR' \quad (1.23)$$

$$ROO\bullet + R'OO\bullet \rightarrow ROOR' + O_2 \quad (1.24)$$

Besides the recombination of radical site, cross-linking of polymers can also happen through copolymerization (if there are unsaturated bonds on the polymer chain) or reaction between functional groups[7] which are beyond the scope of this dissertation. Since both chain scission and cross-linking start from radical site creation, there is a constant competition between the two during plasma treatment.[17] A unique dynamic balance between chain scission and cross-linking can be established based on the specific plasma-polymer system.

1.3 The role of incident plasma species

In this section, we review the interaction of a few major plasma species with polymers. The generation and consumption pathways of these species in the gas phase are also mentioned. For other properties of these species, we refer readers to reviews[20, 21] and the following articles for O,[22] O_2(a),[23] O_3,[24] N_2 (a),[25] HNO_2,[26] HNO_3,[27] H_2O_2,[28] H,[29] NO,[30] NO_2,[31] OH [32] and UV photons.[33]

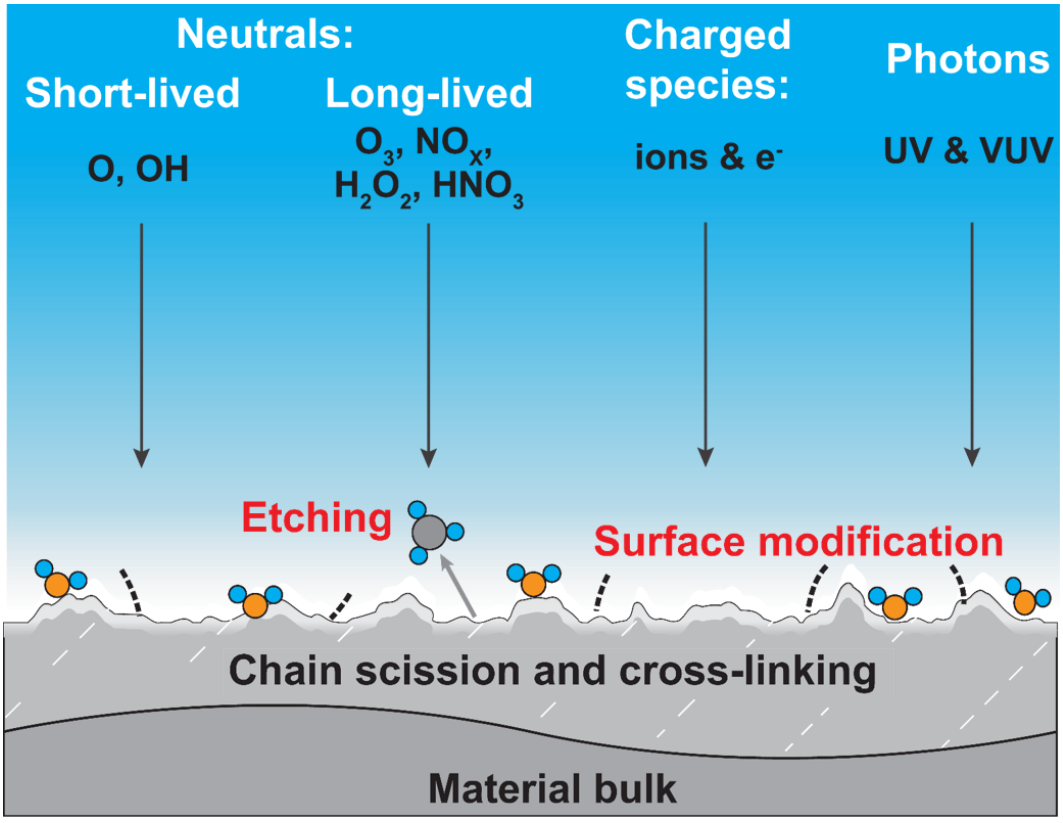

Figure 1.2 (a) Schematic diagram of plasma polymer interaction. Many reactive species generated by plasma could be transported to materials surface and participate in chemical reactions.

1.3.1 Atomic oxygen

Due to their short life time and high reactivity, large quantities of O atoms do not exist naturally in room environment. With APP sources, ppm level of atomic O can be generated by O_2 containing discharges. The existence and quantity of O atoms can be characterized by optical emission spectroscopy (OES)[34] or two photon laser induced fluorescence (TALIF),[35] although the former method actually measures the O atoms in exited states. Typical maximum density of atomic O found in APP sources ranges from 10^{16} – 10^{22} m^{-3}.[35-37] However most of these O density values are measured without the presence of a target surface. Study by Schröder *et al.*[38] showed that although dielectric targets do not change the distribution of atomic O, the implementation of a conductive surface near the effluent of a micro-atmospehric pressure plasma jet (APPJ) could increase the atomic O density and spread its distribution close to the target.

The main generation pathway of atomic O in APP is the dissociation of molecular oxygen by electrons, photons and excited species such as argon atoms (Ar*), argon excimers (Ar_2^*) and nitrogen metastables ($N_2(A)$).

$$O_2 + e^- \rightarrow 2O + e^- \quad (1.25)$$

$$O_2 + h\nu \rightarrow 2O \quad (1.26)$$

$$O_2 + Ar^* \rightarrow 2O + Ar \quad (1.27)$$

$$O_2 + Ar_2^* \rightarrow 2O + 2Ar \quad (1.28)$$

$$O_2 + N_2(A) \rightarrow 2O + N_2 \quad (1.29)$$

The decomposition of ozone can also contribute to the production of atomic O in both ground (^{3}P) and exited states (^{1}D),[39] such as the well-known ozone photolysis process:[40]

$$O_3 \xrightarrow{h\nu} O_2 + O(^1D, ^3P) \quad (1.30)$$

Atomic O can also be generated by the collisions between O_3 and $O_2(a^1\Delta_g)$. Simulation results suggest that this process can be responsible for the generation of almost all O atoms outside the plasma glow region:[41]

$$O_2(a^1\Delta_g) + O_3 \rightarrow 2O_2 + O \quad (1.31)$$

Atomic O can be easily destroyed in the gas phase before reaching the target surface. They are mostly consumed by the reactions with themselves or other neutral species such as O_2, OH and NO:[42]

$$O + O + M \rightarrow O_2 + M \quad (1.32)$$

$$O + O_2 + M \rightarrow O_3 + M \quad (1.33)$$

$$O + NO + M \rightarrow NO_2 + M \quad (1.34)$$

$$O + OH \rightarrow H + O_2 \quad (1.35)$$

Due to the abundance of O_2 molecules in room environment, usually reaction 1.33 is the main destruction channel for atomic O. In humid air conditions, the presence of water vapor can also be a strong quencher of O atoms. For example, Gaens *et al.* reported the reduction of atomic O density when adding H_2O into Ar + 2 % air RF APPJ.[43] Using pulsed corona discharge of humid-air, Ono *et al.* also found that water vapor could reduce atomic oxygen density and quench the production of ozone.[44]

The effect of atomic O on polymers has been studied since 1960s. In their early works, Hansen *et al.* applied "atomic O stream" on over 30 types of polymers and they found that atomic O could rapidly ablate polymer surfaces but leave the polymer bulk intact.[45] They distinguished the effect of atomic O on polymers from thermal oxidation by stating that "… atomic oxygen is a direct and rapid attack on the polymer and

responsible for a much greater proportion of the overall oxidation of the polymer than … simple thermal oxidation". Shortly after, this concept of etching and oxidation by atomic O was applied to improve polymer adhesive bonding.[46] A linear relationship between polymer etch rate and either atomic O concentration in the plasma[47] or the O atoms consumed during etching[48] has also been reported, consistent with a direct role of O atoms in the etching process. By the late 1980s, the role of atomic O on polymers under low pressure condition was generally established.[49]

The most important role of atomic O on polymers is its ability of creating free-radical sites. Atomic O has very high potential energy (4.8 eV above ground state O_2) and is capable of abstracting hydrogen from C-H bond as shown in reaction 1.5. This H-abstraction by atomic O is one of the most effective radical site creation channels in plasma processing of polymers, as will be shown in chapters 2 and 3.

Besides H-abstraction, a O atom can also add itself to an unsaturated bond such as C=C which leads to two neighbouring radical sites:[49]

$$-C = C - + O \rightarrow -\dot{C} - C\dot{O} - \tag{1.36}$$

In addition, as shown in reaction 1.9 atomic O can participate in radical site propagation. Interestingly the C-C bond strength at alkyl sites is not affected after H-abstraction, but the addition of oxygen to the unsaturated molecules, leading to a radical site on the carbon atom adjacent to the site of the addition, results in a weakened C-C bond.[49] This weak bond may react and form epoxides or carbonyl compounds.[50] Besides, atomic O can also react with aromatic rings, which form phenols by addition reactions.[8] These oxidation reactions with carbon rings consume a great amount of O atoms which

might explain why aromatic polymers are harder to etch. We will further discuss these reactions in chapters 6 and 7.

1.3.2 Singlet delta oxygen (SDO)

The ground state molecular oxygen O_2 ($X^3\Sigma_g^-$) has two lowest-energy excited states i.e. $a^1\Delta_g$ (0.98 eV) and $b^1\Sigma_g^+$(1.64 eV) and they are both spin singlets. The two excited states differ from each other by the structure of π-antibonding orbitals. The $b^1\Sigma_g^+$ state is less important in terms of processing materials because (1) it is short lived and quickly relaxes to ground state (7-12 s in gas[51] and 10^{-6}-10^{-3} s in solution), [52] and (2) it is less reactive with other molecules.[53, 54] In contrast, the transition of $a^1\Delta_g$ state (also called singlet delta oxygen, or commonly referred as "singlet oxygen") to ground state through electric dipole radiation is forbidden by selection rule,[55] therefore it has a relatively long (relaxation) life time of 45 min in the gas[51] and 10^{-6}-10^{-3} s in solution.[52] Besides, singlet delta oxygen is also highly electrophilic and known to be reactive in photo-oxygenation reactions.[56] These properties of singlet delta oxygen make it important for the plasma processing of materials.

The reactivity of singlet oxygen has been widely studied in fields ranging from atmospheric chemistry to biology and medicine.[57] Among the many generation pathways,[58] in non-local thermodynamic equilibrium (LTE) plasma it is mainly created through photoexcitation, collision induced photoexcitation, photolysis of ozone[40] and other reactions that involve O atoms. The absolute densities of singlet delta oxygen can be measured using infrared optical emission spectroscopy.[55, 59] For example Sousa *et al.* measured the $a^1\Delta_g \rightarrow X^3\Sigma_g^-$ (0.98 eV) emission line at 1265 nm,[23] and they found that the singlet delta oxygen density can be up to 6×10^{15} cm^{-3} in He/O_2 RF APPJs.

In the gas phase singlet delta oxygen is destroyed mainly through radiative or collisional induced decay. When reaching material surfaces, singlet oxygen can react rapidly with unsaturated bonds, phenols, anionic and neutral nucleophiles including sulfides and amines.[56, 58, 60] Early work by organic chemists found that singlet oxygen was able to oxidize materials that are unaffected by ground molecular oxygen. Although these reactions between singlet oxygen and organic compounds are mentioned less in the plasma community, organic chemists have been applying them for chemical synthesis for decades.[61]

Many reaction mechanisms with regard the oxidation of organic compound by singlet oxygen have been proposed, and the details can be found elsewhere.[56, 60, 61] The most important aspect about singlet oxygen is its ability of oxidizing certain moieties on the polymer chain without causing dramatic chain scission (and hence no etching). Besides, some polymers such as polystyrene cannot be oxidized by singlet oxygen alone.[62] However, in the presence of other more reactive constituents of the plasma effluent (e.g. atomic O and hydroxyl radicals), singlet oxygen can react with the radical sites on polymer chains.

1.3.3 OH

Hydroxyl radicals are one of the most oxidative neutral species produced by APP. They are also considered as the building blocks for the formation of other reactive species such as HO_2, H_2O_2, HNO_2 and HNO_3.[63, 64] Hydroxyl radicals are usually generated in water containing plasma where water vapor may be fed or entrained from ambient. The production and loss mechanisms of hydroxyl radicals in plasma have been thoroughly reviewed by Bruggeman and Schram.[65]

The main generation pathways of OH are the electron impact dissociation of H_2O, electron dissociative attachment to H_2O, electron-water ion dissociative recombination, positive-negative ion recombination, water ion hydration and the dissociation of H_2O by radicals and metastables. Because of water's relatively low ionization energy (12.6 eV) compared to He (24.59 eV), Ar (15.76 eV) and N_2 (15.58 eV), water ions would be the dominant types of ion in water containing plasma even when water is not the main gas constituent. Under atmospheric pressure, water ions usually exist in cluster form, i.e. $H_3O^+(H_2O)_n$, due to the strong hydration caused by high gas density.[66] Reactions with water ion clusters can be a major OH generation channel besides electron dissociation. It is worth mentioning that O_2 has a similar ionization energy of 12.07 eV, which might compete with water ionization process when both O_2 and H_2O are involved in the plasma.

Hydroxyl radicals can be lost through gas phase reactions.[64, 65] One interesting channel is the destruction of OH by atomic O (reaction 1.35). Verreycken *et al.* has suggested that a further reaction cycle might exist for a net production of one O_2 molecule from a net loss of two O atoms:[67]

$$OH + O \longrightarrow H + O_2; \quad k = 2.7 \times 10^{-17}\ m^3/s \tag{1.35}$$

$$H + O_2 + M \longrightarrow HO_2 + M; \quad k = 5.6 \times 10^{-19}\ m^3/s \tag{1.37}$$

$$HO_2 + O \longrightarrow OH + O_2;\ k = 4.8 \times 10^{-17}\ m^3/s \tag{1.38}$$

with rate coefficient k at 400 K. In chapter 2 we will show the loss of OH when adding O_2 to Ar/H_2O RF APPJ.[68]

When interacting with polymer surfaces, hydroxyl radicals are effective on creating radical sites through homolytic bond cleavage as shown in reaction 1.6. The resultant carbon radical sites can further react and eventually cause polymer chain scission as

described in section 1.2. The etching of polymers[69] and carbon allotropes, such as amorphous carbon and carbon nanotubes,[70] by water plasma were observed in low pressure conditions. In chapters 2 and 5, we will explore the fast etching of polymers by OH generated in atmospheric pressure water containing plasma.[68]

Another behavior of OH is its reaction with aromatic structures, which was widely discussed in aqueous solutions[71] and polluted atmospheres.[72] Besides H abstraction, hydroxyl radicals can also hydroxylate benzene ring to form free radicals:[8]

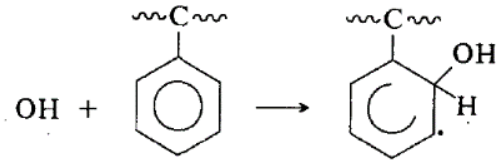

(1.39)

These radicals can further react with other species from plasma and cause oxidative cleavage of the phenol ring. Although it is hard to quantify such processes, one should expect slower etch rate for aromatic polymers treated by water containing plasma since the ring structure serves as a sink for OH species.[68] This will later be demonstrated in chapters 2 and 5.

1.3.4 Ozone

Since the early experiments by Siemens,[73] ozone generation by oxygen containing plasma has been widely studied and industrialized in the past century.[74] In O_2 containing APP sources, ozone is generic and usually abundant due to its long lifetime. The main creation channel of ozone is the collisional combination of atomic O and oxygen molecules with a third party, as shown in reaction 1.33. Interestingly this process is also the main loss mechanism for atomic O in the gas phase. The main loss pathways of ozone are through ozone photolysis under UV light (reaction 1.30),[40] thermal decomposition (major when

the gas temperature is high) and reactions with OH and H radicals (presence of water vapor).[44] The density of ozone can be easily measured by UV absorption based on Beer's law.

Ozone is highly electrophilic and known for its ability to react with unsaturated bonds such as alkenes, alkynes and azo compounds which is commonly referred as ozonolysis process.[75] The ozonolysis of elastomers, also called ozone cracking, usually starts from a direct 1,3-dipolar addition of one ozone molecule to the double bond. Such reaction leads to the formation of unstable intermediates (called ozonide) which quickly cleaves at room temperature into acids, esters, ketones, and aldehydes.[75]

The ozone cracking of elastomers is not an etching process. In fact, the cleavage of unsaturated bonds by ozone does not lead to the continuous formation of volatile products at atmospheric pressure. This was confirmed by the fact that cracking only happens when the rubber is stretched above a critical elongation. Unstretched elastomers react with ozone until all of the unsaturated double bonds on the surface are depleted, and then the reaction stops due to the saturation of surface oxidation.[76] The thickness of ozone affected layer on rubber is estimated to be 6 – 24 nm (10 - 40 monolayers).[77]

The polymer surface treatment by ozone under UV light, sometimes referred as UVO process, is a common technique used to increase surface energy and wettability. When the UVO treatment time is long enough, polymers may experience chain scission. The UVO oxidation products, also known as low molecular weight oxidized material (LMWOM), is not volatile and only weakly bonded to the polymer surface.[78],[79] Studies on the UVO of polypropylene[78] and poly(ethylene terephthalate)[80] have shown that the surface modification actually comes from atomic oxygen (generated by ozone photolysis,

reaction 1.30). Although ozone exposure of polymers without UV also causes surface oxidation, it takes rather long time to reach the same amount of modification compared to that treated by UVO.[80] The polymer oxidation by ozone without UV might also be largely due to atomic oxygen generated through thermal decomposition of ozone. Aromatic polymers can also be oxidized by UVO treatment. Besides the effect of atomic O, Klein *et al.* proposed that ozone might react directly with the unsaturated bonds on phenyl rings and form carbonyl groups.[81]

1.3.5 Reactive nitrogen species (RNS): NO, NO_2 and NO_3

Reactive nitrogen species (RNS) commonly refers to nitrogen containing radicals with unpaired electron such as NO_x (x=1,2,3), and their derivatives such as nitrous oxide (N_2O), dinitrogen pentoxide (N_2O_5) nitrous acid (HNO_2), alkyl peroxynitrites (ROONO) and alkyl peroxynitrates (RO_2NO_2).[82]

In APP, many nitrogen containing species can co-exist with a highly dynamic balance. As indicated in figure 1.3, nitrogen species can be converted back and forth via various pathways.[83] For material etching/modification, the importance of these species depends on their reactivity and density at the target surface. Due to the complexity of reaction kinetics involving RNS,[84] we focus on discussing NO_x radicals, the most fundamental RNS, and other RNS will be mentioned along the way.

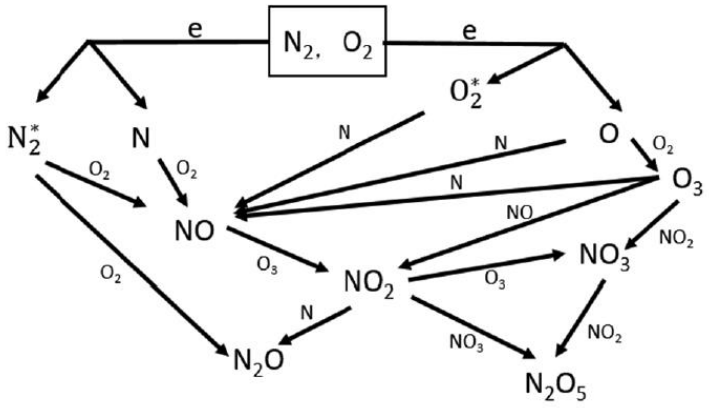

Figure 1.3 Reaction pathways between reactive nitrogen species.[83]

First, NO is the simplest RNS and it is responsible for the generation of other nitrogen containing species. Besides reactions shown in figure 1.3, NO can also be produced by reactions with metastable $N_2(A^3\Sigma_u^+)$, $N(^2D)$ atoms and NH. When NO is exposed to oxidative environments, it can be rapidly converted into other nitrogen containing derivatives, the particularly two of them being NO_2 and NO_3. The density of NO_x species generated by APP sources can be on the ppm level, for example, Ham *et al.* measured over 10^{20} - 10^{21} m^{-3} of NO in the effluent of a RF APPJ with Ar + 2% air feed gas.[85] Simulations by Gaens *et al.* showed that Ar APPJ operated in humid air could generate ~10^{21} m^{-3} NO, 10^{20} m^{-3} NO_2, ~10^{20} m^{-3} of HNO_2 and HNO_3.[41]

The reactivity of NO_x increases with the amount of oxygen x in the molecules. Although NO contains an unpaired electron, its reactivity lies at the low extreme among radicals and appears to be only slightly more reactive than the ground state O_2.[86] NO usually reacts with the radical sites on polymer by adding itself to them, e.g. reaction 1.43 and 1.44.

In contrast, NO_2 [87] and NO_3 [88] are more reactive and can cause both oxidation and nitration of other materials - they react with organic compounds through: (1) hydrogen abstraction, and (2) addition reactions with radical sites and/or unsaturated bonds. The H abstraction reaction of NO_2 and NO_3 is similar to that of O and OH, with the formation of carbon radical site and HNO_2/HNO_3:[4]

$$RH + NO_2 \rightarrow R\bullet + HNO_2 \quad (1.40)$$

$$RH + NO_3 \rightarrow R\bullet + HNO_3 \quad (1.41)$$

As expected, the ease of H abstraction by NO_2/NO_3 is in the order of tertiary > secondary > primary site. The gas phase reaction rate of NO_3, OH and atomic O with some organic compounds can be found in reference.[4] In most cases, the reaction rate constant for NO_3 is two orders of magnitude lower than that of atomic O.

The addition reaction of NO and NO_2 to polymeric radical sites usually leads to a complex mixture of products including nitrate ester ($RONO_2$), alkyl peroxynitrites (ROONO) and alkyl peroxynitrates (RO_2NO_2). Particularly, during radical site propagation (section 1.2.2), alkyl radicals are oxidized to form alkoxy and peroxy radicals which may further react with NO and NO_2:

$$RO\bullet + NO_2 + M \rightleftharpoons RONO_2 + M \quad (1.42)$$

$$R - OO\bullet + NO \longrightarrow RONO_2 \quad (1.43)$$

$$R - OO\bullet + NO \longrightarrow [ROONO]^* \longrightarrow RO\bullet + NO_2 \quad (1.44)$$

$$R - OO\bullet + NO_2 + M \rightleftharpoons RO_2NO_2 + M \quad (1.45)$$

The addition of NO to an alkene which forms nitroso alkyl radical might be possible, but Philips *et al.* have shown that pure NO does not react with isobutene.[89] Reactions of NO_2 and NO_3 with alkene can happen very easily. In such situation, NO_2 and

NO_3 can add themselves to the least sterically hindered end of the C=C bond to form a radical adduct intermediate:

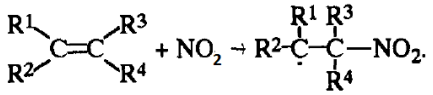

(1.46)

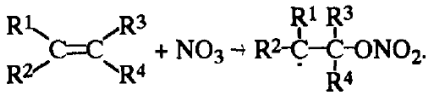

(1.47)

These intermediates contain alkyl radical sites, and they could further react as discussed in section 1.2.2.

Aromatic rings are relatively inert to NO_x radicals. This can be seen by the extremely slow reaction rate between NO_3, the most reactive among NO_x, and benzene with only the upper limits of the rate constant measureable (296 K, $< 2.3 \times 10^{-17}$ cm^3 $molecule^{-1}$ s^{-1}).[90] In the same article, Atkinson *et al.* studied the reactions of NO_3 with a series of aromatic compounds and they found that most reactions proceed via hydrogen abstraction from the substituent groups.[90]

Reactions of NO_x with organic material usually do not lead to faster material removal/etching. Knopf *et al.*[91] studied the heterogeneous oxidation of saturated alkane hydrocarbon monolayers by NO_3, and through characterizations by XPS they found that NO_3 did not cause much removal of organic material – a maximum of 10% of the organic layer was volatilized under the most extreme conditions. Interestingly, they confirmed that the reaction caused the formation of C-O groups, ketones/aldehydes and carboxyl groups, but only 1% of total surface elemental composition could be assigned to nitrogen (attributed to nitrate group). They also calculated the uptake coefficient - the fraction of collisions with the surface that result in a reaction - of NO_3 by an alkane monolayer which is about $(8.8 \pm 2.5) \times 10^{-4}$. Gross *et al.*[92] studied the oxidation of alkene monolayers by

NO_3. Their results were consistent with those by Knopf *et al.*: the treated surface showed the formation of C-O, aldehyde/ketone, carboxyl groups, and nitrogen species. Using IR spectroscopy and SIMS, they also confirmed the formation of $RONO_2$ which helped explain why NO_3 does not cause material etching - the formation of $RONO_2$ consumes alkyl peroxy (ROO•) and/or alkoxy (RO•) radicals from the surface, and hence reduces further chain scission. Recently Bartis *et al.* observed the formation of surface nitrate on various polymers and biomolecules treated by surface micro-discharge (SMD) and APPJ.[93, 94] They speculated that the surface nitrate, less than 1% of total surface elemental composition from XPS measurement, might come from gas phase NO_x species. In chapters 4, 6 and 7 we will further characterize the SMD treated polymers with both real-time Ellipsometry and XPS. We will show that the NO_3 only forms on the top 2 nm of the polymer surface and evaluate the polymer thickness change under SMD treatment.[95]

1.3.6 Ion Bombardment

Because of the quasi-neutral property of plasma bulk, the ion energy distribution in a diffusive glow discharge is thermal which is much less than 1 eV on average. However, in the region where plasma directly interacts with a target, called a plasma sheath, the situation is much different. Due to the potential drop in plasma sheath and pre-sheath,[96] ions can be greatly accelerated within the sheath thickness (~ Debye length λ_D). Depending on RF biasing condition, the ion energy can be from a few eV to hundreds of eV when reaching a dielectric material surface.[97] The bombardment of these energetic ions plays an essential role in the LPP-based pattern-transfer processes widely applied in semiconductor industry. For the direct interaction of polymers with a diffusive APP source (Townsend breakdown regime), the ion bombardment process can be comparable to that

of LPP. However, if the target material is not in direct contact with a diffusive APP, ion bombardment is prevented due to the short mean free path of ions at atmospheric pressure.

Since most of APP sources are rather filamentary with a distinctive streamer breakdown mechanism, the formation and transport of the positively charged streamer head in filamentary plasma can lead to a very different ion bombardment mechanism compared to diffusive plasma. When the filament is far from target surface, the enhanced electric field in the streamer can reach 200 kV/cm or 800 Td.[98] When the streamer strikes a target surface, the majority of the electric field results in the formation of plasma sheath at the dielectric surface. According to works by Natalia and Kushner,[99, 100] the APP sheath - with plasma densities of 2×10^{14} cm^{-3} to 10^{15} cm^{-3} and potential drops of 2–10 kV in the sheath – can last many nanoseconds with a thickness of a few tens of μm and an electric field of a few hundreds of kV/cm. Ions are accelerated in this transient plasma sheath and carry up to tens of eV when hitting the target surface.[99, 100] Another interesting phenomenon is the spreading of streamers on material surface, often called surface streamers, which typically happens in a few nanoseconds with a width of a few mm.[100, 101] When there are multiple streamers striking the surface, the nearby surface streamer may interact with each other and form self-organized lateral structures.[102]

When striking polymer surface, ions first loose its kinetic energy and subsequently can be neutralized. There are two major ion-material interaction pathways during these two processes: (1) interaction with the electrons or (2) interaction with the nuclei. The former pathway leads to bond breaking whereas the latter results in atomic displacement in the material or sputtering. The penetration depth of ions depends on not only the type of ions

and their energy but also the target material properties. For common polymers and ions generated by low temperature plasma (up to hundreds of eV), it is usually a few nm.[103]

As discussed in section 1.2.2, ion bombardment can cause the formation of polymer radical sites which may further lead to chain scission, etching and/or cross-linking. With other elemental components such as O and N from the polymer or gas phase, ion bombardment may result in significant chemical modification and etching of polymer surfaces. However the specific effect of ion bombardment relies on the polymer properties as well as the nature of the ions such as type, energy and dose. For example, Gokan *et al.* found that polymer etching by oxygen ion bombardment was 15 times faster than that under argon ion bombardment, though the etch rate enhancement of oxygen ion was considered to be ion-assisted chemical etching.[104] The authors also found that the polymer etch rate under ion bombardment has a linear dependence on the $N/(N_C-N_O)$ factor of the etched materials which is later known as the Ohnishi number/factor[105] where N, N_C, and N_O stands for the total number of atoms, carbon atoms and oxygen atoms in a repeating unit. Another interesting behavior of polymers under the exposure of highly energetic ions (~hundreds of eV) is the formation of dense amorphous carbon (DAC) layer as reported by Bruce *et al.*.[106] At last, we want to mention that reports with regard to the control and application of ion bombardment by APP sources are still scarce. Although moderately energetic (up to tens of eV), ion bombardment by APP may find its application in processing biological materials due to the local sheath formation and high filed strength at target surface such as cell membranes.[100, 101] We will provide evidence on ion induced effects from APP sources in chapter 3.

1.3.7 UV effects

Low temperature plasma is known as a source of UV and VUV radiations whose intensity and wavelength depend on the pressure, gas composition and power density.[107] In glow discharges, strong UV radiation may come from atomic emission lines, such as those of rare gas, and molecular emission bands in the case when molecular gas, e.g. nitrogen or hydrogen, exists.

The effect of energetic photons on polymers, especially in the UV and VUV region, has been widely studied and well documented in reviews and textbooks.[108-111] The UV photons can participate in all the four stages of PPI discussed in section 1.2.2. During photo-initiation, UV photons are able to create polymer radical sites by H-abstraction (reaction 1.4) or the photo-cleavage of peroxides (reaction 1.7), hydroperoxides (reaction 1.8), carbonyls, disulfides and azo compounds.[14] UV photons can also facilitate radical site propagation such as reaction 1.11 and 1.13.[111] For UV induced chain scission, low molecular weight products may form as a result. In the report by Skurat *et al.*, the chain scission efficiency of UV photons was estimated to be 4–5 times greater than H removal.[112]

Another factor that makes UV photons important for polymer treatment is its neutrality and relatively deep penetration depth (up to hundreds of nms)[113] compared to other plasma species. Although short wavelength photons have shallower penetration depth, they contain more energy and hence are more effective in causing chemical reactions.[110] Some gas molecules in air have large cross section to certain wavelengths of UV photons, e.g. the strong absorption around 124.6 nm by O_2.[114] Due to the high gas

density at atmospheric pressure, the UV effect from APP might be strongly attenuated when the interaction happens in air or O_2-rich environment.[6, 115]

1.4 The influence of target material properties

1.4.1 Substrate temperature dependence

Kinetically, the rate of chemical reactions related to PPI increases with temperature. Although polymer etch rate are controlled by many chemical reactions and most of them are far from being elementary, Arrhenius equation may still be used to empirically fit the temperature dependence of polymer etch rate:[116]

$$k = A \cdot \exp(\frac{-E_a}{k_b T}) \tag{1.48}$$

where k is the rate constant, A is the pre-exponential factor, k_b is the Boltzmann constant and T is the temperature. The empirically fitted parameter E_a represents the conglomeration activation energy of a group of etching related chemical reactions. The E_a value for a given polymer/gas system can be a function of processing parameters such as power and gas flow rate etc.

The substrate temperature dependence of polymer etch rate, especially for LPP, has been studied in great detail.[48, 117] Typically the E_a of photoresists processed by low pressure O_2 plasma is in the range of 0.1 – 0.64 eV. In chapter 3 of this dissertation we will discuss such measurements for polymers processed by APP.[1, 118] Surprisingly our measured E_a values are small compared to those of LPP which can be associated to the facilitating effect of energetic species such as ions and UV photons from APP sources.

1.4.2 Compositional and Structural dependence

The PPI process is highly dependent on the composition and structure of target polymers. Usually plasma parameters have to be intentionally tailored for the accurate etching of certain polymers. In the early works from the 1980s, the compositional and structural dependence of polymer etching by LPP has been intensively investigated.[117] Despite the difference between LPP and APP sources, some core findings of the structural dependence of polymer processing by LPP may still apply in APP.

In a comprehensive study by Taylor and Wolf,[119] 40 types of polymers were etched by O_2 LPP and the authors found that polymer etch rate strongly depended on the strength of the side chain bonds attached to the backbone. Stronger bonds on the polymer side chain, such as aromatic, polar functional groups and metallic atoms, decrease the etch rate whereas weaker bonds directly linked to the chain or in the chain greatly accelerate the etch rate. This interesting observation was further confirmed by several other reports[8, 104, 120] with the generic conclusion that aromatic polymers, such as those found in positive photoresists, have higher etching resistance than their aliphatic analogues such as PMMA. Interestingly, Taylor and Wolf also concluded that the weaker bonds had little or no effect to the etch rate if they were remote from the backbone. Thus, polymers with phenyl, cyano, and fluorine substituents on the backbone showed the most etch-resistivity, and the majority of aromatic polymers was found to etch 2-4 times slower than their nonaromatic counterparts.[8]

The stability promoted by polar functional and aromatic groups might be due to the reaction competition between backbone cleavage and the destruction of the side chains. In the early works of plasma etching, it was believed that the stability of aromatic polymers

lied in the influence of weaker tertiary C-H bond, or in the catalytic property of aromatic ring for the recombination of oxygen atoms. However in 1986, Moss *et al.* pointed out that this may not be true.[8] They found that the stability was rather independent of where the benzene ring was in relation to the polymer backbone. They suggested that the explanation was more likely to be the consumption of atomic oxygen with benzene ring to from phenols:

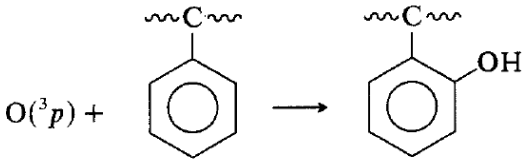

(1.49)

This reaction competes with the usual H-abstraction of atomic oxygen which creates free radical cites that could lead to polymer backbone cleavage. Thus the aromatic sidechains could serve as a "sink" for oxygen atoms and impede the initiation stage.

Besides functional groups, the crystallinity of polymers can also affect PPI. Generally, the crystallinity of polymers influences the accessibility of plasma species to the reactive sites on polymers. The general consensus is that amorphous (non-crystalline) phase has higher plasma etch rate than its crystalline counterpart, or in other words plasma etching has certain selectivity on amorphous phase. For example, Okuno *et al.* investigated the correlation between crystallinity and etching by air plasma with two model systems, i.e. PET and nylon 66 fibers.[121] They found that air plasma preferentially interacted with macromolecules in the non-crystalline domain, whereas the crystalline and quasi-crystalline phases were least affected by the plasma treatment. Later on Olde *et al.* found that CF_4 plasma treatment of polyethylene resulted in a preferential etching on amorphous phase than the crystalline phase.[122] More recently Junkar *et al.* studied the role of polymer

crystallinity on the etching of PET by oxygen plasma.[123] They found that the polymer crystallinity not only influenced the surface topography, the formation of new functional groups, etching and hydrophobic recovery (ageing) but also affected the recombination probability of neutral atoms on polymer surface.

1.5 Reaction products of PSI

Because plasma etching is a material removal process, volatile products must be formed at or near the polymer surface and subsequently removed to the gas phase. Direct measurement of volatile products from polymer is hard to achieve because of the interaction of the products with reactive species in the gas phase. This is especially difficult for APP-polymer systems due to the short mean free path of etch product at atmospheric pressure. It is worth mentioning that some volatile products produced in LPP (e.g. LMWOM mentioned in Section 1.3.4) might not be volatile at atmospheric pressure.

Besides volatiles, the etched polymer surface can also be viewed as the product of etching reactions. Since we have discussed surface modification previously, here we only mention one important characteristic of the etched surfaces. The etched polymer surfaces are rarely well-defined and homogeneous. Based on the treatment conditions, the etched surface might be highly cross-linked or composed of much shorter polymer chains. In the former case, the cross-linking can cause the densification of polymer surface which might further reduce the permeability of the surface layer. It is expected that the presence of a cross-linked surface layer could suppress the diffusion of gas or solid phase additives into the polymer bulk.[124] In the latter case, smaller molecular weight non-volatile products might be formed from the chain scission processes.[125]

In addition, many reaction intermediates may also be formed during plasma treatment. These intermediates are usually unstable and may decompose into a conglomerate of many different functional groups on the etched surface.[126] This is due to the reactions between surface radical sites which are created during plasma exposure and left on polymer surface. Usually these reactions are slow and might take hours to complete. Such post-reactions after plasma exposure is also called aging and have been widely discussed in the field of polymer wettability and adhesion improvement by both LPP[127, 128] and APP[17, 129] treatments.

1.6 The approach of studying PSI at atmospheric pressure

As a rule of thumb, the type and density of these reactive species on the gas-solid interface directly determines the end result of plasma treatment. Therefore controlling the composition of plasma species near the interface is the key for studying PSI mechanisms. There are two major factors that influence the type and amount of reactive species near the interface: (1) the generation of reactive species by the plasma sources and (2) their subsequent transport through and interaction with the ambient environments. Since the particles in LPPs transport through free molecular flow, the effect of individual species on material surface can be determined by using controlled beams.[130, 131] However, APP processing performed at ambient conditions is characterized by short mean free paths (e.g. for air λ_{MFP} is about 65 nm)[132] which makes beam methods hard to apply because the interaction of the originally well-defined fluxes with the environment results in the conversion to other reactive species.

Thus, the most important objective of this dissertation is to develop an alternative approach of studying PSI at atmospheric pressure and to verify the role of plasma species

on surfaces measured previously in low pressure conditions. In this section, we show our practice of using well-controlled source-ambient-sample systems and comprehensive characterization techniques of both gas/plasma phase and material surface to realize these goals.

1.6.1 Plasma Sources

The popularity and simplicity of APP sources stimulated many new source designs and power configurations, however the effect of different APP sources or same source operated at different conditions can be dramatically different. This causes difficulties with regard to reaching a universal understanding of APP effect on polymers.[133] To resolve this issue, we chose two representative and well-characterized APP sources, namely RF-APPJ and SMD, as our main processing tools.

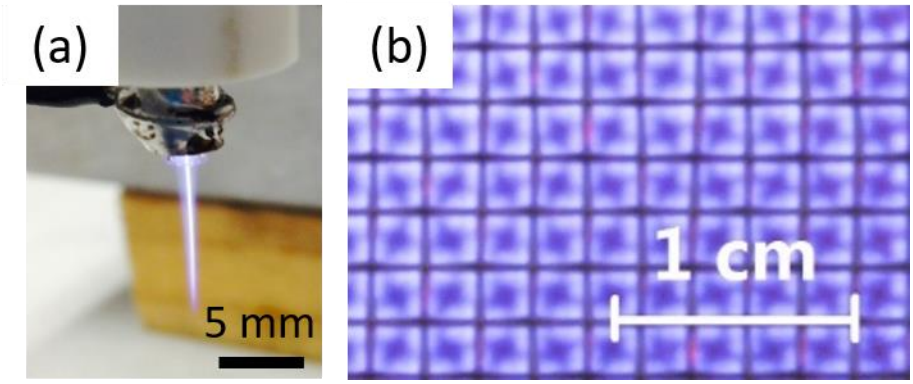

Figure 1.4 The optical image of APP sources: (a) RF-APPJ and (b) SMD

The RF-APPJ operates with noble carrier gas (e.g. Ar) and is originally developed by Bruggeman.[134] Its property has been studied in joint effort by many research groups with regard to its flow dynamics,[135] gas temperature,[134] electron temperature and density,[134] density of reactive species such as NO,[136] O and O_3,[137] as well as computer simulations of its chemical reaction pathways.[43, 138] With these shared information of the

same plasma source, the interpretation of surface characterization results can be greatly improved,[1, 68] as shown in chapters 2, 3 and 5.

The SMD[139] source and its variation SMD tube array (SMD-TA) operate without noble gas (usually N_2/O_2 mixtures). Target surfaces of SMD do not serve as part of the electrode or dielectric and are completely independent of the plasma generation process. This separation between discharge generation and surface interaction makes SMD treatment more stable, easier to control and more flexible on target geometry. Besides, It is the diffusively long-lived neutral reactive species rather than the discharge filaments are responsible for surface reactions, which makes the SMD source an excellent platform for studying effect of less reactive plasma species.[140]

Detailed operating parameters of these plasma sources are given in the experimental section of each chapter.

1.6.2 Controlled gaseous environments

Since both the APP sources and material surfaces are constantly exposed to their atmospheric environments, one also needs to consider the interaction of ambient gas molecules with plasma species and target surfaces.[140, 141] The difficulty of evaluating ambient gas effect lies in the uncertainty of room air compositions. By controlling the gaseous environment wherein PSI took place, we could suppress certain unwanted interactions of plasma species with the ambient and regulate the delivery of reactive species to material surfaces. As shown in later chapters, we achieved such control by refilling vacuum chambers with desired gas composition.[142] In chapters 2 and 3, the effect of gas admixtures in the environment were also studied using these techniques, for example water vapor [136, 140, 143, 144] and oxygen.[1, 141, 145]

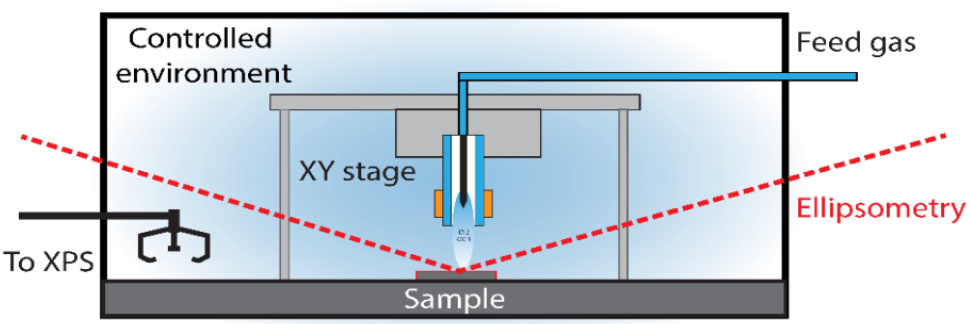

Figure 1.5 A schematic of polymer processing by RF-APPJ in controlled environment. Material property can be monitored in real time through *in-situ* Ellipsometry. The surface chemistry of materials can be characterized by vacuum-transferred X-ray photoelectron spectroscopy (XPS).

1.6.3 Simplified model materials

To further reduce the complexity of PSI, we use polymers with representative functional groups to study the effect of plasma species on certain surface moieties.[68] We choose vinyl polymers PS, Poly(methyl methacrylate) (PMMA) and polyvinyl alcohol (PVA) for investigating aromatic rings, ester and alcohol groups, respectively.

To bridge the link between the principles of PSI and APP applications, we will explore the effect of APP treatment on the cell membrane of live bacterium. We choose *Escherichia coli* (*E. coli*) and its major cell membrane components lipopolysaccharide (LPS) and peptidoglycan (PGN) as a model biological system. Correlation between plasma effect on biomolecules and live bacterium will be made in chapter 8.

1.6.4 Characterization techniques

Due to the multi-phase nature of PSI, we integrated many characterization techniques in our study, including that of plasma/gas phases such as optical emission

spectroscopy (OES), Fourier transform infrared spectroscopy (FTIR) and UV absorption, and that of material surfaces such as X-ray photoelectron spectroscopy (XPS), attenuated total reflection (ATR) FTIR, atomic force microscopy (AFM) and Ellipsometry. We will explore a new ultrathin (< 10 nm) film characterization method using p-polarized light enhanced ATR-FTIR in chapters 6 and 7. The detailed instrumentation and operating parameters will be given in the experimental section of each chapter.

Chapter 2: Model Polymer Etching and Surface Modification by a Time Modulated RF Plasma Jet: Role of Atomic Oxygen and Water Vapor

P. Luan[1], A. J. Knoll[1], H. Wang[1], V. S. S. K. Kondeti[2], P. J. Bruggeman[2] and G S Oehrlein[1]

[1] Department of Materials Science and Engineering and Institute for Research in Electronics and Applied Physics, University of Maryland, College Park, MD 20742, USA

[2] Department of Mechanical Engineering, University of Minnesota, Minneapolis, MN 55455, USA

Journal of Physics D: Applied Physics, 50 (3), 03LT02 (2017)

Abstract

Surface interaction of a well-characterized time modulated radio frequency (RF) plasma jet with polystyrene, poly(methyl methacrylate) and poly(vinyl alcohol) as model polymers is investigated. The RF plasma jet shows fast polymer etching but mild chemical modification with characteristic carbonate ester and NO formation on the etched surface. By varying plasma treatment conditions including feed gas composition, environment gaseous composition, and treatment distance, we find that short lived species, especially atomic O for Ar/1% O_2 and 1% air plasma and OH for Ar/1% H_2O plasma, play an essential role for polymer etching. For O_2 containing plasma, we find that atomic O initiates polymer etching and the etching depth mirrors the measured decay of O atoms in the gas phase as nozzle-surface distance increases. The etching reaction probability of O atom ranging from 10^{-4} to 10^{-3} is consistent with low pressure plasma research. We also find that adding O_2 and H_2O simultaneously into Ar feed gas quenches polymer etching compared to adding them separately which suggests the reduction of O and OH density in Ar/O_2/H_2O plasma.

2.1. Introduction

Cold atmospheric pressure plasma jets (APPJs) are able to generate chemically reactive species desired for material processing [146, 147] and biomedical applications such as wound healing, disinfection and decontamination [148, 149]. While a great amount of attention has been devoted to characterizing these APPJ sources [146, 150-153] and applying them to cell culture studies [154], *in vitro* experiments [155], clinical trials [156] and other applications, comparatively little is known about the interaction mechanisms between cold atmospheric pressure plasma and cells, biomolecules, polymers [140] or dielectrics [157].

Since both plasma source and material surfaces are constantly exposed to the surrounding ambient, the gaseous environment is coupled with the plasma and material surface and influences plasma-surface interactions (PSI). Particularly for plasma medicine applications, plasma sources are operated in humid air environment which contains water vapor that might play an important role in both gas phase and surface characteristics since the dissociation of H_2O can initiate a wide variety of plasma and surface chemical processes [63].

Previously we reported plasma processing of model polymers and biomolecules by kHz double ring-APPJ [141, 158, 159], kHz pin-APPJ [6] and surface micro-discharge [93, 94] sources using well-controlled environments. Surface chemical modification by these plasma sources was generically observed, whereas etching was highly source dependent. The lack of quantified reactive species measurement for these plasma sources impedes the interpretation of material surface response with plasma treatment.

In the present work, the surface interaction of a well-characterized time modulated radio frequency (RF) plasma jet with model polymers is investigated using both controlled

and uncontrolled environment. This plasma source has been previously described [134] and studied in detail including flow dynamics [135], gas temperature [134], electron density and temperature [134], biochemically reactive species density such as NO [136], O and O_3 [137]. Numerical simulations of the NO and O density profile in the plume region have also been performed which predict significant quenching of O and NO density with additional water impurities in the feed gas [43]. The available information provides the opportunity to improve our understanding of PSI under atmospheric pressure.

In this work we have investigated the interaction of the RF jet with several model polymers namely polystyrene, poly(methyl methacrylate) (PMMA) and poly(vinyl alcohol) (PVA). We find that the RF jet can induce fast polymer etching but mild chemical modification, both of which reflect plasma treatment conditions such as feed gas composition, composition of the gaseous environment and treatment distance. Based on measured atomic O density data of this source [43], we provide evidence of the direct relation between the polymer etching rate and the incident atomic O flux onto the surface. By introducing H_2O from either the feed gas or the environment to Ar/O_2 plasma, we also demonstrate the quenching of atomic O by water vapor (H_2O) predicted by the simulation [43].

2.2. Experiments and methods

A schematic diagram and optical image of the time modulated RF jet are shown in figure 2.1. The jet consists of a 1 mm diameter RF driven tungsten needle surrounded by a quartz tube (3 mm outer, 1.5 mm inner diameter) around which is wrapped by a grounded copper ring electrode. A total flow of 1.5 standard liters per minute (slm), either of pure Ar or Ar plus 1% molecular gas admixture, is fed through the quartz tube. The molecular gas

admixtures that we have studied include air, O_2, H_2O and O_2/H_2O mixtures. The plasma is generated using a 20 kHz time modulated 13.3 MHz RF signal with 20% duty cycle (10 µs on, 40 µs off). The average dissipated power by the plasma is measured using the method described elsewhere [134]. In order to avoid direct coupling of charged species with material surfaces [160], the average dissipated power applied to the jet is maintained as 0.83 W for pure Ar and 3.8 W for Ar plus 1% molecular gas admixture. These values are close to the maximum power without direct coupling to the surface at the closest treatment distance studied (4 mm) while maintaining a comparable plume length for all treatment conditions.

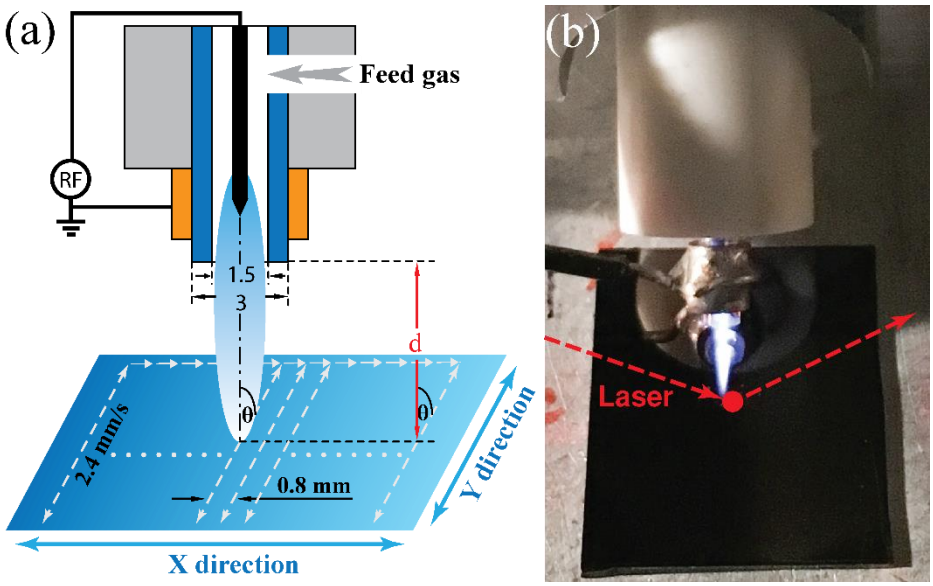

Figure 2.1 (a) Schematic diagram and (b) optical image of the time-modulated RF jet and its interaction with a polymer surface. The RF jet scans over the surface at a speed of 2.4 mm/s with the trajectory shown in (a). Distance d from end of the quartz tube nozzle to the surface can be varied from 4 mm to 8 mm. The RF jet is tilted at $\theta = 30°$ to facilitate *in-situ* ellipsometry characterization - the laser optical path of which is also illustrated in (b).

Since the plasma plume has a small cross sectional area (0.018 cm^2) due to the small

inner diameter (1.5 mm) of the quartz tube, the RF jet is mounted on a 2D scanning stage to produce uniformly treated material surfaces that can be more easily characterized. As shown in figure 2.1(a), the jet scans over the polymer surfaces with a speed of 2.4 mm/s and the distance between scanning lines is 0.8 mm which is about half of the ID of the quartz tube. These parameters are chosen to help improve treatment uniformity and avoid heat accumulation. During scanning, the RF jet is tilted at $\theta = 30°$. Three treatment distances of d = 4, 6 and 8 mm from the end of the nozzle to the top of the surface are investigated. To study the composition effect of the gaseous environment on PSI, the material is processed in both uncontrolled (humid room air) and controlled environments using a sealed 50 L chamber that was evacuated to 8×10^{-5} Torr and then refilled to atmospheric pressure with desired $N_2/O_2/H_2O$ mixture. Water vapor is generated by a custom-built delivery system utilizing a MKS M330AH mass flow controller (MFC). The inlet of the MFC is connected to a sealed cylinder in which liquid water is contained, while the outlet of the MFC is connected to the dry feed gas line of the plasma jet. The temperature of the MFC (135 °C), water cylinder (110 °C) and connecting pipelines (110 °C) is controlled by proportional–integral–derivative (PID) controllers. The film thickness and surface chemical composition change of model polymers are investigated to show the interaction of RF jet with surfaces. Polymers are characterized by both in-situ and ex-situ ellipsometry [159] using 1.5mW HeNe laser at 632.8nm as shown in figure 2.1(b). An optical model is applied to the raw ellipsometric data to extract polymer thickness and refractive index. To avoid contamination and removal of plasma induced weakly bound species by the exposure of surfaces to ambient air [158], the processing chamber is immediately evacuated and polymer samples are transferred through vacuum to a X-ray photoelectron

spectroscopy (XPS) system (Vacuum Generators ESCALAB MK II) for surface chemical composition analysis. The treated surface area is 1 × 1 cm^2 for ellipsometry and 2 × 2 cm^2 for XPS.

2.3. Results and discussion

The first observation concerns the significant polymer etching by the RF jet. In humid room air environment, polymers processed using pure Ar or Ar + 1% admixture show thickness reduction at all three (4, 6 and 8 mm) treatment distances. Figure 2.2 shows the dependence of polymer etching depth on feed gas chemistry and treatment distance using *in-situ* ellipsometry. The total amount of removed C atoms is estimated by the etching depth and the density of each model polymer (1.04 g/cm^3, 1.18 g/cm^3 and 1.19 g/cm^3 for polystyrene, PMMA and PVA, respectively). *Ex-situ* thickness change evaluation, i.e. comparing film thickness between pre- and post-treatment, agrees well with the *in-situ* data. When comparing different feed gas chemistries, we find that pure Ar plasma is generally less effective than Ar plus 1% molecular feed gas admixtures if experiments are performed at constant plume length and with the required differences in dissipated power. For these conditions, Ar with 1% molecular admixture plasma generates more reactive species responsible for polymer etching than pure Ar whose effect is mainly from the VUV [6] and ambient gas entrainment [145]. At the same treatment distance Ar + 1% O_2 plasma shows significantly more etching than other feed gases. The maximum instantaneous etch rate at 4 mm can be 100 – 500 nm/min depending on the polymer treated.

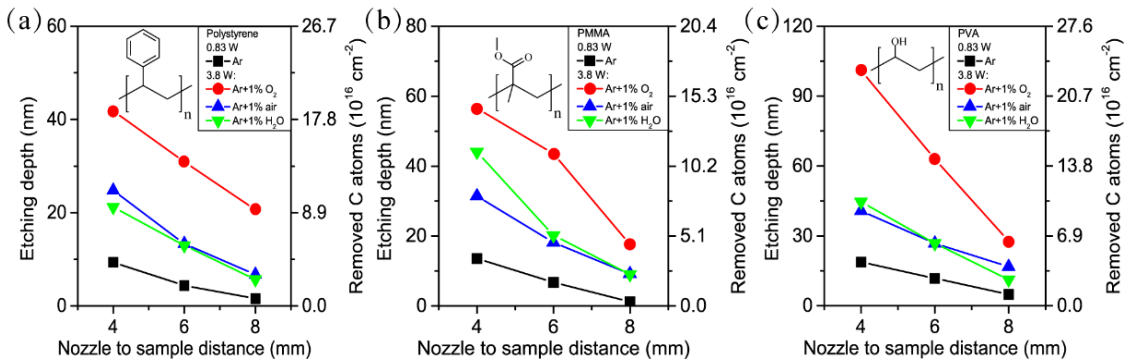

Figure 2.2 (a)Polystyrene, (b) poly(methyl methacrylate) (PMMA) and (3) poly(vinyl alcohol) (PVA) etching depth comparison of pure Ar, Ar + 1% O_2, Ar +1% air and Ar + 1% H_2O plasma with 4, 6 and 8 mm treatment distance. The area density of removed C atom is calculated from the etching depth. The inserts are molecular structures of the corresponding polymer. The environment condition is not controlled and mostly humid ambient air mixed with Ar feed gas.

Former reports of the same plasma jet have shown that Ar + 1% O_2 plasma has lower electron temperature and density [161], and produces less NO but more atomic O [162] than Ar + 1% air plasma. Along with results shown in figure 2.1, they suggest that atomic O plays an essential role for polymer etching in the case of Ar, Ar + 1% O_2 and Ar + 1% air plasma. When comparing the impact of treatment distance for each feed gas, we find that polymer etching depth decreases linearly with the distance away from the nozzle. This is consistent with the observed linear decrease of the atomic O density with distance in the gas phase reported for the same jet [43]. Numerical simulations indicate that this linear decrease of atomic O density with the distance results from the destruction of O atoms by the impurities from the environment [43]. Besides, the reduction of virucidal activity of feline calicivirus (FCV) also decreases with increasing treatment distance by the same RF plasma jet as reported in literature [163]. It is worth mentioning that due to the strong VUV

photon absorption of O_2, the VUV effect from Ar excimers is minimal in Ar + 1% admixture plasma [6].

To evaluate the relation between polymer etching and estimated incident atomic O flux, the C flux leaving the surface versus the O flux bombarding the surface is plotted in figure 2.3 for polystyrene, PMMA and PVA treated by Ar + 1% air plasma. The average O flux is estimated from the measured and simulated gas temperature and spatial O density profiles of Ar + 2 % air plasma [43] by using equation 2.1 from kinetic theory of ideal gas:

$$\overline{\Phi} = \frac{1}{4} n \overline{v} = \frac{1}{4} n \sqrt{\frac{8RT}{\pi M}} \tag{2.1}$$

Here $\overline{\Phi}$ is the average gas flux, n is the gas density, $\overline{v}$ is the average speed, R is the gas constant, T is the gas temperature, M is the atomic weight of O. For our plasma conditions, the O density and gas temperature used at 4 mm, 6mm and 8 mm are 8×10^{15} cm^{-3} 420 K, 5×10^{15} cm^{-3} 390 K and 2×10^{15} cm^{-3} 375 K, respectively. For additional information about the RF jet, the reader is referred to more detailed descriptions by Bruggeman et al. on the plasma properties, i.e. n_e, T_e and T_g [134], flow dynamics [135] and production of NO [136], O, O_3 [137]. The C flux is calculated from the measured etching depth of the three polymers treated by Ar + 1% air plasma. Experiments show little difference in O density between 1 and 2% molecular admixtures into the Ar feed gas when the power is in excess of 3 W and gas flow rate is between 1 and 5 slm [164]. Figure 2.3 indicates that the removed C flux is proportional to the estimated incident O flux, and a similar etching reaction probability of O atoms (slope of the curves in figure 2.3) is seen for all three polymers which is roughly $1.8 \times 10^{-4} \sim 3.3 \times 10^{-4}$. It is worth noting that although the value of the O/C ratio depends on the accuracy of measured O density spatial profile, the order of magnitude we estimated

here agrees with that seen in other work [10]. However Benedikt et al. estimated the etching reaction probability to be ~10^{-2} by matching the profile of He/O_2 micro-plasma treated hydrogenated amorphous carbon (a-C:H) films to the simulated O flux profile at the surface [115]. Considering the difference between the model systems used in these reports, the exact O/C ratio value might need further investigation. Furthermore, compared to the O density of air admixtures in Ar feed gas, O_2 admixtures yield a 2.5 times higher O density at similar plasma power [137, 165]. This value is in good agreement with the ~2 times higher etching rate for Ar + 1% O_2 compared to Ar +1% air. For Ar + 1% H_2O plasma we expect more OH species which may impact polymer etching and will be discussed in more detail below.

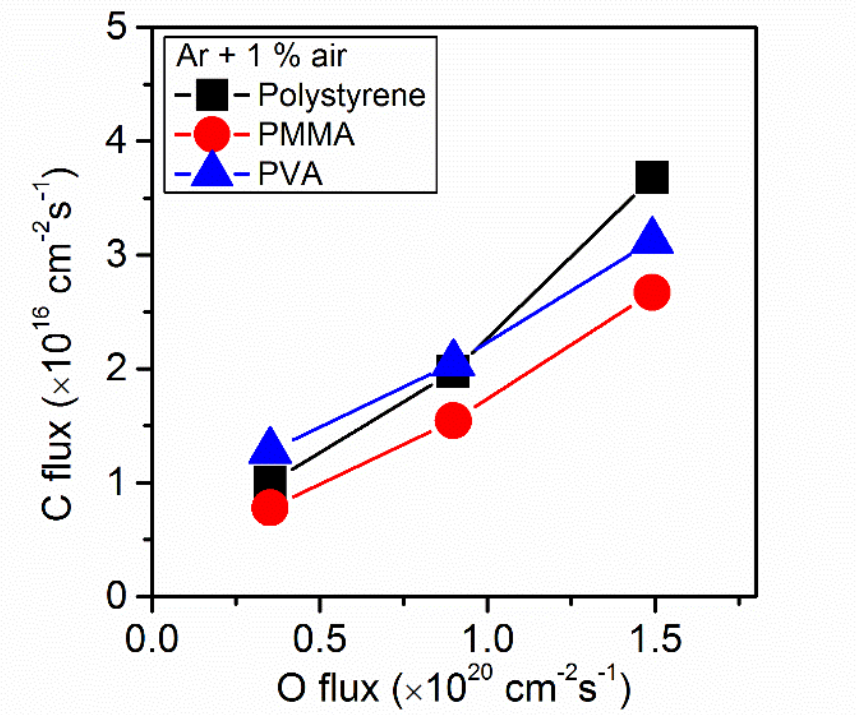

Figure 2.3 Relation between estimated incident O flux onto polymer surface and calculated C flux out of polymer surface for Ar + 1% air plasma in room air environment.

Surface chemical composition of plasma processed polystyrene films in N_2 environment with 4 mm treatment distance is shown in figure 2.4. Since C and H-based

pristine polystyrene contains no O and N, this makes it ideal for studying O and N uptake on surface as a result of plasma treatment. The most distinctive feature of the RF jet etched polystyrene surface is oxidation, especially the formation of carbonate ester (O-CO-O) groups. As shown in figure 2.4(c), the O 1s spectrum of polystyrene treated by both Ar + 1% O_2 and Ar + 1% H_2O plasma in N_2 environment shows a peak (533.9 eV) which can be assigned to carbonate ester. Correspondingly, the C 1s spectrum of treated polystyrene also shows a carbonate ester peak at 290.2 eV (figure 2.4(a)). Other surface changes include the damage to the polymer carbon backbone (C-C/H at 285 eV) and phenyl ring (π- π^* shake-up at 291.7 eV) along with the formation of C-O (286.5 eV), O-C-O/C=O (288 eV) and O-C=O (289 eV) groups. As to surface N, the N 1s spectrum (figure 2.4(b)) only shows a weak NO signal, despite the fact that the gas phase NO density measured by laser-induced fluorescence (LIF)[24] and molecular beam mass spectrometry (MBMS) [85] is very high (between 10^{20} and 10^{21} m^{-3}). Surface chemical composition of polystyrene treated by other plasma conditions, such as different feed gas or environment gaseous compositions, were also studied. They all exhibit the same functional groups as shown in figure 2.4, although relative amount differs. Therefore, we show elemental compositions obtained from the XPS raw data in the rest of this report.

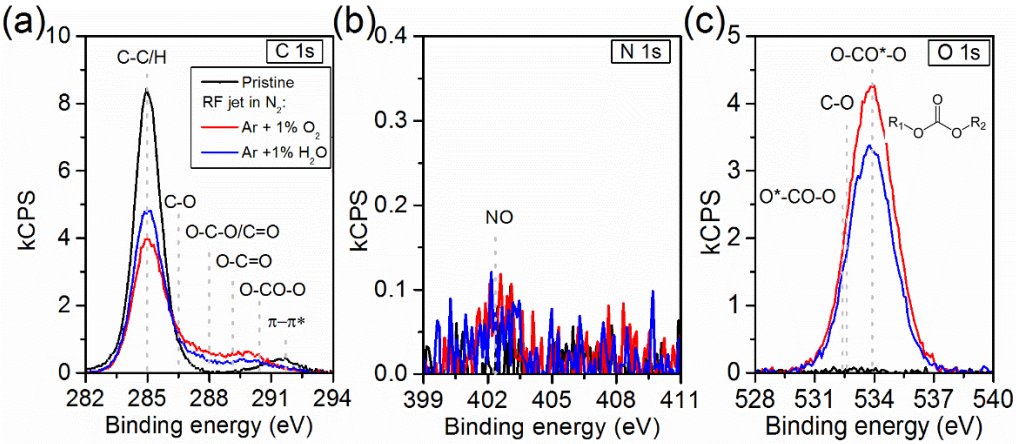

Figure 2.4 High resolution XPS (a) C 1s, (b) N 1s and (c) O 1s spectra of polystyrene treated by the RF jet with Ar + 1% O_2 and Ar + 1% H_2O plasma in N_2 environment. Pristine polystyrene is also shown for comparison. The RF jet treated surface shows characteristic carbonate ester (O-CO-O) and NO formation.

To explore the effect of H_2O on polymer etching by the RF jet, Ar + 1% O_2/H_2O mixtures with various O_2/H_2O ratios were used as feed gas to treat polystyrene surfaces. Pure N_2 was used as the processing environment to exclude interaction of environmental O_2 with the plasma plume or polystyrene surfaces. Therefore all observed surface oxygen originates from the feed gas. In figure 2.5 polystyrene etching rates and surface chemical compositions are compared. On the left Y-axis of figure 2.5 (a), etching depth of polystyrene is plotted against the O_2/H_2O ratio of the feed gas. For both Ar + 1% O_2 (O_2:H_2O = 1:0) and Ar + 1% H_2O (O_2:H_2O = 0:1) significant polymer etching can be seen. The total etching depth drops strongly if Ar + 1% O_2/H_2O mixtures are used instead. This indicates that: (1) the species responsible for etching in Ar + 1% O_2 plasma and Ar + 1% H_2O plasma are different, and (2) the reactive species generated in Ar/O_2 plasma and Ar/H_2O plasma interact and might be mutually exclusive with each other. In the surface

reaction model proposed by Dorai and Kushner [10], O and OH both initiate the attack of polymers by H abstraction. Compared to other species available with sufficient densities at the polymer surface, e.g. $O_2(a^1\Delta_g)$, O_3, N, NO, H and HO_2, the reactivity of O and OH is several orders of magnitudes higher for hydrogen abstraction from either the carbon backbone or the aromatic ring and these reactions of O and OH initiate polymer ablation and further surface oxidation [10]. For non-water containing plasma the above results, especially figure 2.3, show great consistency with the notion of atomic O initiating the etching process. In agreement with the literature [10], it is also reasonable to assume that OH species are the controlling factor for high rate polystyrene etching by Ar + 1% H_2O plasma as seen here. The reduction of etching depth by mixing a small amount of H_2O into Ar/O_2 plasma observed in figure 2.5(a) can be explained by the processes proposed by Gaens et al. who has reported the reduction of atomic O density when adding H_2O into Ar + 2 % air plasma of the same RF jet [43]. Water addition to the plasma leads to the generation of H-containing species, such as H, OH and HO_2, which cause the loss of O atoms through reactions 2.2 – 2.4 with rate coefficient k (m^3/s) at 400 K [67]:

$$OH + O \longrightarrow H + O_2; \quad k = 2.7 \times 10^{-17} \tag{2.2}$$

$$H + O_2 + M \longrightarrow HO_2 + M; \quad k = 5.6 \times 10^{-19} \tag{2.3}$$

$$HO_2 + O \longrightarrow OH + O_2; \; k = 4.8 \times 10^{-17} \tag{2.4}$$

In fact these processes are a cycle in which the H atoms, after being generated from H_2O, are converted into HO_2 radicals (reaction 2.3) which are subsequently reduced to OH (reaction 2.4). The cycle ends with a further reduction that creates H atoms again (reaction 2.2). These reactions give rise to a net production of one O_2 molecule from a net loss of

two O atoms [67]. Our finding on the reduction of etching depth by mixing a small amount of O_2 into Ar/H_2O plasma further suggests that feed gas O_2 and its related reactive oxygen species (ROS) could also quench OH radicals through destruction pathways such as reaction 2.2. We plan to further investigate this mechanism using direct measurement of OH densities. On the right Y-axis of figure 2.5 (a), surface elemental composition of treated polystyrene is plotted against the feed gas O_2/H_2O ratio. As shown by the dotted lines, the surface C and O composition are proportional to the feed gas O_2 concentration rather than the etching depth (black solid line). This indicates that for the RF jet the surface chemical modification is not the rate limiting step for the etching process. The two processes - etching and surface modification – are separately controlled by different group of plasma species. One possible surface reaction mechanism could be that the O and OH flux to the surface controls the total etching depth but the density of other ROS near the surface, such as $O_2(a^1\Delta_g)$, O_2 and O_3, controls the oxidation level by reacting with the active alkyl radical sites on the etched polymer surface to form various oxygen containing functional groups.

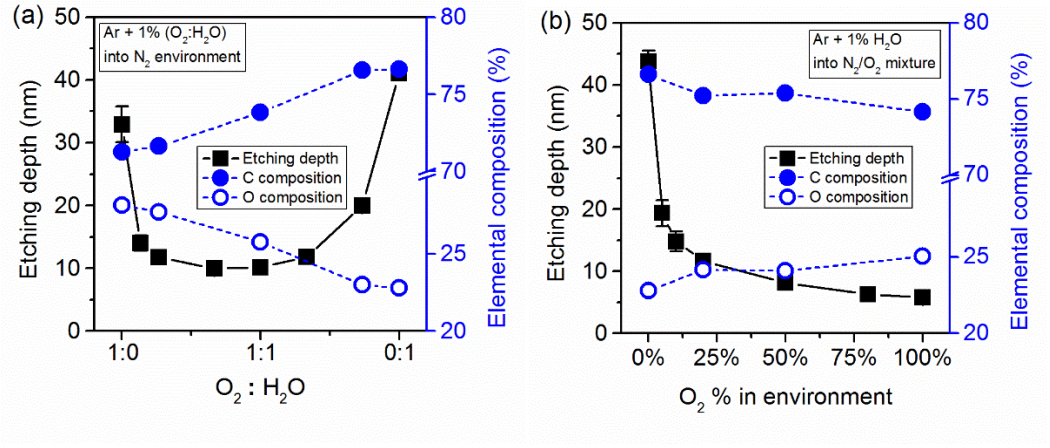

Figure 2.5 (a) Feed gas H_2O and O_2 mixture effect on the etching depth and surface elemental composition of polystyrene treated in N_2 environment. (b) Environment O_2 effect

on the etching depth and surface elemental composition of Ar + 1% H_2O plasma treated polystyrene.

The interaction of species generated in Ar/O_2 and Ar/H_2O plasma is further demonstrated by studying the plasma treated polystyrene surfaces in controlled environment with various O_2 concentration. Figure 2.5 (b) shows the relation between environmental O_2 concentration and polystyrene surface response treated by Ar + 1% H_2O plasma. With the increase amount of environmental O_2, the polymer etching depth decreases whereas the surface O elemental composition increases. The cause of etching and surface modification can be explained as following. Since the amount of O_2 entrainment into Ar + 1% H_2O plasma effluent is proportional to the environmental O_2 concentration, the response of etching depth with ambient O_2 should behave similar to adding O_2 directly into the Ar + H_2O feed gas as discussed in figure 2.5 (a): the loss of OH is caused by O_2 related reactive species such as O, O_3, NO and HO_2 [64]. Alternatively, with more O_2 and consequently more ROS in the surrounding environment of the material surface, the reactive radical sites on etched polymer surface may quickly combine with these species and thus cause the increase of surface elemental O composition as shown in figure 2.5 (b). In addition, we also studied environmental H_2O effect on Ar + 1% O_2 plasma by adding 1% and 2% humidity into N_2 ambient. The result is similar to directly mixing H_2O into Ar/O_2 plasma: compared to dry N_2 ambient the etching depth of 1% and 2% humidity drops from 33.6 nm to 29.3 nm and 22.5 nm, respectively.

The relatively fast polymer etching and carbonate ester rich surface after etching is very characteristic of this RF jet. We have investigated other atmospheric pressure plasma

sources using similar approaches, e.g. a surface micro-discharge (SMD) for which we see no etching [93, 94, 140]. A key difference is the higher OH and O densities generated in the RF jet effluent due to the higher power density and less O_2 near the surface compared to the kHz driven SMD.

2.4. Conclusion

In summary, we have demonstrated that a time modulated RF jet in close proximity to model polymer surfaces induces relatively fast etching and characteristic carbonate-ester formation along with minor NO uptake on the polymer surfaces. For these treatment conditions, short lived species, especially O atoms and OH radicals, play an essential role in the polymer etching process. The etching reaction probability of atomic O with different model polymers based on the ratio of removed C flux to incident O flux is estimated to be $1.8\times10^{-4} \sim 3.3\times10^{-4}$. Other longer lived ROS surrounding the etched surface determine the final surface oxidation level. Whereas separate addition of O_2 or H_2O admixture to Ar induces polymer etching at fairly high rates, simultaneous adding O_2 and H_2O to Ar reduces polymer etching, which indicates the reduction of O and OH density in $Ar/O_2/H_2O$ plasma.

Acknowledgement

The authors gratefully acknowledge financial support by the National Science Foundation (PHY-1415353) and the US Department of Energy (DE-SC0001939). We also thank C. Anderson and D. B. Graves of UC Berkeley for helpful discussions on this collaborative project. We are grateful to E. A. J. Bartis, D. Metzler, C. Li and A. Pranda for helpful discussions and collaborations.

Chapter 3: Plasma-Surface Interaction at Atmospheric Pressure: A Case Study of Polystyrene Etching and Surface Modification by Ar/O_2 Plasma Jet

P. Luan[1], A. J. Knoll[1], P. J. Bruggeman[2], and G. S. Oehrlein[1]

[1] Department of Materials Science and Engineering and Institute for Research in Electronics and Applied Physics, University of Maryland, College Park, MD 20742, USA

[2] Department of Mechanical Engineering, University of Minnesota, Minneapolis, MN 55455, USA

Journal of Vacuum Science & Technology A: Vacuum, Surfaces, and Films, 35 (5), 05C315 (2017)

Abstract

In this paper we studied atmospheric pressure plasma-surface interaction (PSI) using a well-characterized radio-frequency (RF) Ar/O_2 plasma jet with polystyrene (PS) polymer films in controlled gas environments as a model system. A number of plasma processing parameters, such as treatment distance, environmental gas composition as well as substrate temperature, were investigated by evaluating both the changes of thickness and surface chemical composition of PS after treatment. We found that the polymer average etch rate decayed exponentially with nozzle-surface distance whereas the surface oxygen composition increased to a maximum and then decreased. Both the exponential decay constant and oxidation maximum depended on the composition of gaseous environment which introduced changes in the density of reactive species. We previously reported a linear relationship between measured average etch rates and estimated atomic O flux based on measured gas phase atomic O density. In this work we provided additional insights on the kinetics of surface reaction processes. We measured the substrate temperature dependence of PS etch rate and found that the apparent activation energy (E_a) of the PS etching reaction was in the range of 0.10 – 0.13 eV. Higher values were obtained with greater nozzle-to-surface distance. This relatively low E_a value suggests that additional energetic plasma species might be involved in the etching reactions, which is also consistent with the different behavior of etching and surface oxidation modification reactions at the polymer surface as treatment distance is varied.

3.1. Introduction

Cold atmospheric plasma (CAP) sources are able to produce chemically reactive species that have been proven effective at modifying material surfaces,[147, 166] sterilizing microorganisms,[167, 168] healing wounds[148, 149] and even treating cancer.[169] These applications all share an interaction between CAP sources and surfaces, e.g. of polymers,[140] dielectrics,[157] biomolecules[158] and cells.[154] While an impressive amount of results on CAP source characterization have been achieved,[146, 150-153, 170-172] less is known about the mechanisms of plasma-surface interaction (PSI), especially under atmospheric pressure.

Although one can easily observe CAP induced effects on polymers,[147] cells[173] and tissues,[174] the difficulty of studying PSI originates from the complex nature of both the gas phase and surface reactions. Unlike thermal plasma, CAP is not in local thermal equilibrium (non-LTE) and a wide variety of chemically active conditions can be achieved by changing external parameters such as source geometry, electromagnetic field structure and gases supplied to the source or in the environment.[175] Compared to low pressure glow discharges, CAP sources have lower cost and relatively simpler designs. This affordability increases the accessibility of CAP to both research and industrial communities which in return stimulated numerous new source and power supply configurations. This multi-dimensional parameter space of CAP gives rise to its chemical freedom but also cause difficulties with regard to both characterizing the generated chemical species and establishing standards across CAP's expanding applications.[133] When a target is present, the rapidly changing fluxes of incident and outgoing species at the material surface interact with each other, which complicates the spatial and temporal profile of plasma species.[38]

In addition, PSI frequently involves synergistic effects of multiple reactive species, which adds to the difficulty of interpreting results both computationally and experimentally.

The constant exposure of CAP sources and material surfaces to atmospheric environments further complicates studying PSI.[140] The plasma-environment interaction has a large impact on not only the plasma source behavior but also the species arriving at material surfaces.[141] Controlling the gaseous composition of the CAP source and the PSI vicinity has attracted increasing attention in recent years. For example, by applying a gas curtain around an atmospheric pressure plasma jet (APPJ) operated in humid room air, Reuter *et al.* were able to reduce the inflow of ambient species drastically.[176] Shimizu *et al.* reported the effect of different humidity levels on the SMD treatment of bacteria using a large environmental chamber (microbiological incubator).[144] In fact more rigorously controlled environments are desired for the study of PSI because CAP sources are sensitive to even trace impurities.[142]

To understand the mechanisms of PSI, researchers need to establish correlations between reactive species and treated surfaces. This requires a well-characterized CAP source, a controlled gaseous environment, a defined material surface, comprehensive surface characterization techniques and the understanding of both gas phase and surface reaction kinetics. Early attempts of studying PSI at atmospheric pressure focused on describing the change of material surface with one or several external parameters of the CAP source, such as power, treatment time and distance. Two types of changes on surfaces after plasma exposure were distinguished: (1) removal/etching of materials[177], [178] and (2) irreversible modification on the composition/structure of a few molecular layers at or near the surface.[18] For the systematic understanding of etching reactions, the work of

Winters,[3] to whom this special issue is dedicated, and his colleague Coburn has provided a foundation.

With the progresses on CAP characterization, works of correlating gas phase species to either etching[115] or modification[94, 141] have emerged. To achieve the goal of deciphering PSI, joining surface characterization, optical diagnostic techniques and modeling of an established CAP device is indispensable.

Previously we have studied the PSI of model polymers and biomolecules with multiple CAP sources such as kHz double ring-APPJ,[141, 158, 159] kHz pin-APPJ[6] and surface micro-discharge (SMD).[93, 94] We found that surface modification by CAP sources was generic whereas etching was highly source dependent. More recently, we adopted a well-characterized radio frequency (RF) APPJ whose properties have previously been studied and described,[134] including flow dynamics,[135] gas temperature,[134] electron density and temperature,[134] density of reactive species such as NO,[136] O and O_3.[137] The reaction pathways of several bio-medically reactive species, including O, O_3, $O_2(a^1\Delta_g)$, H, HO_2, OH, $N_2(A)$, NO_x and HNO_x generated by this jet have also been obtained by numerical simulations.[43, 138] The available information provides the opportunity to improve our understanding of PSI and interpretation of surface characterization results. By interacting this RF jet with several selected model polymers in highly-controlled environments, we correlated polymer etching with O atoms in the gas phase.[68] We found a linear response between the incident O flux and the etched C flux of polystyrene (PS), poly(methyl methacrylate) (PMMA) and poly(vinyl alcohol) (PVA) at the near plume region of the jet: the etching reaction probability of O atoms to C atoms is in the range of 10^{-4} to 10^{-3}.

In this paper, we further extend our studies of plasma-surface interactions to the far effluent of the Ar/O_2 jet. A number of plasma processing parameters, such as treatment distance, environment gaseous composition as well as substrate temperature, are investigated by evaluating the changes of both thickness and surface chemical composition of PS after treatment. The role of atomic O on polymer surfaces is discussed. We also evaluate the apparent activation energy of Ar/O_2 plasma etching reactions with PS. Finally we discuss the possibility of polymer etching and surface modification with other plasma species besides atomic O.

3.2. Experimental

3.2.1 Materials

PS beads were purchased from Sigma-Aldrich (St. Louis, MO, USA) with an average molecular weight of 35 000. Thin films of PS (~180 nm, as measured by ellipsometry) were prepared by the spin-coating of 5 wt% PS in propylene glycol methyl ether acetate (PGMEA, Sigma-Aldrich, ReagentPlus, $\geqslant$99.5%) solution at 2000 rpm onto Si substrates (25.4 mm × 25.4 mm). The C- and H- based pristine PS film surface contains negligible amount of oxygen and nitrogen impurities, as measured by X-ray photoelectron spectroscopy system (XPS), which makes it ideal for studying O and N uptake as a result of plasma treatment. These spin-coated PS films have an RMS surface roughness of 0.35 nm as measured by atomic force microscopy (AFM).

3.2.2 Plasma processing

The plasma source studied in this work is a time-modulated radio-frequency (RF) plasma jet. As shown in figure 3.1, the RF jet is composed of three major parts: a 1 mm diameter RF driven tungsten needle, a quartz tube (3 mm outer and 1.5 mm inner diameter,

ID) and a grounded copper ring electrode. The RF signal was generated by a function generator (Tektronix AFG3021B) with 20 kHz time modulated 14.0 MHz sine wave at 20% duty cycle (10 µs on, 40 µs off) and then amplified by a power amplifier (ENI A500). The average dissipated power of the plasma jet was measured as 2 W for the majority of this work using the method described elsewhere.[134] The RF jet feed gas used was Ar plus 1% O_2 with a total gas flow of 1.5 standard liters per minute (slm). The average flow velocity of the feed gas can be calculated as 14.15 m/s. The visible plume length is approximately 3 mm.

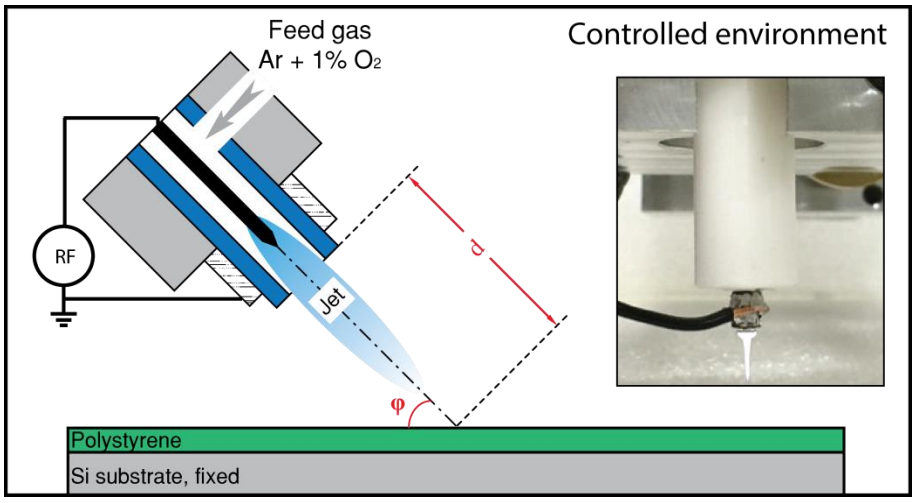

Figure 3.1 Schematic diagram of the time-modulated RF jet and its interaction with PS film. The treatment angle φ and treatment distance d are adjustable. During material processing the RF jet scans over PS surface at a speed of either 1.2 mm/s or 2.4 mm/s. The distance between scanning lines is 0.8 mm. Insert shows the RF plasma jet in vertical (φ = 90°) configuration.

In order to uniformly process large material surfaces, the RF jet was installed on a homemade 2D scanning stage driven by stepper motors.[68] During treatment, the RF jet

scans over sample surfaces with a line-by-line processing pattern at a constant speed of 1.2 mm/s unless otherwise noted. The distance between scanning lines is 0.8 mm which is about half of the quartz tube ID. The RF jet scans over the same processing line back and forth then jumps to the next line. With a total treatment time of 200 seconds, an area of 9.6 mm × 9.6 mm can be processed. The RF jet scans 12 times (back and forth) during the entire course of treatment. As shown in figure 3.1, the treatment angle φ and distance d relative to the material surface are adjustable. In this work, the φ investigated was 30° (tilted) and 90° (vertical) and distance d from the end of the nozzle to the surface was varied as 4, 8, 12, 16 and 20 mm. We selected 30° for all surface composition analysis using XPS. In order to directly compare etching and surface modification, we performed comparative etching experiments also with a 30° tilt angle. However, we chose the etching data collected at 90° to be correlated with the measured and simulated density of gas phase species which were also collected at 90°.

The potential heating of the scan-treated target surfaces by the RF jet was evaluated by measuring the thermal expansion of 745 nm SiO_2 during plasma treatment using ellipsometry. We found a temperature increase of less than 20 °C for the processing parameters chosen above. We also measured the thickness reduction of PS films due to heating alone, and no observable thickness loss was obtained at 40 °C. We observed ~ 2 nm of thickness reduction at 80 °C, and most of this took place in the first minute. Since the PS samples are always pre-heated to target temperature before plasma treatment, the effect of heating alone on the etching depth of PS is considered as negligible.

To study the ambient gas composition effect on PSI, the processing of polymer surfaces by RF jet was conducted in both controlled (pure N_2 or N_2/O_2 mixture) and

uncontrolled (humid room air) environments. The controlled environments were achieved using a sealed 50 L chamber that was pre-evacuated to below 50 mTorr and then refilled to atmospheric pressure with high-purity N_2 and/or O_2 gas (Airgas, > 99.998%).

To study the substrate temperature effect on PSIs, a proportional–integral–derivative (PID) controlled heating stage was integrated into the controlled environment. PS coated Si wafers were pre-heated to the desired temperature (30, 45, 60, 75 °C) before scanning treatment. In order to avoid excessive amount of etching at high temperature, all the temperature dependence experiments were performed with 2.4 mm/s scanning speed. PS thickness loss was evaluated using in-situ ellipsometry.

3.2.3 Surface characterization

The optical property of PS films was characterized using both in-situ and ex-situ ellipsometry with1.5mW HeNe laser (632.8nm).[159] An optical model was applied to the raw ellipsometric data to extract polymer thickness and refractive index information. To evaluate the etch rate and film densification of PS, in-situ ellipsometry was used to acquire thickness and refractive index in real-time. For scanning processing, the probing laser spot of the ellipsometer was pointed to the center of the treated area. Surface morphology of PS film was measured using tapping mode of atomic force microscopy (AFM, Bruker MultiMode AFM).

Surface chemical composition of PS films was characterized by a XPS system (Vacuum Generators ESCALAB MK II) with Al K_α X-ray source (1486.3 eV). Both survey and high-resolution spectra of C 1s, N 1s and O 1s were obtained at electron take-off angles of 90° (probing depth $\approx$ 8 nm) and 20° (probing depth $\approx$ 2 nm). For quantitative analysis, spectra taken at 20° were selected and processed in CasaXPS software.[158] For

the C 1s spectrum, peaks corresponding to C=C (284.7 eV), C-C/H (285 eV), C-O (286.5 eV), O-C-O/C=O (288 eV), O-C=O (289 eV), O-CO-O (290.2 eV) and pi–pi* shake-up (291.6 eV) were used. Due to the overlapping of peaks in the O 1s spectrum, we combined oxygen moieties with binding energy from 532.2 eV to 533.1 eV into a single peak at 532.7 eV, and combined another group of peaks from 533.6 eV to 535.3 eV into another single peak at 533.9 eV. For the N 1s spectrum, nitroso (401.8 eV) and nitrate (407.5 eV) peaks were fitted. All spectra were calibrated by the C-C/H peak with binding energy of 285 eV. After Shirley background subtraction, the film composition was calculated by integrating peak areas of C 1s, N 1s and O 1s with sensitivity factors of 1, 2.85 and 1.77, respectively.[179]

3.2.4 Fluid model of RF jet

A fluid model of the RF jet gas flow combined with reactionless species transport has been created and solved using the commercial Fluent solver (ANSYS Workbench 17.2). The molar ratio of air entrainment into the plasma plume and near the sample surface was investigated. Four treatment geometries, corresponding to the nozzle-sample separations of d = 4, 8, 12 and 16 mm with tilt angle $\varphi = 90°$ were simulated. The gas flow in the fluid model was assumed as an incompressible Newtonian fluid. The turbulent kinetic energy k and turbulent dissipation epsilon (k-Ɛ) model was used to simulate the mean flow characteristics of turbulent flow near the material surface. The governing equations are therefore conservation of mass, momentum, k and Ɛ.[180] For boundary conditions, the quartz tube of the jet and material surfaces were considered as no slip walls. The inlet gas was selected as Ar + 1% O_2 at 450 K with average convection velocity of 14.15 m/s (corresponding to 1.5 slm). Constant pressure of 101 325 Pa was chosen for the

outlet boundaries. The transport of Ar and O_2 species from the jet inlet into air ambient was simulated through the solution of reactionless convection-diffusion equations for each of the species:

$$\frac{\partial n_i}{\partial t} = -\nabla \cdot \vec{J_i} - \nabla \cdot (\vec{u} \cdot n_i) \qquad ((3.1)$$

where $\vec{J_i}$ is the diffusion flux and $\vec{u} \cdot n_i$ is the convection flux of species i.

3.3. Results

3.3.1 Real-time etching profile

In-situ ellipsometry was used to evaluate real time thickness change of PS films during scan-processing with the RF jet.[159],[6] The etching profile of PS with Ar + 1% O_2 plasma in air environment is shown in figure 3.2. The plasma jet was held vertically to the material surface, and four treatment distances from 4 mm to 16 mm were evaluated. The real time etching curve showed a "staircase" shape, which can be explained by the line-by-line scan processing pattern. Since the size of the ellipsometer probing laser spot (3 – 4 mm) is larger than the diameter of the RF jet nozzle (1.5 mm) and the scanning steps (0.8 mm), there are cases when only part of the material inside the probing laser spot is etched. These situations are reflected as the artifact of etching steps with slower etch rate shown in figure 3.2. Real time etching profiles of other plasma chemistries also have a similar "staircase" shape. The real-time etching depth profile in figure 3.2 showed faster etching speed when the plasma jet moved closer to the center of the probing location. In the insert of figure 3.2, we showed the magnified view of the fastest etching step which occurred when the plasma jet was directly over the probing location. Maximum transient etch rate can be calculated from the slope of the etching curves. At 4 mm distance we observed an etch rate of 79.8 nm/min for Ar + 1% O_2 plasma in air. Similarly, the maximum etch rate

of other treatment distances can also be calculated as 11.9 nm/min, 3.62 nm/min and 2.14 nm/min for 8, 12 and 16 mm, respectively. However, the accuracy of these instant etch rate calculations is doubtful due to the artifact of large probing laser spot and decreases at longer treatment distances because of the small transient etch rate. Since we only compare PS treatments with the same scan-processing parameters, the total etching depth which is an indicator of the average etch rate and free of artifact will be discussed in the rest of the paper.

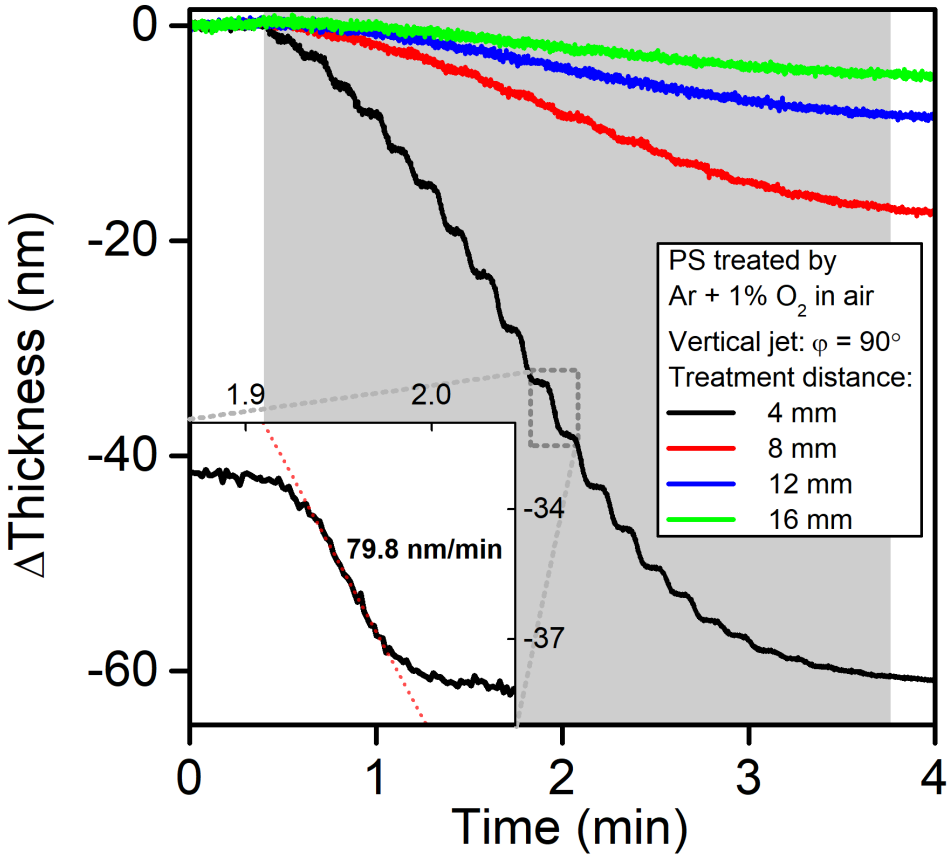

Figure 3.2 Real-time etching profile of PS treated by Ar +1% O_2 plasma in room air environment. Four treatment distances, 4, 8, 12 and 16 mm are shown. The gray area shows the *in-situ* film thickness change during plasma treatment. The treatment angle φ is

90°. Insert is the magnified view of the fastest etching step at 4 mm treatment distance. The transient etch rate can be fitted as 79.8 nm/min.

3.3.2 Etching depth vs. atomic O density

When comparing different treatment distances, we found that etching depth dropped exponentially with treatment distance. Figure 3.3 shows the etching depth of Ar + 1% O_2 plasma in both N_2 and air environment versus end-of-nozzle to sample distance. From the absolute etching depth value, we found that Ar/O_2 plasma etched more PS in N_2 than in air. The etching depth curve in each environment can be empirically fitted by an exponential decay formula with least-square method:

$$\Delta = \mathrm{A} \cdot \exp(-\frac{\mathrm{d}}{\lambda}) \qquad (3.2)$$

where Δ is the etching depth, d is the treatment distance, A and λ are fitting coefficients. The empirically fitted λ, a decay constant, is the distance at which the etching depth is reduced to 1/e or 0.368 times of its initial value. For the vertical (φ = 90°) jet configuration with Ar + 1% O_2 plasma in air environment, we fitted $\lambda_{O_2,\mathrm{air},90^\circ} = 2.81$ mm with adjusted $R^2 = 0.998$ in contrast to in N_2 environment where $\lambda_{O_2,N_2,90^\circ} = 4.02$ mm and adjusted $R^2 = 0.999$. The smaller $\lambda_{O_2,\mathrm{air},90^\circ}$ than $\lambda_{O_2,N_2,90^\circ}$ indicates that etching depth decays faster in air environment than in N_2 environment.

Interestingly, the experimentally measured atomic O density[43] (by two-photon absorption laser induced fluorescence, TALIF, in air environment) of the same plasma jet with Ar + 2 % air plasma also showed a similar decay profile along the plume axis. As shown in figure 3.3, we could fit the measured O density data with exponential decay formula which yields a decay constant $\lambda_{\mathrm{O,air,measured}} = 4.06\ mm$ and adjusted $R^2 =$

0.971. The measured atomic O density data is only available up to 6 mm due to the strong collisional quenching at long nozzle-to-sample distances which makes the TALIF measurements difficult to perform. However simulation result of atomic O density based on GlobalKin for this RF jet with Ar + 1% O_2 feed gas has also been reported before with distance up to 12.5 mm.[181] As plotted in figure 3.3 (open circles), simulated atomic O density shows similar exponential decay behavior with $\lambda_{O,air,simulation} = 2.37$ mm which is very close to the decay constant of PS etching depth $\lambda_{O_2,air,90°} = 2.81$ mm. Both the measured and simulated atomic O density profiles correlates well with the etching depth profile which suggests that atomic O might be the main etchant for Ar + 1% O_2 plasma.

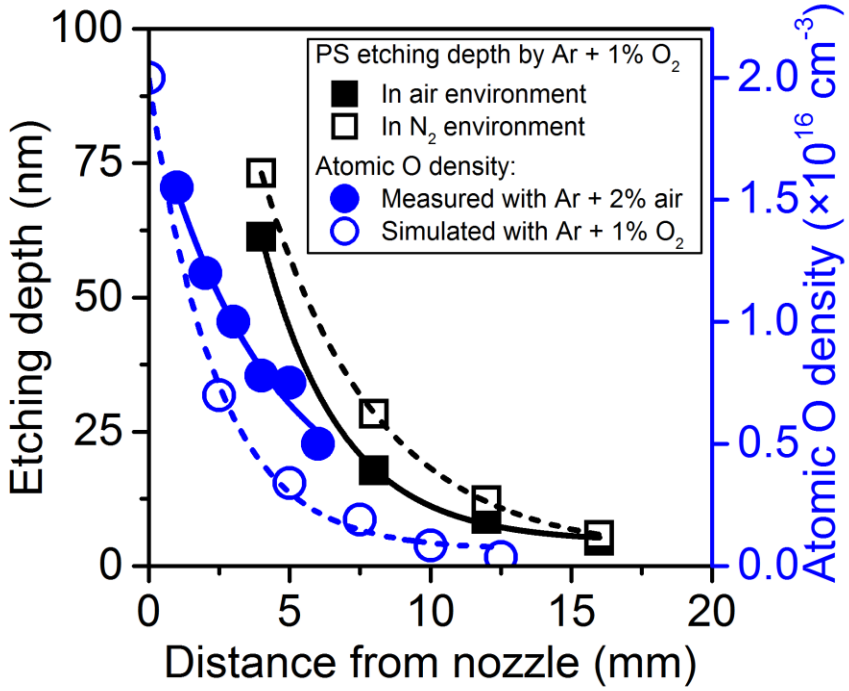

Figure 3.3 Comparison between the profile of PS etching depth and that of atomic O density along treatment distance. Left axis: etching depth of PS treated by Ar + 1% O_2 plasma in both N_2 and air environment. Right axis: measured atomic O density of Ar + 2% air plasma in air environment[42] and simulated atomic O density of Ar + 1% O_2 plasma in

air environment.[46] Both the etching depth curves and the atomic O density profile fall exponentially with distance. The treatment angle φ was 90°.

3.3.3 Surface morphology and chemistry

The RF jet treatment also modified the morphology and chemical composition of the polymer surface in addition to inducing etching. AFM was used to study the surface morphology before and after RF jet treatment. As shown in figure 3.4, pristine PS film has a RMS roughness of 0.35 nm. After Ar/O_2 plasma treatment in N_2 environment with a distance of 8 mm, the thickness of PS film reduced by 29.5 nm and the RMS roughness increased to 3.24 nm. The features on Ar/O_2 treated PS film are also more distinct.

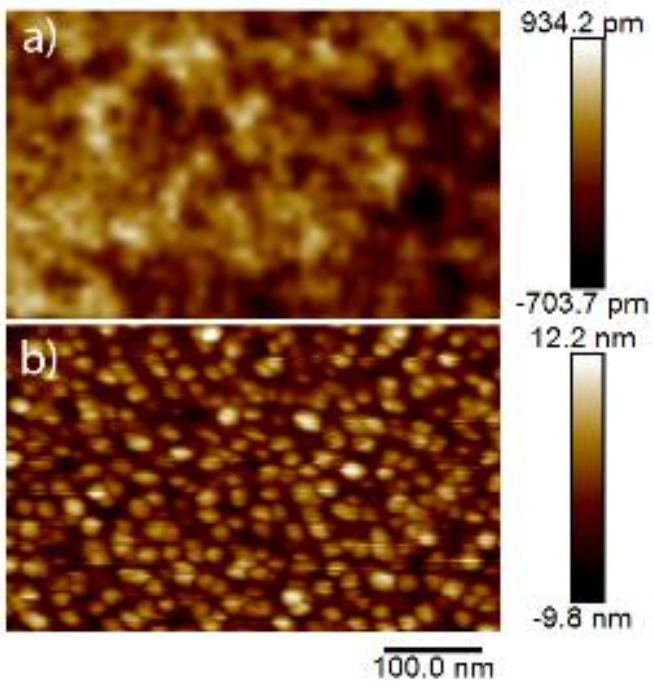

Figure 3.4 PS surface morphology measured by AFM: (a) pristine PS film with RMS roughness of 0.35 nm, and (b) Ar + 1% O_2 treated PS film with RMS roughness of 3.24 nm. Treatment angle was 90°, distance was 8 mm and gaseous environment was N_2.

Surface chemical composition of PS films was characterized by XPS. To illustrate the change on PS surface moieties, high resolution C 1s, N 1s and O 1s spectra of pristine and Ar + 1% O_2 plasma treated PS films are shown in figure 3.5. Plasma treatment was performed at 8 mm and 16 mm in N_2 environment with tilted jet configuration ($\varphi = 30°$). Since PS structure has long hydrocarbon chains wherein alternating carbon centers are attached to phenyl groups, the C 1s spectrum of pristine sample shows 91.1% C-C/H bond (285 eV) and 5.4 % of π - π^* shake-up (291.6 eV, phenyl ring) with negligible amount of O and N.

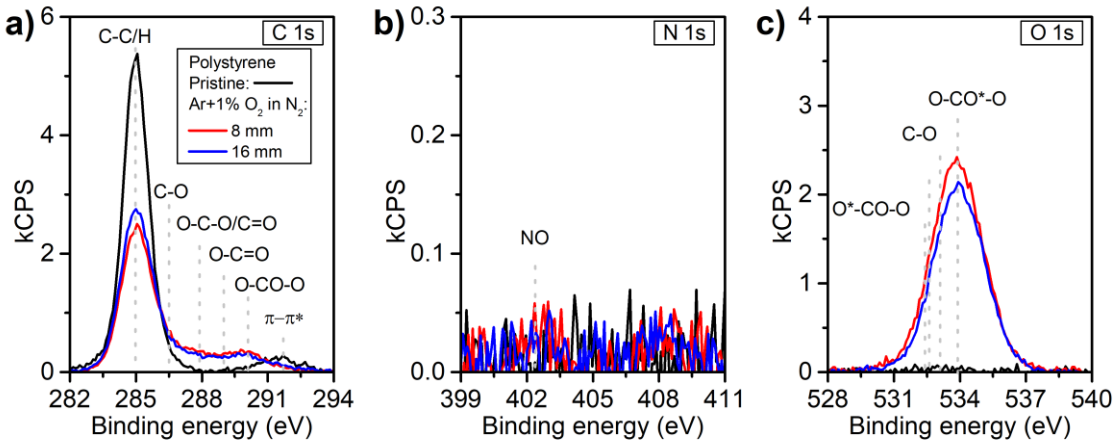

Figure 3.5 High resolution XPS (a) C 1s, (b) N 1s and (c) O 1s spectra of PS treated by the RF jet with Ar + 1% O_2 plasma at 8 mm and 16 mm in N_2 environment. Pristine PS is also shown for comparison. The treatment angle was 30°.

After treatment, the etched PS surface showed oxidation but no NO uptake for both distances. For the C 1s spectrum (figure 3.5 a), we found that plasma treatment induced destruction of C-C/H bond and phenyl ring as well as the formation of C-O, O-C-O/C=O, O-C=O and O-CO-O groups. The relatively large amount of carbonate ester (O-CO-O)

group is a distinctive feature of the RF jet etched polymer films compared to other CAP sources we have studied, including surface micro-discharge and double-ring kHz APPJ.[141], [94] Correspondingly, in the O 1s spectrum (figure 3.5 c) a peak at 533.9 eV is observed and can be assigned to this carbonate ester group. As to the N 1s spectrum (figure 3.5 b), NO signal was not observed although the gas phase NO density[85, 162] is high (~ 10^{14} cm^{-3}) at long nozzle-to-sample distances. When comparing the two treatment distances, we found similar functional groups as shown in figure 3.5, whereas the absolute amount of surface oxidation was different.

3.3.4 Ambient gas composition effect on etching and modification

To understand the effect of environment gas composition on PSI, we evaluated the etching efficiency of Ar/O_2 plasma in controlled environments consisting of various O_2/N_2 mixtures. The studied O_2 concentration ranges from 0% - 100% (N_2 concentration varies accordingly) and all treatments were performed at 4 mm with tilted configuration ($\varphi = 30°$). The average plasma power was 3.8 W and the scanning processing speed was 2.4 mm/s. As shown in figure 3.6, the polymer etching depth and the absolute value of its slope decrease with environmental O_2 concentration. These changes of etching depth with environment gas composition are largely due to the gas entrainment, especially the O_2 component, which alters the flux of reactive species impinging the target surfaces. The relative amount of O_2 entrainment in the plume increases with environmental O_2 composition which causes the drop of etching depth in figure 3.6. More discussions about the effect of O_2 entrainment can be found in IV. C.

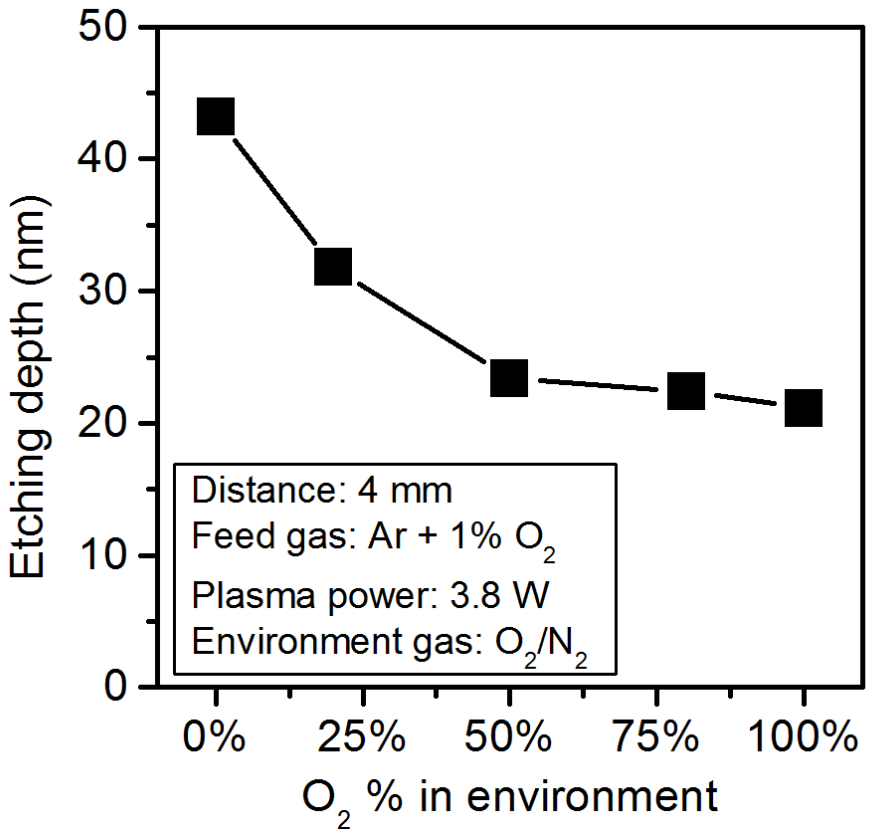

Figure 3.6 Environment gaseous composition effect on the PS etching depth treated by Ar + 1% O_2 plasma. All treatments were performed at 4 mm distance with tilted configuration ($\varphi = 30°$) and 3.8 W plasma power. The scan-processing speed was 2.4 mm/s.

To further understand the effect of ambient gas entrainment on PSI, we studied the treatment distance response of both etching and surface modification of PS films processed in room air and N_2 environment. Because the high resolution XPS data showed that all treated films exhibited the same type of functional groups that differed only in relative amount, we presented the elemental compositions extracted from these high resolution XPS data for the ease of discussion. As shown in figure 3.7, one generic observation for both environments is that the etching depth drop exponentially with treatment distance but the corresponding surface oxygen composition reached a maximum at intermediate

distances and then decreased. This is mainly because the density and dominant type of ROS are changing as a function of distance from the nozzle. Although the etching depth can be easily correlated to atomic O, the increase of surface oxygen composition is hard to interpret. Among the dominant reactive oxygen species (ROS) generated by this RF jet, i.e. O, $O_2(a^1\Delta_g)$ and O_3, only O_3 density increases with nozzle-to-sample distance.[182] However former reports[80, 183] have shown that O_3 alone has weak and slow oxidative effect on polymers, and UV light is frequently required for effective surface treatment. This suggests that the observed surface oxidation could be due to other ROS or the synergistic effect of a few types of ROS including O_3. The observed increase of surface oxygen composition from 4 mm to 12 mm is most likely due to the competition between surface etching and modification processes rather than the ROS density profile of one plasma species. More detail about the surface kinetic process is discussed in Section 3.4.4.

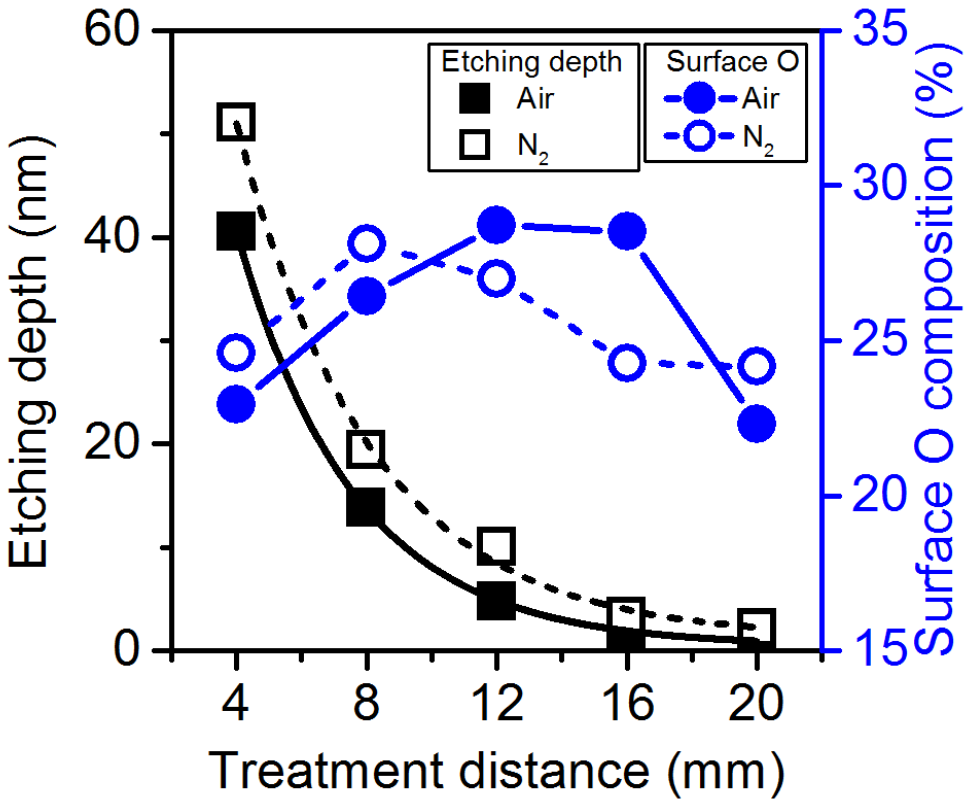

Figure 3.7 Comparison between air and N_2 environment on the etching depth and surface oxygen composition of PS film treated by Ar + 1% O_2 plasma. The treatment angle was 30°.

The observed difference in the etching depth between figure 3.3 and figure 3.7 results from not only the treatment angle effect but also experimental uncertainty due to the changes in the experimental setup. Since changing treatment angle requires adjustment of the RF jet on the scanning stage which slightly varies the treatment distance, the resulted etching depth of polymer films might differ by 10-20 nm at 4 mm treatment distance considering the exponential decay behavior of etching depth along nozzle-to-sample distance. Although we are unable to conclude in detail how treatment angle affects polymer etching behavior, the difference seen between $\varphi = 30°$ and $\varphi = 90°$ is much smaller than that of changing feed gas chemistry reported previously.[68]

We also found that using air environment rather than N_2 had a relatively small influence on both etching depth and surface oxidation. This can be seen from the absolute etching depth and the empirically fitted decay constant as $\lambda_{O_2,\mathrm{air},30°} = 3.63$ mm compared to $\lambda_{O_2,N_2,30°} = 4.15$ mm with only 0.52 mm difference. Although the surface oxygen composition of films treated in the two gas environments falls in the same range of 20% - 30%, the maximum surface oxygen composition appears at different treatment distances of 8 mm and 12 – 16 mm for N_2 and air environments, respectively. In N_2 environment, all surface oxygen originates from the plasma plume. For the air environment, the O_2 entrainment from ambient can change the density profiles of certain reactive species which may lead to the shift of surface oxidation maximum shown in figure 3.7.

In order to gain more insight into the gas entrainment effect, fluid dynamic (FD) simulation was performed to calculate the molar fraction of air mixed into the RF jet plume. Figure 3.8 shows the simulated air molar fraction at the sample surface for four treatment distances (4 mm to 16 mm). It can be seen that the amount of air mixture is only dramatically different within a 4 mm radius circle on the material surface. At the surface beyond this 4 mm circle, the air mole fraction is comparable for all treatment distances and always higher than 60%. Because we used 0.8 mm steps between scan-processing lines, the gray area (0 - 0.4 mm off the axis) in figure 3.8 shows the scale of the line-scan processing steps. At the plume axis, only 2.9% molar fraction of air was observed at 4 mm treatment distance. However for longer distances the amount of air mixture increases exponentially to 70.5% at 16 mm as shown in the insert of figure 3.8. These FD simulation results agree well with the air partial pressure measured by molecular beam mass spectrometry (MBMS) with the same plasma jet.[85] Although a large difference in the amount of gas entrainment was observed between near and far treatment distances, the difference of etching depth between two environments in Figs. 3 and 7 (black solid and black dotted lines) is small and does not change significantly with treatment distance. This indicates that the polymer etch rate and the density of etchant plasma species may not respond linearly with the amount of environmental gas entrainment in the plasma core. Similar behavior can also be seen in figure 3.6 as the etching depth at 4 mm approaches steady when the ambient gas composition is more than 50% of O_2. The initial small amount (less than 2%) of gas entrainment makes much greater influence on the plasma gas chemistry and its subsequent effect on polymer than the further increase of it.

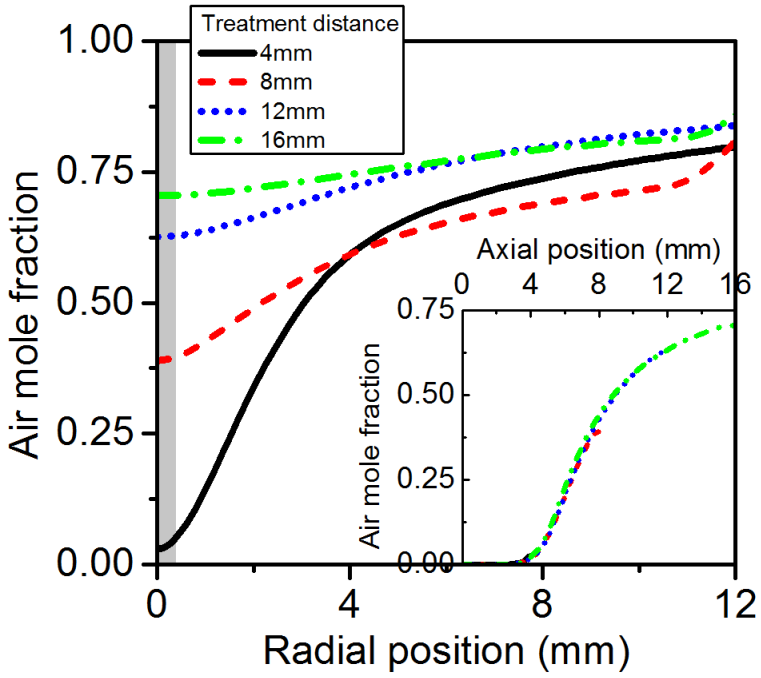

Figure 3.8 Air molar fraction on sample surface and in the plasma plume axis (insert) calculated by fluid dynamic simulation. Axial-symmetric configuration was applied. Four processing distances from 4 mm to 16 mm were evaluated. Gray area shows the scale of the line-scan processing steps.

3.3.5 Substrate temperature effect

The substrate temperature effect on PS etching depth was evaluated with vertical jet configuration in N_2 environment. Three distances, i.e. 4 mm, 12 mm and 20 mm, were evaluated. We found that the etching depth of PS treated by Ar + 1% O_2 plasma increased with temperature (or decreased with $1/T_{sub}$, as shown in figure 3.9).

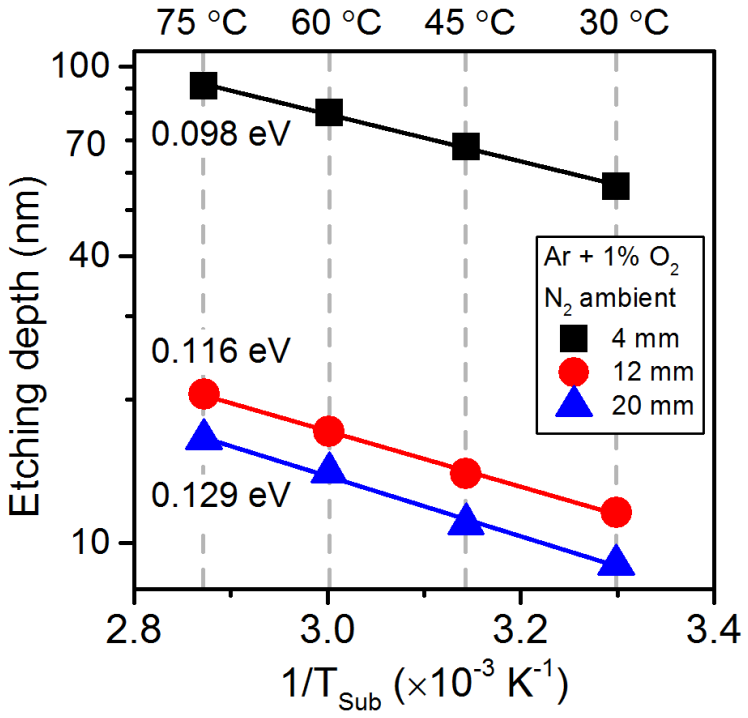

Figure 3.9 Substrate temperature effect on the etching depth of PS treated by Ar + 1% O_2 plasma in N_2 environment. Semi-log plot of etching depth, Log(etching depth), vs. reciprocal of substrate temperature ($1/T_{sub}$) was shown to illustrate the Arrhenius form of the etching reaction rate. Apparent activation energy E_a calculated from the linear fit of Log(etching depth) to $1/T_{sub}$ was labeled. The treatment angle was 90°.

3.4. Discussions

3.4.1 Apparent activation energy of etching reaction

The increase in etch rate at higher temperatures indicates that polymer etching by the RF jet is an activated process. For the ease of discussion, we can use the following formula to represent the conglomeration of all interfacial reactions:

$$\text{Etchant(g)} + \text{Surface(s)} \xrightarrow{k_{ER}} \text{Product(g)} + \text{Surface}^*\text{(s)} \qquad (3.3)$$

where Surface* is the etched surface and k_{ER} is the apparent rate constant of all etching reactions. If we use Arrhenius equation to describe the temperature dependence of rate constant k_{ER}[48, 117], then we have

$$\mathrm{k_{ER}} = \mathrm{A_{ER}} \cdot \exp(\frac{-\mathrm{E_a}}{\mathrm{k_b T}}) \qquad (3.4)$$

where A_{ER} is the pre-exponential factor, k_b is the Boltzmann constant and T is the substrate temperature. The apparent activation energy E_a is an empirically fitted parameter that represents the effective activation energy of various reactions taking place during the etching process. The E_a value for a given polymer/gas system can be a function of processing parameters such as plasma power, gas flow rate and treatment distance[117]. Since the total etching depth can be directly correlated to the rate constant k_{ER}, we obtained apparent activation energy E_a by plotting logarithm of etching depth against $-\frac{1}{k_b T}$. As long as the affinity of etchant species on the material surface and E_a do not change with temperature, a linear fitting can be achieved.

As shown in figure 3.9, the apparent activation energy of Ar + 1% O_2 plasma slightly increases with treatment distance and falls in the range of 0.10 – 0.13 eV which is lower than the ~0.5 eV value reported consistently with pure O_2 low pressure plasma with various polymer structures or etching configurations.[116] Despite the difference of plasma properties between CAPs and low pressure plasma[175], this lower E_a value suggests that the energy barrier of the etching process may have been reduced by some additional energetic plasma species. There are multiple possibilities for such species in our situation, including positive ions which were observed previously by molecular beam mass spectrometry (MBMS) for the same plasma jet.[85] These energetic species can (1) transfer energy and momentum to the surface and cause particle ejection, and (2) change the

coverage of chemically reactive elements on the surface and/or the rate of refreshment.[184] However at this time we do not have enough information to state conclusively that energetic species are directly involved, let alone to identify what these energetic species are and the detailed reaction processes. Nevertheless, other explanations are possible and we will report further investigation on the relation between apparent activation energy and treatment conditions of CAP sources.

It is worth noting that polymer etching and temperature effects are highly source dependent. We have investigated another CAP source known as surface micro-discharge (SMD) using similar approaches, and with the substrate at room temperature we did not observe etching with N_2/O_2 mixtures as working gas.[93, 94, 140] Key differences between these sources are the higher O density in the effluent, the use of Ar which can give rise to energetic species, and the convective transport of gas phase species in the case of the RF jet.

3.4.2 Etching reaction probability of atomic O

Plasma etching of polymers usually starts from free-radical site creation through bombardment by UV photons, electrons, ions and chemical reaction with gas phase atoms or excited species. Among these creation channels, H-abstraction by atomic O from the polymer chain has been discussed by different research groups as the most important channel for both low pressure plasma[8] and atmospheric pressure plasma:[9],[10]

$$RH + O \rightarrow R\bullet + OH \qquad p = 10^{-3}, 10^{-4}, 10^{-5} \qquad (3.5)$$

where p is the estimated reaction probability for the tertiary, secondary and primary carbon site provided by Bhoj *et al.*[9] It can be seen that the tertiary H has the highest abstraction reaction probability.

For the Ar/O_2 RF plasma jet, atomic O is the dominant reactive species in the glow region due to the high cross-section of electron-impact dissociation of O_2.[185] These atomic O can be further transported to the far effluent region through convection and diffusion. Although the density of atomic O in Ar + 1% O_2 plasma has not yet been measured, simulation results[181] show that both Ar + 1% air and Ar + 1% O_2 plasma share similar exponential decay profiles along the nozzle-to-sample distance and only the absolute value of atomic O density in Ar + 1% O_2 plasma is slightly higher. The atomic O density profile of the same plasma jet with Ar + 2% air feed gas in air ambient has been previously measured.[43] It is worth noting that this O density profile was measured without a target surface, however according to Schroder et al.[38] the presence of a plastic (Polyethylene terephthalate, PET) target does not significantly disturb the atomic O distribution measured by TALIF.

In order to evaluate the relationship between PS etching and atomic O species in the gas phase, we estimated the average O flux bombarding the PS surface from the atomic O density data in figure 3.3 by using equation 3.6 from kinetic theory of ideal gases:

$$\overline{\Gamma} = \frac{1}{4} n \overline{v} = \frac{1}{4} n \sqrt{\frac{8RT_{gas}}{\pi M}} \qquad (3.6)$$

where $\overline{\Gamma}$ is the average gaseous flux, n is the gas density, $\overline{v}$ is the average speed, R is the gas constant, T_{gas} is the gas temperature, M is the atomic weight of O. For the atomic O density measured by Van Gaens *et al.*,[43] the density and gas temperature values used at 4 mm, 6 mm and 8 mm are 8 ×10^{15} cm^{-3} 420 K, 6 ×10^{15} cm^{-3} 390 K and 2 ×10^{15} cm^{-3} 375 K, respectively. For the atomic O density simulated by Wende *et al.*,[181] the density and gas temperature values used at 4 mm, 8 mm and 12 mm are 4.2 ×10^{15} cm^{-3} 420 K, 1.8 ×10^{15}

cm^{-3} 375 K and 0.45 $\times 10^{15}$ cm^{-3} 320 K, respectively. The average etched C flux from PS surface was calculated from the measured etching depth by Ar + 1% O_2 plasma in air environment. Since PS only contains C and H and the ratio C:H is 1, the total amount of etched C atoms (N_c) over the whole scan processing period can be estimated as:

$$N_c = \frac{\Delta \cdot A_{treated} \cdot \rho}{A_C + A_H} \cdot N_A \qquad (3.7)$$

where Δ is the etching depth in figure 3.3, $A_{treated}$ is the scan processed area (0.922 cm^2), ρ is the density of PS (1.04 g/cm^3), A_C = 12 and A_H =1 are the atomic mass of carbon and hydrogen atoms, N_A is the Avogadro's number. Although the PS surface was being scan treated, most of the etching happened under the direct exposure of the RF jet plume. At any moment the transient processed area can always be approximately viewed as the cross section area of the jet nozzle ($\pi/4 \cdot ID^2$). Therefore the average etched C flux can be estimated as:

$$\overline{\Gamma_c} = \frac{N_c}{\pi/4 \cdot ID^2 \cdot t} \qquad (3.8)$$

where ID is the inner diameter of the RF jet quartz tube (1.5 mm), t is the total processing time (200 s).

As shown in figure 3.10, by plotting the incident O flux and removed C flux together we found a linear correlation between the two at treatment distances up to 12 mm. The etching reaction probability of O atoms can be estimated from the fitted slope in figure 3.10, and is found to be in the range of 2 $\times 10^{-4}$ - 4 $\times 10^{-4}$. This order of magnitude is comparable to the p values of H abstraction probability by O atoms shown in equation 3.5 and published work[10]. It is also consistent to the values that we have formerly reported[68]

by measuring the etching of three polymers, i.e. PS, PMMA and PVA, with higher plasma dissipated power (~3.5 W) and faster scan-processing speed (2.4 mm/s).

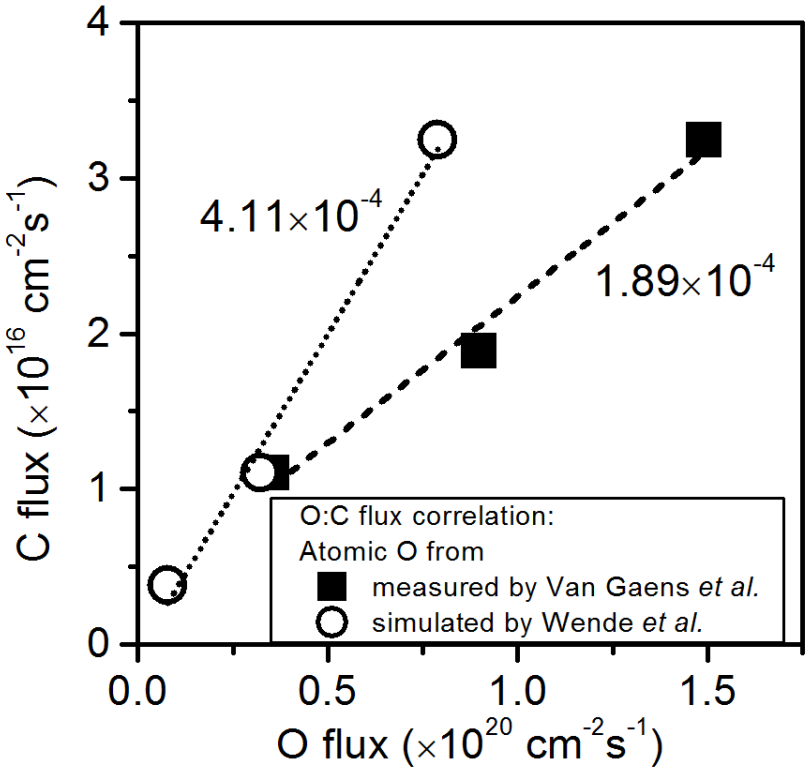

Figure 3.10 Correlation between the estimated incident O flux onto PS surface and the calculated C flux out of PS surface. The atomic O density of solid squares were measured in Ar + 2% air plasma by Van Gaens *et al*.[43] whereas that of open circles were simulated with Ar + 1% O_2 plasma by Wende *et al*.[181] The etching reaction probability of O atoms can be estimated from the fitting slopes and is found to be in the order of 10^{-4}.

3.4.3 Exponential decay of etching depth along treatment distance

The exponential decay of etching depth indicates that the flux of etchant species bombarding the material surface might also drop exponentially with treatment distance. Plasma etching process involves (1) the chemical reactions taking place at the gas-solid

interface and (2) the transport of reactants to the reaction front. It is usually the latter that limits the overall reaction rate. Although the interfacial reactions are inherently complex, the average time needed for etching reaction steps[8, 49, 117] is on the level of ps, e.g. a few ps for H-abstraction[186] and tens of ps for C-C/O bond cleavage.[187] Therefore the density of etchant species near gas-solid interface can be considered as proportional to the etching depth. From equation 3.2, the density of etchant species [etchant] can be expressed as:

$$[\text{etchant}] = A' \cdot \exp(-\frac{d}{\lambda}) \tag{3.9}$$

where $A'$is the pre-exponential factor, λ is the same decay constant as in equation 3.2

The exponential decrease of etchant species in Ar/O_2 plasma, presumably atomic O, along nozzle-to-sample distance is mainly a result of local generation and consumption of O atoms, though these reactions might also be influenced by forced convections. The lifetime of atomic O can be estimated from the temporally resolved O density measurement with the same RF jet (reported by Zhang *et al.*[137] with Ar + 2% O_2 in air environment) used in this work which leads to a lifetime of 0.2 - 0.3 ms. The apparent lifetime (t_a) of atomic O can be defined by the exponential decay constant through:

$$t_a = \frac{\lambda}{\overline{v_{flow}}} \tag{3.10}$$

where λ is the decay constant in equation 3.9, $\overline{v_{flow}} = 14.15\ m/s$ is the average feed gas velocity. For etching by Ar + 1% O_2 plasma in N_2 and air environment (figure 3.3), we could calculate the apparent lifetime of $t_{a,N_2,90^\circ} = 0.284$ ms and $t_{a,air,90^\circ} = 0.199$ ms from the decay constant of $\lambda_{O_2,N_2,90^\circ} = 4.02$ mm and $\lambda_{O_2,air,90^\circ} = 2.81$ mm, respectively. These t_a values agree well with the atomic O lifetime 0.2 – 0.3 ms estimated from published results by Zhang *et al*.[137]

The difference in the exponential decay constant between N_2 and air can be attributed to the O_2 and H_2O entrainment from ambient air. According to the simulation results by Van Gaens *et al.*,[41] in the far effluent region the atomic O is mainly consumed through O_3 generation reaction:

$$O + O_2 + M \rightarrow O_3 + M \qquad k = 6.40 \times 10^{-35} \exp(663.0/T_{gas})\ cm^6 s^{-1} \qquad (3.11)$$

whereas in the plume region water impurities can have a large impact on the atomic O kinetics which might lead to over 80% of the total loss of atomic O.[41] It is worth mentioning that atomic O can also be generated locally in the afterglow region up to 15 mm by the collisions between $O_2(a^1\Delta_g)$ and O_3 with rate coefficient:[188]

$$O_2(a^1\Delta_g) + O_3 \rightarrow 2O_2 + O \qquad k = 5.2 \times 10^{-11} \exp(-2840/T_{gas})\ cm^3 s^{-1} \qquad (3.12)$$

Simulation results suggest that this is a slow O release process and can be responsible for almost all O generation in the far effluent region.[41]

3.4.4 PSI: possibility of other plasma species besides atomic O

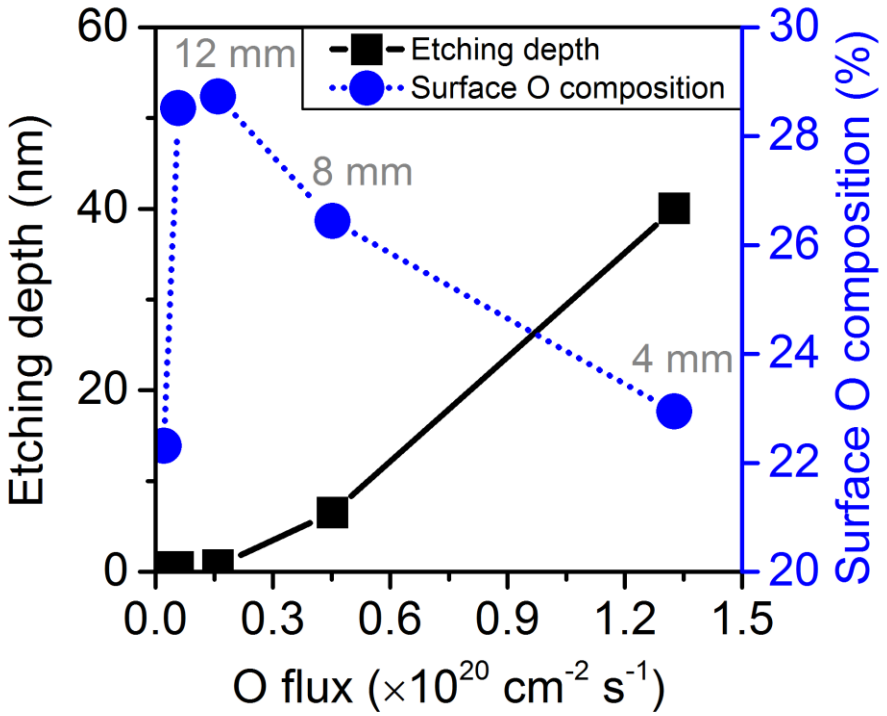

Figure 3.11 Correlation of etching and surface modification of PS (in terms of etching depth and surface oxygen composition, respectively) with estimated atomic O flux impinging the PS surface. The PS films were treated by Ar + 1% O_2 plasma in air environment.

The data presented in this work indicate that the etching and modification of polymers by the RF plasma jet involve surface interactions with multiple plasma species. In order to illustrate this, we correlated the PS etching depth and surface oxygen composition with the incident atomic O flux, as shown in figure 3.11. The measured etching depth and surface oxygen composition are abstracted from figure 3.7, and the corresponding atomic O flux is calculated from the fitted atomic O density from simulation (blue dotted line) in figure 3.3 by using method described in section 3.4.2. Figure 3.11 indicates that the etching depth of PS has a relatively simple relationship with the flux of atomic O which we have correlated in section 3.4.2. However the surface oxygen composition of PS shows a rather complex behavior with the impinging atomic O flux which can be varied by adjusting the nozzle-to-surface distance. This suggests that either the O related surface reactions are complex or there are other important quantities besides atomic O. The additional plasma species, if exist, might exhibit a different behavior with nozzle-to-surface distance than atomic O, which is consistent with the fact that the apparent activation energy varies as the nozzle-to-surface distance is increased. Besides, the decrease of surface oxygen composition with the increase of atomic O flux shown in figure 3.11 suggests that etching and modification might not be entirely independent: the etching process might impede the accumulation of surface modification by removing oxidized

sites. We are currently working on a detailed PSI model that considers these factors and we will report it in the near future with further experimental evidences.

3.5. Summary and Conclusions

In this paper we studied atmospheric pressure plasma-polymer surface interaction using a well-characterized RF Ar/O_2 plasma jet and PS as a model system. The surface response of PS to a number of plasma processing parameters, namely treatment distance, environmental gas composition, as well as substrate temperature, were characterized by evaluating both the thickness and surface chemical composition change after treatment. Kinetics of surface reactions were discussed and correlated to the plasma gas phase.

We showed that Ar/O_2 RF plasma jet can induce fast etching and mild oxidation of the PS surface. We found that the etching efficiency of Ar/O_2 plasma dropped exponentially with nozzle-surface distance. The correlation of the etching depth profile of PS with the density profile of atomic O measured/simulated in the gas phase indicates that atomic O can be the dominant etchant species. The etching reaction probability of atomic O is estimated to be in the range of 2×10^{-4} - 4×10^{-4}. Different from the etching depth profile, we showed that surface oxygen composition of PS reached to a maximum and then fell down with treatment distance. The difference between etching and surface oxygen composition profiles along treatment distance implies that surface etching and modification can be controlled by different interfacial processes involving multiple plasma species.

The apparent activation energy (E_a) of the etching reaction was estimated by measuring etch rate versus substrate temperature. We measured the apparent activation energy of Ar/O_2 plasma etching reaction with PS and it is in the range of 0.10 – 0.13 eV and increases slightly with treatment distance. This relatively low E_a value suggests that

additional energetic plasma species might be involved in the PSI processes. This is also consistent with the different behavior of the etching and modification reactions at the polymer surface as nozzle-to-surface distance is varied.

Acknowledgement

The authors gratefully acknowledge financial support by the National Science Foundation (PHY-1415353) and the US Department of Energy (DE-SC0001939). We thank H. Wang for his contribution on preparing part of the ellipsometry and XPS data. We also thank D. B. Graves and C. Anderson of UC Berkeley for helpful discussions on this collaborative project. We are grateful to E. A. J. Bartis, A. Pranda, C. Li and L. Shafi for helpful discussions and collaborations.

Chapter 4: Stages of Polymer Transformation during Remote Plasma Oxidation (RPO) at Atmospheric Pressure

P. Luan[1] and G. S. Oehrlein[1]

[1] Department of Materials Science and Engineering and Institute for Research in Electronics and Applied Physics, University of Maryland, College Park, MD 20742, USA

Journal of Physics D: Applied Physics, 51 (13), 135201 (2018)

Abstract

The interaction of cold temperature plasma (CAP) sources with materials can be separated into two types: “direct” and “remote” treatments. Compared to the “direct” treatment which involves energetic charged species along with short-lived, strongly oxidative neutral species, “remote” treatment by the long-lived weakly oxidative species is less invasive and better for producing uniformly treated surfaces. In this paper we examine the prototypical case of remote plasma oxidation (RPO) of polymer materials by employing a surface micro-discharge (SMD, in N_2/O_2 mixture environment) treatment on polystyrene (PS). Using material characterization techniques including real-time ellipsometry, X-ray photoelectron spectroscopy (XPS) and Fourier-transform infrared spectroscopy (FTIR), the time evolution of polymer film thickness, refractive index, surface and bulk chemical composition were evaluated. These measurements revealed three consecutive stages of polymer transformation, i.e. surface adsorption and oxidation, bulk film permeation and thickness expansion followed by surface etching as a result of RPO. By correlating the observed film thickness changes with simultaneously obtained chemical information, we found that the three stages were due to the three effects of weakly oxidative species on polymers: (1) surface oxidation and nitrate ($R\text{-}ONO_2$) chemisorption, (2) polymer surface and bulk oxidation and (3) etching. Our results demonstrate that surface adsorption and oxidation, bulk oxidation and etching can all happen during one continuous plasma treatment. We show that surface nitrate is only adsorbed on the top few nanometers of the polymer surface. The polymer film expansion also provided evidence for the diffusion and reaction of long-lived plasma species in the polymer bulk. Besides, we found that the remote plasma etched surface was relatively rich in O-C=O (ester or carboxylic acid).

These findings clarify the roles of long-lived weakly oxidative plasma species on polymers and advance the understanding of plasma-polymer interactions on a molecular scale.

4.1. Introduction

Study of the possible applications of cold atmospheric plasma (CAP) on modifying material surfaces [147, 166], sterilizing microorganisms [167, 168], and possible therapeutic treatments [148, 149, 169] has experienced rapid growth in recent years. Although the interaction between plasma generated reactive species and target materials serves as the foundation for these applications, progress on the interaction mechanism at plasma-material interface has been slow and less impressive compared to CAP's ever expanding new applications [140]. For oxidizing environments, the difficulty of studying plasma-material interaction originates from the complex nature of plasma generated reactive species which include energetic charged species, UV photons, short-lived strongly oxidative neutrals and long-lived weakly oxidative neutrals [189]. When interacting with polymers and bio-molecules, CAP sources are known to cause etching [159] and surface oxidation [141]. However the explicit role of each type of plasma species on materials is hard to determine and can sometime be concealed by the synergistic effects of multiple plasma species.

The interaction of CAP sources with materials can be classified into "direct" and "remote" treatments. A "direct" treatment indicates that the target material might serve as part of plasma generation circuit, and CAP is generated on or near the target surface. In such situation charged species i.e. ions and electrons directly interact with material surface, and the short-lived neutral species also play a more important role since they are generated close to the target. For "remote" treatments, the targets do not serve as part of the electrical circuit and are located in the far effluent of the CAP source. The visible plasma plume does not touch the target surface, and the number of short-lived species interacting with the

sample surface is significantly reduced. It is the long-lived, typically weakly oxidative, neutral species that dominate the plasma-surface interaction. In this paper, we use "remote" to specifically refer to long-lived, weakly oxidative plasma species, such as $O_2(a)$, O_3, NO, NO_2 and HNO_3.

Recently we studied the effect of vacuum ultraviolet (VUV) photons [6] and short-lived strongly oxidative species such as atomic O [1] and OH [68] using model plasma source and polymer systems, and we found both type of plasma species could cause fast etching of polymers. We also indirectly evaluated the effect of energetic species, e.g. ions, and we found that they might provide extra energy to facilitate etching [190]. For the long-lived, weakly oxidative neutral species, we evaluated their effect on the surface chemistry of polymers/biomolecules and we found surface oxidation and nitrate formation with 7 minutes of treatment without etching [93]. However, it is still unknown how material surface changes over a long treatment time and whether they will eventually cause etching of the material surface. Besides, since the effect of VUV photons and ions is negligible in remote plasma oxidation (RPO, exchangeable with remote plasma treatment in this article) [6], a highly cross-linked surface layer which blocks other gas phase particles from penetrating through cannot be formed. This raises the question whether the prolonged RPO can cause modification of the polymer bulk.

In this work, we evaluate the effect of RPO on the temporal evolution of polymer film properties, including thickness, refractive index, surface chemical moieties and bulk chemical composition, over long treatment times (up to 290 minutes). We choose surface micro-discharge (SMD) [139] as a model remote CAP source for this study based on several reasons. First, effect of ions can be ignored since they are generated within a thin layer on

the dielectric surface then transported onto target surface which does not serve as part of the electrical circuit [167, 191]. Second, when the SMD sources are operated with N_2 and O_2 working gas, the effect of UV photons and invasive etchant species such as atomic O and OH on target can be minimized because both species are confined in the thin discharge layer and hard to be transported to target surfaces [6, 68, 191]. We choose the C- and H- based polystyrene (PS) as a model polymer since it does not contain O and N which makes it ideal for studying oxidation and nitration as a result of RPO. In this paper we will examine the experimentally observed polymer transformation stages during RPO. We will also discuss the phenomena of surface adsorption, surface and bulk oxidation, polymer film expansion, as well as etching based on characterization by comprehensive techniques.

4.2. Experiments and methods

4.2.1 Materials and thin film preparation

PS beads were purchased from Sigma-Aldrich (St. Louis, MO, USA) with average molecular weight of 35 000 and used as is. Thin films were prepared by the spin-coating of PS in propylene glycol methyl ether acetate (PGMEA, Sigma-Aldrich, ReagentPlus, ≥99.5%) solution onto Si substrates with or without a ~100 nm SiO_2 top layer. For ellipsometry analysis, 14 - 35 nm PS films were coated on SiO_2/Si substrate. For XPS and FTIR analysis, ~180 nm and ~350 nm PS films were coated on Si substrate, respectively. The pristine PS film has a refractive index of 1.5853 and a RMS surface roughness of 0.35 nm as measured by spectroscopic ellipsometer (J.A.Woollam alpha-SE) and atomic force microscopy (Bruker MultiMode in tapping mode), respectively [1].

4.2.2 Plasma source and scan processing of polymers

To study the generic behavior of PRO of polymers, we selected surface micro-discharge tube array (SMD-TA), a variation of the traditional planar configuration SMD [93, 140], as the model remote plasma source. As shown in figure 4.1, the SMD-TA features curved discharge metal meshes which are fitted in multiple plasma generation tubes. Each of these tubes consists of a stainless steel (SS) woven mesh as powered electrode, a quartz tube as dielectric barrier and a perforated center rod as working gas distributor. Outside of these quartz tubes is a grounded metallic chassis that conducts electrical current and heat. The reactor was powered by a sinusoidal power supply with 6 kV peak-to-peak (kV_{pp}) voltage at a frequency of 23 kHz (power consumption density [140] < 0.1 W/cm^2). The SMD-TA was operated with 2 standard liters per minute (slm) of 95% O_2 and 5% N_2. Since the SMD-TA is essentially a SMD type of plasma source and the behavior of it is very similar to the planar configuration SMD, we use the term SMD instead of SMD-TA in the rest of this report. It is worth mentioning that our results of polymer transformation stages with SMD-TA treatment are also observed with planar SMD treatment.

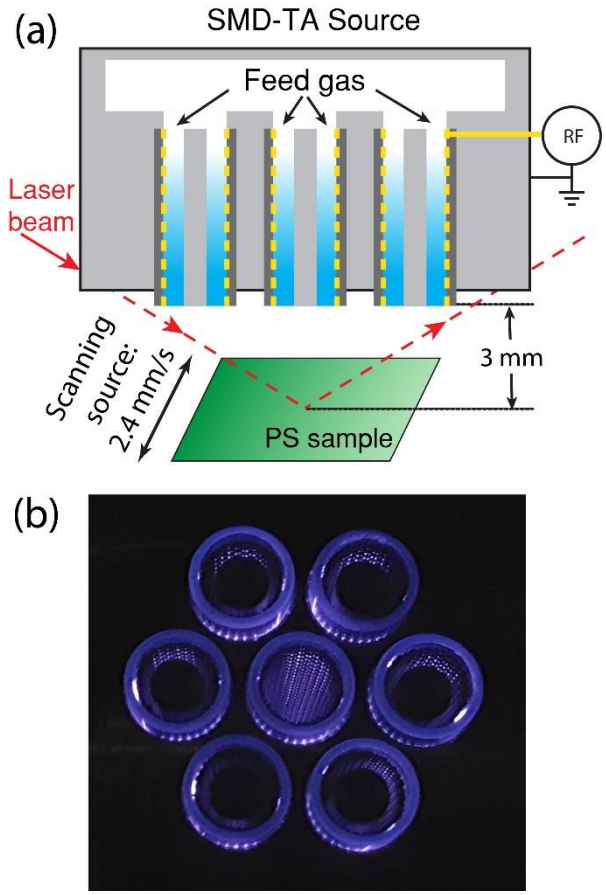

Figure 4.1 (a) Schematic diagram of polymer processing by the SMD-TA source used in this work. The target material is placed underneath the nozzle with a distance of 3 mm. The SMD-TA source is mounted on a scanning stage with a scanning speed of 2.4 mm/s. (b) Optical image of SMDTA source operated with N_2 feed gas at 6 kV_{pp} and 23 kHz. The perforated center rod of the discharge tube at the center of the array was removed for demonstrating the uniformity of the glow discharge.

In order to uniformly process material surfaces for further characterizations, the SMD reactor was mounted on a homemade 1 dimensional (1-D) scanning stage similar to the one reported before [68]. During plasma treatment, the SMD source scans over sample surfaces located 3 mm underneath it with a speed of 2.4 mm/s. The treatment time for each

back-and-forth scan is 38 seconds. The temperature of the aluminum chassis of the SMD source was monitored by a thermocouple and found to be below 52 °C. The heating effect on target materials by the SMD was evaluated through measuring the thermal expansion of 745 nm SiO_2 using ellipsometry, but no observable thickness change due to heating was recorded during scan treatment which indicates the temperature variation is less than 10 °C. We also measured the thickness reduction of PS films due to heating and we did not observe etching at 40 °C. Therefore the heating effect of SMD reactor on PS films is considered as negligible in this work. To control the environment wherein plasma-polymer interaction occurs, all experiments were performed in a sealed 50 L chamber. The chamber was pre-evacuated to a base pressure lower than 50 mTorr and then refilled to atmospheric pressure with 95% O_2 and 5% N_2 before experiments.

4.2.3 Surface characterization

The optical property of PS films was characterized using an automated rotating compensator ellipsometer (SOFIE STE70) in the polarizer-compensator-sample-analyzer (PCSA) configuration with He-Ne laser (λ = 632.8 nm) at ~73° angle of incidence [159]. Upon the reflection of laser beam on polymer sample, the change in phase difference (Δ) and the angle (Ψ) whose tangent is the ratio of the magnitudes of the total reflection coefficient were recorded and analyzed [192]. Because the large size of the SMD source, high incident light angle (73°) and the small distance from the source to the sample surface (3 mm), Ψ- Δ values were measured at the end of each scan cycles (38 seconds) when the SMD source is removed away to allow the laser beam to pass through.

The surface chemical composition of pristine and treated PS films was characterized by a XPS system (Vacuum Generators ESCALAB MK II). Both survey and

high-resolution spectra of C 1s, N 1s, O 1s and Si 2p were obtained at electron take-off angles of 20° (probing depth ≈ 2 nm) and 90° (probing depth ≈ 8 nm) for angle resolved XPS (AR-XPS) analysis. For peak fitting and elemental composition analysis, we used CasaXPS software with the constraint of full width at half maximum (FWHM) of C 1s, N 1s and O 1s peaks in the range of 1.4 – 1.6 eV, 1.5 – 2 eV and 1.6 - 2.0 eV, respectively [158]. Si 2p spectra were neglected during elemental composition analysis due to the absence of peaks which indicates that miniscule amount of Si has been deposited on polymer surface from the SMD source. Peaks corresponding to C-C/H (285 eV), C-O (286.5 eV), O-C-O/C=O (287.9 eV), O-C=O (289.1 eV), O-CO-O (290.2 eV) and pi–pi* shake-up (291.5 eV) were used for the fitting of C 1s spectrum. Due to the overlapping of peaks in O 1s, two peaks at 532.7 eV and 533.9 eV were used to fit the spectrum with each representing oxygen moieties with binding energy from 532.2 eV to 533.1 eV and from 533.6 eV to 535.3 eV [1]. For the N 1s spectrum, only nitrate (408.2 eV) peaks were fitted due to the absence of peaks from 398 eV to 406 eV [193, 194]. All spectra were calibrated to the C-C/H peak at 285 eV. After Shirley background subtraction, the chemical composition of the film was calculated by integrating peak areas of C 1s, N 1s and O 1s with sensitivity factors of 1, 1.77 and 2.85, respectively [179]. The detection limit of elemental composition by XPS is 0.5%. More information on analyzing the XPS results can be found elsewhere [1, 158].

Attenuated total reflectance - Fourier transform infrared (ATR-FTIR) spectroscopy [195] (IRPrestige 21 from Shimadzu and VeeMAX II from PIKE) was used for characterizing the chemical composition in the bulk of the PS films. The contact status (the amount of clearance between Ge crystal and polymer) of different samples was calibrated

by matching the peak intensity at 699 cm^{-1} which is the peak with highest intensity in the measured IR range (650 – 3500 cm^{-1}). The contact area was further corrected by converting absolute absorbance to the ratio against the peak at 699 cm^{-1}.

4.3. Results and discussion

4.3.1 Real-time Ellipsometry during RPO

In figure 4.2 two exemplary real-time ellipsometry trajectories along with optical simulation results based on single layer ellipsometry model are shown to illustrate the three distinct stages of polymer oxidation by RPO. In figure 4.2 (a) the SMD treatment started from point A, and after two turning points B and C the treatment was ended at point D which corresponds to 60 minutes. For the sample in figure 4.2 (b), we extended the processing time to 290 minutes to show the long-term effect of RPO. As seen in both plots, the gaps between groups of data points in section AB are due to the scan processing - the larger the gap between data points, the more dramatic changes on PS films each scan treatment (38 seconds) introduces. We also labeled the time consumption for reaching point B, C and D in figures 4.2 (a) and (b), and it can be seen that during section AB (first 3 minutes of treatment) the polymer films showed dramatic changes on its optical property after each treatment scan. After a mild turn at point B and a slow BC stage, we observed a sharp turn at point C for 20-23 minutes of treatment time. Due to the similarity between figures 4.2 (a) and (b), we will focus on discussing figure 4.2 (a) and then compare it to figure 4.2 (b).

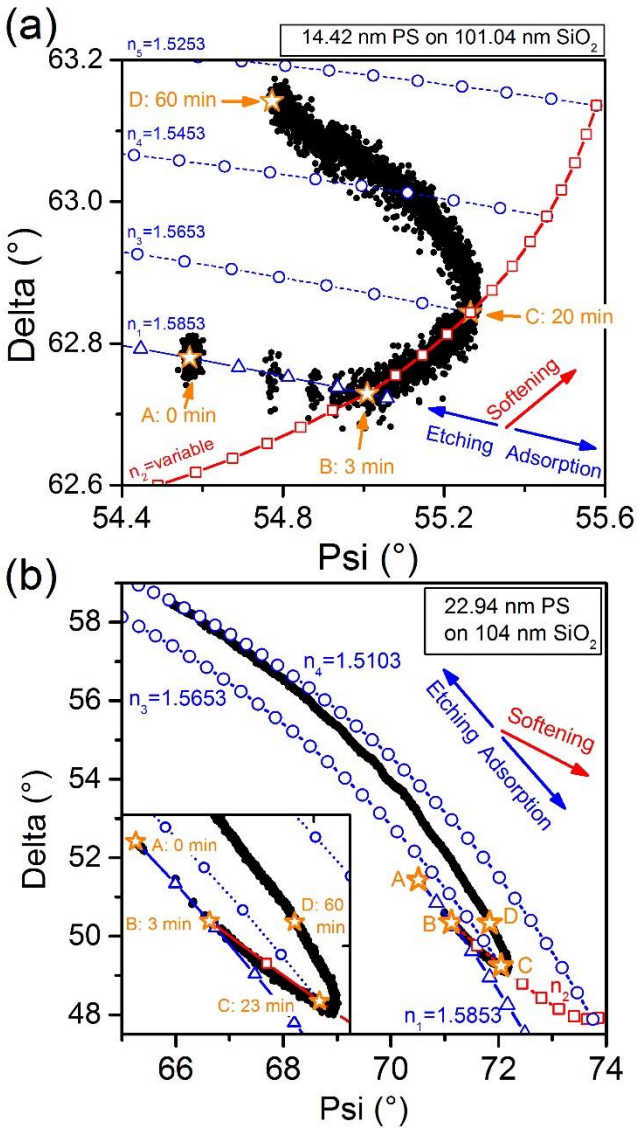

Figure 4.2 Ellipsometry Ψ-Δ data obtained during SMD treatment of (a)14.42 nm PS for 60 min and (b) 22.94 nm PS for 290 min. The PS films were coated on Si substrate with ~100 nm SiO_2 top layer. The experimental data is shown by solid dots. The single layer ellipsometry model simulations are shown by lines with open symbols. Three distinct sections of RPO of polymer are defined: 1) AB: surface adsorption/oxidation, 2) BC: bulk film expansion and 3) CD and beyond D: etching. Point A corresponds to the beginning of the experiment. At point B, a surface adsorption/oxidation layer was formed in about 3 minutes with a thickness of ~3.6 Å regardless of pristine film thickness. Point C denotes

the end of polymer film expansion which is proportional to the pristine film thickness (~ 6 %). Point D indicates 1 hour of treatment. Inset in (b) is the enlargement of A to D sections. The etching of polymer film takes place at a rate of 0.7 nm/hour.

To better interpret the real-time ellipsometry data, we overlaid optical models on top of the measured Ψ-Δ trajectory in figure 4.2 (a). Because of the thin thickness of the polymer film, the difference in material property at different depth is minimized, which justifies the use of a single layer optical model. Curve n_1 (blue line with open triangle) is the modelling result of Ψ-Δ angles that relates to growing pristine PS film (n_0=1.5853) on SiO_2/Si substrate. The interval between the triangle symbols corresponds to a thickness change of 1 Å. In fact the experimental Ψ-Δ data overlap with the 14.42 nm symbol of curve n_1 at point A, which indicates the original PS film thickness before plasma treatment. As the SMD treatment begins, the experimental Ψ-Δ values move along curve n_1 to point B which corresponds to a thickness increase of 3.6 Å compared to point A.

The increase of film thickness during section AB might come from either the surface adsorption/oxidation of plasma species or the expansion of the PS film due to plasma modification. If it was due to bulk expansion, the net thickness gain in AB would depend on the pristine film thickness. However when comparing PS films ranging from 15 nm to 100 nm, we found that the thickness increase in section AB was always ~3.6 Å. For example in figure 4.2 (b), although the PS film is 1.6 times as thick as that in figure 4.2 (a), similar amount of net increase (3.7 Å) is observed. Furthermore, polymer film expansion, e.g. through chain scission or oxidation, usually leads to the decrease of refractive index (more discussion in Section 4.3.5). However the AB section in both figures 4.2 (a) and (b)

did not show such change. Finally, the time needed for completing the AB stage is also a constant regardless of PS film thickness, which indicates that AB stage is not a time controlled process such as diffusion in the polymer bulk. In fact, surface chemistry analysis by XPS shows that the AB stage corresponds to moderate surface oxidation and the chemisorption of surface nitrate ($R\text{-}ONO_2$), which will be discussed in section 4.3.2.

After the turn at point B, the real-time Ψ-Δ trajectory in figure 4.2 (a) follows curve n_2 (red line with open square) which is the modeling results of Ψ-Δ angles that relate to the softening of the polymer bulk. In the optical model of curve n_2, we assumed linear relationship between the change of film thickness and that of refractive index. Without better knowledge about the physical process during expansion, we chose this assumption due to its simplicity. The physical meaning of curve n_2 can be understood as the expansion of the polymer bulk by plasma modification without losing any material (etching). This hypothesis of bulk expansion during BC stage is further validated by the thickness dependence of the net thickness gain and the oxidation of polymer bulk which will be discussed in later sections. The difference between symbols in curve n_2 is 2 Å and 0.005 for thickness and refractive index, respectively. Thus at point C the polymer film has a thickness of 15.58 nm and a refractive index of 1.5653.

After the sharp turn at point C, the Ψ-Δ trajectory in figure 4.2 (a) changes its direction from the increase of Ψ to the decrease of Ψ, which indicates the onset of polymer etching. The Δ value keeps increasing after point C which suggests that the softening of the polymer film still continues in the etching stage. To better illustrate this, we mapped three models in figure 4.2 (a) (curve n_3, n_4 and n_5 with blue dashed lines and open circles) that relate to the etching of homogenous polymer films with refractive index of n_3=1.5653,

n_4=1.5453, n_5=1.5253. The thickness interval between symbols is 1 Å, and each model starts from a symbol on curve n_2. It can be seen that after point C the experimental Ψ-Δ values did not follow curve n_3 which corresponds to steady-state etching with no change on the refractive index. Instead, the Ψ-Δ trajectory intercepts curve n_4 and moves toward curve n_5. This indicates that the etching process is accompanied by the further softening of the film through bulk modification. At the end of the experiment, i.e. point D, the treated PS film has a thickness of 16.22 nm and a refractive index of 1.5325. It is worth pointing out that although we attributed CD as the etching stage, the thickness at point D 16.22 nm is actually thicker than point C 15.58 nm. This is due to the continued expansion of the polymer bulk in the etching stage which surpasses the thickness removed by etching.

Similarly the three stages of polymer transformation were also observed in figure 4.2 (b). Because of the thicker starting thickness, the Ψ-Δ trajectory is in a different region compared to figure 4.2 (a). We also overlaid the optical models with the experimental Ψ-Δ data, and curves n_1 through n_4 have the same meaning as those in figure 4.2 (a). The major difference between models in figures 4.2 (a) and (b) is the change of thickness and refractive index between symbols. For curve n_1, n_3 and n_4, the thickness change is 2 Å whereas for curve n_2 the thickness and refractive index change is 7.4 Å and 0.01, respectively. It can be seen that the thicker PS film in figure 4.2 (b) has expanded more during the BC stage (14.8 Å vs. 8 Å in figure 4.2 a). Interestingly, the expansion ratio to its pristine film thickness is comparable (6.4% vs. 5.5 % in figure 4.2 a). The refractive indexes at C points are also the same (1.5653). These facts provide further evidence that the expansion stage BC is a bulk effect. The similarity between the two Ψ-Δ trajectories in figures 4.2 (a) and (b) indicates that the three stages of modification is generic regardless

of film thickness which has also been seen in additional experimental results not reported here. We extended the treatment time in figure 4.2 (b) to 290 minutes and we found that the Ψ-Δ trajectory gradually approached curve n_4 after D point. This indicates that in the later stage of RPO of polymers, the bulk expansion slows down while etching continues. More discussion about figure 4.2 (b) can be found in Section 4.3.5.

4.3.2 Surface composition: high resolution XPS

Since the pristine PS contains only C and H, the elemental analysis of surface chemical composition can provide more information on the evolution of PS films under RPO. In figure 4.3 the high resolution N 1s, O1s and C1s spectra of pristine, 5 minutes and 90 minutes treated PS were shown to demonstrate the surface composition at different stages of RPO. After 5 minutes of treatment, the PS film has passed the surface oxidation and adsorption stage (AB in figure 4.2) and is in the early expansion stage (BC in figure 4.2), whereas after 90 minutes of treatment the PS film has proceeded to the etching stage. It can be seen that the SMD treatment results in nitrate (R-ONO_2, 408.2 eV) formation as shown in figure 4.3 (a) and surface oxidation as shown in figure 4.3 (b). Interestingly, the amount of nitrate on the PS surface remains comparable between 5 and 90 minutes of treatment. In the O 1s spectra, a large portion of the O composition with 5 minutes of SMD treatment (red curve in figure 4.3 b) is from surface nitrate. However the O 1s spectrum with 90 minutes treatment shows a larger peak with its center position shifted to the lower binding energy side which indicates the increasing amount of C-O, C=O and O-C=O groups on the surface after prolonged SMD treatment.

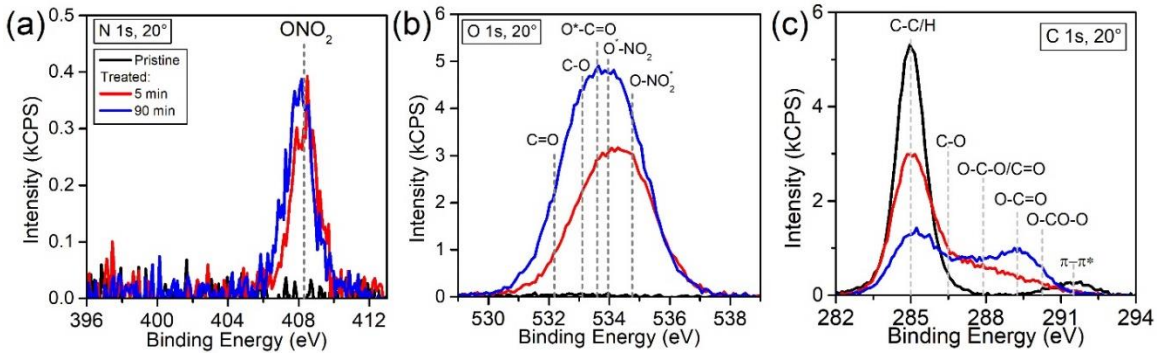

Figure 4.3 High resolution XPS of (a) N 1s (b) O 1s and (c) C 1s of 180nm PS films. Spectra of both pristine and SMD treated films are shown for comparison. The pristine PS does not contain N or O. The treated PS showed surface nitrate ($R\text{-}ONO_2$) formation and oxidation. The electron take-off angles are 20° in all spectra which correspond to the top ~ 2 nm of the PS surface.

More details about the surface functional groups can also be found in the high resolution C 1s spectra, as shown in figure 4.3 (c). Because the peak positions in C 1s spectrum are better separated from each other, peaks corresponding to C-C/H (285 eV), C-O (286.5 eV), O-C-O/C=O (287.9 eV), O-C=O (289.1 eV), O-CO-O (290.2 eV) and pi–pi* shake-up satellite (291.5 eV) can be fitted and analyzed individually. As shown in figure 4.3 (c), the pristine PS contains mostly C-C/H bond (91.1%), and the π - π* shake-up peak (5.4 %) indicates the presence of carbon rings. After 5 minutes of treatment (red curve in figure 4.3 c), oxygen containing functional groups, i.e. C-O, O-C-O/C=O and O-C=O, start to appear. For the 90 minutes treated films (blue curve), the PS surface shows more oxidation with a distinct secondary peak at 289.1 eV which corresponds to O-C=O (ester or carboxylic acid) group. The formation of the large amount of O-C=O during

etching stage is a distinct feature for the SMD treated polymers compared to other APP sources we have studied, including both MHz APPJs [1, 68] and kHz APPJs in which highly reactive etchant (atomic O and OH) and energetic species (ions and UV photons) are present [141] [94]. Correspondingly, the O-C=O group can also be seen in the O 1s spectrum at 533.6 eV as shown in figure 4.3 (b).

4.3.3 Evolution of surface composition over treatment

To better demonstrate how the surface composition evolves during plasma treatment, we showed the calculated surface N, C and O composition as a function of time in figures 4.4 (a) and (b). For the ease of correlating with the real-time ellipsometry data in figure 4.2, we labeled the A, B, C and D points in figure 4.4. Similarly, the AB, BC and CD section corresponds to the three stages discussed above. We extended the SMD treatment time beyond point D (60 minutes) to 290 minutes for studying the dynamic process during prolonged etching.

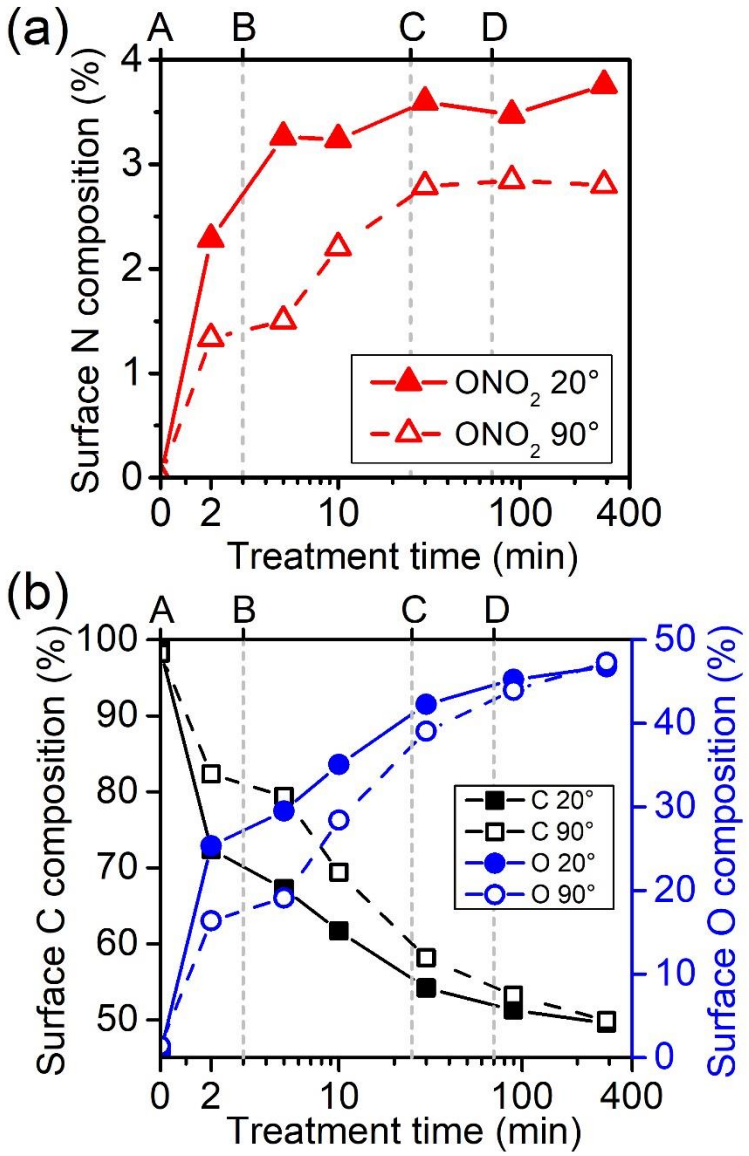

Figure 4.4 The time evolution of surface (a) N, (b) C and O composition. Both 20° and 90° electron take-off angles were shown in (a) and (b) for comparing the elemental composition at different probing depth (~2 vs. ~8 nm). The label of A, B, C and D corresponds to those in figure 4.2.

First and foremost, we observed the saturation of surface N composition for both 20° and 90° electron take-off angles in figure 4.4 (a), but the time needed for reaching such

saturation was different: at point B vs. at point C. Since high resolution N 1s spectra, e.g. figure 4.3 (a), show that all surface N composition comes from nitrate groups, the N 1s composition is equivalent to the surface nitrate composition. In figure 4.4 (a) the difference of N composition between the two electron take-off angles persists regardless of treatment time, which shows that the nitrate moieties always have a composition gradient with film depth at any treatment time. Because 20° and 90° electron take-off angles correspond to chemical information from the top 2 nm and 8 nm of the surface respectively, we conclude that the nitrate in the top 2 nm of the surface is formed during the AB stage and extra nitrate is added to the deeper section of the film (2~8 nm) during the BC stage.

Similar to figure 4.4 (a), figure 4.4 (b) shows the evolution of C and O composition of polymer surface during treatment. Because hydrogen has only one valence electron and does not produce a core photoelectron peak [196], the pristine PS film (0 second treatment time) shows a composition of 100% C. As plasma treatment progresses, the polymer surfaces show continuously increasing amount of O composition. Interestingly, this oxidation of the polymer film continues even when the film enters the etching stage, which correlates well with the continuous reduction of the refractive index and the further expansion of the film during the etching stage in figure 4.2.

We also found that most of the surface oxidation occurred during the first 30 minutes of treatment, i.e. in the surface adsorption/oxidation stage and expansion stage. After 2 minutes of SMD treatment, 25.3 % of the top 2 nm of the surface (20° take-off angle) is composed of O as shown in figure 4.4 (b). Since the O composition contributed by $–ONO_2$ is three times as much as the N composition (2.3 % for 20° scan in figure 4.4 a), this shows that the O composition from various O containing groups other than $–ONO_2$

is about 18.4% on the top 2 nm of the polymer film. The decomposition of the C 1s spectrum in figure 4.3 (c) also confirms the formation of various surface carbon oxygen (C/O) moieties. Therefore the AB stage in figure 4.2 features both surface nitrate adsorption and moderate surface oxidation. Since the real-time ellipsometry data in figure 4.2 shows a consistent thickness increase of ~3.5 Å during the AB stage regardless of the original film thickness, the XPS data indicate that the surface oxidation and nitrate adsorption is responsible for it.

When comparing the surface C and O composition measured for different electron take-off angles in figure 4.4 (b), we find that the treated PS surface shows a composition gradient versus film depth and this gradient is reduced with increasing treatment time. The composition gradient finally disappears at 290 minutes which indicates that the top ~8 nm of the surface is eventually homogenously oxidized in the late etching stage. The existence of a composition gradient indicates that the SMD generated neutral reactive species can penetrate into and react with the sub-surface of the polymer film. We also performed a series of back-etching experiments where 3.5 - 42 nm of material was removed from the top of the SMD treated PS films by low pressure Ar plasma [197], and our vacuum transferred XPS results on the back-etched PS surface verified the deep oxidation in the polymer bulk. We suspect that the oxidation in the deeper section of the film might result from the diffusion of plasma species into the polymer bulk which is made possible by not having (1) a ion induced densely cross-linked surface layer and (2) fast material removal by rapid etching. More details about this will be featured in our future publications.

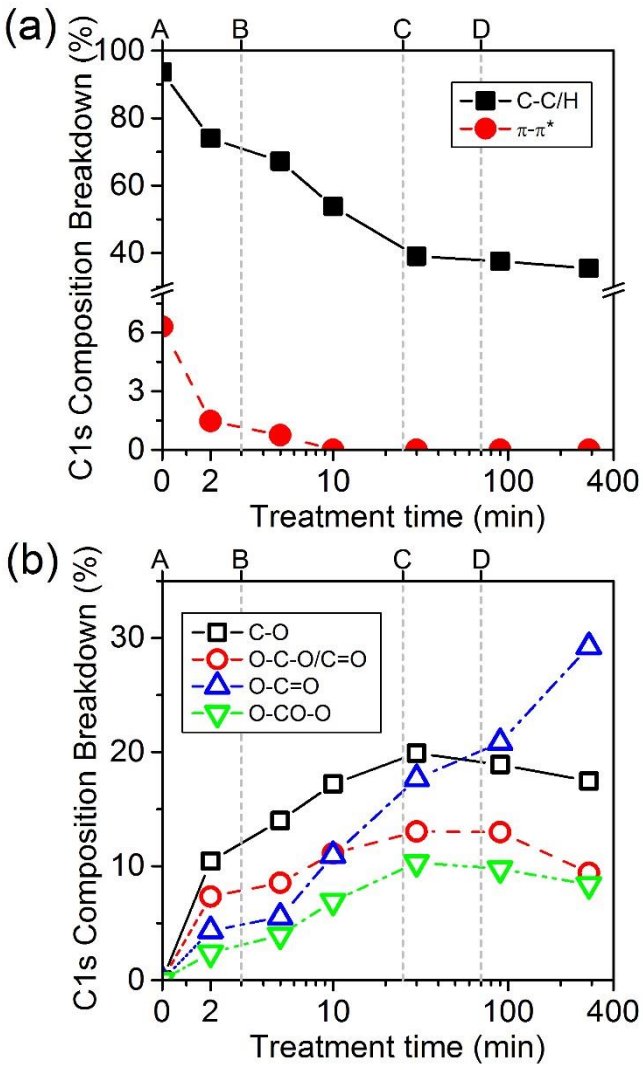

Figure 4.5 The decomposition of XPS C 1s spectra for (a) C-C/H and π-π* shakeup peaks and (b) various carbon oxygen bonds plotted as a function of treatment time. Only data from 20° electron take-off angle were shown. The label of A, B, C and D corresponds to those in figure 4.2.

The evolution of various carbon containing moieties fitted from high resolution C 1s spectra is shown in figures 4.5 (a) and (b). It can be seen that plasma treatment converts C-C/H bonds and carbon rings into various C/O groups. After point C, the π- π* shake up

peaks disappeared which suggests that the carbon ring structures were destroyed by RPO during the first two stages, i.e. adsorption/oxidation stage and expansion stage. Furthermore, the composition of most O containing moieties shown in figure 4.5 (b) stopped increasing in the etching stage except for the O-C=O group. This might be related to the unique etching mechanism of RPO. One possible explanation is that O-C=O is the precursor for forming etching product CO_2. Once certain amount of O-C=O group, i.e. 17.7 % as shown in figure 4.5 (b), is accumulated on the surface, the etching process can be initiated – plasma species might directly or indirectly attack the final bonds that connect each O-C=O group to the polymer chain and subsequently release it as volatile product CO_2. The increase of O-C=O composition in the etching stage implies that other surface moieties are converted into O-C=O which will be eventually etched away through CO_2 formation. We also expect that the composition of O-C=O will reach saturation after certain treatment time ($\geq$ 5 hours) due to the balance between the generation and removal of O-C=O through polymer oxidation and CO_2 formation, respectively. In figure 4.6 we showed the high resolution XPS C 1s spectrum of 290 min treated PS film along with its decomposition into various functional groups. It can be seen that the second peak around 289.1 eV corresponds to the O-C=O group. Due to the fact that there is no difference in the C and O composition between 20° and 90° XPS scans of the 290 minutes treated sample (figure 4.4 b), we think that the spectrum in figure 4.6 might be close to the most extreme oxidation state achieved from the balance between polymer oxidation and etching.

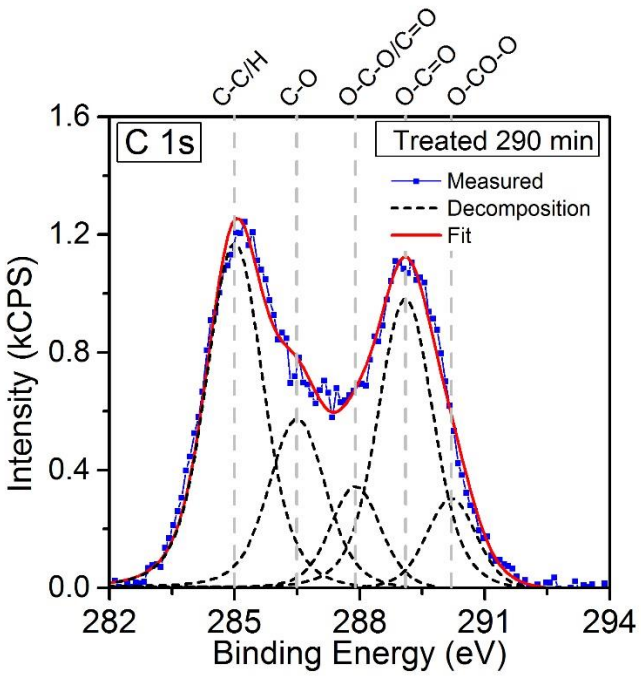

Figure 4.6 High resolution XPS C 1s spectrum of 290 min treated PS film. The decomposition of measured data into various oxygen containing functional groups is also shown. The electron take-off angle is 20°.

4.3.4 Bulk composition: ATR-FTIR

The plasma effect on the bulk of the polymer film was evaluated by ATR-FTIR. The penetration depth of IR light with Ge crystal at 60° light incidence angle (~600 nm) [198] is larger than the polymer film thickness (~350 nm), which ensures that the measured IR spectra reflect the chemical composition of the entire film. The full IR spectrum, data not shown here, of pristine PS reveals four groups of IR peaks: (1) the aromatic C-H stretching at 3025 cm^{-1}, (2) the aromatic C=C stretching at 1602 cm^{-1}, (3) the deformation of CH_2 and C=C of the aromatic ring at 1492 and 1452 cm^{-1}, and (4) the aromatic C-H deformation at 1027, 908, 758 and 699 cm^{-1}. After plasma treatment, we observed two

additional features on the IR spectra: a weak peak at 1282 cm^{-1} (0.005 with respect to the highest peak at 699 cm^{-1}) and a group of strong peaks in the range of 1600 cm^{-1} - 1800 cm^{-1} as shown in figure 4.7 (a). The former peak can be assigned to C-O stretching and/or symmetric NO_2 stretching. The latter group of peaks can be attributed to the general C=O stretching modes (1600 cm^{-1} - 1800 cm^{-1}) and asymmetric NO_2 stretching (1615 cm^{-1} - 1660 cm^{-1}) from nitrate [195, 199]. For the C=O stretching peaks, various functional groups such as phenol or vinyl ester (1770 -1780 cm^{-1}), saturated ester (1750 -1735 cm^{-1}), aldehydes (1740 - 1720 cm^{-1}), unsaturated ester or ketone (1730 - 1715 cm^{-1}), as well as conjugated aldehydes (1710 -1685 cm^{-1}) and ketones (1685 - 1666 cm^{-1}) can be fitted, which suggests that the plasma modified polymer is not homogeneous and several types of moieties might coexist. Due to the overlapping of peaks in IR spectrum, we could not determine whether the nitrate groups were formed in the polymer bulk. However, as mentioned in section 4.3.3 we measured the XPS N 1s spectrum of 3.5 nm – 42 nm back-etched PS films (SMD treated for 290 mins before back etching) by low pressure Ar plasma, and we observed no nitrate signal in any of these back-etched thicknesses, which provides evidence that nitrate is not formed in the polymer bulk. More about this will be reported soon.

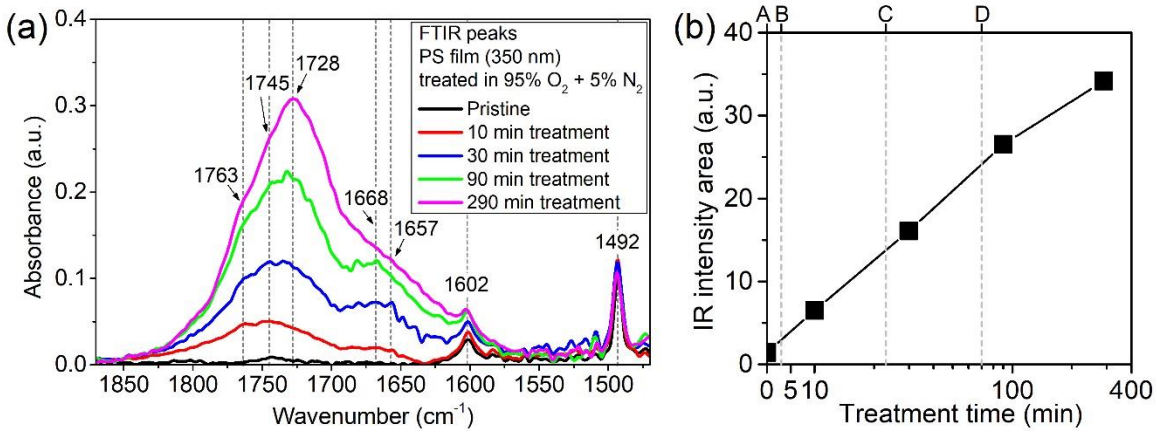

Figure 4.7 (a) ATR-FTIR spectrum of 350 nm PS film treated by SMD for 10 – 290 minutes. The contact area between PS and Ge crystal has been calibrated and corrected. (b) Integrated IR intensity area of peaks in the range of 1550 cm^{-1} ~ 1850 cm^{-1} as a function of SMD treatment time. The label of A, B, C and D corresponds to those in figure 4.2.

Interestingly, the intensity of this group of overlapping peak in the range of 1600 cm^{-1} - 1800 cm^{-1} increases with treatment time. To better illustrate this, we calculated the integrated intensity of these peaks by summing the intensity from 1560 to 1850 cm^{-1} minus the area of C=C stretching peak from carbon ring at 1602 cm^{-1}. As shown in figure 4.7 (b), the area intensity increases logarithmically with treatment time, which indicates that plasma induced polymer modification is fast at the beginning of the treatment but slows down considerably as the reaction sites on pristine polymer are depleted. The last data point in figure 4.7 (b) is slightly off the trend of logarithmic growth which indicates that an upper bound of total modification might exist.

4.3.5 Mechanism of polymer transformation

With the additional information of surface and bulk chemical composition, we fitted the exemplary real-time Ψ-Δ trajectory in figure 4.2 (b) with single layer ellipsometry model, which resulted in the evolution of thickness and refractive index during RPO as shown in figure 4.8. It can be seen that the polymer thickness increases to a maximum near point D and then decreases. The inset of figure 4.8 emphasizes the polymer thickness change in the first 60 minutes of treatment (Point A to D in figure 4.2 b), and the thickness jump in AB stage indicates the fast surface adsorption/oxidation whereas the continuous growth in BC and CD stage suggests the polymer bulk expansion. The change of growth

rate at point C indicates the onset of etching from polymer surface, and the subsequent change from thickness increase to decrease at point D illustrates that etching finally surpasses bulk expansion and becomes the dominant influence on thickness behavior. After point F the rate of thickness change stays relatively stable and a linear fitting yields an etch rate of 0.69 nm/hour which is 2 – 4 orders of magnitude slower than other typical APP sources that involve invasive etchant such as ions [1], atomic O and OH [68].

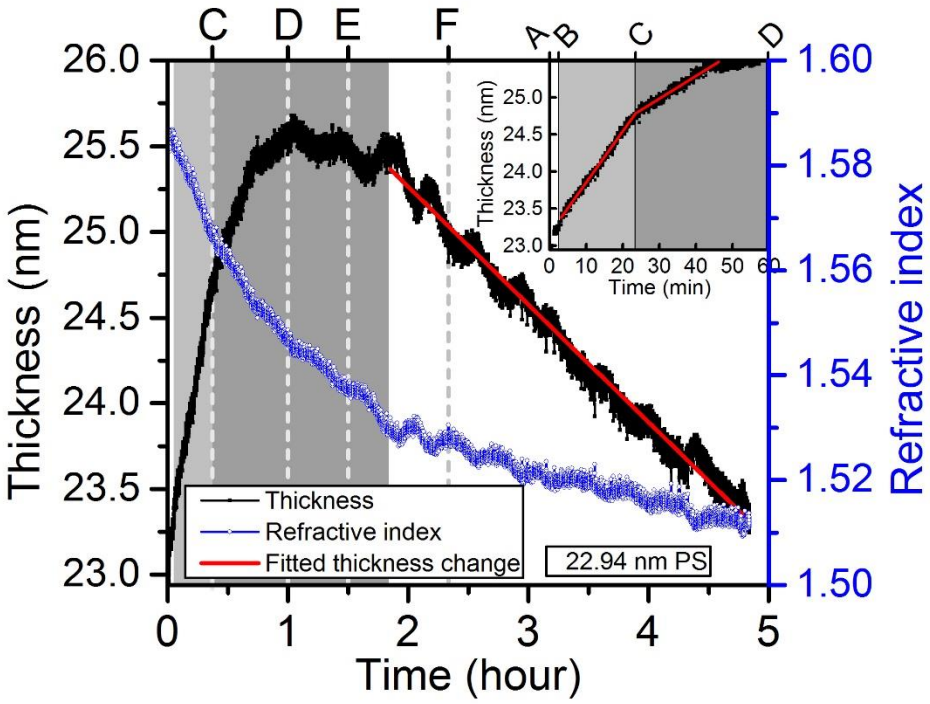

Figure 4.8 The thickness and refractive index change of PS film shown in figure 4.2 (b) as a function of time. Inset is the enlargement of the first 45 minutes of treatment. Labels A through D correspond to those in figure 4.2, whereas E and F correspond to 1.5 and 2.25 hours.

In figure 4.8 we also find that the polymer refractive index continuously decreases throughout the plasma treatment with the rate of decrease slowing down with time.

Previously we attributed this to the oxidation of the polymer, and here we provide a more detailed discussion which follows the method developed by Groh and Zimmerman [200]. The macroscopic refractive index of a material is determined by its microscopic polarizability (i.e. the dipole moment per unit volume induced by the electromagnetic field) through the well-known Lorenz-Lorentz equation:

$$\frac{n^2-1}{n^2+2}\cdot V_L = R_L \tag{4.1}$$

Here n is the refractive index and V_L is the molar volume:

$$V_L = \frac{M}{\rho} \tag{4.2}$$

where M is the molecular weight, ρ is the mass density. R_L is known as the molar refraction and is correlated to the polarizability of molecules (α):

$$R_L = \frac{4\pi N_A}{3}\cdot \alpha \tag{4.3}$$

where N_A is the Avogadro's number. From equation (4.1), the refractive index n can be expressed as:

$$n = \left[\frac{1+2\frac{R_L}{V_L}}{1-\frac{R_L}{V_L}}\right]^{1/2} \tag{4.4}$$

When the material is a mixture of different chemical constituents, molar fraction mixing rule [201], i.e. the molar refraction of a mixture is given by the linear average of the partial molar refraction of the individual components in the mixture weighted by their molar fraction, can be approximately applied to calculate the refractive index:

$$R_L = \sum_{j=1}^{J} k_j \cdot R_j \tag{4.5}$$

$$V_L = \sum_{j=1}^{J} k_j \cdot V_j \tag{4.6}$$

Here k_j, R_j and V_j are the molar fraction, molar refraction and molar volume of substance j, respectively. For amorphous polymers with periodically repeating units, the macroscopic refractive index can be also estimated by these values of individual substructure j in the repeating unit. According to the calculation from Groh and Zimmerman [200], the quotient $x = R_j/V_j$ indicates the direct contribution of each substructure to the resulting refractive index. In table 4.1 we selectively listed the R_j and V_j values [200] of a few functional groups observed from our XPS results, and it can be seen from the x values that all oxygen containing functional groups except C=O can cause the decrease of refractive index compared to pristine PS. Generally, the presence of ether (C-O) group dramatically reduces the polymer refractive index due to its large volume occupied by oxygen in this binding structure, which also helps explain the expansion of polymer film during oxidation. From figures 4.5 (a) and (b), we find that the lowest refractive index of the top few nanometers (20° XPS scan) of the polymer film (n_{min}) presents in the etching stage. Using equation 4.4 and values in table 4.1, we can estimate that n_{min} is between 1.457 ± 0.009 and 1.486 ± 0.009. This value is lower than that fitted in figure 4.8 which indicates that the material in the polymer bulk is not as oxidized as that on the surface.

Table 4.1. Increments of various polymer substructures [200]

Function	*Chemical formula*	R_j	ΔR_j	V_j	ΔV_j	x	Δx
Main chain	-(CH_2C^*H)-	7.915	± 0.63	23.613	± 2.64	0.335	± 0.046
Side group	-C_6H_5 (arom)	25.824	± 0.69	74.129	± 2.9	0.348	± 0.011
Side group	C-O (ether)	1.625	± 0.68	9.052	± 2.86	0.18	± 0.094
Side group	O-C-O	7.754	± 0.96	33.631	± 4.06	0.231	± 0.04
Side group	C=O	4.59	± 0.71	13.17	± 2.97	0.349	± 0.095
Side group	O-C=O	6.289	± 0.28	22.761	± 1.19	0.276	± 0.019
Side group	O-CO-O	6.266	± 1.07	31.608	± 4.5	0.198	± 0.044

In figure 4.9, we summarized and plotted all the physical processes during different stages of RPO of polymers. The labels A through F correspond to those in figures 4.2 – 4.8. Stage AB features the surface oxidation and adsorption of nitrates. This nitrate adsorption and oxidation layer (3.6 Å), not necessarily covers the entire surface (coverage rate $\theta < 100\%$), stays dynamically on polymer surface over the rest of the stages. Stage BC shows the expansion of the polymer film due to the diffusion and reaction of long-lived plasma species in the polymer bulk. There is no material loss in this stage since the surface has not been oxidized enough to form volatile product CO_2. The etching of polymer starts at point C where the amount of O-C=O group has been accumulated to the extent of causing CO_2 formation. The oxidation of the polymer bulk continues in the CD stage, and the thickness increase due to oxidation is larger than that due to etching which yields net thickness increase. The refractive index of the polymer film keeps decreasing in this stage because of the continuous oxidation of the polymer bulk. From point D etching finally surpasses oxidation and becomes the dominant factor for polymer thickness change. This is also reflected from the rate of refractive index decrease which slows down considerably after point D. Although the polymer thickness at point E and point D is similar, the polymer

bulk at point E is more oxidized with a lower refractive index. Point G shows that the film thickness can be smaller than the pristine film at later time of the etching stage.

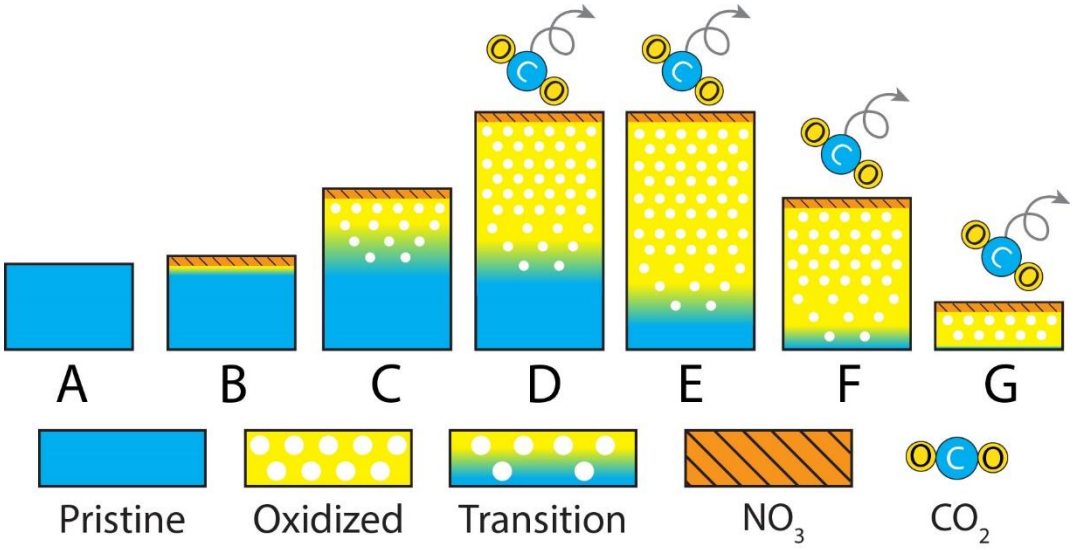

Figure 4.9 Possible reaction processes of PS under RPO. Labels A through F correspond to those in figure 4.8. Label G indicates net thickness loss compared to pristine film when it is treated with even longer time than 5 hours.

4.4. Conclusion

Using SMD and PS as model CAP-polymer system, we evaluated the interaction mechanism of RPO by studying the evolution of polymer film properties, including thickness, refractive index, surface moieties and bulk chemical composition. We found that the polymer film underwent three distinct transformation stages during RPO, i.e. surface adsorption/oxidation, bulk expansion and etching. Analysis of the chemical composition of the treated polymers indicates that the long-lived species generated by remote plasma are able to (1) form surface nitrate adsorption and oxidation layer, (2) diffuse into the polymer and oxidize the polymer bulk (3) cause etching of the polymer surface. Our results

demonstrate that the interaction of polymers with remote plasma is complex and multiple processes such as adsorption, oxidation and etching can take place simultaneously. We also showed that nitrate was only formed at the polymer surface and the remote plasma etched surface was relatively rich in O-C=O (ester or carboxylic acid) groups. Finally, we correlated the evolution of the refractive index of the polymer films with chemical composition changes and showed that the refractive index decrease mirrors the formation of oxygen-containing groups resulting from RPO. Our results illustrate the role of the long-lived weakly oxidative plasma species in a CAP-polymer interaction system, and they can be applied to other plasma-material interaction systems where long-lived neutral plasma species exist. Our findings on the penetration of remote plasma species into polymer bulk and the adsorption of surface nitrate may stimulate new applications in fields such as plasma medicine and microbial sanitation.

Acknowledgement

The authors gratefully acknowledge the financial support by the National Science Foundation (PHY-1415353) and the US Department of Energy (DE-SC0001939). We thank M. Kleinkonradt for his contribution on fabricating the SMD reactor. We are grateful to A. J. Knoll, A. Pranda, C. Li and K. Lin for helpful discussions and collaborations.

Chapter 5: Effect of water vapor on plasma processing at atmospheric pressure: polymer etching and surface modification by an Ar/H2O plasma jet

P Luan[1], V S S K Kondeti[2], A J Knoll[1], P J Bruggeman[2] and G S Oehrlein[1]

[1] Department of Materials Science and Engineering and the Institute for Research in Electronics and Applied Physics, University of Maryland, College Park, Maryland 20742, USA

[2] Department of Mechanical Engineering, University of Minnesota, Minneapolis, Minnesota 55455, USA

Draft manuscript, to be submitted

Abstract

We evaluate the effect of water vapor on the plasma processing of materials using a model system consisting of a well-characterized radio-frequency (RF) plasma jet with Ar carrier gas, controlled gaseous environment, and polystyrene (PS) as target material. We find that the effluent of Ar/H_2O plasma jet is capable of (1) etching polymers with relatively high etch rate and (2) weakly oxidizing the etched polymer surface by forming O containing moieties. When increasing the distance between the polymer and the Ar/H_2O plasma, we find that the polymer etch rate drops exponentially whereas the surface O composition of etched polymer shows a maximum at intermediate treatment distance. A control experiment of Ar/H_2 plasma shows that the observed etching by Ar/H_2O plasma cannot be explained by H atoms. The OH density in the Ar/H_2O jet has been measured near the substrate surface by laser induced fluorescence (LIF), and we find that the exponential decrease of polymer etch rate of Ar/H_2O plasma is consistent with the density variation of OH radicals with treatment distance, which indicates that OH may play a dominant role in the polymer etching process. By correlating the OH flux generated from Ar/H_2O plasma at different axial positions with the polymer etch rate, we find that the presumed dominant etchant species OH has an estimated etching reaction coefficient (number of C atoms removed per incident OH radical) of 10^{-2}. The polymer etch rate of Ar/H_2O plasma is enhanced as the substrate temperature is lowered, which can be explained by enhanced surface adsorption processes of gas phase species. We also find that $Ar/H_2O/O_2$ plasma has reduced etching efficiency compared to both Ar/H_2O and Ar/O_2 plasma for a fixed molecular admixture concentration.

5.1 Introduction

Atmospheric pressure plasma (APP) reactors can be operated as low temperature plasma (LTP) sources in room environments which usually contain certain amount of water vapor. Due to the non-equilibrium nature and highly energetic state of LTP, water vapor in APP is often dissociated which initiates a wide variety of reaction pathways that lead to the generation of highly reactive species such as OH, H, HO_2, H_2O_2, HNO_2 and HNO_3.[63, 202] The effect of adding water vapor to the feed gas and/or the surroundings of the APP reactors has been extensively studied through both experiments [203-206] and computer assisted modeling.[41, 42, 207-209] As a result, the characterization of gas phase species generated by water containing APP, e.g. the space- and time-resolved density profiles of these water-related reactive species, has been reported in many studies.[41, 65, 145, 203-206, 210-214]

Despite the increasing attention given in characterizing water containing APP, less is known about the effect of water containing APP on material surfaces - especially an understanding at the molecular level is missing. Besides modifying polymers,[9, 10, 215] previous publications on the treatment of materials using water containing APP mainly focused on antimicrobial effects and mechanisms.[206, 216-218] However, due to the complexity of microbes and cells, it is difficult to extract information on how water containing APPs interact with materials from such studies, e.g. etching, modification and deposition on surfaces, etc., or to identify the reactive species responsible for these surface phenomena. Nonetheless, the effect of H_2O feed gas in low pressure plasma (LTP) on polymers has been reported previously,[219] and at 50 mTorr pressure the authors observed etching and surface oxidation of polycarbonate (PC). Hydroxyl radicals (OH) were

recognized by the authors as the effective etchant species generated by low pressure H_2O plasma.[219] However, due to the difference between LTP and APP [220] the role of H_2O in APP needs to be examined separately.

Compared to LTP, the difficulty of studying water containing APP comes from the short mean-free path of particles (< 100 nm) at atmospheric pressure.[132] After generation in the plasma zone, reactive species are transported through convection and diffusion from the nozzle to target surfaces that are typically located at distances ranging from 1 – 100's of mm. The interaction of reactive species with each other and the gaseous environment wherein plasma-surface interaction (PSI) takes place may also cause the destruction and conversion of these species.[141] Hence, controlling the gaseous composition of the PSI vicinity is essential for being able to interpret plasma induced surface phenomena.

The correlation between reactive species and the responses of the material surface can help identify the dominant reactant from water APP for material treatments. Besides the composition of the controlled gaseous environment, a model plasma-material system that consists of a well-characterized APP reactor and target materials with defined properties is desired to establish such correlations.[1] Previously we studied the etching and surface modification of polymers by Ar/O_2 plasma using a model system consisting of a RF plasma jet as the APP source and vinyl polymers as target materials.[134-137] We found that O atoms were the dominant etchant generated by Ar/O_2 plasma, and a linear response between the incident O flux and the etched C flux on material surface was observed. We estimated the etching reaction coefficient [221] of O atoms from these measurements and we found it to be of the order of 10^{-4}.[68]

In this work, we use the same model system to study the effect of Ar/H_2O plasma on polymer surfaces. By varying a number of plasma processing parameters such as treatment distance, environmental gas composition, feed gas composition, and substrate temperature, we explored the change of polymer surface properties using *in-situ* ellipsometry and X-ray photoelectron spectroscopy (XPS). The role of OH radicals generated by the Ar/H_2O plasma, whose density was measured by laser induced fluorescence (LIF), was evaluated. We also indirectly assessed the potential effect of H, which is expected to be present at similar concentrations as OH in Ar/H_2O plasma by comparing the results with a Ar/H_2 plasma.

5.2 Experiments and methods

5.2.1 Materials

Polystyrene (PS) beads with an average molecular weight of 35 000 was purchased from Sigma-Aldrich (St. Louis, MO, USA) and used without further purification. Thin PS films were spin-coated on Si substrate using 5 wt.% of PS in propylene glycol methyl ether acetate (PGMEA, Sigma-Aldrich, ReagentPlus®, ⩾99.5%) solution. With 2000 rpm spin-speed and 3 s ramping time, the resulted PS films have a thickness of ~ 180 nm. Our AFM results show that the PS films have a RMS surface roughness of 0.35 nm.

5.2.2 Plasma processing

The model APP reactor selected for studying water containing plasma at atmospheric pressure is the time-modulated RF plasma jet whose detailed characteristics can be found elsewhere.[43, 134, 161] Briefly, the RF jet is a capacitively coupled plasma (CCP) reactor with a 1 mm diameter tungsten needle as the driven electrode, a quartz tube (3 mm outer and 1.5 mm inner diameter, ID) as the dielectric and a copper ring as the

grounded electrode. The 20 kHz modulated 14.0 MHz RF signal with 20% duty cycle [182] was generated through a function generator (Tektronix AFG3021B) and then amplified by a power amplifier (ENI A500). The feed gas of the RF jet studied in this work includes 1.5 standard liters per minute (slm) of Ar plus 1% O_2, 1% H_2O, 1% (O_2 + H_2O) mixture, and 1% H_2. We kept the visible plume length of the RF jet at a constant length of 3 mm for all feed gas conditions. The average plasma power dissipation of the RF jet was measured by Lissajous figure method [134] and is approximately 2 W for Ar plus 1% O_2, 1% H_2O, 1% O_2/H_2O and 1.26 W for Ar plus 1% H_2 unless noted otherwise. Since all feed gas compositions were composed of Ar plus 1% molecular gas admixture, we use the notation of "Ar/molecular gas" (e.g. Ar/H_2O) to represent "Ar + 1% molecular gas" in the rest of this work.

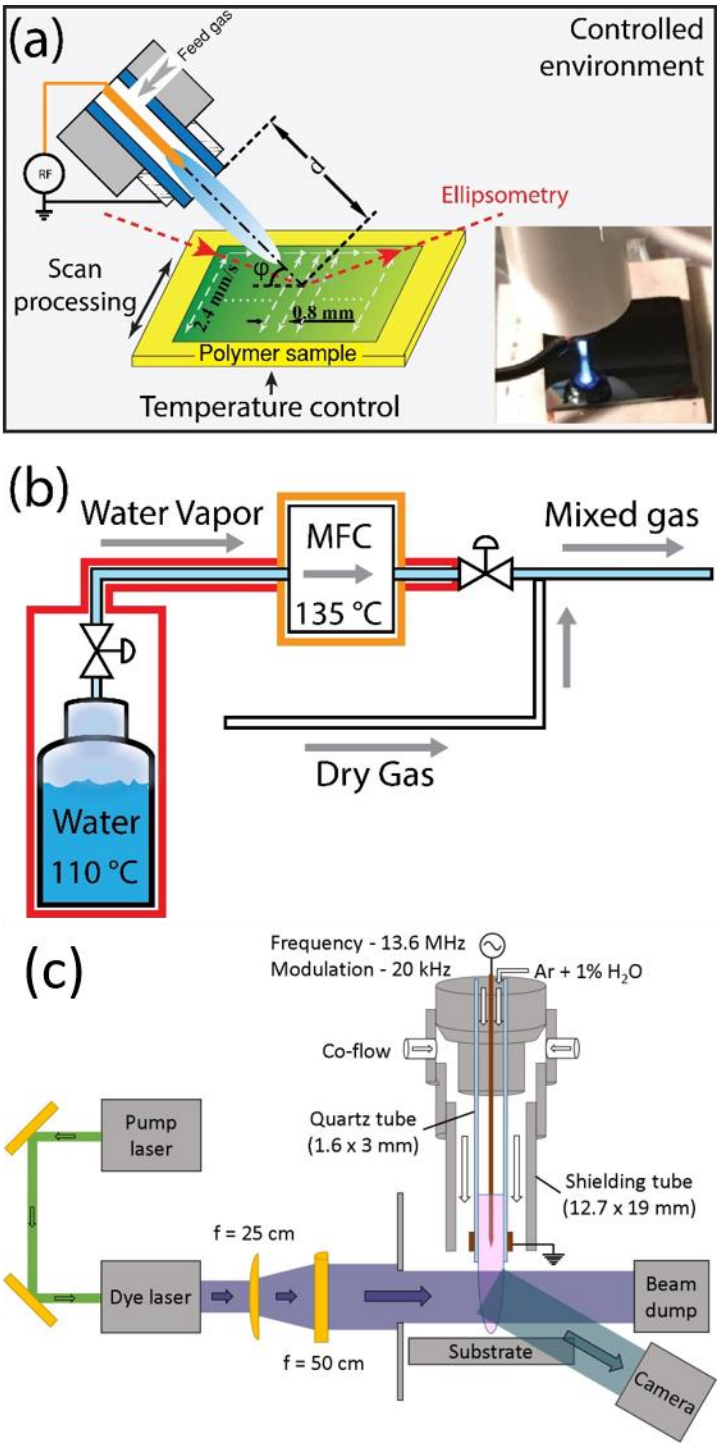

Figure 5.1: (a) Schematic diagram of the time-modulated RF jet and its interaction with a polymer surface. During material treatment, the RF jet scans over polystyrene surface with a speed of either 1.2 mm/s or 2.4 mm/s for avoiding excessive etching. The

treatment angle φ and treatment distance d are adjustable. Inset shows an optical image of the Ar+1% H_2O plasma treating polystyrene coated on Si wafers with d = 4 mm and φ = 90°. (b) Schematic diagram of the water vapor generation setup. The MFC is heated to 135 °C, the stainless steel water container and gas delivery lines are heated to 110 °C. (c) Schematic diagram of the time-modulated RF jet with gas shielding and the laser induced fluorescence (LIF) measurement for OH radicals.

Due to the small cross section area of the RF jet (1.77 mm^2), a homemade 2 dimensional (2D) scan-processing stage was used to achieve uniformly treated target surfaces for further analyses.[1, 68] During treatment, the RF jet scans over the sample surface with a line-by-line processing pattern at a moving speed of either 1.2 mm/s or 2.4 mm/s. After treating the material surface back-and-forth along the same straight line, the RF jet moves to another processing line located 0.8 mm away and repeats the line treatment. As illustrated in figure 5.1 (a), the treatment angle φ (either 30° or 90°) and treatment distance d (4, 8, 12, 16, 20 mm) relative to the material surface can be adjusted. To avoid confusion, we list all treatment configuration used in this work - Figure 5.2: 30°, 2.4 mm/s; Figure 5.3: 90°, 1.2 mm/s; Figures 5.4 – 6: 30°, 1.2 mm/s; Figures 5.7 and 5.8: 90°, 2.4 mm/s. We will further describe the treatment angle and scan-processing speed in the caption of each figure.

5.2.3 Controlled environment, water vapor generation and temperature control

The APP treatment of polymers were conducted in a 50 L sealed chamber. Controlled environments wherein PSI takes place were achieved by refilling this chamber

(pre-evacuated to 10 m Torr) with N_2/O_2 gas mixture at 4 slm constant flow rate. The water vapor admixture in the feed gas of the RF jet was generated by a homemade gas delivery system consisting of a MKS M330AH mass flow controller (heated to 135 °C), a stainless steel water container (110 °C), and gas delivery lines (110 °C), as shown in figure 5.1 (b).The temperatures of the water vapor generation system were monitored by thermocouples and controlled by proportional–integral–derivative (PID) controllers.

To evaluate the effect of substrate temperature on polymer etching by water containing APP, the PID-controlled heating (above 20 °C) and thermoelectric cooling (below 20 °C) stages were integrated in the plasma processing setup, as shown in figure 5.1 (a). Prior to the RF jet treatment, the polymer samples were heated or cooled to the desired temperature (0 - 90 °C). To avoid excessive polymer etching at various temperatures, a scan-processing speed of 2.4 mm/s was used for all experiments assessing substrate temperature dependence. We evaluated the potential heating of target surfaces caused by the RF jet through measuring the thermal expansion of 745 nm SiO_2 during RF jet treatment at 4 mm. Our ellipsometry results show that temperature change caused by the RF jet is less than 20 °C for the processing parameters chosen above. We also measured the thickness reduction of PS films due to heating, and no observable thickness loss was measured at 40 °C.

5.2.4 Surface characterization

The detailed characterization methods of the polymer films treated by the RF jet have been described in previously published work.[1, 68] Briefly, we used *in-situ* ellipsometry and X-ray photoelectron spectroscopy (XPS) to characterize the thickness/refractive index and the surface chemical composition of the plasma-treated thin

films, respectively. To extract the real-time polymer thickness and refractive index information, an optical model was applied to the *in-situ* ellipsometric data. The XPS system (Vacuum Generators ESCALAB MK II) is equipped with Al K_α X-ray source (1486.3 eV), and high-resolution C 1s, N 1s and O 1s spectra were obtained at the electron take-off angle of 20° (probing depth $\approx$ 2 nm). Using CasaXPS software,[95] we fitted the C 1s spectra with peaks corresponding to C=C (284.7 eV), C-C/H (285 eV), C-O (286.5 eV), O-C-O/C=O (288 eV), O-C=O (289 eV), O-CO-O (290.2 eV) and pi–pi* shake-up (291.6 eV). Due to the overlapping of peaks in the O 1s spectra, two peaks with binding energy at 532.7 eV and 533.9 eV were fitted. For the N 1s spectra, nitroso (NO, 401.8 eV) and nitrate (ONO_2, 407.5 eV) peaks were fitted. All spectra were calibrated with the C-C/H peak at 285 eV. After Shirley background subtraction, the elemental composition was calculated with sensitivity factors of C 1s = 1, N 1s = 1.77 and O 1s =2.85, respectively.[179] Surface morphology of the pristine and RF jet treated PS films were measured using atomic force microscopy (AFM, Bruker MultiMode AFM) with the tapping mode.

5.2.5 Absolute gas phase OH density

The absolute density of OH radicals generated by Ar/H_2O plasma was measured by LIF in open air environment as shown in figure 5.1 (c). A polymer target was placed underneath the plasma jet to mimic the polymer treatment experiments. To reduce the influence of environmental O_2, we applied pure N_2 shielding gas in co-axial direction as the Ar/H_2O feed gas. We did not use a sealed chamber for LIF measurement due to the long duration of laser measurements which requires a steady-state gas composition. Our computational fluid dynamics model showed that such steady-state gas composition cannot be obtained on a time scale of 30 minutes in the sealed chamber. For LIF measurement,

fluorescence of OH is induced with a frequency doubled dye laser (Sirah, Precision Scan), with Rhodamine 6G as the dye, pumped by a frequency doubled Nd : YAG laser (Spectra-Physics LAB-170-10H) at 532 nm. The $P_1(2)$ transition of the OH[(A; ν' = 1) ←(X; ν'' = 0)] system at 282.6nm is used and in particular the $f_1(2)$ transition. The laser pulse had a repetition frequency of 10 Hz and a pulse width of about 6 ns full width at half maximum (FWHM). A combination of a spherical (f = 25 cm) and a cylindrical lens (f = 50 cm) was used to shape the laser beam at the position of the plasma into a sheath with a thickness of about 206 μm and a height of approximately 4, 8 or 12 mm. The laser energy was ≈ 6 μJ for 4 mm distance and 9 μJ for 8/12 mm distances resulting in the measurement being performed in the linear LIF region.

Time and spatially resolved images of the fluorescence were taken with an iCCD camera (Andor IStar DH340T) equipped with a Nikkor 105 mm f/4.5 UV lens. The OH density does not vary more than 10% near the substrate during one modulation cycle of the RF power, hence to avoid contributions of plasma emission to the collected fluorescence the LIF measurements are performed in the plasma off period of the modulation cycle. Each measurement is an accumulation of 1000 pulses. The camera gate width was kept at 50 ns to ensure that all fluorescence was collected. The gas temperature was obtained by excitation LIF of OH. The Boltzmann plot yielding the rotational temperature is constructed using 6 levels of the OH ground state obtained by exciting the $P_1(1)$ to $P_1(6)$ transitions. More details about the approach can be found in previous publication.[222]

The absolute calibration of the OH LIF was performed using Rayleigh scattering. We used a four-level LIF model to obtain the absolute OH density from the calibration measurements as described in detail by Verreycken *et al.*.[223] A key unknown in the present

experiment is the gas composition at where the OH LIF is measured. The total fluorescence lifetime of the OH(A) state was measured with a gate of 5 ns. However this did not fully allow us to determine the gas composition as both the H_2O and N_2 concentration can vary in the jet effluent. For this study, we obtained the OH density in the core of the jet 0.5 mm above the substrate to limit the variation of the N_2 and H_2O density to reproduce the measured OH(A) lifetime. This approach leads to a range of OH densities. We report the average OH density obtained from this procedure and use the extreme values as an estimate of the uncertainty on the obtained OH density. The collisional quenching constants used for this calculation were taken from previous publication.[224]

5.3 Results

5.3.1 The effect of ambient gas composition on polymer etching by Ar/H_2O plasma

When treating polymer films with Ar/H_2O plasma generated by the RF jet, we observed fast material removal similar to that found with Ar/O_2 plasma generated by the same RF jet.[1] As shown in figure 5.2 (a), the real time thickness change of PS films during scan-processing was obtained through fitting the *in-situ* ellipsometry data.[95] The RF plasma jet was held at a distance d = 4 mm away from the material surface using titled configuration ($\varphi = 30°$). It can be seen that the polymer thickness decreases with scan-processing time and the curves in figure 5.2 (a) show "staircase" profiles due to the line-by-line scan-processing pattern of the plasma treatment. Since the ellipsometry probing laser spot (diameter 3 – 4 mm) is located at the center of the 9.6 × 9.6 mm^2 etched surface area, at the beginning or the near-end of the scan-processing, the RF jet is located further away from the ellipsometry measurement spot which corresponds to the observed slower

etch rate (ER). The highest instant ER (absolute value of the slope in figure 5.2 a) can be observed when the plasma plume hovers directly over the ellipsometry probing spot. For the Ar/H_2O plasma etching of PS in N_2 environment (black line in figure 5.2 a), the highest ER is 64 nm/min. Because the instant ER changes with the position of the RF jet during scan-processing, it is not accurate to discuss and compare these values for different plasma processing conditions. Since we only compare PS treatments with the same scan-processing parameters, the total etching depth (Δ_t), which reflects the average ER, is better for evaluating the etching efficiency of the plasma treatment and will be discussed in the rest of this work.

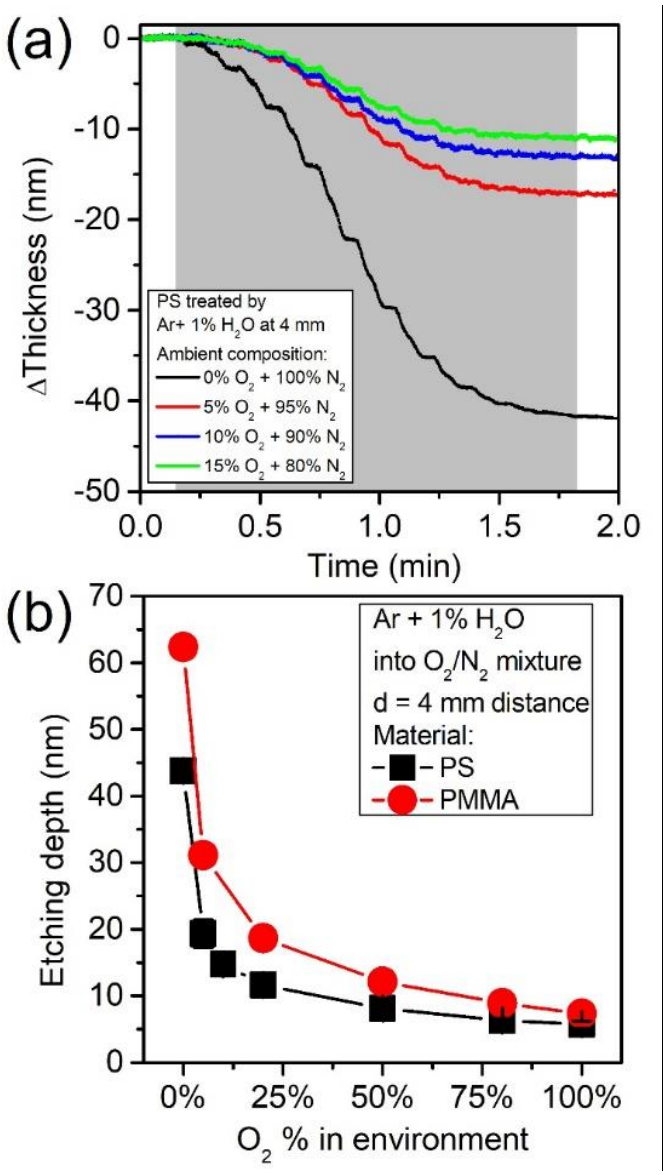

Figure 5.2. (a) Real-time etching depth of PS films treated by Ar + 1% H_2O plasma at 4 mm distance in various N_2 + O_2 mixture environments. The gray area indicates the time when scan-processing by the RF jet takes place. (b) The effect of environment gaseous composition on the polymer etching efficiency of Ar + 1% H_2O plasma evaluated by the total etching depth of PS and PMMA films. For both plots the treatment angle and the scan-processing speed is $\varphi = 30°$ and 2.4 mm/s, respectively.

We find that the gas composition of the environment wherein Ar/H_2O plasma treatment of polymers takes place has a significant influence on the polymer etching efficiency of Ar/H_2O plasma. As shown in figure 5.2 (a), the Δ_t of PS in pure N_2 environment is 41.9 nm, whereas that in 95% N_2 + 5% O_2 environment is 17.1 nm. We further tested other environmental gaseous compositions with higher O_2 content as well as another model polymer i.e. poly(methyl methacrylate) (PMMA) to examine how universal the observed behavior is. As illustrated in figure 5.2 (b), the total etching depth of both PS and PMMA treated by Ar/H_2O plasma quickly drops with small amount of O_2 mixture in the environment. Due to the large difference between artificial air (20% O_2) and N_2 environment (0% O_2) in figure 5.2 (b), in the rest of this work we focus on evaluating the effect of Ar/H_2O plasma on polymers for both air and N_2 environments.

5.3.2 The exponential decay of etch rate with treatment distance

We find that the polymer etching efficiency of Ar/H_2O plasma decreases exponentially with treatment distance d, which is similar to that of Ar/O_2 plasma observed in our previous work.[1] As shown in figure 5.3, the exponential decay of the etching depth with the treatment distance was seen in both N_2 and artificial air environments, though the Ar/H_2O plasma treatment in N_2 is more effective than the same plasma treatment performed in air environment at all treatment distances. By defining the exponential decay constant λ as the distance at which the etching depth is reduced to 1/e = 0.368 times of its initial value, we can fit the etching depth (Δ_t) data in figure 5.3 using the following formula with least-square method:

$$\Delta_t = \mathrm{A} \cdot \exp(-\frac{\mathrm{d}}{\lambda}) \qquad (5.1)$$

Here A is a fitting constant. For the PS film treated by Ar/H_2O plasma with vertical configuration (φ = 90°), the fitted exponential decay constant in N_2 environment is $\lambda_{H_2O,N_2,90°} = 6.07$ mm whereas that in air environment is $\lambda_{H_2O,air,90°} = 3.40$ mm (both adjusted $R^2 > 0.998$), which indicates that the etching depth, and presumably the density of reactive gas species responsible for etching, drops off more rapidly in air than N_2. This also suggests that the diffusion of ambient O_2 into the plasma jet effluent reduces the density of etchant species of Ar/H_2O plasma.

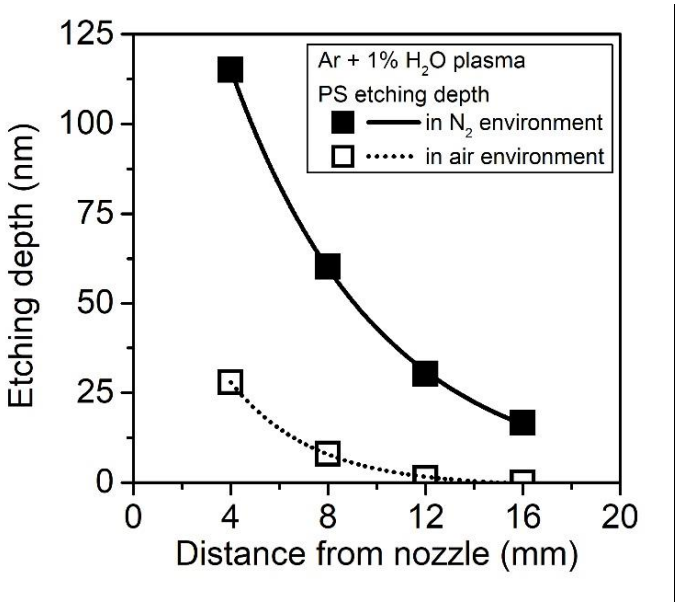

Figure 5.3: The etching depth of polystyrene scan-processed by Ar + 1% H_2O plasma as a function of treatment distance in both N_2 and air environment. The treatment angle is φ = 90° and the scan processing speed is 1.2 mm/s.

5.3.3 Surface chemistry: high resolution XPS

Besides etching, the Ar/H_2O plasma also modifies the chemical composition of the etched polymer surfaces. To illustrate this, high resolution C 1s, N 1s and O 1s spectra of the pristine and treated PS surfaces are shown in figure 5.4. The electron take-off angle of

the XPS measurements is 20° which corresponds to the chemical information from the top ~2 nm of the PS films. The pristine PS film (black line in figure 5.4) shows no surface N and minimal amount of surface O composition which might come from weak oxidation and/or a hydrocarbon contamination layer from the environment. The most abundant surface moiety on the pristine PS surface is the C-C/H bond (91.1% of the C 1s electrons) which can be found on both the main chain and the side ring of the PS structure. Besides, π- π* shake-up (5.4%, due to phenyl ring) and C-O bonds (2.54%, due to surface oxidation or hydrocarbon contamination) were also observed in the C 1s spectrum of the pristine PS.

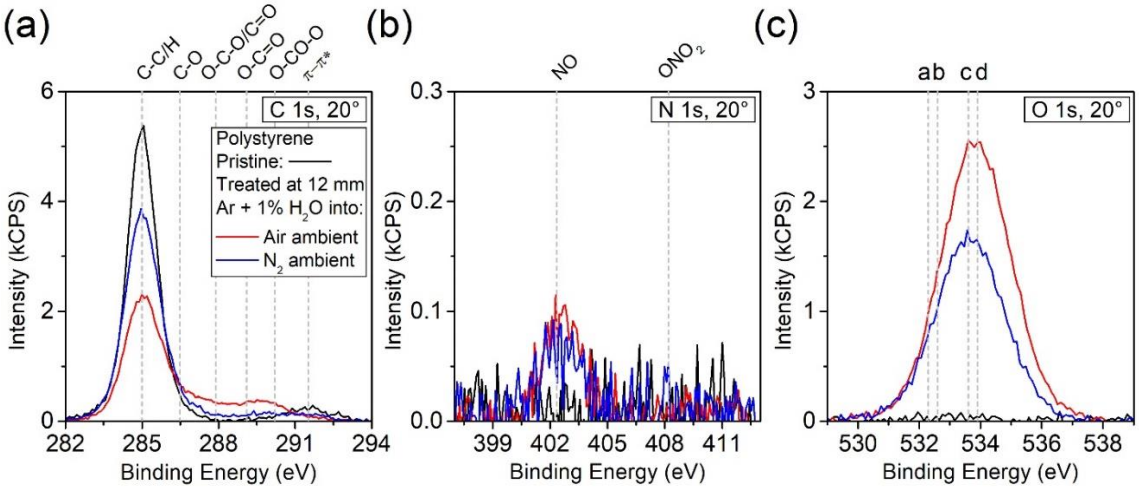

Figure 5.4: High resolution XPS (a) C 1s, (b) N 1s and (c) O 1s spectra of polystyrene treated by the RF jet with Ar + 1% H_2O plasma at 12 mm in N_2 and artificial air environment. Pristine polystyrene is also shown for comparison. Labels in (c) a (532.3 eV): C=O, O-C=O*, O*-CO-O; b (532.6 eV) aliphatic C-O; c (533.6): O*-C=O; d (533.9 eV): O-CO*-O. The treatment angle is φ = 30° and the scan-processing speed is 1.2 mm/s.

After Ar/H_2O plasma treatment in both N_2 and artificial air environment, the PS surfaces show the destruction of both C-C/H bond and aromatic ring structure accompanied

by moderate surface oxidation and the formation of NO, which is similar to changes seen after Ar/O_2 plasma treatment.[1] From the C 1s spectra of figure 5.4 (a), we can observe the decrease of C-C/H and π- π^* shake-up peaks and the formation of C-O, O-C-O/C=O, O-C=O, and O-CO-O groups especially for the PS film treated in air environment. Correspondingly, the O 1s spectra in figure 5.4 (c) show peaks that belong to the aforementioned O containing moieties with carbonate ester (O-CO-O) as the most abundant one. Previously we also observed the formation of this carbonate ester group for the Ar/O_2 plasma treated PS surfaces,[1] but we did not find the enrichment of the O-CO-O group on polymer surfaces treated by other types of APP sources including the surface micro-discharge (SMD) [95] and the double-ring kHz atmospheric pressure plasma jet (APPJ).[94, 141] This indicates that the O-CO-O formation might be characteristic of the RF jet etched polymer surfaces. When comparing PS surfaces treated in N_2 and air environments, we find that the PS surface is more oxidized when treated in air environment than in N_2 environment. For example in figure 5.4, at 12 mm treatment distance the O elemental composition of the PS surface treated in air is 29.2% whereas that treated in N_2 is 19.0%.

The Ar/H_2O plasma treatment can also modify the morphology of the polymer surface. Our AFM measurements show that the RMS roughness of pristine PS surface increases from 0.35 nm to 4.03 nm after Ar/H_2O treatment in N_2 environment with 8 mm distance.

5.3.4 Etching vs. surface oxidation: the effect of treatment distance and ambient gas composition

To evaluate how the etching depth and the surface chemistry of polymer films change with the treatment distance of Ar/H_2O plasma, we performed both ellipsometry and XPS measurements of PS films treated at 4, 8, 12, 16 and 20 mm distance. Due to the similarity of the real time thickness profile and the high resolution XPS data to that shown in figure 5.2 and 5.4 respectively, we only present the total etching depth and the O elemental composition abstracted from the raw XPS and ellipsometry data which simplifies the description and eases the comparison of different operating conditions.

Similar to the vertical jet configuration illustrated in figure 5.3, we observe the exponential decay of total etching depth as a function of treatment distance for both N_2 and air environments. However, the surface O elemental composition of the Ar/H_2O plasma treated PS surfaces show a maximum at 12 mm, as illustrated in figure 5.5. This difference in the trends between etching and surface modification along treatment distance indicates that the etching and modification processes are controlled by different surface reaction pathways, as will be discussed in section 5.4.3.

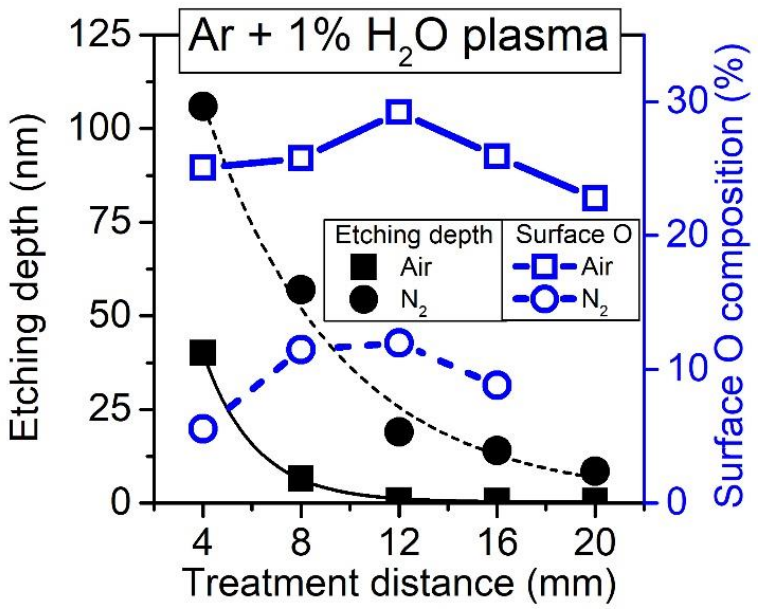

Figure 5.5: The etching depth and surface O elemental composition of Ar + 1% H_2O plasma as a function of treatment distance. Two environment gas compositions, i.e. pure N_2 and artificial air, were tested. The treatment angle and scan-processing speed is 30° and 1.2 mm/s for both etching depth and surface O composition measurements.

When comparing N_2 and artificial air environments in figure 5.5, we find that the additional O_2 from the air environment has significant influence on both the etching efficiency and the surface modification capability of Ar/H_2O plasma. First, polymer etching by Ar/H_2O plasma in N_2 environment is more effective than that in air environment, especially for shorter plasma treatment distances. For example, at 4 mm the etching depth in N_2 is 106.9 nm compared to that in air which is 40.1 nm. Furthermore, the etching depth curve in figure 5.5 also decreases much faster with treatment distance in air environment than in N_2 environment with fitted decay constants of $\lambda_{H_2O,\text{air},30^\circ} = 2.13$ mm and $\lambda_{H_2O,N_2,30^\circ} = 5.47$ mm (both adjusted $R^2 > 0.978$), respectively. These facts suggest that

the O_2 molecules from the environment are able to reduce the amount of etchant species arriving at the polymer surface. Second, the polymers treated by Ar/H_2O plasma in N_2 environment is less oxidized than those treated in air environment for all treatment distances. For treatments performed in N_2 environment, the surface O originates mostly from the Ar/H_2O plasma plume whereas in air environment the environmental O_2 molecules may also participate in the surface oxidation processes. Summarizing the differences between N_2 and air environment indicated in figure 5.5, we find that the O_2 from air could reduce polymer etching but enhance the polymer surface oxidation.

5.3.5 Etching vs surface oxidation: the effect of feed gas composition

Considering the effectiveness of Ar/O_2 plasma on polymer etching [1] and the drop of etching efficiency discovered previously when mixing both O_2 and H_2O admixture in the Ar gas,[68] we compare the etching and surface modification of PS films treated by three different feed gas compositions, i.e. Ar + 1% H_2O, Ar + 1% O_2, and Ar + 0.333% H_2O + 0.667% O_2. All experiments in figure 5.6 were performed with the tilted jet configuration ($\varphi = 30°$) and the same plasma power. We selected N_2 environment instead of air to prevent the interference of additional O_2 from the ambient gas. The Ar/H_2O plasma data in figure 5.6 is the same as that presented in figure 5.5, and to link the present work with our prior works, the Ar/O_2 plasma data is the same as that presented in the previous publication.[1]

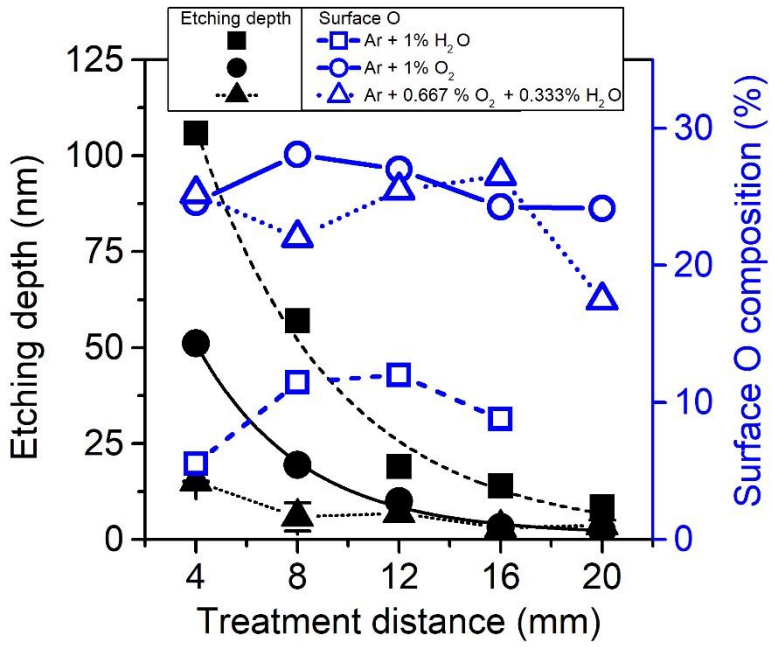

Figure 5.6: Comparison of the effect of feed gas H_2O and O_2 admixture on the etching depth and surface O elemental composition. Polystyrene films were treated in N_2 environment. The Ar/H_2O plasma data is the same as that presented in figure 5.5, and the Ar/O_2 plasma data is the same as that presented in previous publication.[1] The treatment angle and scan-processing speed is 30° and 1.2 mm/s respectively for both etching depth and surface O composition measurements.

As discussed in sections 5.3.2 and 5.3.4, the polymer etching depth of both Ar/H_2O and Ar/O_2 plasma dropped exponentially with treatment distance, and the exponential decay constants for Ar/H_2O and Ar/O_2 plasma can be fitted as $\lambda_{O_2,N_2,30°} = 4.15$ mm (adjusted R^2 = 0.995) and $\lambda_{H_2O,N_2,30°} = 5.47$ mm (adjusted R^2 = 0.978), respectively. In contrast, the surface O elemental composition of the PS films treated by Ar/H_2O and Ar/O_2 plasma show a maximum at 8 and 12 mm treatment distance. When comparing the etching efficiency between Ar/H_2O and Ar/O_2 plasma, we find that Ar/H_2O plasma is more

effective. The surface O elemental composition is also dramatically different between PS films treated by Ar + 1% O_2 and Ar + 1% H_2O plasma. As indicated in the right-axis of figure 5.6, the surface O composition ranges from 24.1% to 28.1% for the Ar/O_2 treated PS films whereas that of Ar/H_2O plasma treated PS films ranges from 5.5% to 12.0%. This difference in surface O composition can be attributed to two possible causes: (1) Ar/O_2 plasma contains more reactive species that lead to surface oxidation, or (2) Ar/H_2O plasma etches more material than Ar/O_2 plasma which hinders the accumulation of surface O containing moieties.

When simultaneously adding both H_2O and O_2 admixtures to the Ar feed gas of the RF jet, we observe much reduced etching depth but similar amount of surface O composition as those treated by Ar + 1% O_2 plasma. As shown in figure 5.6, the etching depth of PS films treated by Ar/H_2O/O_2 plasma is too small to show a clear trend. Interestingly, when comparing adding O_2 to the feed gas of Ar/H_2O plasma (shown in figure 5.6) with adding O_2 to the environment in which the Ar/H_2O plasma operates (shown in figure 5.5), we find similar changes on both the etching efficiency and the surface O composition of the plasma treated polymers. This indicates that the effect of environment gaseous compositions shown in figure 5.2 and figure 5.5 might be due to the O_2 entrainment which results in a similar effect in the far effluent region where polymer surface locates as directly adding O_2 to the feed gas of the RF jet. In fact, the percentage of ambient gas entrainment on the axial direction of this RF jet can rise from a few percentage at 4 mm to near 40% at 16 mm as measured by MBMS.[85] Our previous fluid dynamic modeling of air entrainment [1] also showed that the amount of air mixture is only dramatically different within a 8 mm diameter circle on the material surface. For areas outside of the 8 mm

diameter circle, the air mole fraction is always higher than 60% and becomes comparable for all treatment distances.

5.3.6 Substrate temperature effect

We further studied the effect of substrate temperature on polymer etching by Ar/H_2O plasma. For comparison, the effect of substrate temperature for Ar/O_2 plasma was also evaluated. Both types of plasma treatments were performed at 4 mm with the vertical jet configuration ($\varphi = 90°$) and the same plasma power. The substrate temperature studied ranged from 0 °C to 90 °C. It is worth mentioning that the glass transition temperature of PS is near 100 °C, and the dew point of Ar + 1%H_2O mixture at atmospheric pressure is ~ 4.8 °C.

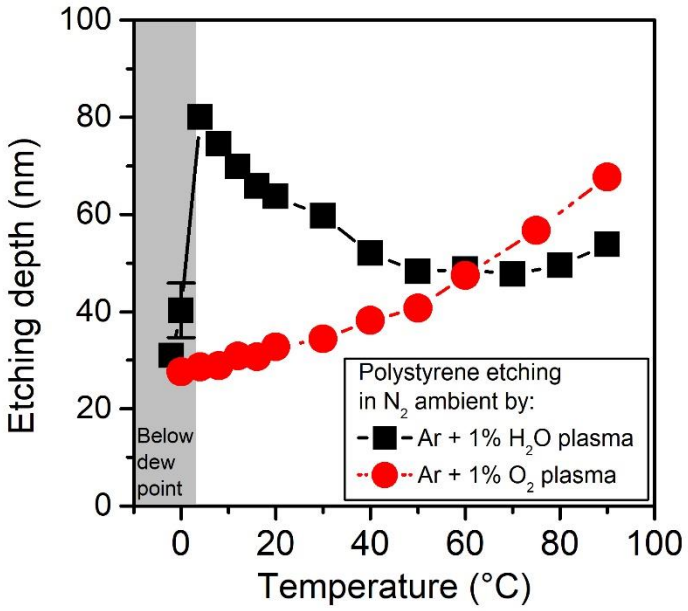

Figure 5.7: The effect of substrate temperature on the etching depth of PS films treated by Ar + 1%H_2O and Ar + 1% O_2 plasma. It can be seen that for Ar + 1% O_2 plasma the etching depth increases with temperature whereas for Ar + 1% H_2O plasma the etching

depth has a complex relation with substrate temperature. The treatment angle and the scan-processing speed is 90° and 2.4 mm/s, respectively.

As shown in figure 5.7, the etching efficiency of Ar/O_2 plasma increases with higher substrate temperature which indicates that polymer etching by Ar/O_2 plasma is an activated process. Previously we evaluated the apparent activation energy (E_a) of Ar/O_2 plasma,[1] and we found that it was ~ 0.1 eV. Similarly we can also calculate the E_a of Ar/O_2 plasma from figure 5.7 and comparable results were obtained.

When it comes to the PS etching by Ar/H_2O plasma, we find a complex relationship between the etching depth and the substrate temperature. At relatively high temperatures (>70 °C), the PS etching depth increases with substrate temperature which is similar to that seen for Ar/O_2 plasma. However, in the temperature range from 4 °C to 70 °C, we find that the polymer etching depth drops as the substrate temperature is increased. We also tested other treatment distances (12 and 20 mm) and polymers (polyvinyl alcohol and PMMA), and the same behavior of decreased etching depth with higher temperature (data not shown) was observed. For substrate temperatures below 4 °C, we observed liquid water condensation on the polymer surface. As shown in figure 5.7, the polymer etching depth falls rapidly at 0 and 2 °C.

The irregular dependence of Ar/H_2O plasma etching efficiency on substrate temperature might be due to the change in surface adsorption processes of various gas phase species. For temperature lower than 4 °C, the condensed liquid water layer on the polymer surface might serve as a protection layer that shields off the reactive species and prevents the polymeric materials from being removed. For the intermediate temperature

from 4 °C to 70 °C, there are two possible channels that might result in the enhanced etching with lower temperature. On one hand, the sticking coefficient of etchant species generated in the Ar/H_2O plasma, presumably OH radicals, might become larger with lower substrate temperature which directly leads to the higher etching efficiency. On the other hand, the physisorption rate of water molecules on the surface increases with lower temperature as can be seen from the isobar plot of water adsorption.[225] These adsorbed water molecules might react with the reactive species generated by the plasma jet and potentially form etchants (e.g. OH) that are capable of removing the polymers.

5.3.7 Ar/H_2 plasma etching of polymers

Recent modeling results of Ar/H_2O plasma generated by APPJs show that H atoms can be produced at similar or even larger concentrations than OH radicals through various reaction pathways.[41, 212] Since H atoms can also participate in the etching of polymeric materials,[226] for the identification of dominant etchant produced by Ar/H_2O plasma it is important to compare the etching efficiency between H atoms and OH radicals.

In figure 5.8 (a) we performed polymer etching by Ar/H_2 plasma with various treatment distances from 4 – 20 mm. Vertical jet configuration ($\varphi = 90°$), N_2 environment and 2.4 mm/s scan-processing speed were used for these experiments. Compared to the data shown in figure 5.3, the power consumption of Ar/H_2 plasma (1.26 W) is smaller. However it is the largest possible power for the stable operation of Ar/H_2 plasma at 4 mm treatment distance without sparking. Recent measurements of H densities by two-photon absorption LIF in the effluent of the same RF jet (without target materials) show that the RF jet can create H densities in excess of $10^{22} m^3/s$ [227] which are larger than the OH densities in Ar/H_2O plasma according to models.[228] Since the dominant reactive species

generated by Ar/H_2 plasma is the H atom, the data shown in figure 5.8 (a) reflects the polymer etching behavior by H atoms. First, it can be seen that Ar/H_2 plasma is not as effective for etching polymers as Ar/H_2O and Ar/O_2 plasmas. Only ~ 20 nm of PS was etched after scan-processing by Ar/H_2 plasma compared to 43.7 nm by Ar/H_2O plasma shown in figure 5.2. Moreover, for Ar/H_2 plasma we did not find the fast exponential decay of etching depth with treatment distance as that seen by Ar/H_2O and Ar/O_2 plasma. As shown in figure 5.8 (a), the PS etching depth did not change much as distance was varied from 4 mm to 20 mm, which suggests that the dominant etchant from Ar/H_2 plasma, i.e. H atoms, behaves very differently from the etchant species produced in Ar/H_2O and Ar/O_2 plasma.

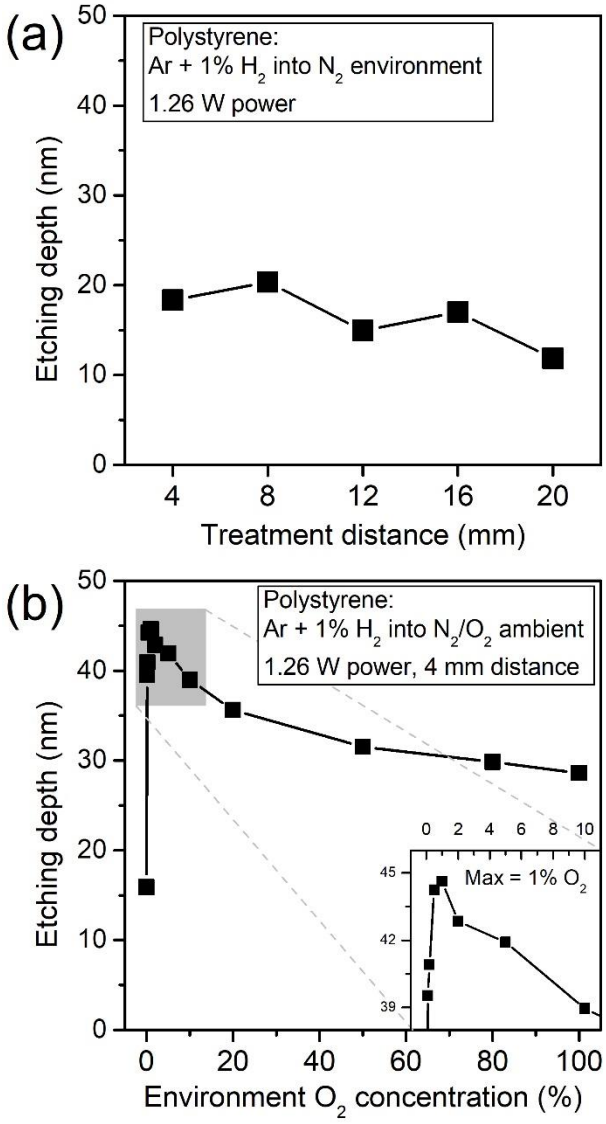

Figure 5.8. The etching depth of PS treated by Ar + 1% H_2 plasma (a) in pure N_2 environment with various treatment distance ranging from 4 – 20 mm, and (b) at 4 mm in N_2/O_2 mixtures with various mixing ratio. The inset of (b) shows the enlarged section of the gray area where we observed maximal etching depth with 1% O_2 + 99% N_2 in the ambient. For both plots, the treatment angle and the scan-processing speed is 90° and 2.4 mm/s, respectively.

Besides N_2 environment, we also studied polymer etching by Ar/H_2 plasma in various N_2 + O_2 environment gas mixtures. As shown in figure 5.8 (b), we observe significant increase of polymer etching when operating the Ar/H_2 plasma jet in O_2 containing environments. The inset of figure 5.8 (b) indicates a maximum of polymer etching depth for Ar/H_2 plasma operated in 99% N_2 + 1% O_2 environment. The etching enhancement of Ar/H_2 plasma caused by O_2 entrainment from the environment might be due to the generation of OH radicals when O_2 diffuses into the atomic hydrogen rich effluent due to fast formation of HO_2 through the reaction:

$$O_2 + H + M \rightarrow HO_2 + M \tag{5.2}$$

In the condition of excessive H atoms, HO_2 can be efficiently converted into OH radicals through reactions with H atoms:

$$HO_2 + H \rightarrow 2OH \tag{5.3}$$

Therefore, for Ar/H_2 plasma operated in O_2 containing environment, the dominant etchant species may be OH radicals rather than H atoms, or the occurrence of synergetic surface reactions for H atoms with other radical species. As reported previously, the reactivity for polymer H-abstraction by H atoms are two to four orders of magnitude smaller than those for O or OH [10] which also indicates that H atoms are less likely to be a significant etchant. The decrease of etching depth by Ar/H_2 plasma with higher environmental O_2 concentration might have similar reason as that of Ar/H_2O plasma seen in figure 5.2 (b), as will be discussed in section 5.4.2.

5.4 Discussions

5.4.1 Etching reaction coefficient of OH

Polymer etching by low temperature plasma is closely related to the chain scission reactions since dry etching relies on the formation of small molecular weight volatile products, such as CO and CO_2 at room conditions. Based on the free-radical reaction mechanism of PSI,[1, 8-10] the chain scission of polymers starts from radical site creation through the bombardment by energetic species (ions, electrons, UV photons, etc.) and/or the chemical reaction with neutral gas phase radicals. One efficient pathway of creating surface radical sites by H_2O and O_2 containing plasma is the H-abstraction by atomic O and OH radicals, which has been discussed widely for both low and atmospheric pressure plasmas:[9, 10]

$$RH + O \rightarrow R^{\cdot} + OH \qquad p = 10^{-3}, 10^{-4}, 10^{-5} \qquad (5.4)$$

$$RH{+}OH \rightarrow R^{\cdot} + H_2O \qquad p = 10^{-1}, 5 \times 10^{-2}, 1.2 \times 10^{-2} \qquad (5.5)$$

where p is the estimated reaction probability of O atoms and OH radicals for the tertiary, secondary, and primary carbon sites provided by Bhoj and Kushner.[9] It can be seen that OH radicals have a much higher reaction probability than O atoms. In addition, the reaction rate of OH radicals is also faster than atomic O when they react with organic substances. For example at room temperature (298 K), the rate constants of H-abstraction from methane by O atoms and OH radicals are:[229, 230]

$$CH_4{+}O \rightarrow CH_3{\cdot}{+}OH \qquad k = 6.1 \times 10^{-18}\text{cm}^3\text{s}^{-1} \qquad (5.6)$$

$$CH_4{+}OH \rightarrow CH_3{\cdot}{+}H_2O \qquad k = 6.7 \times 10^{-15}\text{cm}^3\text{s}^{-1} \qquad (5.7)$$

which indicates that OH radicals are much more reactive than O atoms. Previously we evaluated the etching reaction coefficient for atomic O and we found that it was on the

order of 10^{-4} which indicates that for removing one C atom from the polymer surface, ~ 10^4 O atoms are needed.[1]

Since our measurements suggest that the dominant etchant species in Ar/H_2O plasma are OH radicals, as discussed in sections 5.3.6 and 5.3.7, we can estimate the etching reaction coefficient of OH radicals by correlating the etching depth data shown in figure 5.3 and figure 5.5 with the amount of OH radicals generated by the Ar/H_2O plasma. Using LIF, we measured the OH density at 0.5 mm above the substrate positioned at 4, 8 and 12 mm away from the plasma jet nozzle, and we find that the OH density also decreases with the treatment distance d along the axis of the plasma jet effluent. The average OH flux bombarding the polymer surface ($\overline{\Gamma}_{\mathrm{OH}}$) can be estimated using the measured gas temperature (T_{gas}) and the density of OH radicals ([OH]) by

$$\overline{\Gamma}_{\mathrm{OH}} = \frac{1}{4}[\mathrm{OH}] \cdot \overline{v} = \frac{1}{4}[\mathrm{OH}] \cdot \sqrt{\frac{8RT_{gas}}{\pi M}} \tag{5.8}$$

where $\overline{v}$ is the average kinetic speed of the OH radicals, R is the gas constant, and M is the molecular weight of OH. This estimation does not take into account potential reactions of OH radicals in the stagnant boundary layer near the target surface. Similar to the approach provided previously,[1] we could estimate the average carbon atom flux etched from the PS surface using the following equation:

$$\overline{\Gamma_c} = \left(\frac{\Delta_t \cdot A_{treated} \cdot \rho}{A_C + A_H} \cdot N_A\right) \cdot \frac{1}{\pi/4 \cdot ID^2 \cdot t} \tag{5.9}$$

where Δ_t is the etching depth in figures 5.3 and 5, A_{treated} is the scan processed area (0.922 cm^2), ρ is the density of PS (1.04 g/cm^3), A_C = 12 and A_H =1 are the atomic mass of carbon and hydrogen atoms, N_A is the Avogadro's number, ID is the inner diameter of the RF jet quartz tube (1.5 mm) and t is the total scan-processing time (200 s). This simplified

estimation of etched C flux assumes that material etching only happens in the instantaneously treated area of $\pi/4 \cdot \mathrm{ID}^2$ where the RF jet directly hovers on top, and this location is assumed to correspond to the area of which the OH flux is applied.

In figure 5.9, we show the correlation between the incident OH flux and the etched C flux estimated at treatment distance d = 4, 8, 12 mm. The fitted slope of data in figure 5.3 yields the etching reaction coefficient [221] of OH radicals which is $1.95 \pm 0.50 \times 10^{-2}$. Compared to the etching reaction coefficient of O atoms, this value is two orders of magnitude higher. A potential more accurate etching reaction coefficient of both OH and O could be obtained by the analysis of 2D radical density profiles. Nonetheless, our experimentally obtained etching reaction coefficient of both O and OH are acquired with an identical approach and the 2 orders of magnitude difference between O and OH is consistent with the work of Dorai and Kushner [10] where they proposed reaction probabilities based on work by Gomez *et al.* for O [231] and rate constants for reactions of OH with long chain saturated hydrocarbons.[232]

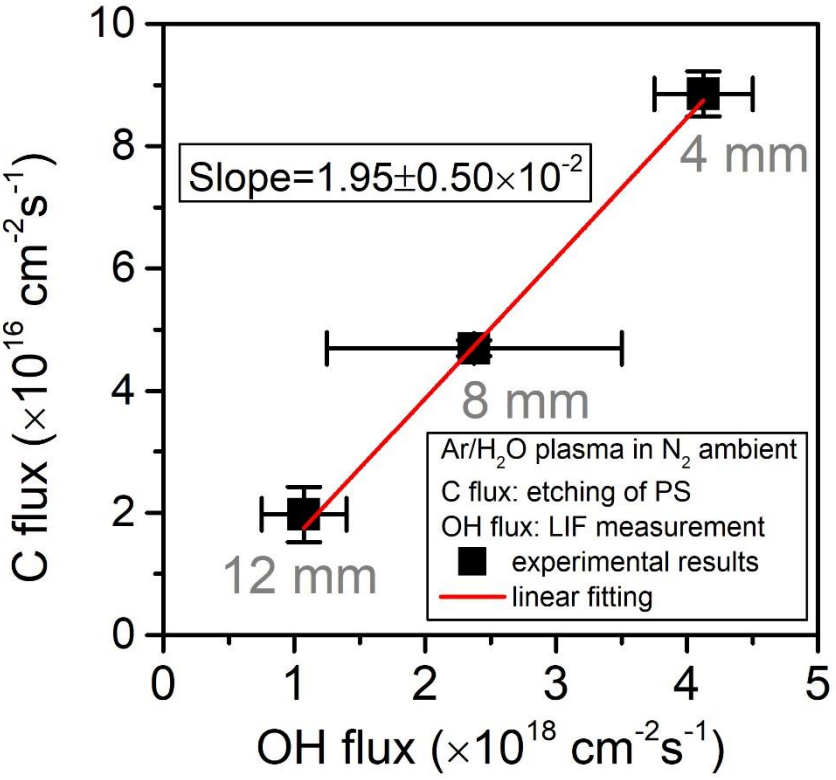

Figure 5.9: The etching reaction coefficient of OH radicals obtained by correlating the incident OH flux and the etched C flux at treatment distance d = 4, 8, 12 mm. The etched C flux is estimated from data in figures 5.3 and 5.5, the incident OH flux is calculated from OH densities at the axial direction measured by LIF.

5.4.2 Linking trends in gas phase O and OH densities with etching by Ar/H_2O and Ar/O_2 plasma

Previously we studied the effect of various 1% (O_2 + H_2O) admixtures in the Ar feed gas of the RF jet with a wide range of mixing ratios between O_2 and H_2O, and we found that, compared to Ar/O_2 or Ar/H_2O plasma, the polymer etching efficiency of Ar + 1% (O_2 + H_2O) plasma at 4 mm treatment distance dropped dramatically.[68] In figure 5.6 we further examined the effect of (O_2 + H_2O) admixtures at longer treatment distances up

to 20 mm, and we observed similar results. Interestingly, the reduction of etching efficiency of Ar/H_2O plasma with increasing environmental O_2 concentration (figure 5.2 b) also seems to be related to the mixing of both O_2 and H_2O in the jet effluent due to the entrainment of environment gas. The O_2 from both feed gas and environmental gas entrainment yields similar impact on the etching rate in spite of the different chemical kinetics in the core of the plasma and the jet effluent.

The reduction of polymer etching efficiency when introducing O_2 in Ar/H_2O plasma or introducing H_2O in Ar/O_2 plasma is consistent with different etchant species for Ar/O_2 and Ar/H_2O plasma – presumably O atoms and OH radicals, respectively. Models of Liu *et al.* [233] for plasmas with $He + H_2O/O_2$ mixtures show that the O density monotonic decreases with increasing H_2O/O_2 ratio while a monotonic increase in the OH density is found. This is consistent with the high etch rates found for Ar + pure H_2O and Ar + pure O_2 plasma and a drop for $Ar + H_2O/O_2$ mixtures as the dominant etching species decrease with adding O_2 or H_2O until at certain ratio their contribution becomes equal and a further addition leads to a change in dominant etchant and an increase in etching rate.

A plug flow model of the RF plasma jet operating with $Ar + H_2O$ in air environment shows an increase in O density with increasing distance from the RF jet nozzle, resulted from the increased mixture of O_2 in the jet effluent at longer distance.[228] As the OH density monotonically decreases with increasing distance from the jet nozzle, the O density becomes significantly larger than the OH density. As the estimated etching probability of O is 2 orders lower than for OH, this increase in O, which does not exceed the original OH density [228] is not expected to compensate for the loss of OH. In addition, the expected increase in O density for Ar/H_2O plasma in air environment compared to N_2 environment

will lead to a reduction in the OH density as O effectively reacts with OH forming HO_2 in a 3-body reaction.[67] This could explain the reduced etch rate of Ar/H_2O plasma in air environment compared to in N_2 environment.

5.4.3 Etching vs. surface modification

The process of PSI involves the generation of reactive species in the plasma source, the transportation of these reactive species to the target surface, and the chemical reactions taking place on the gas-solid interface.[140] When we extend the treatment distance from the RF jet nozzle to the target, the type and density of etchant species can be greatly altered due to the high concentration of reactive species and the short mean-free path of particles at atmospheric pressure.[132]

As shown in figures 5.3, 5.5 and 5.6, the etching efficiency of Ar/H_2O plasma drops exponentially with treatment distance regardless of treatment configuration (φ = 30° or 90°) and environment gas composition (air or N_2). This indicates that the flux of etchant species bombarding the target surface, presumably OH, also drops exponentially with treatment distance which is a collective result of both the generation and consumption of OH radicals during transport. We can define the apparent life-time of OH radicals $\overline{\tau_{\mathrm{OH}}}$ using the exponential decay constant of OH radicals λ_{OH} which can be assumed the same as that of the etching depth in figures 5.3 and 5.5:

$$\overline{\tau_{\mathrm{OH}}} = \frac{\lambda_{OH}}{\overline{v_{\mathrm{flow}}}} \tag{10}$$

where $\overline{v_{flow}} = 14.15\ m/s$ is the average feed gas velocity. Therefore we can estimate the apparent lifetime of OH in N_2 and air environment as $\tau_{\mathrm{OH},N_2} = 0.41 \pm 0.02$ ms and $\tau_{\mathrm{OH},air} = 0.20 \pm 0.05$ ms, respectively. Based on the lifetime OH radicals

estimated by Verreycken *et al.* [234] we can evaluate the density of OH radicals corresponding to this apparent lifetime assuming that the OH density is equal to the H density. This leads to an estimated OH density of 6×10^{13} cm^{-3} which is close to the OH density measured at 4 mm from the nozzle. The reduction in the apparent lifetime of OH by a factor of 2 for air environment can be due to the increase in the OH density or O density. In the former case, it leads to the increase of the OH density by a factor of 2 which is inconsistent with the decrease in polymer etch rate. For the latter case, it would mean an O density between 1-3 $\times 10^{14}$ cm^{-3} depending on the reduction in OH and H density. A potential increase of the O density by a factor 5 compared to the OH density cannot lead to a change in the dominant etchant in view of the 2 orders of magnitude higher etching rate of OH compared to O. Therefore the above quantitative estimates are consistent with the observed differences in etch rates for air and N_2 environment.

When it comes to surface modification by Ar/H_2O plasma, we find that the O elemental composition of the etched polymer surface shows a maximum at intermediate treatment distance (~12 mm) rather than dropping exponentially, as shown in figure 5.5. This suggests that etching and surface modification are controlled by different reactive species or the same species through different surface processes. However, etching and surface modification might not be independent with each other – the low surface O elemental composition at short treatment distance (< 8 mm) can be due to the fast material removal which prohibits the accumulation of oxidized surface sites. The decrease of both etching depth and surface O composition at long treatment distance (> 12 mm) in figure 5.5 is due to the reduction of reactive species arriving at polymer surface. It is worth

mentioning that the same relation between etching and surface modification was also observed for Ar/O_2 plasma treated polymers,[1] as shown in figure 5.6.

5.5 Conclusion

We studied the interaction of Ar/H_2O plasma with polymers using PS and the well-characterized RF jet as a model system. We find that the Ar/H_2O plasma is able to etch polymers at a relatively high etch rate and the resulting etched polymer surface is oxidized. We identified the dominant etchant species generated in Ar/H_2O plasma as OH radicals, and by correlating the amount of OH radicals arriving at the polymer surface with the etched C atoms leaving the polymer surface, we estimated the etching reaction coefficient of OH radicals to be of the order of 10^{-2} which is two orders of magnitude higher than the etching reaction coefficient of O atoms. This indicates that OH radicals are much more reactive than O atoms in terms of etching polymers.

When changing the treatment distance of Ar/H_2O plasma, we find that the polymer etch rate drops exponentially whereas the surface oxidation rate evaluated by the surface O composition shows a maximum at intermediate treatment distance. This difference between etching and surface modification indicates the complex reaction processes during plasma-surface interaction as the etching and surface modification appear to be controlled by different surface processes.

We find that mixing O_2 into the Ar/H_2O plasma, by either directly injecting O_2 in the feed gas or through entrainment of environmental O_2 gas, reduces the etching efficiency of the Ar/H_2O plasma while resulting in higher O elemental composition on the etched surface. This suggests that O_2 admixture in the Ar/H_2O plasma could lead to the reduction of OH radicals while enhance the generation of weakly oxidative species that modify the

polymer surface without etching it. In addition, we find that adding H_2O into Ar/O_2 plasma results in the reduction of its etching efficiency while leaving the surface O composition relatively stable, which indicates that H_2O admixture might quench the generation of O atoms in Ar/O_2 plasma.

Finally, we tested the effect of substrate temperature on the polymer etch rate of Ar/H_2O plasma and observed a complex temperature dependence. The polymer etch rate decreases with increasing substrate temperature from 4 °C – 70 °C. A possible explanation is an increase of the etchant (OH) sticking coefficient or the enhancement of H_2O adsorption on polymer surfaces for lower substrate temperature.

Acknowledgement

The authors gratefully acknowledge financial support by the National Science Foundation (PHY-1415353) and the US Department of Energy (DE-SC0001939). We thank H. Wang for his contribution on preparing the XPS data. We also thank C. Anderson and D. B. Graves of UC Berkeley for helpful discussions on this collaborative project. We are grateful to E. A. J. Bartis, D. Metzler, C. Li and A. Pranda for helpful discussions and collaborations.

Chapter 6: Interaction of Long-lived Reactive Species Produced by Cold Atmospheric Pressure Plasma with Model Polymers. I. Impact of Ozone and Various Reactive Oxygen-Nitrogen Species on the Chemical Modification of Polymer Films

P Luan[1] and G S Oehrlein[1]

[1] Department of Materials Science and Engineering and the Institute for Research in Electronics and Applied Physics, University of Maryland, College Park, Maryland 20742, USA

Draft manuscript, to be submitted

Abstract

Atmospheric pressure plasma (APP) sources are able to generate a variety of reactive species that have different effects on materials, such as functionalization, deposition and etching. In this article, we study the effect of long-lived reactive neutral species on polymers using a model plasma-surface interaction (PSI) system that consists ultra-thin (~10 nm) polystyrene (PS) films as the targets and surface micro-discharge (SMD) operated with various N_2/O_2 working gas mixtures as the plasma source. We characterized and quantified the reactive species generated by the plasma reactor using IR and UV absorption, and we found that O_3, N_2O_5, N_2O and HNO_3 are the dominant reactants near the target surface. By varying the mixing ratio between the N_2 and O_2 feed gases, the composition of reactive species interacting with the target material can be adjusted. When exposing PS films to these long-lived reactive species, we observed many generic responses of the PS films including thickness expansion, oxidation and nitritation, although the amount of the changes varies with the feed gas composition of the plasma source. By correlating the changes of material properties with the abundance of gas phase species, we found that O_3 - the most abundant species generated by the plasma source - might play an essential role in the remote plasma treatment of polymer films. When interacting with PS, O_3 causes surface oxidation, participates in the diffusion-reaction process in the bulk of the PS film, and results in the aromatic ring cleavage and the formation of carbonyl groups. In contrast, we did not find a relationship between surface organic nitrate and individual long-lived reactive species, which indicates that its formation on polymer surface might be a result of multiple reactive species, including both O_3 and nitrogen containing species.

6.1 Introduction

Cold temperature atmospheric pressure plasma (APP) has been used as a material processing technique for improving the wettability and adhesion of plastics,[133, 166] sanitizing microbes,[235, 236] promoting wound healing,[148, 237] cancer treatment,[169, 238] and promoting catalysis.[239, 240] The effectiveness of the APP treatment comes from the interaction between the target materials and the reactive species generated by the plasma which include charged particles, photons and neutral reactive atoms/molecules.[140] Based on the configuration of the APP source and its operating parameters,[146] the type and amount of reactive species interacting with the target can be drastically different [191, 241]. This can lead to diverse impacts on the surface, subsurface and for certain conditions even the bulk of the target materials.[1, 95, 242] In order to realize controlled APP treatment that produce desired effects on targets, it is essential to understand material responses to various types of plasma species.

Using vinyl polymers as model materials, we have previously studied the effect of short-lived neutral species produced by an atmospheric pressure plasma jet (APPJ) source, i.e. atomic O [68, 95] and OH [68, 243], on material surfaces. We found that O and OH species could lead to fast material etching reactions due to their high reactivity. We also evaluated the effect of ultra-violate (UV) photons [6] and charged species [244] using poly-methyl methacrylate (PMMA)-based 193 nm photoresists (PR193), and we found that for APPJ these energetic species can cause directional modification of the target materials.

Long-lived neutral species, although less reactive, are expected to be the dominant gas phase reactants for target materials placed in a remote location [95] because the incident fluxes of short-lived reactive species are greatly reduced for such condition. Recently, we

studied the remote plasma treatment of polystyrene (PS) using a prototypical remote plasma reactor named surface micro-discharge (SMD), and we observed three polymer transformation stages during prolonged plasma exposure, i.e. (1) oxidation and nitritation of the polymer surface, (2) oxidation of the polymer bulk and (3) etching of the polymer surface.[95] Despite the clear plasma-induced changes on materials, it is still unclear which plasma generated reactive species are responsible for these transformation stages, especially the stage of bulk oxidation which might involve the permeation of reactive species underneath material surfaces. Besides, the depth of the plasma modified polymer layer is also unknown, neither does the interaction mechanism between these reactive species and polymers.

In the first installment of a two parts series dedicated to the effect of long-lived reactive species on polymers, we characterized the type and density of long-lived reactive species generated by SMD using Infrared (IR) and UV absorption techniques. Ultra-thin (~ 10 nm) PS films were used as a model material to study the role of these long-lived reactive neutrals on polymers. We characterized the changes of PS film thickness, elemental composition and chemical bonds using ellipsometry, X-ray photoelectron spectroscopy (XPS) and attenuated total reflection (ATR)-Fourier-transform infrared spectroscopy (FTIR). By correlating the SMD induced effects on the PS films with the gas characterization results, key reactive species that cause the PS film expansion, oxidation and nitritation were identified. In the second part of the series (published separately),[242] we discuss the role of macromolecular structure, substrate temperature, and diffusion of reactive species on polymer surface and sub-surface.

6.2. Experiments and methods

6.2.1 Materials and plasma source

We chose polystyrene (PS) as a model polymer for correlating the SMD generated long-lived reactive species to material surface response. Ultra-thin (~10 nm) PS films were prepared using the spin coating of 0.5 wt% PS (Sigma-Aldrich) solution with propylene glycol methyl ether acetate (PGMEA, Sigma-Aldrich, ReagentPlus, ≥99.5%) as solvent. To achieve ~10 nm film thickness, 6000 rpm spin speed with 3 s ramping time was used. Based on the intended use of the polymer films, we coated PS on three different types of substrates: (1) SiO_2/Si substrate with 100 nm-thick SiO_2 surface layer, (2) SiO_2/Si substrate with 1.7 nm-thick native oxide (SiO_2) layer, and (3) Au/Cr/SiO_2/Si substrate with 100 nm Au, 20 nm Cr and 1.7 nm native SiO_2 stacked on top of Si. The SiO_2/Si substrate was used as it is, and the metallic layers (Au and Cr) on the SiO_2/Si substrate were sputter-coated by an ATC 1800 Sputtering system (AJA International). PS films with the first type of substrate were used for ellipsometry studies, and films with the latter two types of substrates were used for material chemical composition analysis by XPS and ATR-FTIR. The thickness of the PS film and the SiO_2 layer was measured by both 633 nm single wavelength [159] and spectroscopic ellipsometer (Sophie STE70 and J.A.Woollam alpha-SE, respectively).

The plasma reactor selected in this work is the surface micro-discharge tube array (SMD-TA)[95, 242, 245] which is a variation of the planar configuration SMD.[93, 140] As shown in figure 6.1 (a), the SMD-TA contains multiple plasma generation tubes wherein a curved metal mesh is fitted as the powered electrode. The reactor is powered by an AC signal with 23 kHz frequency and 6 kV_{pp} voltage. The plasma power consumption is less than 0.1

W/cm^2 (per glow area).[140] To tune the type and density of reactive species generated by the SMD-TA, 2 standard liters per minute (slm) of feed gas with various N_2 and O_2 mixtures was used, namely 100% O_2, 95% O_2, 90% O_2, 80% O_2, 70% O_2, 50% O_2, and 20% O_2 with the rest of the percentage as N_2 (same notation for feed gas composition is applied throughout this report). A sealed 50 L chamber was used to control the plasma processing environment. Before every experiment the chamber was pumped to 20 mTorr and then refilled with 4 slm feed gas to atmospheric pressure. The SMD-TA reactor was mounted on a scanning stage [68, 95] which was programmed to transport the plasma source between the following positions with a speed of 9.6 mm/s: (1) the treatment position where SMD-TA stays on top of the PS film for 10 s, (2) the ellipsometry data acquisition position where SMD-TA is 4.5 cm away from the treatment position and stays stationary for 2 s. Therefore each processing cycle takes 21.375 s.

Since the electrical configuration and the discharge behavior of the SMD-TA reactor is very similar to the planar configuration SMD, we use the SMD-TA to study the generic property of the SMD type of reactors with the benefit of easily controlling the chemical composition of the working gas. Our measurements show that both the long-lived reactive species and the polymer transformation stages show qualitatively comparable results between the SMD-TA and the planar SMD reactors, although the planar SMD is slightly more effective in terms of oxidizing polymers. Therefore we use the term SMD to stand for the SMD-TA reactor in the rest of this report.

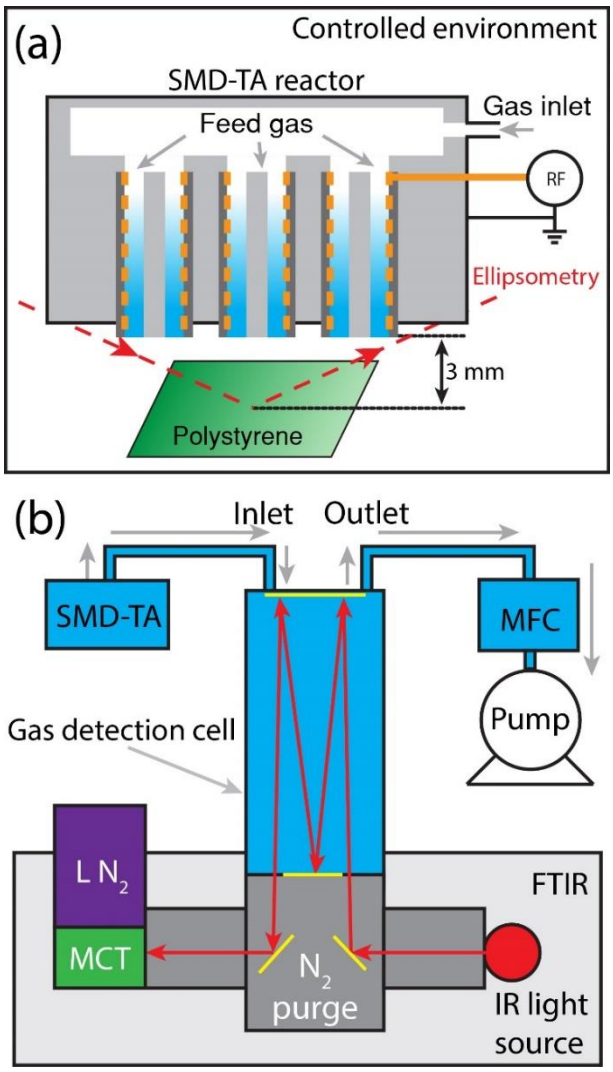

Figure 6.1 (a) Schematic diagram of polymer processing by the SMD-TA. The target PS film is placed underneath the nozzle at a distance of 3 mm. (b) Schematic diagram of the gas phase species characterization by FTIR with a variable-length gas detection cell. A liquid N_2 cooled MCT detector is applied.

6.2.2 Gas phase measurement

The gas phase species generated by the SMD were characterized by both IR and UV absorption. As shown in figure 6.1 (b), we measured the IR spectrum of the SMD

exhaust using an FTIR (Shimadzu IRtracer 100) equipped with a liquid nitrogen-cooled HgCdTe (MCT) detector. For quantifying reactive neutrals with strongly differing densities, a variable path gas detection cell (PIKE technologies 1–16v m) with path lengths set at 1.33 m and 16 m was used. The IR absorption background was measured with N_2/O_2 feed gas mixture before igniting the plasma reactor. The variable path gas cell has a volume of 3.5 L, and was flushed for 20 minutes before spectrum acquisition. To guide the flow of reactive species into the detection cell, the outlet of the gas cell is connected to a mass flow controller (set at 2 slm) and a vacuum pump. To reduce noise from ambient humidity and CO_2, the optical path of IR light outside of the gas detection cell was constantly flushed by pure N_2. The IR spectra of the SMD effluent were acquired in the range of 4000 cm^{-1} to 600 cm^{-1} with 0.5 cm^{-1} resolution and 20-scan averages.

A homemade UV (254 nm) absorption system with 1 cm optical path length was used to quantify the density of ozone generated by the SMD reactor. The UV absorption setup is composed of a Hg-Ar lamp, a 10 nm band pass filter centered at 254 nm (Edmund), a 34 mm^2 effective area deep UV photodiode (Edmund), and a high gain operational amplifier circuit (LMP7721, Texas Instruments). The optical path of the UV absorption measurement was located ~3 mm away from the nozzle of the SMD reactor.

6.2.3 Ellipsometry

We used *in-situ* ellipsometry to monitor the changes of optical properties of the PS films during plasma treatment. The ellipsometer (SOFIE STE70) has a He-Ne laser (λ = 632.8 nm) with ~72° incident angle and an automated rotating compensator in the polarizer-compensator-sample-analyzer (PCSA) configuration.[1, 95] Upon the reflection of polarized laser beam on polymer sample, the ellipsometer records the change in the phase

difference (Δ) and the angle (Ψ) whose tangent is the ratio of the magnitudes of the total reflection coefficient.[192] Polymer thickness and refractive index values can be fitted from the Ψ and Δ data using optical models described previously.[95] Due to the scan processing, ellipsometry data were taken for 2 s after every 19.375 s.

6.2.4 Chemical composition characterization: XPS and ATR-FTIR

To characterize the chemical composition of PS surface, we used an XPS system (Vacuum Generators ESCALAB MK II) with non-monochromatic Al K_α radiation ($h\nu$ = 1486.6 eV) as light source. The survey and high-resolution C 1s, N 1s, O 1s XPS were obtained at electron take-off angles of 20° and 90° (probing depth ~2 nm and ~8 nm, respectively).[246] The peak fitting and elemental composition analysis were performed using CasaXPS software with parameters [1, 95, 158] described as following. First, we fitted the C 1s spectrum with peaks corresponding to C-C/H (285 eV), C-O (286.5 eV), O-C-O/C=O (287.9 eV), O-C=O (289.1 eV), O-CO-O (290.2 eV) and pi–pi* shake-up (291.5 eV). Second, only organic nitrate (ONO_2, 408.2 eV) peaks were fitted in the N 1s spectrum due to the absence of other nitrogen peaks.[193, 194] And last, considering the small chemical shift of O 1s core electrons, two peaks at 532.7 eV and 533.9 eV with each representing oxygen moieties with binding energy from 532.2 eV to 533.1 eV and from 533.6 eV to 535.3 eV respectively were fitted.[1] After calibrating C-C/H peak to 285 eV, we performed Shirley background reduction to all spectra.

The enhanced ATR-FTIR spectra [245] of the ~10 nm PS films were obtained using the same FTIR (Shimadzu IRTracer-100) equipped with MCT detector. We used a variable angle single reflection ATR accessory (VeeMaxIII, PIKE Technologies) along with a ZnSe polarizer installed on its optical inlet to achieve p-polarized IR light interacting with the

polymer films at 60° incident angle. The internal reflection element (IRE) of the ATR accessory is a Ge crystal. A constant torque pressure clamp with 7.8 mm diameter tip (PIKE Technologies) was applied to maintain consistent contact between the Ge crystal and the polymer films. The optical path of the IR light was also purged with pure N_2. The reference backgrounds were obtained with no sample coupled to the Ge crystal. The IR spectra were collected in the range of 3400 cm^{-1} to 600 cm^{-1} with 4 cm^{-1} resolution averaged over 20 scans. Multiple-point baseline correction was consistently applied to all the acquired ATR-FTIR spectrum.

6.3 Results

6.3.1 Gas phase characterization

Based on the position and shape of the IR peaks, we are able to identify a number of long-lived reactive neutrals generated by the SMD reactor. As illustrated in figure 6.2, the IR absorption spectrum of the SMD effluent with 20% O_2 (artificial air) feed gas showed peaks that can be assigned to four reactive neutrals namely O_3, N_2O_5, HNO_3 and N_2O. Based on Beer's law,[242] the density of these species can be determined using their corresponding IR peak intensity/absorbance and cross section values reported previously. For N_2O_5,[247] HNO_3,[248] and N_2O,[249, 250] we can estimate their densities as $1.63 \pm 0.09 \times 10^{15} cm^{-3}$, $6.23 \pm 0.87 \times 10^{14} cm^{-3}$ and $7.90 \pm 0.55 \times 10^{14} cm^{-3}$, respectively. The density of O_3 was measured using UV absorption at 254 nm with cross section $\sigma_{O_3} = 1.15 \times 10^{-17} cm^2$,[94] and it was found to be $2.80 \times 10^{16} cm^{-3}$ at 3 mm away from the nozzle of the SMD.

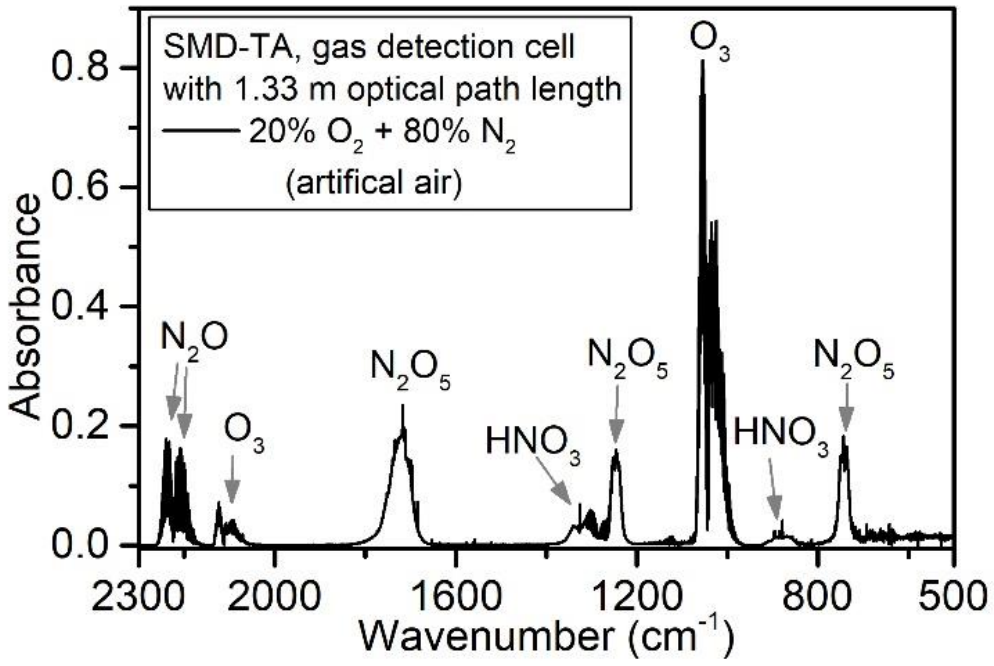

Figure 6.2 The IR absorption spectrum of the SMD effluent with 20% O_2 (artificial air) feed gas. The gas detection cell has an optical path length of 1.33 m.

When changing mixing ratio between N_2 and O_2 in the feed gas, we found that the densities of the long-lived reactive neutrals varied. As shown in figure 6.3 (a) and (b), the position and shape of the IR peaks from N_2O, O_3, N_2O_5 and HNO_3 remain the same, but the absorbance of these IR peaks changes with feed gas composition. We also examined the IR spectrum with 16 m optical path length for NO, NO_2 and NO_3 species, but no observable IR peaks can be found for all feed gas compositions. This suggests that the density of these NO_x species is below the detection limit of our FTIR setup ($1 \times 10^{14} cm^{-3}$).

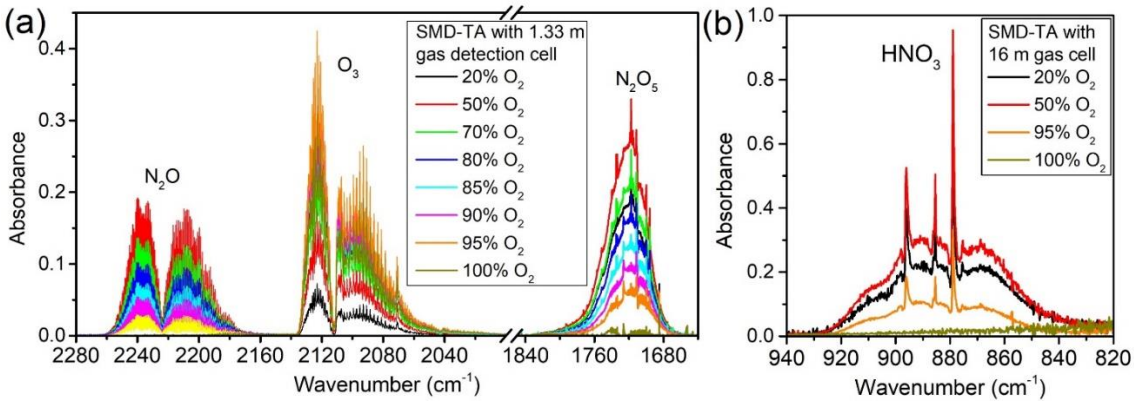

Figure 6.3 The IR absorption spectra of four reactive species, i.e. O_3, N_2O_5, HNO_3 and N_2O generated by the SMD with various feed gas compositions.

In figure 6.4 (a) and (b), we show the densities of O_3, N_2O_5, N_2O and HNO_3 as a function of feed gas composition. We find that O_3 is the most abundant reactive species generated by SMD with a peak density of $1.38 \times 10^{17} cm^{-3}$. Similar to the results shown in figure 6.3, the peak densities of O_3 and reactive nitrogen species (RNS) appeared for different feed gas compositions: 95% O_2 and 50% O_2, respectively. For feed gas O_2 composition higher than 20%, the density of O_3 is generally 1 – 2 orders of magnitude higher than the RNS densities. When comparing different RNS in figure 6.4 (b), we find that the density of N_2O_5 is always higher than that of N_2O and HNO_3. Therefore O_3 and N_2O_5 are the two dominant long-lived reactive neutrals generated by the SMD.

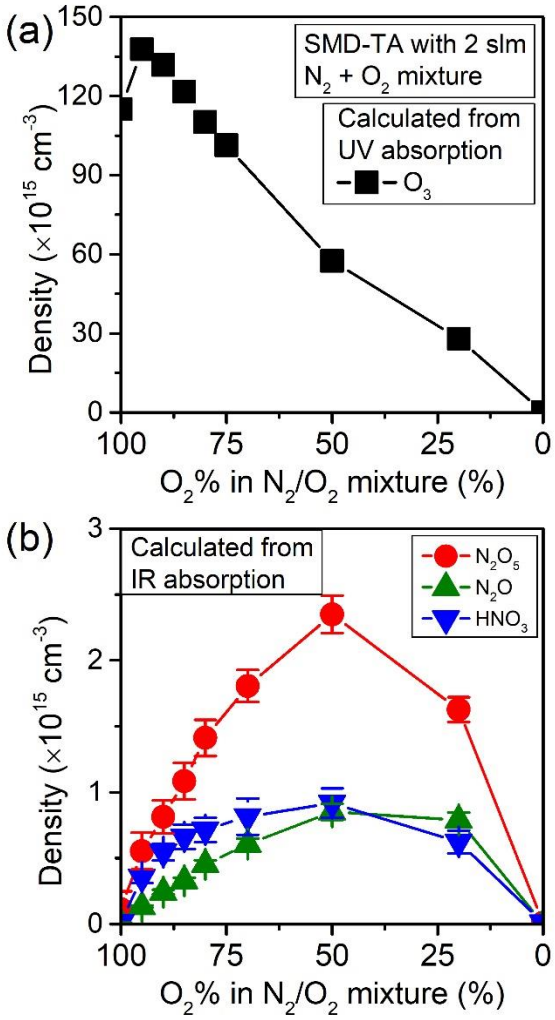

Figure 6.4 (a) The density of O_3 measured by UV absorption as a function of feed gas composition. (b) The density of N_2O_5, N_2O and HNO_3 measured by IR absorption as a function of feed gas composition.

Although short-lived neutral species such as N, O, OH, NO, $O_2(a^1\Delta_g)$ and HO_2 can also be generated within the discharge region of the SMD reactor,[191] minimal amounts of these short-lived neutrals can be transported to the sample surface located 3 mm away from the nozzle. Based on the fluid model of reactionless species transport,[1] the average gas velocity at the nozzle of the discharge tubes can be estimated ~ 0.21 m/s. This indicates

that it would take more than 14 ms for the plasma species to be transported to the sample. The time required for the convective flow of species is much longer than the lifetime of these short-lived neutrals at atmospheric pressure which is typically less than 1 ms. However, this argument does not consider the influence of the stationary boundary layer at the polymer surface where the transport of species might mostly rely on diffusion. We also performed IR emission ($a^1\Delta_g \rightarrow X^3\Sigma_g^-$) measurement of $O_2(a^1\Delta_g)$ with an identical setup as used by Sousa et al.[23]. However, the density of $O_2(a^1\Delta_g)$ is below the detection limit of $4 \times 10^{13} cm^{-3}$ for all feed gas compositions tested. Therefore, our measurements indicate that the dominant reactive gas species at the polymer surface are the long-lived neutrals as characterized by the FTIR.

6.3.2 Ellipsometry: the behavior of polymer film thickness and refractive index

To understand how polymers respond under the exposure of the reactive plasma species generated by the SMD reactor, we performed *in*-situ ellipsometry measurement of the ultra-thin PS films (11 - 12 nm) during treatment with different feed gas compositions. In figure 6.5 we show the *in-situ* Δ-Ψ plot of the PS films along with the fitted thickness and refractive index values obtained by applying a single layer optical model to the raw Δ-Ψ data.[95] Although we investigated all feed gas compositions in figure 6.4, here we discuss the PS films treated by three representative feed gas compositions: 95% O_2, 80% O_2 and 20% O_2.

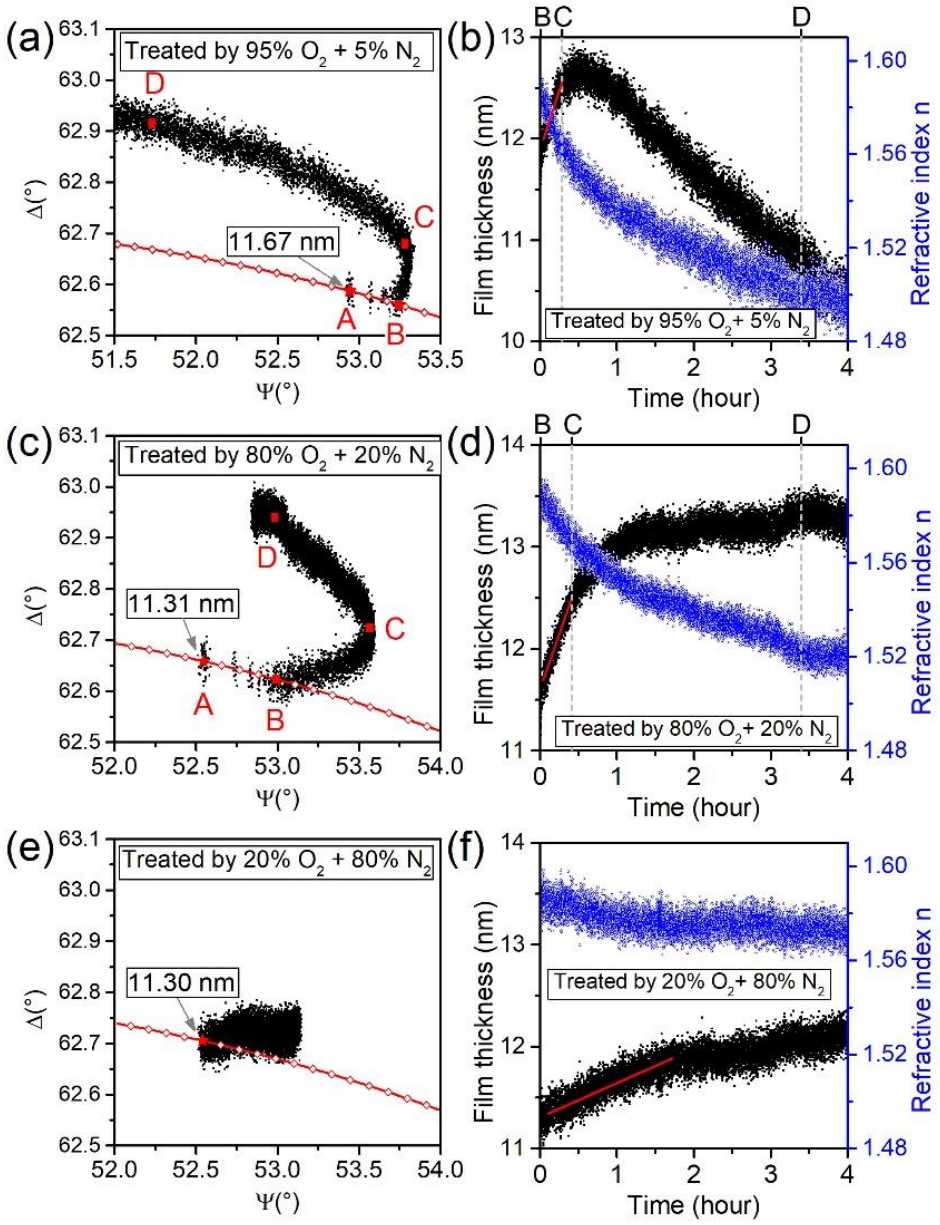

Figure 6.5 The *in-situ* ellipsometry trajectories (a, c, e, g) of PS films under the exposure of SMD and their corresponding fitted thickness/refractive index (b, d, f, h) values as a function of time. Results from different feed gas compositions are shown: (a) and (b): 95% O_2, (c) and (d): 80% O_2, (e) and (f): 20% O_2.

First, for the PS film treated by 95% O_2 feed gas, we observe three distinct polymer

transformation stages. Prior to the SMD treatment, the Δ-Ψ plot of the pristine PS film (figure 6.5 a) starts from point A which corresponds to a film thickness of 11.67 nm. When we start treating the PS film, the Δ-Ψ trajectory moves from point A to two consecutive turning points labeled B and C, and then toward point D which is near the end of the treatment. Previously we examined the behavior of PS films under the remote treatment by SMD, and we attributed the three sections AB, BC and CD in the Δ-Ψ plot to three polymer transformation stages,[95] i.e. (1) AB: surface oxidation and nitritation stage; (2) BC: thickness expansion stage resulted from the oxidation of the bulk of the PS film and (3) CD: thickness reduction stage by etching. In figure 6.5 (b) we show the fitted thickness and refractive index of the PS film as a function of time. We also labeled the three polymer transformation stages, and we find that (a) the surface oxidation and nitritation stage takes ~85 s and shows a polymer thickness increase of 0.30 nm, (b) the thickness expansion stage shows an increase rate of 2.27 nm/h, and (c) the etching stage shows an etch rate of 0.64 nm/h. The continuous drop of refractive index in figure 6.5 (b) indicates the oxidation of polymer bulk during the entire treatment.

Similarly, for the PS film treated with 80% O_2 feed gas, we also see the two turning points B, C in figure 6.5 (c). For the AB stage, the thickness gain due to surface oxidation and nitritation is also 0.30 nm which is achieved after ~85 s of treatment. However, as shown in figure 6.5 (d) the thickness expansion rate in the BC stage drops to 2.16 nm/h. We did not observed an evident thickness reduction stage in figure 6.5 (d) which might be because that the thickness increase from bulk oxidation is larger than the thickness decrease from surface etching.[95] These evidences indicate that the reactive species generated from 80% O_2 feed gas are less reactive than those produced by 95% O_2 feed gas.

For the PS film treated with 20% O_2 feed gas, no turning points in the Δ-Ψ plot can be found in figure 6.5 (e). The fitted PS film thickness and refractive index plot, as shown in figure 6.5 (f), indicates that during the 4 hours of treatment time the PS film only experiences a slow thickness increase stage with an expansion rate of 0.369 nm/h. Compared to the other two feed gas conditions discussed above, the surface oxidation/nitritation and etching stage are absent from both plots. This indicates that the effluent of SMD with 20% O_2 feed gas is even less reactive.

In figure 6.6, we summarize the changes of polymer thickness in the three transformations stages observed with various N_2/O_2 working gas mixtures. As shown in figure 6.6 (a), the thickness gain in the surface oxidation and nitritation stage is correlated to feed gas compositions. Besides 100% and 20% O_2 conditions, we find that the treatment time required for reaching the end of this stage is 85 s for all other feed gas compositions. For PS film treated by 70% - 95% O_2, we observe a 0.3 nm constant thickness gain in the surface oxidation/nitritation stage. In figure 6.6 (b) we plotted the PS film expansion rate during the bulk oxidation stage as a function of feed gas composition. We find that the expansion rate shows a maximum at 95% O_2 working gas and then drops quickly with less O_2 in the feed gas. The shape of this curve resembles that of the O_3 density shown in figure 6.4 (a). In figure 6.6 (c), we show the correlation between polymer etch rate in the etching stage and feed gas composition. Since we did not observe evident film thickness reduction when the working gas O_2 is less than 80%, zero etch rate was shown for these feed gas mixtures. It can be seen that the etch rate has a maximum again at 95% O_2 working gas, however the etch rate curve does not resemble that of the O_3 density curve. This indicates that material etching might be related to O_3 but not controlled by it.

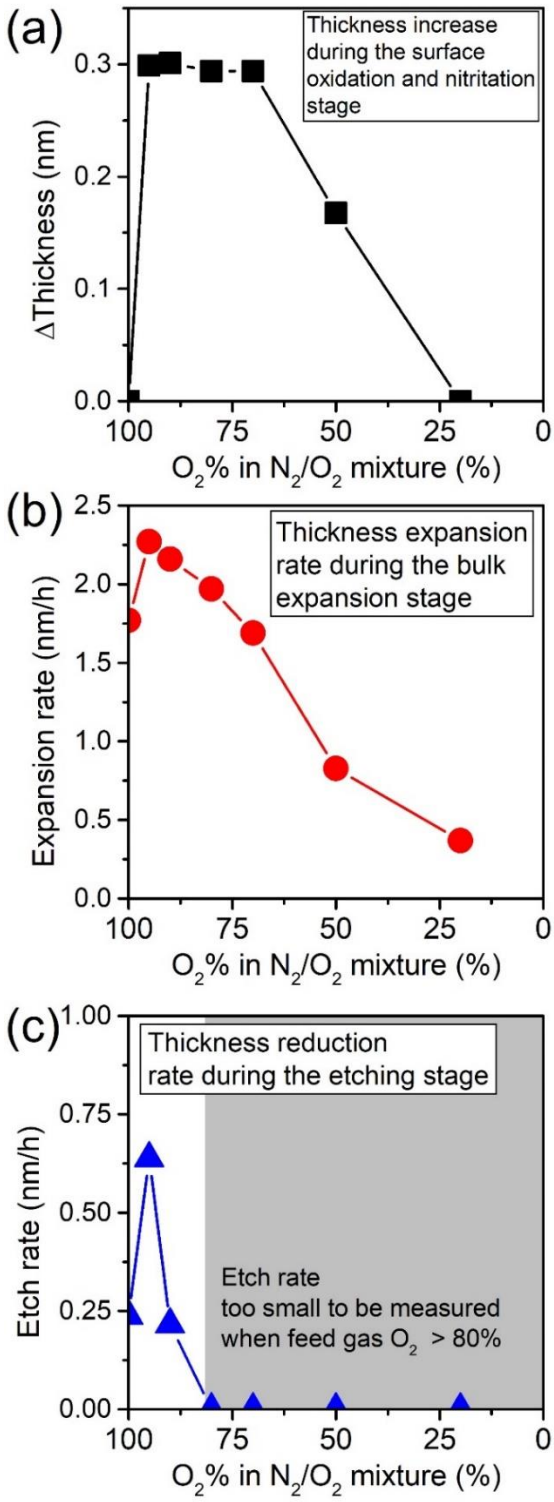

Figure 6.6 (a) The net thickness gain after the surface oxidation and nitritation

stage, (b) the thickness expansion rate during the bulk oxidation stage, and (c) the etch rate during the etching stage of PS transformation as a function of feed gas composition. In (c), zero etch rate was shown for the polymer films treated with < 80% O_2 in the N_2/O_2 mixture due to the lack of an etching stage after 4 hours of treatment.

6.3.3 XPS: surface chemistry

Besides polymer thickness and refractive index, we also characterized the chemical composition of the SMD treated PS films using XPS. In figure 6.7 we show the high-resolution C 1s, N 1s and O 1s spectra of the pristine and the 0.5 hour treated PS films using 95% O_2 and 20% O_2 feed gas compositions. Only spectra with 20° electron take-off angle are shown which contains the chemical composition of the top 2 nm of the PS films. Since there is neither O nor N composition in the pristine PS film, the untreated spectra show only two C 1s peaks with 94% of the core electrons belonging to the C-C/H bond whereas the rest coming from π-π* shake-up satellite.

After 0.5 hours of treatment with both feed gas compositions, we observe the decrease of the C-C/H and π-π* shake-up peaks and the rise of the oxygen containing functional groups such as C-O, O-C-O, C=O, O-C=O and O-CO-O in figure 6.7 (a), which indicates the oxidation of the aromatic ring and possibly the main chain. Moreover, the N 1s spectra of the treated PS films show the emergence of organic nitrate (ONO_2) peaks at 408.2 eV. Correspondingly, the oxidation and nitritation of PS films are confirmed by the O 1s spectra shown in figure 6.7 (c): the broad O 1s peak formed after SMD treatment can be attributed to both the organic nitrate and the O containing functional groups seen in C 1s spectra. When comparing the spectra from 95% O_2 and 20% O_2 treated PS films, we

find similar amount of ONO_2 but higher surface oxidation for the 95% O_2 treated film. The difference of surface oxidation is consistent with that of the thickness expansion rate shown in figure 6.5 where 95% O_2 treatment shows higher expansion rate which indicates more oxidation to the polymer films.

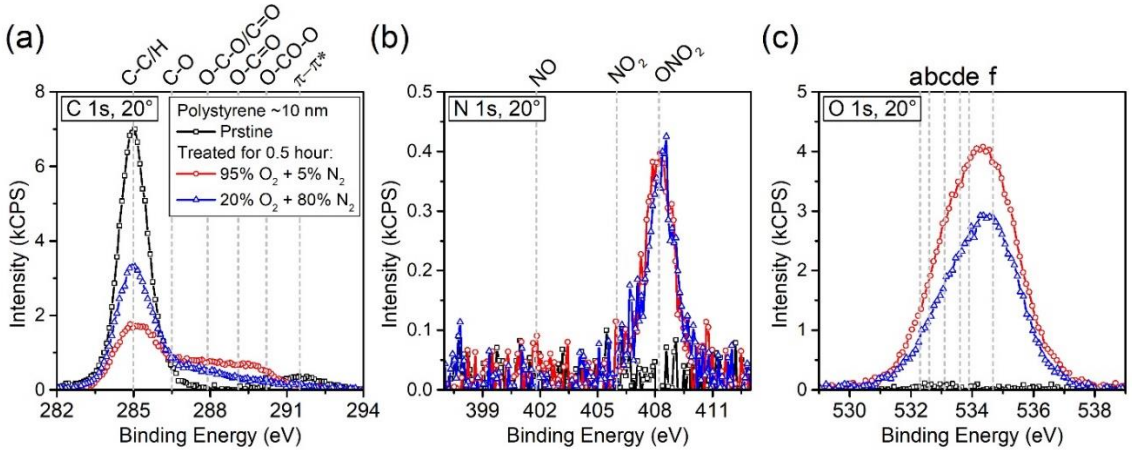

Figure 6.7 High-resolution XPS of pristine and 0.5 hour treated PS surfaces by either 95% O_2 or 20% feed gas: (a) C 1s, (b) N 1s, (c) O 1s. The electron take off angle is 20°. Label a (532.3 eV): C=O, O-C=O*, O*-CO-O; b (532.6 eV) aliphatic C-O; c (533.1 eV): aromatic C-O, O-C-O; d (533.6): O*-C=O; e (533.9 eV): O-CO*-O, O*-NO_2; f (534.7 eV): O-NO_2*.

Besides the 95% O_2 and 20% O_2 treated PS films, we further measured the XPS of PS films treated by other feed gas compositions studied in figure 6.4. For each feed gas composition, two treatment times, namely 0.5 hour and 2 hours, were performed for investigating the surface chemical composition at different polymer transformation stages. Since all high resolution spectra of the treated PS films share the same peak features as those shown in figure 6.7, instead of high resolution spectra we present the calculated elemental composition of C, O and N as a function of feed gas composition. As illustrated

in figure 6.8 (a), the surface O composition shows a maximum when the PS films is treated with large amount of O_2 in the feed gas mixture (95% and 80% for 0.5 hour and 2 hours treated PS films, respectively). Correspondingly, the surface C composition shows a minimum at the same feed gas mixture where we observe the surface O maximum. We also find that longer treatment time generally leads to higher surface O content, which indicates that the polymer surface oxidation may depend on the time integrated flux of reactive species produced by the plasma treatment (dose). [95, 245] Interestingly, the surface O composition curve as a function of feed gas composition in figure 6.8 (a) strongly resembles that of the O_3 density and the thickness expansion rate in figures 6.4 (a) and 6.6 (b), respectively. We will further discuss the correlations in Section 6.4.1.

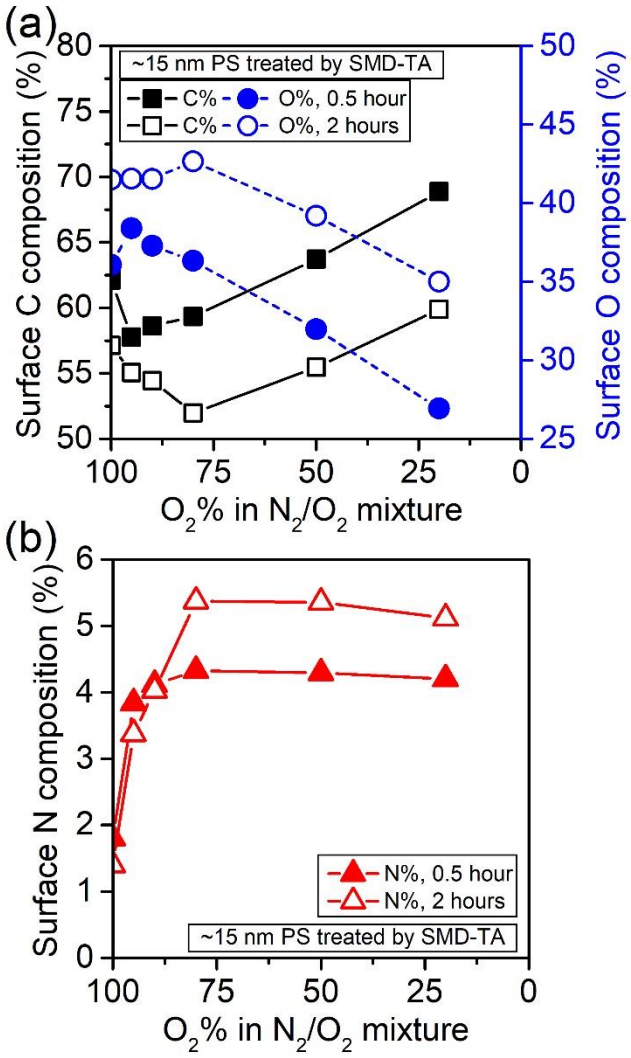

Figure 6.8 The XPS measured (a) surface C, O and (b) surface N composition of the SMD treated PS surface as a function of feed gas composition. Results with two treatment times, i.e. 0.5 hour and 2 hour, are shown. The electron take-off angle is 20° which corresponds to the top 2 nm of the polymer film.

Furthermore, we find that the surface N composition increases with the N_2 composition in the feed gas and eventually reaches a plateau, as shown in figure 6.8. Since all surface N comes from the ONO_2 group as indicated in figure 6.7 b, the trend in figure 6.8 also represents that of the ONO_2 group. The small amount of surface N on PS films

treated with pure O_2 feed gas might be from the residual N_2 absorbed on the vacuum chamber wall and/or leaks during the process of refilling to atmospheric pressure. When comparing the two treatment times, i.e. 0.5 hour and 2 hours, we find that longer treatment time leads to slightly larger amount of surface N composition, especially with smaller O_2 content in the feed gas. Compared to the typical value of less than 1% of surface N on polymers treated by other APP sources such as the plasma jets, corona discharge and direct DBDs, the surface N composition on PS films treated by SMD is relatively high (> 3%). This might be due to (1) the prolonged treatment time which accumulates the surface N composition and (3) the negligible amount of material removal by etchant species which may cause the desorption of N containing surface moieties.

In figure 6.9, we show the C 1s decomposition of PS films treated by the SMD for 0.5 hour as a function of feed gas composition. Each line in figure 6.9 represents the relative concentration of one surface moiety observed in the high resolution C 1s spectra shown in figure 6.7 (a). The relatively large chemical shift among C 1s core electrons from different functional groups makes it suitable for identifying and comparing the relative concentration of these surface moieties. From figure 6.9 (a), we find that higher O_2 concentration in the feed gas leads to smaller amount of C-C/H and π- π^* shake up peaks on the treated PS surface, which indicates that more aromatic ring structures and possibly the polymer main chains are destroyed with higher O_2 content in the feed gas. A minimum of the C-C/H bond concentration can be found with the 95% O_2 treated PS film. Correspondingly, in figure 6.9 (b) we find that higher feed gas O_2 concentration could result in larger amount of O containing functional groups forming on the treated PS surface. Similarly, a maximum of these O containing groups is seen with the 95% O_2 treated film. This indicates that the C-

C/H bonds and the aromatic rings might be converted into various O containing moieties by SMD treatment. When comparing the relative concentration of the O containing functional groups for the 0.5 hour treated PS films, we find the following relation: C-O > O-C-O/C=O > O-C=O > O-CO-O, as indicated in figure 6.9 (b).

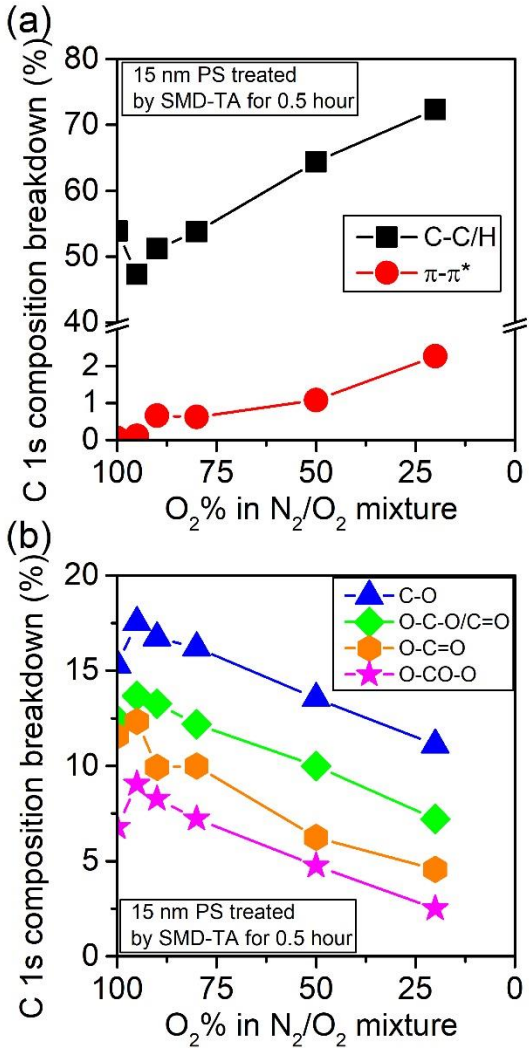

Figure 6.9 XPS C 1s decomposition of SMD treated PS films for 0.5 hour: (a) C-C/H and π-π* shakeup, (b) C-O, O-C-O/C=O, O-C=O, O-CO-O.

In order to show the effect of extended treatment time on surface functional groups, we calculated the difference between 2 hours and 0.5 hour treated PS films for the relative

concentrations of C-O, O-C-O/C=O, O-C=O and O-CO-O groups in the C 1s spectrum. The positive value in figure 6.10 indicates that 2 hours treatment lead to higher concentrations of specified surface moieties than 0.5 hour treatment. It can be seen that although longer treatment with 20% O_2 (artificial air) feed gas results in the even increase of all O containing moieties, generally longer treatment with higher O_2 percentage in the feed gas tends to cause the accumulation of O-C=O groups. As discussed previously,[95] such accumulation of O-C=O bond might be due to the unique etching mechanism of the SMD treatment. After 2 hours of treatment with high O_2 percentage (≥ 80%) feed gas, the PS films has proceeded to the etching stage as indicated in figure 6.5 (e), whereas the PS films treated for 0.5 hour is still in the expansion stage. In the etching stage, other functional groups are converted to O-C=O group which might be the precursor for the formation of etching product CO_2. The concentration of surface O-C=O will eventually saturate when a dynamic balance between etching and oxidation is established on polymer surface. Detailed discussion can be found in reference.[95]

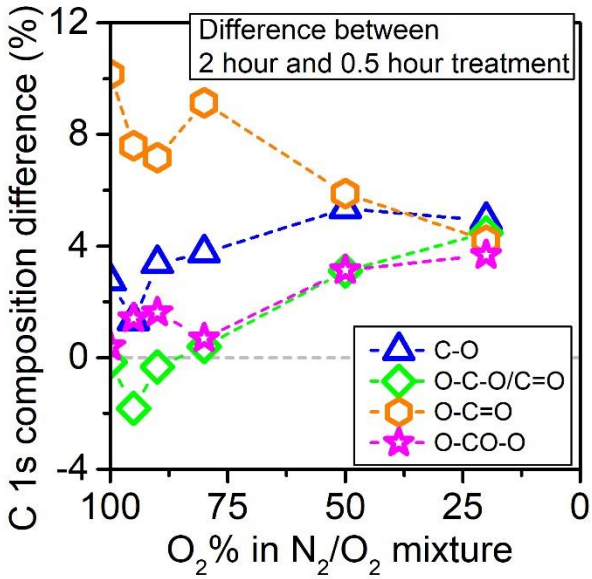

Figure 6.10 The XPS C 1s decomposition difference between the 2 hour and the

0.5 hour SMD treated PS films. Positive value indicates that the 2 hour treated PS film contains higher relative concentration of the moieties than the 0.5 hour treated PS film.

6.3.4 ATR-FTIR: sub-surface chemistry

Because the penetration depth of IR light (hundreds of nm)[251] is much deeper than the thickness of the PS film (~10 nm), the ATR-FTIR spectrum reflects the average chemical composition of the entire ultra-thin film.[245, 251] In contrast, the XPS with 20° take-off angle provides chemical information from the top 2 nm of the polymer film.

In figure 6.11, we show the ATR-FTIR spectrum of the pristine and the 0.5 hour treated PS films coated on Au surface which serves as the enhancing back layer. Due to the lack of a universal reference peak in this sampling configuration, all spectra are normalized to their own IR peak intensity.[245] For the pristine ultra-thin film, characteristic vibrational modes of PS are observed and labeled as A through H in figure 6.11. Besides peak G (aliphatic chain C-H stretch), all labeled IR peaks are from the aromatic ring structure. The two broad IR bands marked as area I and IV can be attributed to carbonyl and ether groups respectively, and these features indicate that either the pristine PS surface or the PS/Au interface is weakly contaminated by hydrocarbon or surface oxidation.

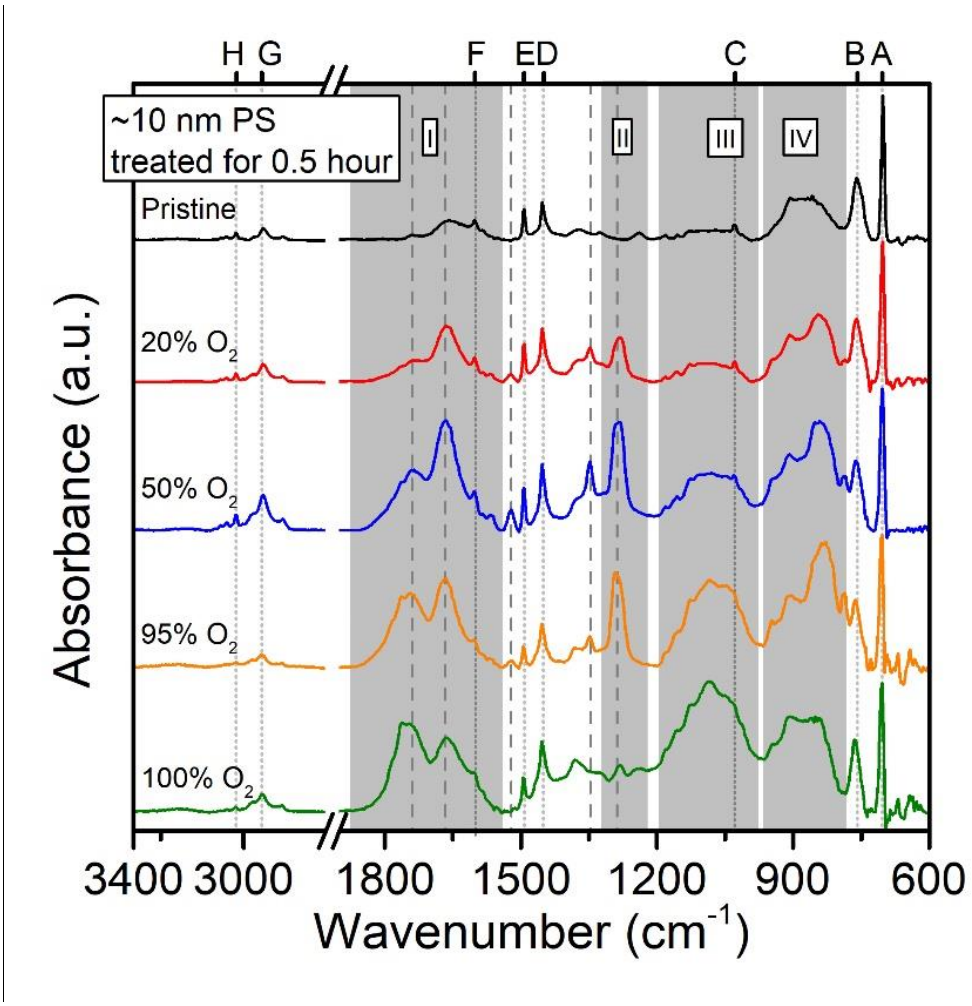

Figure 6.11 Enhanced ATR-FTIR spectrum obtained with ~10 nm PS film coated on Au surface. Spectra from PS films treated by four different feed gas compositions (20% O_2, 50% O_2, 95% O_2 and 100% O_2) are shown. All spectra are normalized to their individual highest peak. Labels A through H notate the IR active vibration modes from polystyrene. A (700 cm^{-1}): aromatic ring out-of-plane deformation; B (760cm^{-1}): out-of-plane C-H bend; C (1029 cm^{-1}): in-plan C-H bend; D, E and F (1452 cm^{-1}, 1492 cm^{-1}, 1602 cm^{-1}): aromatic ring modes; G (3000 – 2800 cm^{-1}): aliphatic C-H stretch; H (3100 - 3000 cm^{-1}): aromatic C-H stretch.

After 0.5 hour of plasma treatment, we observe the significant growth of four IR bands marked as I through IV in the shaded area of figure 6.11. These new bands have broad width which suggests that the product of plasma modification does not have homogeneous structure. Similar to our previous observation,[242, 245] the IR band in area I can be assigned to the general carbonyl (C=O) stretching modes (1600 cm^{-1} - 1800 cm^{-1}) and asymmetric NO_2 stretching mode (1615 cm^{-1} - 1660 cm^{-1}) from organic nitrate.[195, 199] The two peaks labeled within area I (dashed lines) might come from saturated carbonyl and aromatic carbonyl, respectively. The aromatic carbonyl has lower wavenumber because the conjugated system of aromatic ring and carbonyl carbon reduces the force constant of C=O bond. Furthermore, we can assign the IR band in area II (1290 cm^{-1}) to the symmetric NO_2 stretch of organic nitrate group[252] and possibly aromatic ketone and aromatic ester. The IR bands in area III and IV are mostly from the C-O stretch of ether and ester groups. Due to the absence of OH stretch (3500 – 2500 cm^{-1}), aldehyde C-H stretch (2850 - 2700 cm^{-1}) and aldehyde C-H bend (near 1390 ± 10 cm^{-1}) peaks in figure 6.11, we can eliminate the possibility of having alcohol (-OH), carboxyl (-COOH) and aldehyde (O=C-H) groups in the plasma treated films.

Since the spectra in figure 6.11 are not normalized to a generic reference peak with constant intensity, the spectra from different samples cannot be directly compared. In order to solve this issue and compare spectra from PS films treated by different feed gas compositions, we characterized the ATR-FTIR spectra of PS coated on SiO_2/Si substrates which have a 1.7 nm constant thickness native oxide layer. The Si-O-Si peak at 1225 cm^{-1} from the native SiO_2 can be used as the reference peak with unit intensity.[245]

As shown in figure 6.12, the IR spectrum of PS films coated on SiO_2/Si substrate

have similar IR features as those labeled in figure 6.11 except an extra band in the region of 1280 – 1010 cm^{-1} which can be assigned to Si-O-Si stretch. Since peak intensity ratio to Si-O-Si stretch at 1225 cm^{-1} are calculated and presented in figure 6.12, the relative concentration of the same functional group from different samples can be directly compared.[245]

As illustrated by peak A through F in figure 6.12, we notice that the IR peak intensity of aromatic ring diminish for films treated by all feed gas compositions. This is especially evident for the 95% and 100% O_2 treated PS films where the IR peaks from aromatic ring are completely eliminated. Moreover, the plasma treated PS films also show the formation of ether (shaded area III and IV), organic nitrate (area II) and carbonyl (area I) groups. These evidence suggests that the SMD treatment can destroy aromatic ring structures and convert them into O containing functional groups, such as ether, ester, ketone and organic nitrate.

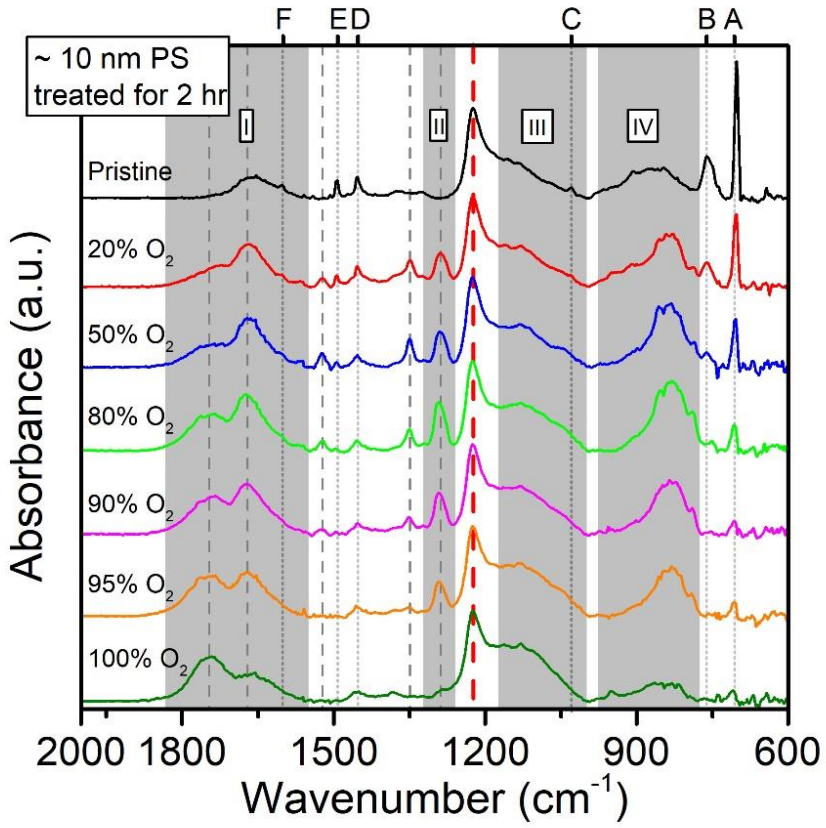

Figure 6.12 Enhanced ATR-FTIR spectrum obtained with ~10 nm PS film coated on SiO_2/Si surface. All spectra are normalized to O-Si-O peak. Labels A through F notate the same IR active vibration modes from polystyrene as those in figure 6.9.

When comparing different spectra in figure 6.12, we find that the chemical composition of the SMD treated PS films changes with feed gas compositions. In figure 6.13 (a), we summarize the relative amount of aromatic ring as a function of feed gas composition using the peak A intensity ratio of the treated PS films to the pristine PS films. We can see that there are fewer aromatic ring structures left in the PS films after treatment with higher O_2 concentration in the feed gas. The shape of the curve in figure 6.13 (a) strongly resembles that of the C-C/H curve measure by XPS in figure 6.9 (a). Furthermore,

we can also calculate the relative amount of carbonyl group using the integrated area intensity of IR band I in figure 6.12. As shown in figure 6.13 (b), we find that the carbonyl group in treated PS film shows a maximum with 80% – 95% of O_2 in the O_2/N_2 feed gas, and the curve has roughly similar trend as that of the O containing surface moieties in figure 6.9 (b). In addition, we also find that longer treatment time could lead to higher amount of aromatic ring destruction and larger amount of carbonyl formation.

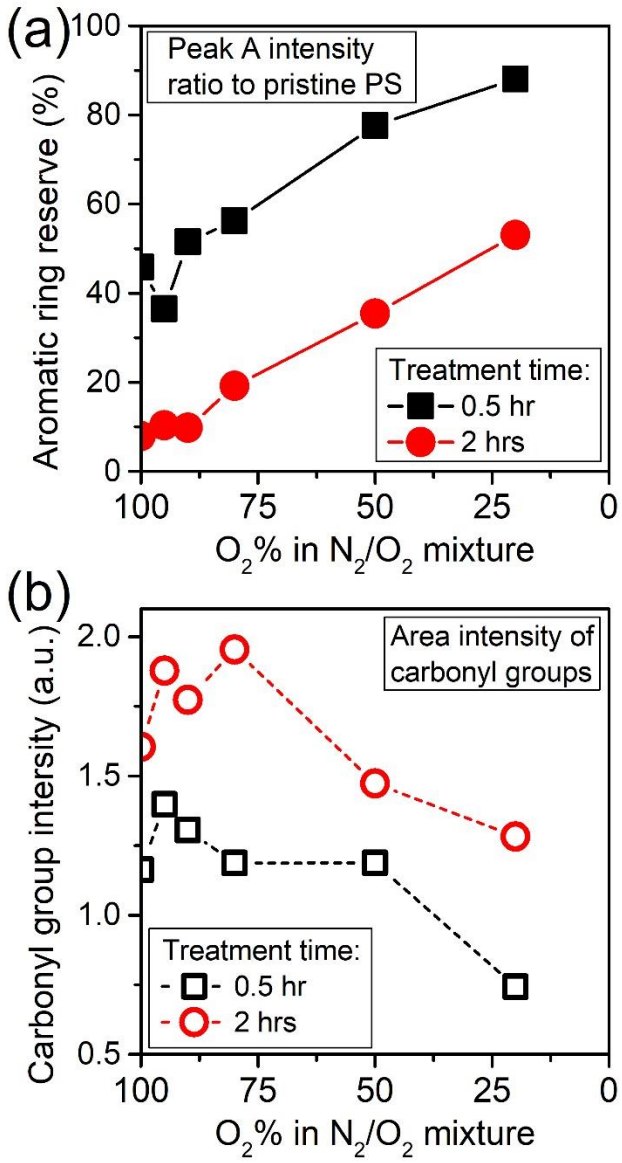

Figure 6.13 (a) The relative percentage of aromatic ring left in the ultra-thin PS film

compared to the pristine PS film calculated by the ratio of the aromatic ring out-of-plane deformation IR peak. (b) the relative amount of carbonyl groups (calculated by the integrated area intensity of the shaded area I in figure 6.11) in the treated PS films as a function of feed gas composition.

Besides, when comparing the two carbonyl peaks in the shaded area I of figure 6.12, we find that treatments by feed gas with lower O_2 concentration might favor the formation of aromatic carbonyl (~ 1672 cm^{-1}) whereas feed gas with higher O_2 concentration might favor the formation of saturated/aliphatic carbonyl (~ 1740 cm^{-1}). We think that this shift from aromatic carbonyl to aliphatic carbonyl comes from the further oxidation of the aromatic ring which indicates that the plasma effluent is more oxidative when larger amount of O_2 is in the feed gas. Evidence can be found in figure 6.13 (a) where more aromatic rings are destroyed when more O_2 is in the feed gas (figure 6.13 a).

6.4 Discussion

6.4.1 The effect of O3 on PS

In order to determine the role of the SMD generated reactive species on polymers, we correlate the thickness and chemical composition of the treated PS films with the flux and dose of the gas phase reactive species characterized in section 6.3.1. Based on the kinetic theory of ideal gases, the average flux of reactive species bombarding a unit area of polymer surface ($\overline{\Gamma}$) can be estimated using its density (n) with the following equation:

$$\overline{\Gamma} = \frac{1}{4} n \overline{v} = \frac{1}{4} n \sqrt{\frac{8RT_{gas}}{\pi M}} \qquad (6.1)$$

where $\overline{v}$ is the average gas speed, R is the gas constant, T_{gas} is the gas temperature

near material surface, M is the molecular weight of the species. The dose of the reactive species interacting with a unit area of material surface can be calculated as the product of average flux and time: $D = \overline{\Gamma} \cdot t$. Since O_3 is the most abundant product in the SMD effluent and its density is one to two orders of magnitude higher than that of the RNS, we first evaluate the effect of O_3 on polymers.

Combining data from figure 6.4 (a) and 6.6 (b), we find that the thickness expansion speed during the bulk oxidation stage is proportional to the O_3 flux or density, as shown in figure 6.14. Since the thickness expansion rate indicates the reaction rate between plasma species and polymers, figure 6.14 suggests that O_3 might play a key role for the oxidation of the PS film bulk. In our previous reports we showed evidence that the thickness increase in the bulk oxidation stage is due to diffusion-reaction of the plasma species with the bulk of the polymer film which leads to the cleavage and oxidation of the aromatic rings.[95, 242] The O_3 molecules might be the dominant reactant for such diffusion-reaction process due to its moderate reactivity compared to atomic O and ground state O_2. The aromatic ring cleavage and oxidation by O_3 was observed previously,[253, 254] and it is known that O_3 can behave as an electrophilic reagent in its reaction with aromatic compounds.[253] An alternative reaction pathway might be through atomic O produced by the dissociation of O_3:

$$O_3 \rightarrow O_2 + O(^1D, ^3P) \qquad (6.2)$$

The O atoms are able to initiate polymer reactions by abstracting H from the tertiary carbon sites on PS structure. The activated carbon site after H-abstraction may lead to further reactions including ring cleavage and oxidation. The low rate constants of reactions involving O_3 at room temperature might help explain the low thickness expansion rate in

figure 6.14 and its linearity with O_3 flux.

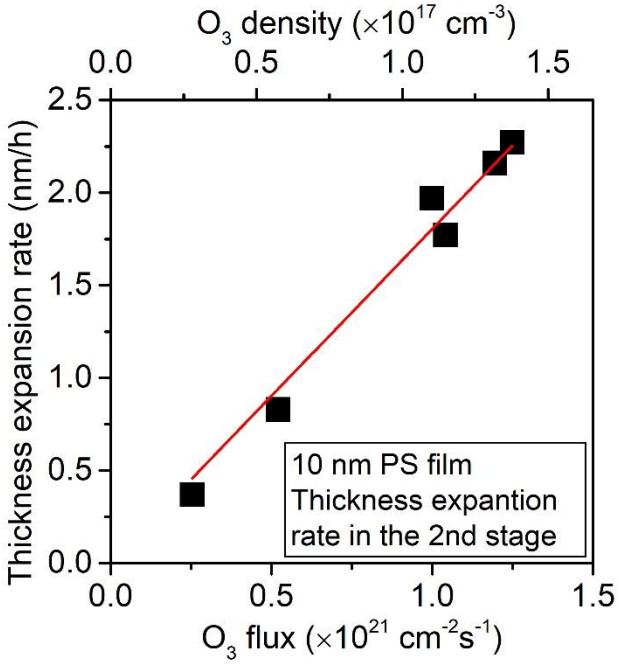

Figure 6.14 The correlation between the O_3 flux/density and the thickness expansion rate in the bulk expansion stage in figure 6.5.

Furthermore, we find that the surface O elemental composition of the SMD treated PS films, measured by XPS, increases rapidly with the dose of O_3 molecules and then saturates at a upper limit as shown in figure 6.15. The curve of O composition as a function of O_3 dose can be fitted with the exponential decay (increasing form) formula:

$$y = C_1 - C_2 \cdot \exp(-\frac{D}{C_3}) \tag{6.3}$$

where y and D stands for the surface O elemental composition and dose of O_3, respectively. The C_1, C_2, C_3 are constants. The exponential decay of the accumulation of surface O composition can be understood as the depletion of the polymeric reactants as treatment continues. At the beginning of the treatment, there are sufficient amount of

polymeric reactants at the surface, and thus the oxidation happens with a higher reaction rate. As the treatment continues, the polymeric reactants within the top 2 nm of the film (20° XPS probing depth) are gradually depleted which explains the decrease of surface oxidation speed with the O_3 dose. When the treatment reaches etching stage, the surface O composition saturates because more oxidation would eventually lead to the formation of volatile products such as CO_2 and H_2O.

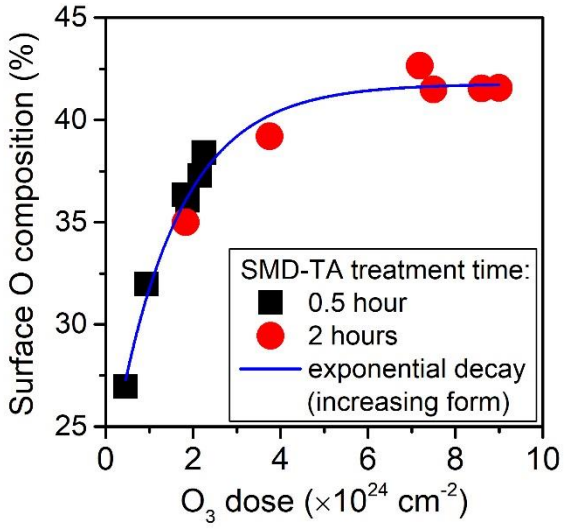

Figure 6.15 The correlation between surface O elemental composition and the dose O_3 applied on polymer surface.

Similarly, we can also correlate the chemical composition of PS films measured by ATR-FTIR with the dose of O_3. As shown in figure 6.16 (a), the relative amount of aromatic ring structure of treated PS films compared to the pristine PS film, estimated by the ratio of peak intensity at 702 cm^{-1} between the treated and the pristine film, were plotted as a function of the O_3 dose. We find that less amount of aromatic ring is left in the ~10 nm PS films when they are treated with higher dose of O_3. In figure 6.16 (b), we show the

amount of carbonyl groups accumulated on PS films after the plasma treatment, estimated by the areal peak intensity of shaded area I in figure 6.12, as a function of the O_3 dose. It can be seen that the amount of carbonyls increases with the increasing dose of O_3. Using the exponential decay formula shown in equation 6.3, we can fit the experimental data in both figures 6.16 (a) and (b) with the decreasing form and the increasing form, respectively. The fitted exponential decay constants (C_3) in figure 6.16 are comparable but smaller than that from figure 6.15. This indicates that (1) the destruction of aromatic ring and the formation of carbonyl groups might be related to the same reaction process, and (2) the reactions inside the ~10 nm PS films takes longer time to complete than that in the top 2 nm of PS film which might be a result of the slow diffusion process of O_3 into the polymer bulk. This also supports that the aromatic rings are cleaved and partially converted into carbonyl groups by reactions involving O_3.

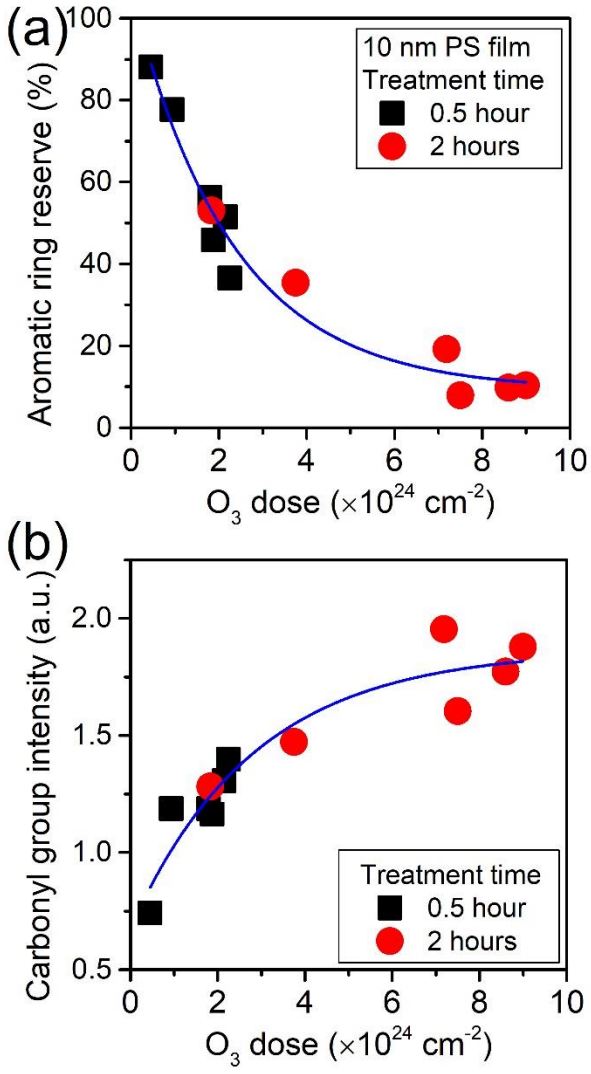

Figure 6.16 (a) The correlation between the dose of O_3 and the relative amount of aromatic ring left in the treated PS film. (b) The correlation between the dose of O_3 and the carbonyl group formed in the treated PS film.

6.4.2 The effect of RNS on PS

Since pristine PS does not contain N element, the formation of organic nitrate group confirmed by XPS in section 6.3.3 comes from the SMD treatment. However, we did not find evident linear or exponential decay relationships between the N elemental composition

of the treated PS films and the dose of RNS namely N_2O_5, HNO_3 and N_2O. For example, in figure 6.17 we plotted the surface N composition of the treated PS films against the dose of N_2O_5, but no direct dependence between the two can be correlated. We also did not find correlation between the surface N composition and the dose of O_3. We suspect that the formation of surface organic nitrate might be a result of the synergistic effect between reactive oxygen species (ROS) and RNS. Due to their low reactivity, the long-lived RNS generated by the SMD, i.e. N_2O_5, HNO_3 and N_2O, might not be reactive enough to cause surface nitritation directly. Instead, an alternative reaction pathway is that the ROS first react with the polymer surface which leads to the formation of surface radical sites. These surface radical sites are highly reactive and may further react with the RNS from the gas phase. Therefore the surface N composition might be determined by both the dose of ROS and RNS.

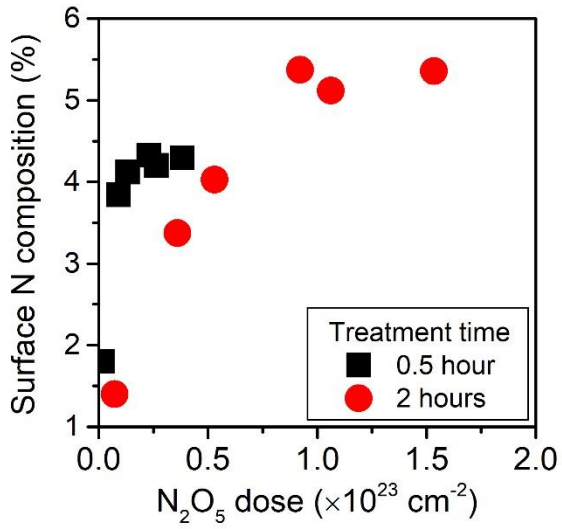

Figure 6.17 The correlation between surface N composition and the dose of N_2O_5.

6.5 Conclusion

In summary, we characterized the reactive species generated in the effluent of the SMD reactor using IR and UV absorption. With N_2 and O_2 mixture as working gas, the dominant reactive species are identified as O_3, N_2O_5, N_2O and HNO_3. We also quantified the density of these reactive species, and we found that it changes with the ratio between N_2 and O_2 in the feed gas. To study the effect of these long-lived reactive species on polymers, we exposed ultra-thin (~10 nm) PS films to the effluent of the SMD with various feed gas compositions. Under such treatment, we observed and quantified the PS film expansion, the oxidation and the nitritation of the polymer film. These treatment induced effects on the PS films varied with feed gas composition. By correlating the thickness expansion rate of the PS film with the flux of the plasma generated reactive species, we found a linear relationship between the expansion rate and the flux of O_3, which suggests that O_3 might be an essential reactant for causing the expansion of the PS film. When relating the quantified chemical composition of the treated PS films with the dose of the reactive species, we found that (1) the O elemental composition of the PS surface (~ 2 nm), (2) the aromatic ring content inside the ~ 10 nm film, and (3) the carbonyl groups inside the film all show the exponential decay, in either increasing or decreasing form, dependence to the dose of the O_3 delivered onto the PS films. This indicates that O_3 might participate in the chemical modification of the PS structure, such as cleaving the aromatic rings and oxidizing them into carbonyls both on surface and in the polymer bulk. At last, we also correlated the surface organic nitrate of the treated PS films with the dose of gas species, but no evident relationship between the surface nitrate concentration and the dose of individual species was discovered. This suggests that the formation of surface organic

nitrate might be a result of the synergistic interaction of ROS and RNS.

Acknowledgement

The authors gratefully acknowledge the financial support by the National Science Foundation (PHY-1415353) and the US Department of Energy (DE-SC0001939). We thank Dr. J. Santous Sousa for the help with SDO detection of the SMD. We thank A. J. Knoll, C. Li, A. Pranda, K. Lin, S. Zhang and M. Lai for helpful discussions and collaborations.

Chapter 7: Interaction of Long-lived Reactive Species Produced by Cold Atmospheric Pressure Plasma with Model Polymers. II. The Role of Macromolecular Structure and Substrate Temperature on Surface and Sub-Surface Modifications

P Luan[1] and G S Oehrlein[1]

[1] Department of Materials Science and Engineering and the Institute for Research in Electronics and Applied Physics, University of Maryland, College Park, Maryland 20742, USA

Draft manuscript, to be submitted

Abstract

In this work, we report (1) the structural dependence of polymer modification and (2) the modification of material sub-surface and bulk by long-lived reactive species generated in cold temperature atmospheric pressure plasma (APP). Six different types of vinyl polymers were used to study the molecular structure dependence of APP treatment. We find that styrene-based polymers show significant thickness expansion whereas polymers with methyl, alcohol and ether side groups show only thickness reduction at a very low etch rate. To understand the thickness expansion of styrene-based polymers, the chemical composition of treated polystyrene (PS) was characterized by X-ray photoelectron spectroscopy (XPS) and attenuated total reflectance (ATR)-FTIR. We find that the treated PS films show the destruction of aromatic rings and the formation of ether, ester and surface organic nitrate groups. The thickness expansion of PS may come from the oxidation of the tightly packed styrene rings to various oxygen containing bonds which occupies more volume. Using a serial sectioning technique by back-etching the PS films with low pressure Ar plasma, we analyzed both the surface and the subsurface chemistry of the treated PS films. We find that the chemical modification by long-lived neutrals happens not only on polymer surface but also in tens of nanometers depth in the polymer bulk. We attribute the oxidation of the polymer sub-surface/bulk regions to the reaction-diffusion of plasma species, especially O_3, which we further investigated using a one-component reaction-diffusion model. We also investigated the reaction mechanism of styrene-based polymers with long-lived species by comparing PS with its derivatives namely P4MS and PαMS. we find that the long-lived neutral species primarily attack the C-H bond on the carbon site where the aromatic ring connects.

7.1 Introduction

Cold temperature atmospheric pressure plasma (APP) is capable of generating many types of chemically reactive species, i.e. electrons, ions, photons and neutrals.[140] When interacting with polymers, these reactive species can induce many changes such as surface modification, etching, and other processes.[146] Depending on the type of the reactive species, the depth of plasma induced changes in polymers may vary from few nanometers[255] to tens of nanometers.[124] For ions, the penetration depth is usually very shallow[256] due to large energy deposition in the surface region of polymers and may lead to the formation of dense amorphous carbon (DAC) layer if the ion energy is on the order 100s of eV.[106] For UV photons, the radiation can penetrate much deeper into the material and the penetration depth relies on the UV absorption spectrum of the target material.[124, 257] When it comes to the reactive neutral species, the modified region is usually believed to be the outmost few atomic layers leaving the polymer subsurface and bulk unchanged.[258] Since the reactive neutrals are the most abundant reactants generated by the APP sources, they dominate the plasma induced effects on polymers. Therefore APP treatments are often considered to primarily affect the surface region of processed materials.

Recently we reported that the polymer subsurface and bulk regions can also be modified by plasma induced oxidation through remote O_2/N_2 APP treatments.[95] Using surface micro-discharge (SMD) and polystyrene (PS) as a model plasma-polymer system, we observed three polymer transformation stages during one continuous treatment, i.e. (1) surface oxidation and nitritation, (2) bulk oxidation and (3) surface etching. We also measured a chemical composition gradient within the top 8 nm of the polymer film after

the O_2/N_2 APP treatment. Although we attributed these phenomena, especially the bulk oxidation stage and the composition gradient, to the diffusion of reactive species into the polymer bulk, it is unclear how deep the plasma modified layer was and why some APP treatments showed only surface effects and some showed both surface and bulk effect. Another open question relates to the organic nitrates ($R\text{-}ONO_2$) observed in that work - whether $R\text{-}ONO_2$ can also be formed underneath the polymer surface.

Although little is known about subsurface modifications of polymers, evidence shows that long-lived neutrals may play a major role in such process.[95] Considering the processing condition of remote APP treatment which usually contains significant amount of O_2 in the system, UV photons are strongly absorbed by the ambient and their effect on materials is usually negligible.[6] The short-lived neutrals such as atomic O and OH radicals are highly reactive, and they can be quickly consumed by the polymer surface which leads to fast material removal.[1, 68] In contrast, the life time of long-lived neutral species (1) is sufficient to be transported over large distances, (2) may not be consumed right away when touching polymer surface, and (3) do not cause the formation of densely cross-linked surface layer. These features make them possible to diffuse into and react with the polymer subsurface and bulk. Such properties of the long-lived neutral treatments make them very appealing for applications including bacterial inactivation,[259] food processing,[260] skin and tissue treatments,[237] where plasma effects both on and under the surface is desired.

In the part I of this series,[261] we characterized and quantified the reactive species generated by a remote APP reactor using IR and UV absorption, and we found that the long-lived neutrals O_3, N_2O_5, N_2O and HNO_3 are the dominant reactants interacting with target surface. By correlating the changes of material properties with the abundance of gas

phase species, we identified the role of O_3 and other reactive oxygen-nitrogen species on the chemical modification of polymers. However, the chemical composition of materials underneath the surface and the mechanism of material bulk oxidation by these species was not discussed.

Besides, another interesting aspect of plasma-polymer interaction is the role of molecular structure. When interacting with the same plasma species, polymers with different functional groups may have different reaction rates and reaction products. For example, depending on the chemical structure, the mechanism of plasma induced polymer degradation may involve cross-linking, main-chain scission, and side-chain removal processes.[106] Polymers that had a hydrogen bonded opposite the side group on the carbon backbone (α-H) are prone to cross-linking while polymers with a methyl group bonded instead (α-methyl) are prone to main-chain scission reactions.[106] Knowing the effect of long-lived neutrals on certain chemical bonds and functional groups is essential for understanding the mechanisms of the sub-surface modification processes.

In this work, we further extend our study on the effect of long-lived reactive neutrals to examining their (1) chemical modification to the material subsurface and bulk as well as (2) reaction with different molecular structures. First, the type and density of long-lived reactive species generated by the same APP reactor, i.e. surface micro-discharge (SMD), will be confirmed by IR and UV absorption. We select six different types of vinyl polymers to investigate the effect of long-lived neutrals on specific functional groups including methyl, alcohol, ether and aromatic ring. We will also evaluate the change of polymer film thickness during treatment, and the surface/subsurface/bulk chemistry after treatment. The depth of the plasma modified layer underneath the polymer surface is

estimated, and we will compare the polymer bulk modification with a one-component reaction-diffusion model. Finally, we discuss the aromatic ring destruction mechanism based on the structural dependence and chemical analysis of the observed effects.

7.2 Experiments and methods

7.2.1 Description of materials

As shown in figure 7.1, six different types of vinyl polymers were selected to study the remote plasma interaction with polymers. We prepared polymer samples as thin films on substrate by spin-coating. Specifically, polypropylene (PP) films were deposited following the procedure by Große-Kreul [262] as ~100 nm films on Si wafer. Poly(methyl methacrylate) (PMMA, Sigma-Aldrich, $M_w \sim 15\,000$) was dissolved in propylene glycol methyl ether acetate (PGMEA, Sigma-Aldrich, ReagentPlus, ≥99.5%) to make 5 wt% solution, and PMMA films with ~ 200 nm-thickness were spin-coated on Si substrate with 2000 rpm ramped over 3 s. Similarly, polyvinyl alcohol (PVA, Sigma-Aldrich, $M_w = 89\,000$–$98\,000$) was dissolved in water at 90 °C to make 3wt % solution, and PVA films with ~ 200 nm-thickness were coated on Si substrate with 2000 rpm ramped over 30 s. For polystyrene (PS), films acquired from two different preparation approaches were used. First, when comparing PS with its derivatives, i.e. poly(4-methylstyrene) (P4MS) and poly(α-methylstyrene) (PαMS), we used the same materials as those described by Bruce *et al.*[106] and all three types of styrene-based polymers were synthesized with similar degree of polymerization (~200), spin-coated onto Si wafers, and then baked at 90°C for 1 minute to form ~400 nm films. In other situations involving PS, the films were prepared by spin-coating PS beads (Sigma-Aldrich, Mw ~ 35 000) dissolved in PGMEA solution, and films with various thicknesses (10 nm – 400 nm) can be obtained by tuning the concentration of

PS/PGMEA solution and the spin-coating speed. Besides the samples for enhanced ATR-FTIR characterization where Au coated Si wafer was used as an enhancing substrate,[245] Si wafer was always used as the substrate.

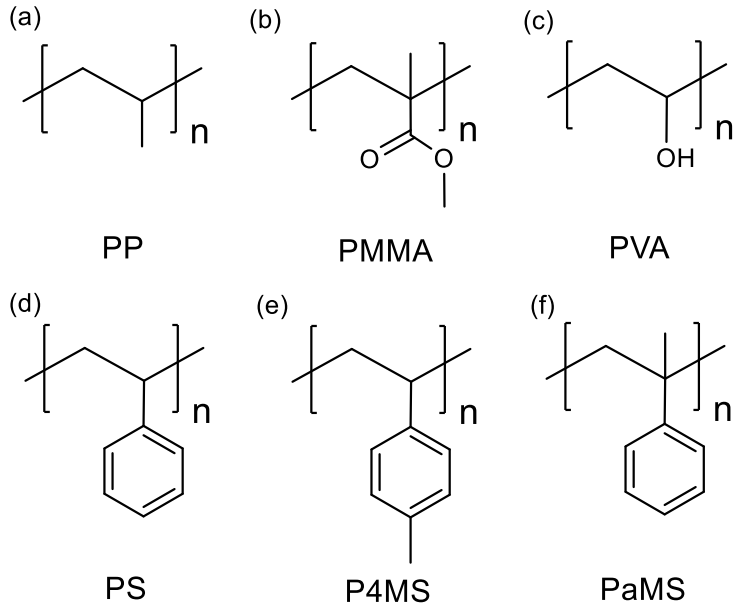

Figure 7.1 Chemical structure of the model polymers used in this work: (a) PP = polypropylene, (b) PMMA = poly(methyl methacrylate), (c) PVA = polyvinyl alcohol, (d) PS = polystyrene, (e) P4MS = poly(4-methyl styrene) and (f) PαMS = poly(α-methyl styrene)

7.2.2 Plasma processing of polymers

Remote plasma processing at atmospheric pressure

The APP source used in this work, called surface micro-discharge tube array (SMD-TA),[95, 245] is a variation of the planar configuration SMD[93, 140]. Detailed description of this reactor can be found in part I of this work[261] and other prior publication.[95] Briefly, as shown in figure 7.2 (a) the SMD-TA source is composed of many individual discharge

tubes, and each of these discharge tubes features a curved stainless steel (SS) woven mesh as the powered electrode. Cold temperature APP is generated near the SS mesh at atmospheric pressure. The SMD-TA reactor used in this work contains 7 discharge tubes with hexagonal packing arrangement for increasing the density of the reactive species near its nozzle. The reactor is powered by a sinusoidal power supply with 6 kV peak-to-peak (kVpp) voltage at 23 kHz. The calculated power consumption density [140], i.e. the power consumed by plasma per glow area, is less than 0.1 W/cm^2. Due to the similarity between SMD-TA and planar SMD,[261] we use the term SMD to stand for the SMD-TA reactor in the rest of this report.

To control the environment wherein the SMD interacts with the polymers, a sealed 50 L chamber was used and pumped to 20 mTorr before refilling to atmospheric pressure with 95% O_2 + 5% N_2 at 2 slm. The same gas and flow rate were also used during polymer treatments.

To improve the uniformity of APP treatment, the SMD reactor is mounted on a 1-dimensional motion stage for performing scan-processing.[68, 95] As shown in figure 7.2 (a), the SMD source moves back and forth above the polymer sample with a constant speed of 2.4 mm/s. The treatment time for each scan cycle is 38 seconds, and in the last 2 seconds of each scan cycle the optical information of the polymer film is characterized by ellipsometry. The treatment distance from the nozzle of the SMD reactor to the surface of the polymer films was maintained at 3 mm.

To study the remote plasma oxidation of polymers at elevated temperatures, a proportional–integral–derivative (PID) controlled heating stage was positioned underneath the samples, as indicated in figure 7.2 (a). Polymer samples were pre-heated to the desired

temperature (45, 60, 75, 90° °C) before plasma treatment. Sample heating by the SMD treatment was evaluated by monitoring the thermal expansion of 745 nm SiO_2 using ellipsometry, and no observable thickness was recorded during scan treatment which indicates less than 10 °C of temperature fluctuation.[95]

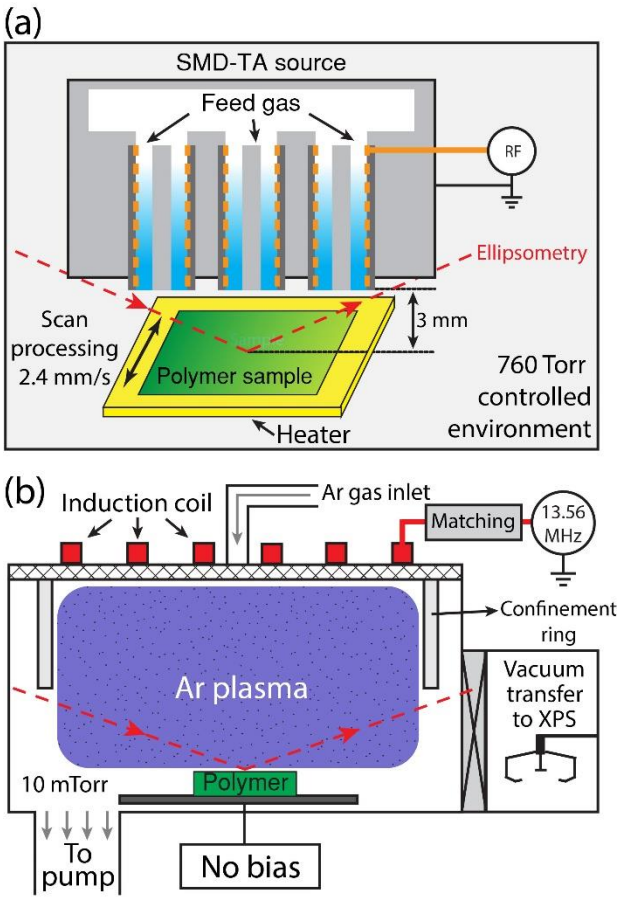

Figure 7.2 Schematic of plasma processing setups used in this work. (a) Remote plasma oxidation of polymers at atmospheric pressure by surface micro-discharge tube array (SMD-TA). (b) Back-etch of SMD-TA treated polymers by low pressure Ar inductive coupled plasma (ICP). No additional bias power was applied to the polymer sample. Back-etched polymer samples are vacuum transferred to XPS for surface characterization.

Inductively coupled plasma (ICP) processing at low pressure

The low pressure plasma processing system used for the back-etching of SMD treated polymers is a well characterized inductively coupled plasma (ICP) reactor.[5, 263] After SMD treatment at atmospheric pressure, polymer samples were air-transferred to the load lock of the ICP reactor which allows for sample loading without exposing the ICP chamber to atmosphere. In this way the base pressure of the ICP reactor can be maintained in the 5×10^{-4} mTorr range. As shown in figure 7.2(b), the ICP is powered by a water cooled planar coil located on top of a quartz window, and the plasma was confined within 195 mm diameter by an anodized Al ring. To feed constant 300 W power to the ICP, the source power supply was operated at 13.56 MHz, and a L-type matching network was also used for matching the impedance. With a constant Ar flow of 40 sccm, the ICP processing pressure was maintained at 10 mTorr. Polymer samples were located 150 mm below the ICP source and sit on a 125 mm diameter Si chuck with no external bias voltage applied. The ion energies were determined by the plasma potential which is about -20 V and the floating potential of the polymer surface.[106] During ICP processing, the temperature of the polymer samples was stabilized at 10 °C by a chiller. Standard chamber cleaning with oxygen plasma and conditioning with Ar plasma [263] were performed between experiments, which allows the starting condition of the chamber to be comparable for all polymer back-etching experiments. The optical properties of the polymer films was monitored by *in-situ* ellipsometry during ICP processing, and after that the polymer films were vacuum-transferred to an XPS system where the surface chemistry of the back-etched polymer films was studied.

7.2.3 Characterization techniques

IR and UV absorption

The IR spectrum of neutral reactive species generated by the SMD was recorded by a FTIR (Shimadzu IRTracer-100) with 1 cm^{-1} resolution. For characterizing reactive species at different density range, two measurement gas cells, i.e. single path 0.05 m cell and multiple-path 1.33 m cell, were used. The home-made 0.05 m gas detection cell has a volume of 125 mL and is equipped with two KBr windows. For characterizing reactive species with density value on the level of $1 \times 10^{15} molecules/cm^3$, a multiple-path gas detection cell (PIKE Technologies, 1-16 m) with 1.33 m path length and 3.5 L volume was used. The effluent from the SMD reactor was guided to the gas cell which was then flushed for 30 minutes with the plasma effluent before measurement. In order to enhance signal to noise ratio (S/N), a liquid nitrogen-cooled HgCdTe (MCT) detector was used along with the 1.33 m multiple-path cell. The density of ozone was measured by UV absorption at 254 nm with 1 cm path length. The home-made UV absorption system is composed of a Hg-Ar lamp as the UV light source, a 10 nm band pass filter centered at 254 nm (Edmund), a 34 mm^2 effective area deep UV photodiode (Edmund), and a high gain operational amplifier circuit (LMP7721, Texas Instruments).

Ellipsometry

Using ellipsometry, we monitored the optical property of the polymer films during both SMD treatment at atmospheric pressure and low pressure ICP back-etching experiments. The ellipsometers used in this work are SOFIE STE70 with He-Ne laser (λ = 632.8 nm) and automated rotating compensator in the polarizer-compensator-sample-analyzer (PCSA) configuration at ~72° angle of incidence.[1, 95] Upon the reflection of polarized laser beam on polymer samples, the ellipsometers record the change in phase

difference (Δ) and the angle (Ψ) whose tangent is the ratio of the magnitudes of the total reflection coefficient [192]. Optical models described previously[95] were used for interpreting the Ψ and Δ data as polymer thickness and refractive index values. For ICP back-etching experiments, the ellipsometer sampling rate was 5 Hz; whereas for the APP treatment with SMD, Ψ- Δ values were recorded at the last 2 seconds of each scan cycle with 5 Hz sampling rate.

XPS

The XPS system used in this work is a Vacuum Generators ESCALAB MK II with Al/Mg twin anode. The non-monochromatic Al K_α radiation (hv = 1486.6 eV) was used for exiting photoelectrons. High-resolution C 1s, N 1s, O 1s, Si 2p and survey spectra were collected at electron take-off angles of 20° and 90° which corresponds to the probing depth of ~2 nm and ~8 nm, respectively.[246] The plasma treated polymer samples were transferred to the analysis chamber (1×10^{-9} mbar) of XPS within 20 min after treatment. Either vacuum- or air-transfer was used and details about the transfer technique can be found in the results section.

Methods for XPS peak fitting and elemental composition analysis have been described previously. [1, 68, 95] Briefly, C 1s peaks corresponding to C-C/H (285 eV), C-O (286.5 eV), O-C-O/C=O (287.9 eV), O-C=O (289.1 eV), O-CO-O (290.2 eV) and pi–pi* shake-up (291.5 eV) were fitted. For N 1s, due to the absence of other nitrogen peaks we only fitted organic nitrate (-ONO_2) at 408.2 eV.[193, 194] For O 1s, two peaks at 532.7 eV and 533.9 eV were fitted to represent oxygen moieties with binding energy from 532.2 eV to 533.1 eV and from 533.6 eV to 535.3 eV, respectively.[1] The full width at half maximum (FWHM) of the fitted peaks was restricted in the range of 1.4 – 1.6 eV, 1.5 – 1.9 eV and 1.6 – 2.0 eV for C 1s, N 1s and O 1s peaks, respectively. We calibrated all spectra to the

C-C/H peak at 285 eV. For quantifying the elemental composition, Scofield cross section values [264] of C 1s, N 1s and O 1s spectra, i.e. 1, 2.85 and 1.77 respectively, were used as the Relative Sensitivity Factors (RSF) for scaling the measured peak areas. The CasaXPS software was used for both peak fitting and quantitative analysis.

ATR-FTIR

The enhanced ATR-FTIR spectra [245] of SMD treated polymers were measured using Shimadzu IRTracer-100 equipped with a variable angle single reflection ATR accessory (VeeMaxIII, PIKE Technologies). Single reflection Ge crystal was used as the internal reflection element (IRE), and the light incident angle was fixed at 60°. The IR light was p-polarized by a ZnSe polarizer at the incident side of the ATR accessory. A liquid nitrogen-cooled MCT detector was used to improve S/N. We used a pressure clamp with constant torque to control the contact between the sample and the Ge crystal. The entire optical path was constantly purged with pure N_2, and the ATR-FTIR spectra were acquired in the range of 4000 cm^{-1} - 600 cm^{-1} with 4 cm^{-1} resolution and 20 scan averages. The referencing backgrounds were obtained with no sample coupled to the Ge crystal. Multiple-point baseline correction was consistently applied to all acquired ATR-FTIR spectrum. The polymer samples were characterized within 10 min of the SMD treatment.

7.3 Results

7.3.1 Long-live neutral reactive species generated by SMD

FTIR was used to measure the vibrational spectroscopy of SMD effluent. Based on the IR peak position, peak shape and peak strength, we are able to identify a number of reactive gas phase species. We also quantified these reactive species using Beer's law which describes that the Absorbance (A) shown in IR spectrum is proportional to the

optical path length (l), the cross section of the species (σ), and the density of the reactive species ([n]):[265]

$$A = \log_{10} e \cdot l \cdot \sigma \cdot [n] \quad (7.1)$$

To reduce the larger instrument error introduced by the FTIR measurement when A value is over 0.9 or less than 0.01, two optical path lengths, i.e. 0.05 m and 1.33 m, were chosen for measuring reactive species with density in the range of sub-percentage and parts-per-million (ppm) level, respectively. In our previous work, we evaluated the reactive species generated in various N_2/O_2 mixtures.[261] Here we focus on one working gas chemistry: 95% O_2 + 5% N_2.

In figure 7.3 (a) we show the IR spectrum of SMD effluent measured with 0.05 m gas detection cell. As shown in the inset, the IR light transmits through the detection cell at a distance about 3 mm away from the nozzle of the SMD reactor. In the IR spectrum we observed 2 major peaks around 2122 cm^{-1} and 1054 cm^{-1} which can be assigned to O_3,[191] and a small peak around 1720 cm^{-1} that can be attributed to N_2O_5.[247] To further confirm the generation of O_3, we also performed the real-time UV absorption of the SMD effluent (data not shown here). With the cross section of $\sigma_{O_3} = 1.15 \times 10^{-17} cm^2$ at 254 nm,[94] we calculated the O_3 density at 3 mm away from the nozzle as $1.36 \pm 0.03 \times 10^{17} cm^{-3}$.

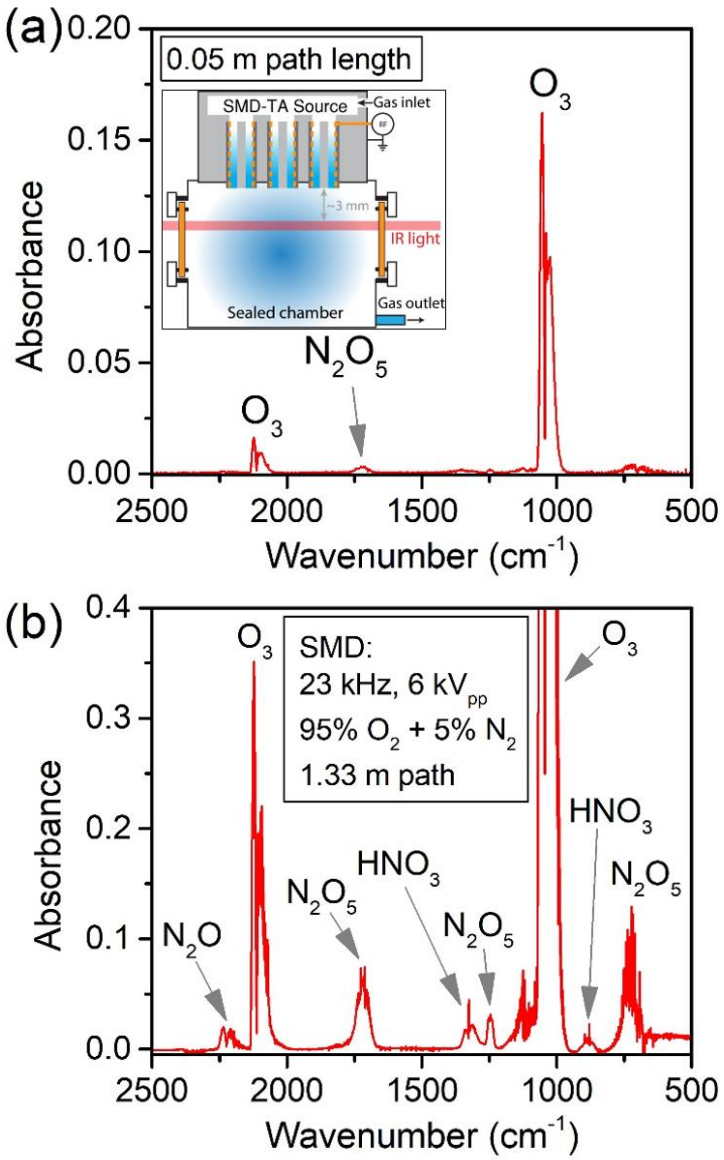

Figure 7.3 SMD generated long-lived neutral species measured by FTIR with (a) 0.05 m and (b) 1.33 m optical path length. Two different optical path lengths were used for detecting reactive species in different density range.

To better characterize the IR spectrum of low density (~ppm) plasma species, we increased the optical path length to 1.33 m. As shown in figure 7.3 (b), vibrational modes that belong to N_2O_5, HNO_3 and N_2O are observed whereas the O_3 absorption peak near

1054 cm^{-1} reaches saturation. Using equation 7.1 and cross section values reported previously, the density of these reactive species can be estimated as $5.53 \pm 1.39 \times 10^{14} cm^{-3}$, $3.55 \pm 0.42 \times 10^{14} cm^{-3}$ and $1.33 \pm 0.09 \times 10^{14} cm^{-3}$ for N_2O_5,[247] HNO_3,[248] and N_2O,[249, 250] respectively. Interestingly, we did not observe any IR peaks that can be assigned to nitric oxide (NO) in the region of 600 – 4000 cm^{-1} even with further increased optical path length of 16 m. This suggests that the density of NO in the SMD effluent is less than $1x10^{-13}$ cm^{-3}.

Besides the long-lived reactive neutrals shown in figure 7.3, modeling results by Sakiyama, et al.[191] suggest that the SMD reactor is also able to generate short-lived neutral species such as N, O, OH, NO, $O_2(a^1\Delta_g)$ and HO_2 in the discharge layer around the metal mesh. However, in the SMD configuration, minimal amount of short-lived reactive neutrals can be transported to the far effluent due to their short lifetime (< 1 ms) and the slow gas velocity. With 2 slm of feed gas, our fluid model indicates that the average gas velocity at the nozzle of the discharge tubes is ~ 0.21 m/s, which suggests that it takes more than 14 ms for the plasma species to be transported from the nozzle of the discharge tube to the sample surface located at 3 mm away. Therefore the majority of the gas phase reactants near the material surfaces are long-lived neutrals, e.g. O_3, N_2O_5, HNO_3 and N_2O, as detected by the FTIR.

7.3.2 Polymer film thickness response

Room temperature behavior

To understand the effect of these long-lived neutrals on polymers, we treated 6 different polymer materials and monitored how their optical properties changed using Ellipsometry. The thickness and refractive index information of treated polymer films was

obtained by fitting the ellipsometric data with a single-layer polymer model described previously.[95] As will be discussed later, the SMD treated polymer films show a composition gradient along their normal direction which discourages the use of single-layer model. However, due to the small change of polymer refractive index (less than 0.09), the single-layer ellipsometry model provides an averaged film thickness value that is accurate enough to show the polymer thickness response as a function of treatment time.

First, we compared the response of aliphatic carbon, ester, aromatic ring and alcohol groups under SMD treatment by evaluating the thickness change of PP, PMMA, PS and PVA, respectively. As shown in figure 7.4 (a), all four types of polymers were treated using the same plasma condition for 0.4 hour. Since we only collect ellipsometric data at the last 2 s of a 38 s scan-treatment cycle, the gaps between small groups of data points in figure 7.4 (a) indicates the thickness change between scan cycles. The thickness change of less than 2 nm after 0.4 hour of treatment time indicates that the SMD has minimal effect on the thickness of PP, PMMA and PVA. However, in the case of PS we find that the film thickness has increased by 17.62 nm after 0.4 hour of treatment. The difference between PS and other polymers suggests that aromatic ring might behave very differently during reaction with the long-lived neutrals generated by SMD.

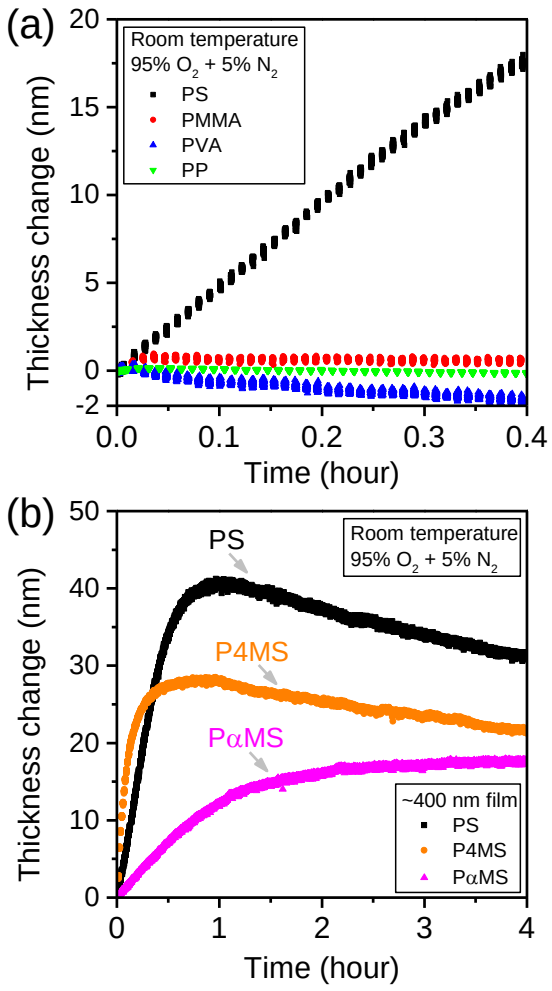

Figure 7.4 Thickness change of polymers when exposed to reactive species generated by SMD at room temperature (21 °C): (a) PS vs. PMMA, PVA and PP. (b) PS vs. P4MS and PαMS. The starting thicknesses of the polymer films are (a) PS 188.3 nm, PMMA 219.8 nm, PVA 209.5, PP 108.8 nm; and (b) PS 416.1 nm, P4MS 400.3 nm, PαMS 403.9 nm, respectively.

In our previous publication,[95] we investigated the behavior of PS thickness and refractive index change in detail and we found that the interaction of PS with SMD can be separated into 3 distinct stages: (1) < 0.5 nm thickness increase caused by surface oxidation

and nitritation; (2) ~10% thickness increase resulted from polymer bulk oxidation and (3) thickness reduction by etching. Since similar treatment conditions were also used for the polymer treatments in this work, we assume that the thickness increase of PS observed in figure 7.4 (a) is also due to the surface and bulk oxidation.

To further explore this film expansion behavior of PS, we treated and compared two derivatives of PS, namely P4MS and PαMS, and all three types of polymer films were prepared with similar thickness ~ 400 nm. As shown in figure 7.4 (b), we extended the treatment time to 4 hours, and we observed significant thickness increase for all three styrene-based polymers. Interestingly, the PS showed the most thickness increase (40.5 nm, 9.7 % of original film thickness) with P4MS (27.9 nm, 7.0 %) and PαMS (17.6 nm, 4.4 %) following behind. The time needed for reaching the maximum thickness is also different for each styrene-based polymer, which indicates that the reactivity of styrene-based polymers with long-lived neutrals is polymer structure dependent. After 1 hour of treatment, both PS and P4MS showed a thickness reduction with an etch rate of 3.29 nm/hr and 2.05 nm/hr, whereas PαMS still had not yet reached the peak thickness after 4 hours of treatment. The small etch rate and long treatment time needed for reaching maximum thickness reflects the low reactivity of long-lived neutrals with polymers at room temperature.

Elevated temperature behavior

Since elevating the substrate temperature can increase the reaction rate of plasma interaction with materials,[1] we performed polymer treatments with SMD at 70 °C. As shown in figure 7.5 (a), at elevated substrate temperature we also observed the initial thickness increase stage of PS within the first 2 min of treatment. Subsequently the SMD started to slowly etch PS as seen from PMMA and PVA films. Using linear fitting of the

curves in figure 7.5 (a), we estimated the averaged etch rate of PS, PMMA and PVA to be about 1.21 nm/min, 0.89 nm/min and 1.06 nm/min, respectively. Similarly, we also compared the effect of SMD on the ~400 nm PS, P4MS and PαMS at 70 °C. As shown in figure 7.5 (b), we observed the initial thickness increase and the subsequent thickness reduction for all three styrene-based polymers. The relative relationship among PS, P4MS and PαMS at 70 °C, such as the maximum film thickness and the time needed for reaching maximum thickness, is the same as that at room temperature. Although we did not see the etching of PαMS at room temperature after 4 hours of treatment, it was observed at 70 °C after only 0.1 hour of treatment.

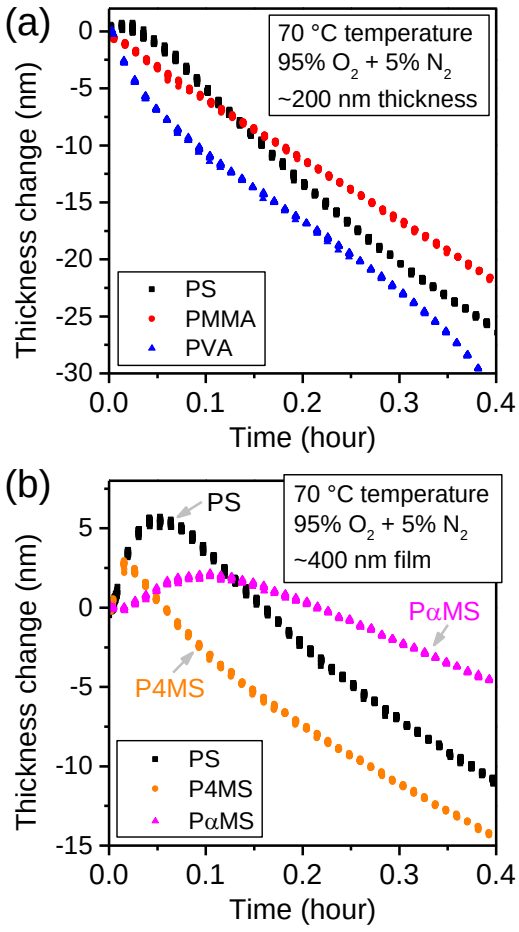

Figure 7.5 Thickness change of model polymers under the exposure of reactive

species generated by SMD at 70 °C: (a) PS vs. PMMA and PVA. (b) PS vs. P4MS and PαMS. The original thickness of polymer films in (a) is: PS 200.8 nm, PMMA 190.2 nm, PVA 190.0; and that in (b) is: PS 413.7 nm, P4MS 405.7 nm, PαMS 394.0 nm. It can be seen that all model polymers experiences etching after 10 minutes of treatment. The same trend of thickness change for each model polymer studied in figure 7.4 was also observed.

Thickness expansion ratio

The results shown in figures 7.4 and 7.5 indicate that the oxidation of aromatic ring structure in the polymer bulk may lead to the thickness increase. To further investigate the film thickness expansion ratio and the chemical composition of the treated films, we choose PS as the primary model polymer.

When treating PS films with different starting thicknesses, we found that the maximum net thickness gain is roughly proportional to the starting thickness. As shown in figure 7.6, PS films with starting thickness ranging from 12.0 nm to 416.2 nm were treated with the same plasma condition at room temperature, and we found that the expansion rate of PS films – maximum net thickness gain divided by the starting thickness of the pristine film –is in the range of 7.8 % - 12 .3 %. Besides, the treatment time required for reaching the maximum film thickness also becomes longer for thicker PS films. This dependence of starting film thickness indicates that the thickness increase might come from the bulk expansion of the polymer film instead of material deposition on the polymer surface.

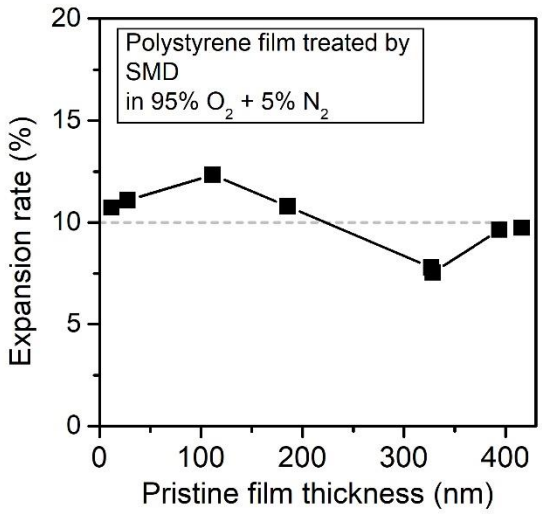

Figure 7.6 Maximal film thickness expansion rate as a function of pristine PS thickness. It can be seen that the max expansion ratio is around 10% regardless of film's starting thickness.

7.3.3 Polymer surface and sub-surface chemistry

Angle resolved XPS

To understand the chemical composition of materials on and near the surface (sub-surface), we performed angle resolved XPS analysis on the plasma treated PS films. As shown in figure 7.7, we collected the C 1s, O 1s and N 1s spectra of both pristine and 10 minutes treated PS films. Two electron take-off angles, i.e. 20° and 90° which corresponds to the probing depth of ~2 nm and ~8 nm, were applied for the depth profiling of the chemical composition of PS films. As shown in figure 7.7, both 20° and 90° spectra of pristine PS film show only C 1s peaks, and 94% of the C 1s electrons belongs to the C-C/H bond whereas the rest comes from π-π* shake-up. Furthermore, the difference between 20° and 90° XPS-scans is minimal which suggests that the chemical composition of the pristine

PS film is uniform in the top ~8 nanometers.

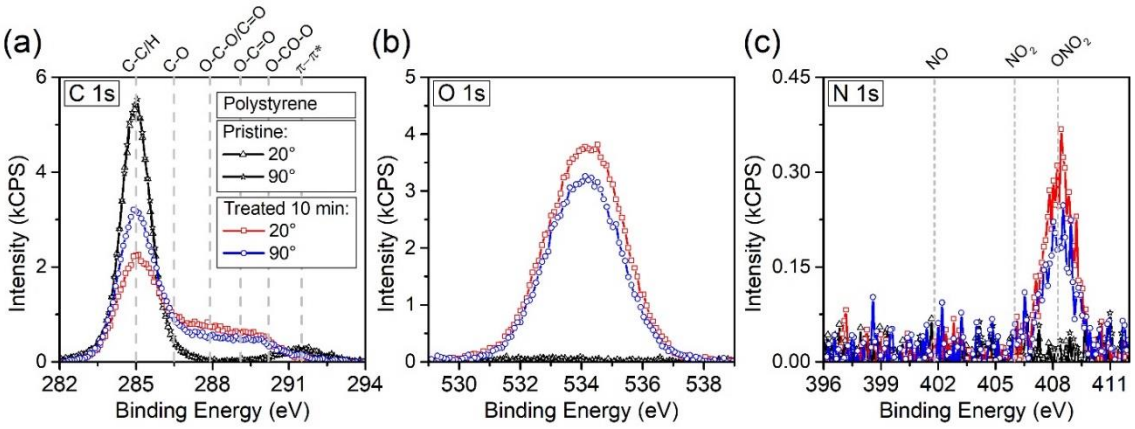

Figure 7.7 High resolution (a) C 1s (b) O 1s and (c) N 1s XPS of PS taken with electron take-off angle of 20° and 90° which corresponds to the surface chemistry information from the top ~2 nm and ~8 nm of the polymer film, respectively. The spectra of pristine and 10 min treated PS films are shown. For pristine PS, there is no observable difference between 20° and 90° scans, whereas for 10 minutes treated PS film the difference between 20° and 90° scan indicates a composition gradient in the PS sub-surface.

After 10 min of treatment by SMD, we observed the reduction of C-C/H bond and π-π* shake-up peak. In the meanwhile, we also saw the formation of various oxygen containing functional groups in figure 7.7 (a), such as C-O, O-C-O, C=O, O-C=O and O-CO-O, which indicates the oxidation of aromatic rings and possibly the main chain. In figure 7.7 (b), such oxidation of PS film is further confirmed by the formation of new O 1s peaks. Compared to the pristine PS where negligible amount of O was seen, the O elemental composition of the 10 min treated PS film is 35.1% and 28.4% for 20° and 90° scans, respectively. In the N 1s spectra, small amount of organic nitrate (~ 3 % of the total

elemental composition) was found after treatment. Interestingly, we observed a clear difference between the 20° and 90° scans for the 10 min treated PS film, and the 20° spectrum shows more oxygen and organic nitrate than 90° spectrum. This suggests that the degree of polymer oxidation and nitritation by plasma treatment reduces with depth. One possible cause of such a composition gradient might be the reaction-diffusion of plasma species from the polymer surface into the polymer bulk. We will further discuss this in section 7.4.3.

ATR-FTIR

Despite the detailed surface and sub-surface chemistry information that XPS provides, it suffers from a few issues: e.g. insensitivity to hydrogen containing bonds,[266] and weak π-π* shake-up peak intensity that are not proportional to the concentration of aromatic rings.[267] To compensate the drawbacks of XPS, we further characterized the PS films using enhanced ATR-FTIR spectroscopy. Since this technique measures the averaged chemical composition of the polymer slab that the IR light penetrates,[251] ultrathin (~10 nm) polymer films were used for studying the effect of SMD on polymer surface and sub-surface.

As labeled in figure 7.8, the spectrum of the pristine PS film showed characteristic vibrational modes typically seen in the transmission IR spectrum of PS. Specifically, we observed C-H stretch from aromatic ring (peak H, 3100 - 3000 cm^{-1}) and aliphatic chain (peak G, 3000 – 2800 cm^{-1}), aromatic ring modes (peak F at 1602 cm^{-1}, peak E at 1492 cm^{-1}, peak D at 1452 cm^{-1}), in-plane C-H bend (peak C at 1029 cm^{-1}), out-of-plane C-H bend (peak B at 760cm^{-1}), and ring out-of-plane deformation (peak A at 700 cm^{-1}). The two broad peaks in the range of 1750 – 1550 cm^{-1} and 970 – 790 cm^{-1} can be assigned to carbonyl and ether groups respectively. This indicates that the surface of the pristine PS

film is either oxidized or contaminated by a hydrocarbon adsorption layer under atmospheric condition.

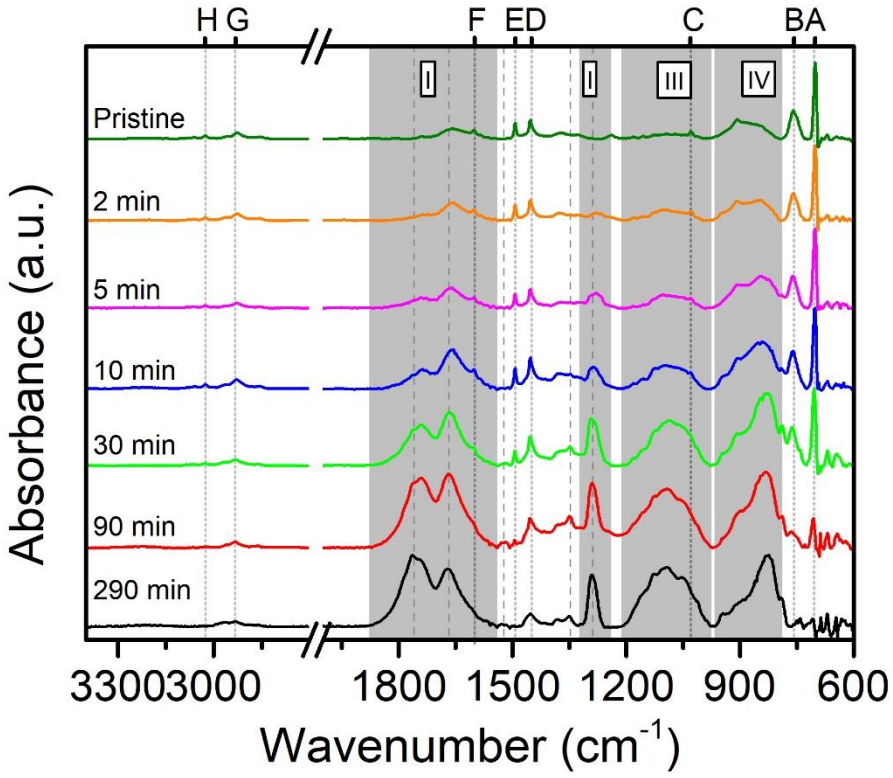

Figure 7.8 Enhanced ATR-FTIR spectrum obtained with 10 nm PS film coated on Au surface. To illustrate plasma-induced effects on polymers, pristine, 2 - 290 min plasma-treated films are shown for comparison. All spectra are normalized to their individual highest peak. Labels A through H notates the IR active vibration modes from polystyrene. A: aromatic C-C bend; B: out-of-plane C-H bend; C: in-plan C-H bend; D, E and F: aromatic ring modes; G: aliphatic C-H stretch; H: aromatic C-H stretch.

The ATR-FITR spectra of the plasma treated PS films, in contrast, showed four new IR bands that are marked as the shaded area I through IV in figure 7.8. These new IR bands can be assigned to the formation of chemical bonds that do not exist in pristine PS.

Specifically, area I may be attributed to carbonyls (C=O) (stretching mode 1600 cm^{-1} - 1800 cm^{-1}) and organic nitrates (asymmetric NO_2 stretch, 1615 cm^{-1} - 1660 cm^{-1});[195, 199] area II might be due to organic nitrates (symmetric NO_2 stretch, 1290 cm^{-1}) [252] or possibly aryl ether and aryl ketone; area III and IV are mainly from the C-O stretch of ether and ester groups with the possibility of having NO symmetric stretch (near 860 cm^{-1}) from organic nitrates.[252] The bandwidth of these new IR bands are wide, which indicates that the plasma modified polymer films are not chemically homogeneous.

We can further assign the general carbonyl stretch band in area I as ketone and ester with the following reason. Since we did not observe IR bands from the aldehydic C-H stretch (2850 - 2700 cm^{-1}) and aldehydic C-H bend (near 1390 ± 10 cm^{-1}), we can rule out the formation of aldehydes after treatment. Because there is no OH stretch peak (3500 – 2500 cm^{-1}) in the IR spectra, we can eliminate the possibility of having alcohol (-OH) and carboxyl (-COOH) in treated films. We can also exclude the presence of anhydride (-OC-O-CO-) in the treated films due to the absence of symmetric C=O stretching peak around 1820 cm^{-1}.

Besides the new IR bands, we also observed the loss of IR peaks that belong to aromatic rings, (A through F and H in figure 7.8) especially for the 290 minutes treated PS film where the ring-related peaks have completely disappeared. Combined with the XPS results in figure 7.7, polymer surface characterization shows that remote plasma treatment is able to destroy aromatic rings and convert them into various oxygen containing moieties such as ether, ester, ketone and organic nitrate.

7.3.4 Polymer bulk chemistry: back-etching with ICP reactor

Thus far, indirect evidences have shown that the thickness increase of styrene-based

polymers might be due to the bulk expansion caused by the oxidation of styrene rings. A more straightforward proof for such hypothesis is characterizing a series of polymer sections from the top to the bottom of the film. Here we performed the serial sectioning of SMD treated PS films by removing materials (back-etching) with low pressure Ar ICP with no biasing. The back-etch rate and the chemical composition of back-etched surfaces were measured by ellipsometry and XPS, respectively.

First, the back-etch rate of PS films can reflect the level of oxidation after SMD treatment. According to Ohnishi et al., under Ar ion beam bombardment the etch rate of polymers has strong correlation to their oxygen composition.[104] By investigating the back-etch rate as a function of back-etching depth, we can estimate the level of plasma oxidation in polymer sub-surfaces. As shown in figure 7.2 (b), since no bias power was applied to the PS films, the Ar ICP etches polymers mainly by low energy ions accelerated through plasma sheath and UV photons generated by Ar metastables. Due to the low ion energy and the resistance of styrene-based polymer to UV light, a low etching rate is seen for such conditions. In figure 7.9, we measured the etch rate of pristine PS as 2.47 nm/min. Such weak etching condition of Ar ICP could reduce the post-processing-induced artifacts typically caused by high energy ion bombardments,[255] such as the formation of densified carbon layer and surface roughness. These artifacts could also significant alter the original chemical property of the PS films which will be a subject for the surface chemistry analysis.

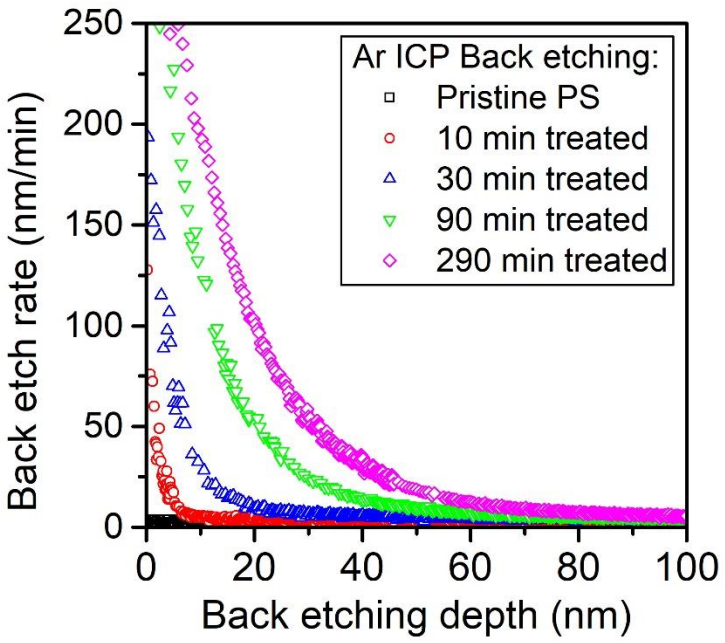

Figure 7.9 The etch rate of SMD treated PS films under the exposure of Ar ICP plasma as a function of back-etching depth.

For the back-etching of SMD treated PS films, we observed significant changes in the back-etch rate as a function of the back-etching depth and the SMD treatment time. As shown in figure 7.9, the back-etch rate of each back-etching curve drops dramatically as more material is removed from the surface. This indicates that the O composition of the SMD treated polymer films decreases with the depth away from the surface. Furthermore, at the same back-etching depth, PS films with longer SMD treatment time show higher back-etch rate which suggests that longer SMD treatment can lead to more and deeper oxidation to the PS films. Since the oxidized PS film will always have higher back-etch rate than the pristine film, we can define the modification depth of plasma treated polymers as the back-etching depth where the back-etch rate drops to the similar level (<5 nm/min)

of the pristine sample. For example, from the data in figure 7.9 we can estimate that the modification depth of the 10 minutes treated 200 nm PS film is about 8 nm, whereas that of 30 min, 90 min and 290 min treated PS films is about 30 nm, 60 nm and 96 nm, respectively. More discussion about the back-etching of PS films can be found in section 7.4.3.

To characterize the change of chemical composition over depth into the polymer film, we measured the XPS data of 90 min treated PS films with various back-etching depths from 3.5 nm to 42 nm.[197] In order to avoid contamination from the exposure of ambient air, the back-etched samples were vacuum-transferred to the XPS within 15 minutes after treatment. As shown in figure 7.10, we compared the spectrum of 3.5 nm-back-etched film with that of the non-back-etched film, and we found that the back-etched surface had no organic nitrate, more C-C/H bonds, and less amount of oxygen containing moieties especially ester (O-C=O) and ketone (C=O) groups. These results correlate well with the angle resolved XPS data shown in figure 7.7, and together they confirm that the materials under polymer surface (~2 - 4 nm) is less oxidized. Since the organic nitrate group is completely removed after 3.5 nm of back-etching, we conclude that the organic nitrate is only present at the material surface. This is further supported by the peak shift in the O 1s spectrum in figure 7.10 (b) – the back-etched film showed less amount of core electrons with higher binding energy at 534 eV and 534.7 eV which can be correlated to the oxygen from the $-ONO_2$ group.

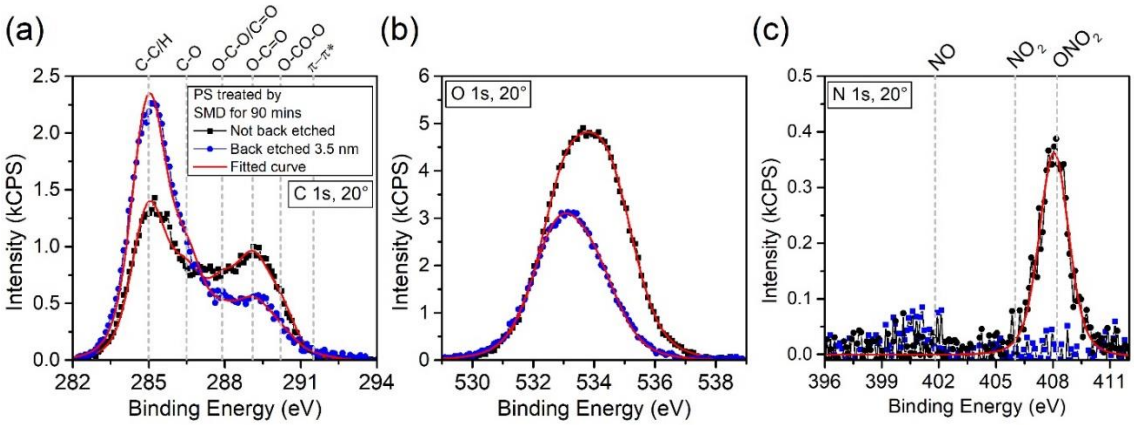

Figure 7.10 High resolution (a) C 1s (b) O 1s and (c) N 1s XPS of 90 minutes SMD treated PS taken with electron take-off angle of 20°. The spectra of both 3.5 nm back-etched and non-back-etched PS were shown for comparison. It can be seen that after 3.5 nm of back-etching, the organic nitrate peak at 408.2 eV has disappeared.

Since the XPS of all back-etched PS surfaces show similar high resolution spectra as those shown in figure 7.10, though the relative composition of each functional group varies, we quantified these spectra into elemental compositions (percentage of each element) and C 1s decomposition (percentage of each chemical bond in the C 1s spectrum) for the ease of comparison. In figure 7.11 we plot the C and O elemental composition of the back-etched PS surfaces as a function of back-etching depth. The XPS data with 90° electron take-off angle are selected because they represent the SMD treated polymer better than that with 20° electron take-off angle which might have been influenced by Ar ICP treatment. We find that the SMD treated PS films become less oxidized at deeper sectioning depth. For example, the O elemental composition of the SMD treated PS surface before back-etching is 43.9%. It quickly drops to 26.9% after 10.3 nm of back-etching and then to 17.3% after 42.0 nm of material removal. Correspondingly, the C elemental composition

rises quickly with deeper back-etching depth.

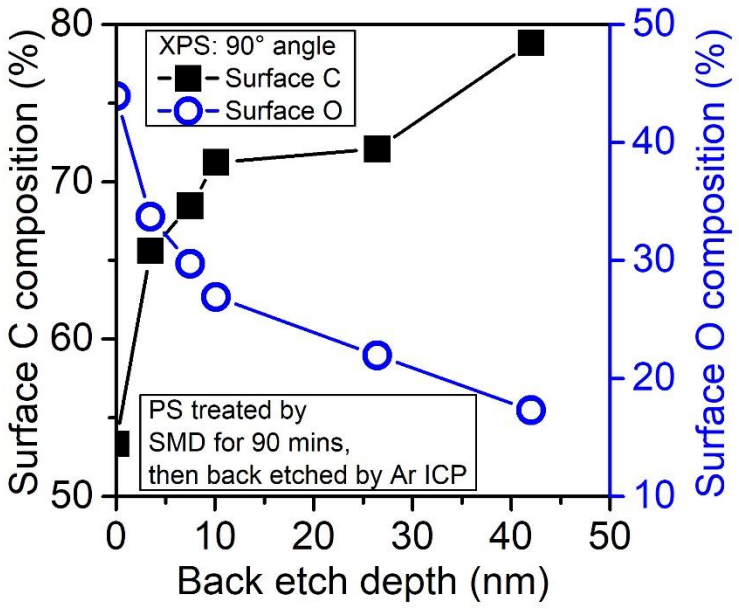

Figure 7.11 The surface C and O composition of back-etched PS as a function of back-etch depth. The PS films were treated by SMD for 90 min before back-etching. The XPS electron take-off angle is 90°. The surface C composition increases in the deeper section of the SMD treated PS film, whereas the O composition decreases. This indicates a gradient profile of plasma oxidation in the polymer film. PS is oxidized even at > 40 nm underneath the surface.

In figure 7.12 we show the C 1s decomposition of back-etched PS films as a function of back-etching depth. Each line in figure 7.12 represents one type of function group in the high resolution C 1s spectra. In figure 7.12 (a), we find that both C-C/H and π- π^* shake up peaks increase with back-etching depth, which indicates that materials are less oxidized and there are more aromatic ring structures in the deeper section of the SMD

treated PS film. Correspondingly, in figure 7.12 (b) we find that materials in the deeper section of the film have less oxygen containing moieties especially ester (O-C=O) which dropped from 25.0% at surface to 4.23% at 42 nm-deep into the film.

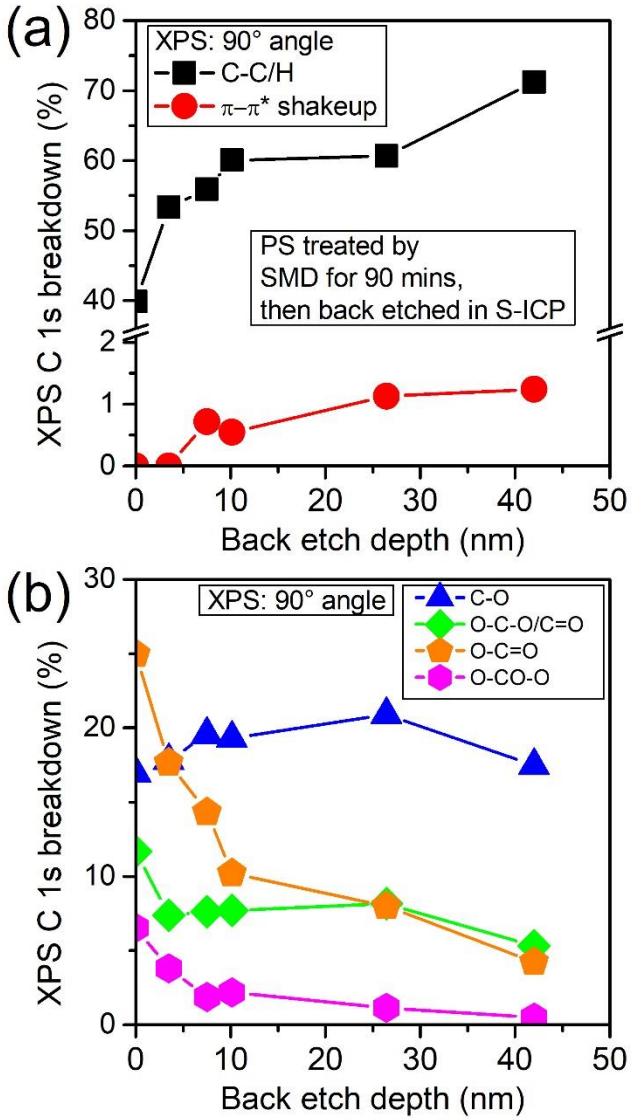

Figure 7.12 The XPS C 1s breakdown of back-etched PS as a function of back-etch depth: (a) C-C/H, π- π* shakeup peaks, and (b) C-O, O-C-O/C=O, O-C=O, O-CO-O. The electron take-off angle is 90°. It can be seen that the percentage of C-C/H and π- π* shakeup peaks increases with back-etch depth whereas the various oxygen containing moieties in

(b) decrease.

7.4 Discussions

7.4.1 Material structural dependence, mechanism of remote oxidation

Role of aromatic ring in thickness expansion

As shown in figure 7.4 and 7.5, we only observed significant thickness expansion from styrene-based polymers, i.e. PS, P4MS and PαMS. Their counterparts with other types of functional groups, e.g. methyl, alcohol and ether, only showed etching. This leads us to suspect that it is the reaction of aromatic rings with long-lived reactive neutrals that are responsible for the polymer thickness expansion.

The expanded film thickness might come from the newly formed oxygen containing bonds which occupy more volume than the tightly packed styrene rings. From the XPS and ATR-FTIR characterization of the SMD treated PS films in figure 7.7 and 7.8, we know that the aromatic ring structure of PS is consumed and possibly converted into ether, ketone and ester groups. Combined with the slow chain scission reactions due to the weak reactivity of the long-lived neutrals, a net thickness increase might occur when large amount of aromatic rings in the bulk of the polymer is oxidized. We also found additional support from the change of refractive index (n) during SMD treatment: the n values drops continuously during treatment especially in the bulk expansion stage. As discussed in our previous work,[95] the presence of ether and ester group can dramatically reduce the polymer refractive index due to its large volume occupied by oxygen in this binding structure.

Mechanism of aromatic ring cleavage

There are two more questions that we would like to discuss: (1) how are the

aromatic rings cleaved and converted into ether and ester groups by SMD treatment and (2) why does the thickness expansion of styrene-based polymers show structural dependence in figures 7.4 (b) and 7.5 (b)? It is well known that the aromatic ring is chemically stable, and when the aromatic ring is connected to a secondary or tertiary carbon, the oxidation reaction prefers to happen on the secondary and tertiary carbon site instead of the aromatic ring. Direct oxidation of aromatic ring is more likely to happen when then ring structure is linked to a quaternary carbon.

When comparing the thickness change of PS, P4MS and PαMS under SMD treatment, we find that the speed of thickness expansion follows the relation P4MS>PS>PαMS whereas the maximum expansion ratio follows the relation PS>P4MS>PαMS, as shown in figure 7.4 (b) and 7.5 (b). In the case of PαMS, the aromatic ring is connected to a quaternary carbon, therefore the ring structure is more prone to be directly cleaved[254] by the electrophilic ROS. However due to the stability of aromatic rings, the ring cleavage reaction is slow – hence the slowest thickness expansion speed of PαMS observed in figure 7.4 and 7.5. For PS, the aromatic ring is linked to a tertiary carbon site where the oxidative reactions with reactive species, such as H-abstraction by atomic O, is preferred to occur. The radicals formed on these tertiary carbon sites have a free electron that might be able to increase the reactivity of aromatic rings by electron-releasing inductive effect. When it comes to P4MS, since the aromatic ring is connected to the para-substituted secondary and tertiary carbon sites, radicals can be created on both the 4-methyl group and the tertiary carbon site which might further increase its reactivity.

Based on the characterization results shown in this report, we still cannot explain why PS showed higher maximum expansion ratio than P4MS and PαMS. Many causes

could lead to this phenomenon. However here we want to mention the competition between surface etching and bulk expansion: with the same amount of bulk expansion, polymer film can show less thickness increase if more material is removed from the surface. In the case of PαMS, since the ring reaction is slow, the polymer main chain might have been cleaved greatly when the film thickness reaches maximum. For P4MS, since the cleavage reaction is faster than PS and PαMS, less amount of ROS might have been diffused into the polymer bulk when the etching dominates the apparent thickness behavior, which might be the cause of smaller amount of total thickness expansion.

7.4.2 Temperature dependence of etching reactions

Besides the thickness expansion of the polymer bulk, SMD treatment could also cause polymer etching as shown in figures 7.4 and 7.5. Although the etch rate is only a few nanometer per hour at room temperature, we measured higher etch rate up to ~1 nm/min at 70 °C. Such the increase of etch rate at elevated temperature has been generically observed for plasma etching of polymers in both low pressure and atmospheric pressure,[116-118] and the temperature dependence of the etching reaction rate constant k_{ER} can be expressed as:[1, 48]

$$k_{ER} = A_{ER} \cdot exp\left(\frac{-E_a}{k_b T}\right) \tag{7.2}$$

where A_{ER} is the pre-exponential factor, k_b is the Boltzmann constant and T is the substrate temperature. The apparent activation energy E_a is an empirically fitted parameter that represents the energy required for the etching reaction to take place. It is a measure of how sensitive the etching reaction is to substrate temperature. For a given plasma/polymer system, the E_a value can be significantly influenced by the nature of the etching reaction.[116] For example, polymer etching by atomic O generated in low pressure plasma

has an E_a value about 0.5 eV,[116] and polymer etching by Ar/O_2 atmospheric pressure plasma jet (APPJ) has an E_a value around 0.1 eV.[1]

In figure 7.13 (a), we evaluated the etching of PMMA by the SMD reactor at various temperatures from 45 °C to 90 °C. It can be seen that at all temperatures the polymer thickness drops linearly with treatment time, and the etch rate of PMMA increased from 2.23 nm/hour at 45 °C to 99.0 nm/hour at 90 °C. Since etch rate reflects the etching reaction rate, we can obtain the E_a value by fitting the semi-log plot of the etch rate against $1/k_bT$. As shown in figure 7.13 (b), using the least-squares method, the E_a of PMMA etching by SMD can be estimated from the absolute slope of the curve as 0.84 eV.

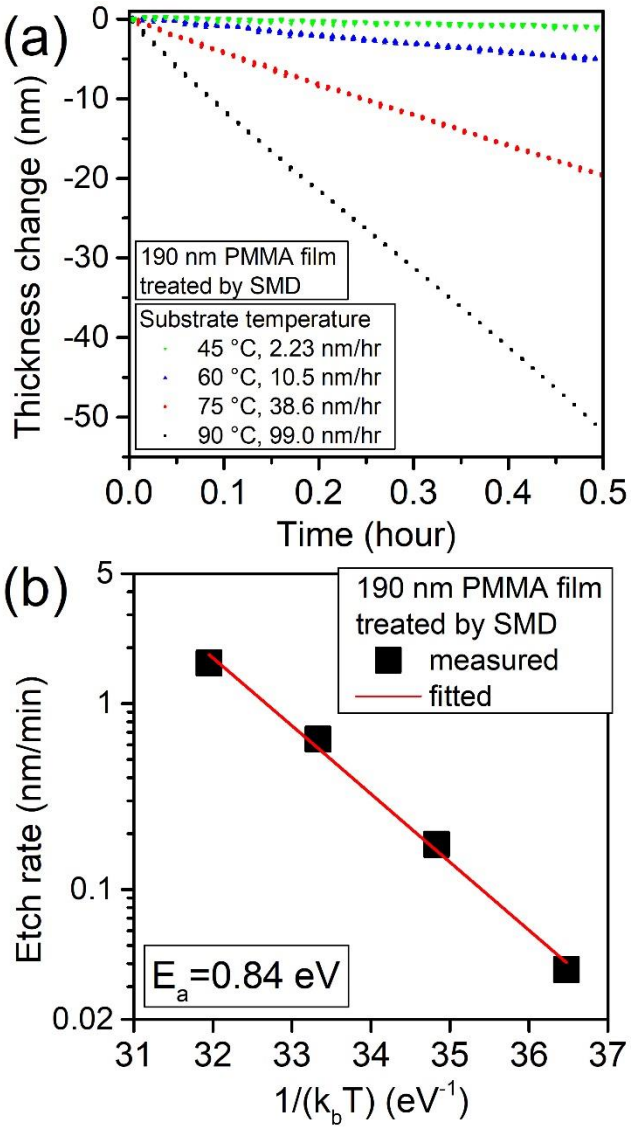

Figure 7.13 (a) The thickness change of PMMA under SMD treatment at different temperatures. (b) The substrate temperature effect on the etch rate of PS treated by SMD. Semi-log plot of etch rate vs. reciprocal of substrate temperature ($1/k_bT$) was shown to illustrate the Arrhenius form of the etching reaction rate. The apparent activation energy E_a calculated from the linear fit of Ln(etch rate) to $1/k_bT$ is 0.84 eV.

Since E_a can be considered of as the energy required for etching reactions, the relatively higher E_a value of the SMD etching of PMMA indicates that the etchant from

SMD is less reactive. From the gas phase measurement in section 7.3.1, we know that the dominant ROS at polymer surface are long-lived neutrals such as O_3, N_2O_5 and HNO_3. However, these species alone generally do not lead to the etching of vinyl polymers. One possible reaction pathway of polymer etching is through an intermediate step of converting long-lived neutrals into the strongly oxidative short-lived species on site. These short-lived neutrals could initiate the first reaction step required for polymer etching: H-abstraction.[117] For example, the thermal- and photo-lysis of O_3 and the balance of N_2O_5 with NO_2 and NO_3:[268]

$$O_3 \xrightarrow{heat,hv} O_2 + O(^1D,^3P) \tag{7.3}$$

$$N_2O_5 \leftrightarrow NO_2 + NO_3 \tag{7.4}$$

The Atomic O, NO_2 and NO_3 are all able to cause the H-abstraction on carbon sites which leaves a radical carbon that may further result in chain cleavage and eventually etching.[4]

7.4.3 Diffusion model of plasma species into the polymer bulk:

The profiles of the back-etch rate and chemical composition with back-etching depth shown in figures 7.9, 7.11, 7.12 may be resulted from the diffusion of plasma generated reactive species into the polymer bulk. Comparing the mobility of gas phase reactive oxygen species (ROS) and that of the condensed phase polymers, we can model the interaction between ROS and polymers as a one-component reaction-diffusion system.[269] For the normal direction (z) from the polymer surface to the bulk, the concentration of ROS ([n]) satisfies the following relation:

$$\frac{\partial[n]}{\partial t} = D_n \cdot \frac{\partial^2[n]}{\partial z^2} + R([n]) \tag{7.5}$$

where D_n is the apparent diffusion coefficient of ROS, R([n]) represents the reaction

term that consumes ROS which is expressed as a function of [n].

When the reaction term R([n]) dominates equation 7.5, the diffusion term vanishes which corresponds to the situation that either (1) ROS quickly react with polymers before reaching to the deeper section of the polymer film or (2) it is difficult for the ROS to move through the materials due to the small D_n. In any of these situations, diffusion of reactive species into the polymer bulk can be ignored and the kinetics becomes reaction-controlled. For instance, during polymer ashing the reactive neutrals are consumed mostly at the material surface. Another example is the formation of highly cross-linked surface layer during high energy ion bombardment which blocks the transportation of neutrals.

When the ROS are only weakly reactive and the reaction term R([n]) vanishes, equation 7.5 becomes Fick's second law and it represents diffusion-controlled kinetic process. From the result of ROS measurement in section 7.3.1 and the slow reaction speed between ROS and polymers shown in section 7.3.2, pure diffusion model can be used to fit the back-etch rate curves shown in figure 7.9. Considering the SMD treatment configuration shown in figure 7.2 (a), the following boundary condition can be assumed: when t=0, [n]=0; and when t>0, the concentration of ROS at polymer surface (z=0) is a constant: $[n] = [n]_0$.

If the apparent diffusion coefficient of ROS D_n is small enough to satisfy $2\sqrt{Dt} \ll$ d, the diffusion process is similar to the doping of a semi-infinite slab with fixed surface concentration $[n]_0$.[269] Here $2\sqrt{Dt}$ is the diffusion length and d represents the thickness of the polymer film which is ~200 nm for those in figure 7.9. In this condition, the solution of equation 7.5 can be written as:

$$[n] = [\mathrm{n}]_0 \cdot [\,1 - \mathrm{erf}(\frac{\mathrm{z}}{2\sqrt{D_n t}})] \tag{7.6}$$

If the apparent diffusion coefficient of ROS D_n is large enough to satisfy $2\sqrt{Dt} \gg$ d, "thin film" solution of equation 7.5 can be obtained:[269]

$$[n] = \frac{\mathrm{C}}{\sqrt{\pi D_n t}} \exp\left(\frac{-\mathrm{z}^2}{4D_n t}\right) \tag{7.7}$$

where C is a constant.

If we further assume that the back-etch rate difference (ΔER) between the treated film and the pristine film is proportional to the concentration of ROS [n] diffused into the polymer bulk, the analytical solution of Fick's second law shown in equations 7.6 and 7.7 can be used to fit the back-etch curve in figure 7.9. Because we can easily estimate the plasma modification depth (section 7.3.4) which is smaller than the thickness of the polymer film (d~200 nm), the diffusion length of ROS can also be evaluated as smaller than d. Therefore, the semi-infinite slab diffusion model of equation 7.6 should be used for fitting instead of equation 7.7. In figure 7.14 we showed the fitted curve of back-etch rate along with the experimental data. From the fitting results we find that the diffusion length ($2\sqrt{D_n t}$) of 10 min, 30 min, 90 min and 290 min treated PS film is 3.6 nm, 8.5 nm, 19.7 nm and 31.4 nm, respectively. Thus the apparent diffusion coefficient of ROS generated by SMD can be estimated as $D_n = 1.19 \pm 0.42 \times 10^{-16} cm^2/s$. Compared with the diffusion coefficient of O_2 in PS at 25 °C, which is about $4.3 \pm 0.4 \times 10^{-7} cm^2/s$, the D_n of ROS is very small. This might be due to the large size and small concentration of the ROS species that penetrate into the material, along with competing reaction processes leading to the loss of ROS as a function of depth.

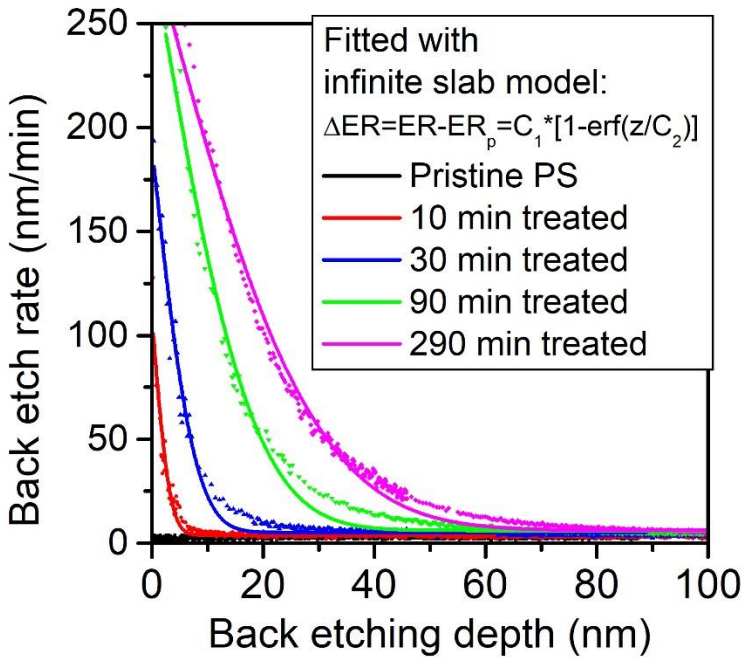

Figure 7.14 The fitted curve of back-etch rate shown in figure 7.9. The semi-infinite slab diffusion model was used. The fitting parameter C_2 represents the diffusion length whereas ER_p is the back-etch rate of the pristine film.

7.5 Conclusion

To summarize, we studied the interaction between long-lived reactive neutrals generated by APP source and six different types of vinyl polymers, i.e. PS, P4MS, PαMS, PMMA, PVA and PP.

First, structural dependence of polymer modification by these long-lived reactive species was observed: for methyl, alcohol, ether based polymers (PP, PVA, PMMA), we found material removal caused by prolonged treatment; whereas for styrene-based polymers (PS, P4MS PαMS), we saw that the film thickness increased to a maximum then decreased. To understand the complex thickness variation of styrene-based polymers

during long-lived neutral treatments, we chose PS as a model and performed a series of material characterizations. We found that the net thickness gain of PS at the saturation of expansion was proportional to the starting thickness of the pristine PS film. The XPS and ATR-FTIR characterization of the treated PS films showed the destruction of aromatic rings and the formation of ether, ester and surface organic nitrate groups. The thickness expansion of the styrene-based polymers may come from the oxidation of the tightly packed styrene rings to various oxygen containing bonds which occupies more volume. We also investigated the reaction mechanism of styrene-based polymers with long-lived species by comparing PS with its derivatives namely P4MS and PαMS. We find that the reactive species generated by SMD primarily attack the C-H bond on the carbon site where the aromatic rings connect. The radical site formed after H-abstraction might facilitate the cleavage of the aromatic rings.

We also performed the back-etching of PS films treated by long-lived reactive neutrals to examine their effect on the polymer subsurface and bulk. Compared to pristine PS films, the top 10 nm – 40 nm of the treated PS films (depending on treatment time) is greatly oxidized after long-lived reactive neutral treatment. We also find proof that organic nitrates only form on the top few nm of the polymer surface. Since the treated polymer films do not have (1) an ion induced high density cross-linked surface layer and (2) fast consumption of reactive species by rapid surface etching, the oxidation of polymer films may be resulted from the reaction-diffusion of plasma species into the polymer bulk which can be modeled by a one-component reaction-diffusion system.

At last, we also evaluated the apparent activation energy of SMD etching reactions with PMMA which we estimated as 0.84 eV.

Acknowledgement

The authors gratefully acknowledge the financial support by the National Science Foundation (PHY-1415353) and the US Department of Energy (DE-SC0001939). We thank C. Corbella for preparing polypropylene samples, and B. K. Long and C. G. Willson for providing PS, P4MS and PαMS samples. We thank A. Pranda, K. Lin, A. J. Knoll and C. Li for collaborations and helpful discussions.

Chapter 8: Sterilization of Raw Produce by Surface Micro-discharge (SMD) and the Evaluation of its Damage to Cellular Components by ATR-FTIR

P Luan[1], L J Bastarrachea[2,3], A R Gilbert[2], R Tikekar[2], and G S Oehrlein[1]

[1] Department of Materials Science and Engineering and the Institute for Research in Electronics and Applied Physics, University of Maryland, College Park, Maryland 20742, USA

[2] Department of Nutrition and Food Science, University of Maryland, College Park, Maryland 20742, USA

[3] Department of Nutrition, Dietetics and Food Sciences, Utah State University, Logan, Utah 84322, USA

Draft manuscript, to be submitted

Abstract

We evaluate the use of surface micro-discharge (SMD), a cold atmospheric plasma (CAP) reactor operated with room air or N_2/O_2 mixtures as working gas, as a cost-effective sterilization tool for raw produce contaminated by bacteria. After 1 min of SMD treatment, over 2 logarithmic reduction of *Escherichia coli* O157:H7 was consistently observed with both *E. coli* O157:H7 inoculated agar plates and spinach leaves. The optical microscopy and scanning electron microscopy (SEM) of treated *E. coli* O157:H7 show that SMD treatments can damage the bacterial cell membrane and lead to cell expansion which are responsible for cell lysis. To provide evidence for the plasma induced oxidation of the cellular components after SMD treatment, Attenuated Total Reflectance Fourier Transform Infrared Spectroscopy (ATR-FTIR) was used to characterize both the *E. coli* O157:H7 cells and the cell membrane component lipopolysaccharides (LPS). The ATR-FTIR spectra of plasma treated *E. coli* O157:H7 and LPS show that SMD treatment causes (1) the oxidation of cellular components by forming carboxylic acid (COOH) and carboxylate (COO^-) groups inside the bacteria and/or on the bacterial cell wall, and (2) the modification of polysaccharides and phosphor containing groups typically found in phospholipids and DNA. To further study the effect of SMD on cell membrane, we performed X-Ray Photoelectron Spectroscopy (XPS) analysis of LPS and the results suggest that SMD treatment in air mainly modifies the O-chain and core-polysaccharide part of LPS. Because the SMD reactor can be scaled up and integrated into existing production lines, its potential application for large-scale raw food processing in centralized facilities may be possible.

8.1 Introduction

In recent years, the increasing popularity of healthy diet drives a great demand for fresh and minimally processed food products. Because these fresh food products are often consumed raw, the percentage of foodborne disease outbreaks related to fresh foods has increased dramatically from 0.70% in the decade of 1970 to 33% in 2012.[259, 270, 271] For most vegetables, Gram-negative bacteria are the dominant human pathogens,[272] whereas yeasts and molds account for the majority of the microflora on fruits.[273] The source of these microbial contaminants can be from pre-harvest (e.g. agronomic practices, geographical area) or/and post-harvest operations (e.g. during processing, handling, packaging and transportation).[270] In order to fulfill the need of safe and high quality fresh foods, a number of non-thermal sterilization techniques, such as high pressure processing (HPP), ultraviolet (UV), pulsed light (PL), ultrasound, irradiation, anti-microbial packaging, ozone, and cold atmospheric plasma (CAP) have been developed to replace the traditional methods of washing with aqueous sanitizers (e.g. chlorine and chlorine dioxide).[270]

Among the novel sterilization techniques mentioned above, CAP processing shows great potential due to its high efficiency, cost-effectiveness and environmental friendliness.[168] Due to its non-thermal property, CAP is composed of a cornucopia of reactive species such as electrons, ions, UV photons and reactive neutrals. The latter include O, OH, singlet O_2, O_3, N_2O_5, HNO_2, HNO_3, etc. which are capable of inactivating the microbial contaminants on food surfaces and whose relative importance will depend on the nature of the CAP source and conditions used. The effectiveness of CAP for the anti-microbial decontamination of fresh produce has been demonstrated in a great number of

publications with many plasma reactor configurations [146, 235] and has been reviewed in several publications.[168, 259, 260, 274-278] Despite these exciting progresses, two major challenges remain to be addressed for CAP sterilization: (1) an appropriate reactor configuration that can be scaled up and integrated in the existing food processing lines[260] or used directly by the end consumers in remote locations, and (2) an understanding of the mechanism of bacterial inactivation by CAP treatment,[259] as discussed below.

Among the CAP reactors used for food sterilization, the dielectric barrier discharge (DBD) [74] and the plasma jet[279] are the most commonly studied.[146, 235] For these reactors, food products are usually placed in between the electrodes and sometimes serve as part of the electrical circuit which limits the size and shape of the foods. The cross section of the active plasma zone is usually small which leads to low processing throughput. This is especially the case for plasma jets for which large-scale processing is difficult unless an array of jets is used. In addition, plasma jets frequently operate with noble gases which can be costly and undesirable for applications.

Largely due to the complexity of both CAP and microbiological systems, the mechanisms underlying the bacterial inactivation by CAP are still elusive. The commonly accepted mechanisms of bacterial inactivation include DNA damage, lipid peroxidation, protein modulation, oxidative stress induced apoptosis and electrostatic disruption.[259] In many of the studies mentioning inactivation mechanism, the reactive species generated by the CAP reactor are poorly characterized, the interaction between the CAP source and the bacteria may not be well controlled, and the proposed effect of plasma on bacterial cell components are often measured indirectly. In addition, CAP reactors with different configurations or operating parameters can produce substantially different type and amount

of reactive species which leads to inconsistent bacterial inactivation mechanisms. Therefore, it is necessary to discuss mechanisms based on specific reactors.

In this work, we evaluate the surface micro-discharge (SMD),[93, 94, 139] a variation of DBD reactor, as an alternative solution for microbial inactivation in fresh produce. Compared to the DBD, the food targets of SMD are placed outside of the discharge zone which gives more flexibility to the target geometry and makes it easy for reactor integration without affecting the existing production line. Compared to the plasma jets, SMD has a larger effective surface area and can be easily scaled-up.[235] In addition, SMD reactors can be operated with ambient air which is cost-effective and attractive for applications in remote locations.

Our previous works on the characterization of the SMD reactor [191, 280] and its interaction with polymers/biomolecules [93, 94] show that SMD is capable of generating long-lived neutral reactive species,[261] such as O_3, N_2O_5, N_2O and HNO_3, which could (1) strongly oxidize the material surface and eventually lead to material removal (etching) and (2) permeate into the material bulk and cause the oxidation of the bulk.[95],[242] It is believed that all surface oxidation, etching and bulk oxidation could result in bacterial inactivation[259] - these behaviors of SMD treatment along with its non-thermal characteristic make it an viable option for disinfecting raw foods. Besides, as will be discussed in this paper, our previous characterization results could also facilitate the understanding of bacterial inactivation mechanism of SMD.

To evaluate the bacterial inactivation efficacy of the SMD reactor, two types of bacteria contaminated substances, i.e. growth agar media and spinach leaf stacks, are treated. Besides ambient air, the effectiveness of SMD treatment with varying N_2/O_2

mixtures as working gas was also studied. To understand the plasma induced oxidation of bacterial cell by SMD treatment, the Attenuated Total Reflectance Fourier Transform Infrared Spectroscopy (ATR-FTIR) spectra of bacteria and cell membrane component lipopolysaccharide (LPS) are measured. Additionally, the effect of plasma species on the chemical integrity of the bacterial cell membrane was studied by X-ray photoelectron spectroscopy (XPS) analyses of SMD treated LPS.

8.2 Experiments and methods

8.2.1 Plasma source configuration

The SMD reactor has a sandwich structure with both the powered electrode (50 × 50 mm^2 copper plate) and the ground electrode (stainless steel metal mesh) in contact with the single dielectric continuum (fused quartz plate),[235] as shown in figure 8.1 (a). The reactor was powered by 40 kHz, 6 kV_{pp} sinusoidal wave. The plasma power consumption density measured by the Lissajous figure method is ~ 0.3 W/cm^2.[140] As indicated in figure 8.1 (c), during operation many individual micro-discharges can be generated within a thin layer on the dielectric surface and around the metal wires of the ground electrode. More information about the SMD reactor can be found in our previous publications.[140]

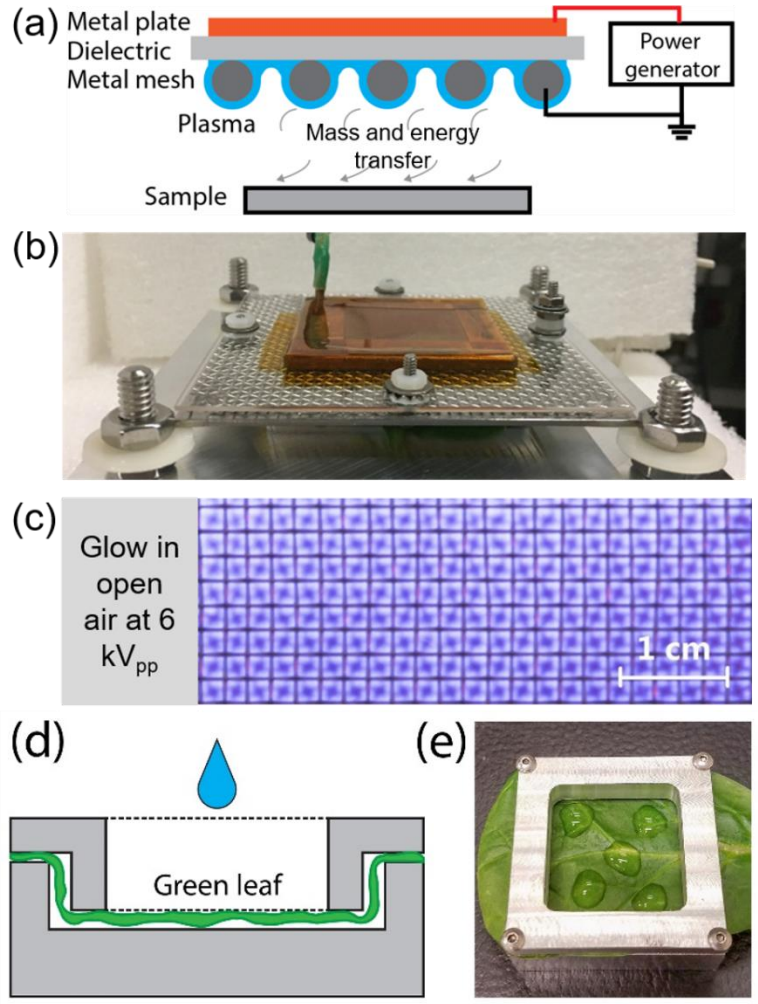

Figure 8.1 (a) Schematic diagram of the SMD reactor and its operating principle. (b) The optical image of the SMD processing setup – targets are usually positioned underneath the SMD reactor. (c) The optical image of the glow discharge generated by SMD source operated in air environment. The (d) schematic and (e) optical image of a homemade inoculation cell used for inoculating one side of the spinach leaf.

8.2.2 Materials: spinach leaves and LPS

Organically grown spinach (*Spinacia oleracea*) was purchased from a local retailer and used without further processing. Lipopolysaccharide (LPS) extracted from *Escherichia*

coli (*E. coli*) J5 (Rc mutant) was purchased from Sigma-Aldrich and selected as a model biomolecule to study the effect of SMD on bacterial cell membrane. The thin films of LPS on Si substrate were fabricated by spin-coating 150 µl of 500 µg/mL 9:1 methanol:water solution onto silicon substrates [158]. The thickness of the film can be tuned by the spin-coating speed and ramping time. For ATR-FTIR analysis the LPS films had a thickness of ~ 13 nm whereas for XPS analysis the thickness of the LPS films was ~ 100 nm.

8.2.3 Bacterial strains and culture conditions

Attenuated biosafety level 1 (BSL-1) *Escherichia coli* O157:H7 (ATCC 700728, Manassas, VA) was used to inoculate sterile Si substrates, agar plates and baby spinach leaves. Stock cultures of the microorganism kept at -80 °C in 20% glycerol were thawed, and a loopful of the stock culture was streaked onto a Tryptic Soy Agar (TSA, Difco, Becton Dickinson, Sparks, MD) plate which was then incubated at 37 °C for 24 h. Subsequently, an individual colony from the TSA plate was inoculated into 9 mL of Tryptic Soy Broth (TSB, Difco, Becton Dickinson, Sparks, MD) which was incubated overnight at 37 °C. This overnight broth was used to inoculate by streaking onto new TSA plates which were then incubated at 37 °C for 24 h and kept under refrigeration for up to 3 weeks. For plasma processing experiments, the TSA plates with *E. coli* O157:H7 were transferred into 9 mL of new and sterile TSB, and then incubated overnight at 37 °C. This overnight broth would be used to prepare the aqueous bacterial suspensions used in the different evaluations described in the following sections.

8.2.4 Inoculation of bacteria

For evaluating the efficacy of SMD on *E. coli* O157:H7, three types of supporting substrates, i.e. Si wafer, agar plates, and baby spinach leaves, were used in this work. The

preparation of each type of substrate is described in the following paragraphs.

For the inoculation of *E. coli* O157:H7 on Si substrates, 9 mL TSB with ~ 10^9 CFU/mL at stationary phase (absorbance of 1.5 at 600 nm) was centrifuged at 7830 rpm for 10 min and then re-suspended in sterile deionized (DI) water to a microbial load of ~ $10^{10}\mathrm{CFU/mL}$. A volume of 200 μL of the *E. coli* O157:H7 aqueous suspension was then spin coated on 25.4 × 25.4 mm Si chips with three spin-coating steps: (1) 0 – 400 rpm for 30 s ramped over 30 s, (2) 400 – 600 rpm for 30 s ramped over 30 s, and (3) 600 – 1000 rpm for 10 s ramped over 5 s.

For the inoculation of agar plates, the bottom of sterile Petri dishes (35 mm diameter, 10 mm height) was completely filled up to the edge with Plate Count Agar (PCA, Difco, Becton Dickinson, Sparks, MD) and allowed to solidify. An overnight of TSB with *E. coli* O157:H7 was centrifuged at room temperature and at 7830 rpm for 10 min. Then, the supernatant was removed and replaced with the same volume of sterile DI water to re-suspend the cells. A 10% dilution of this aqueous suspension was prepared with DI water to get a microbial load of ~ 10^8 CFU/mL. A volume of 35 μL of the aqueous suspension with ~ 10^8 CFU/mL was inoculated onto individual PCA samples by evenly spreading on the agar's exposed surface. The microbial load in the PCA samples is ~ 10^6 CFU/g.

For the inoculation of baby spinach, the spinach leaves were first individually immersed in 10 mL of sterile DI water and vortexed for 1 min to remove the natural microflora from their surface. A homemade bacterial inoculation device for leafy samples shown in figure 8.1 (d) and (e) was applied to inoculate only one side of the spinach leaf. First, 2 mL of aqueous bacterial suspension with ~ 10^8 CFU/mL of *E. coli* O157:H7 (prepared from an overnight TSB as described in the previous paragraph) was applied

aseptically over the exposed area of each individual leaf and left under a biosafety cabinet for 30 min to allow the cells to attach to its surface. Subsequently the aqueous bacterial suspension was removed through pipetting without the contaminating the opposite side of the leaves with bacterial TSB. The leaves were separated from the inoculation device and allowed to dry under laminar flow inside the biosafety cabinet for 30 min. The leaves were then aseptically cut into 38 × 38 mm^2 squares to be subjected to SMD treatment as described in the following section.

8.2.5 Plasma treatment

Plasma treatments of bacteria and model biomolecules with the SMD reactor were performed in a sealed plastic chamber with a dimension of 21 × 18 × 12 cm^3. As shown in figure 8.2, four different treatment configurations were used for (a) *E. coli* O157:H7 inoculated PCA samples, (b) 3-layer stack of *E. coli* O157:H7 inoculated spinach leaves, (c) *E. coli* O157:H7 inoculated Si chips, and (d) LPS spin-coated on Si chips. The distance from the top of the target to the edge of the ground electrode d is 3 mm for all treatment configurations. For the green leaf stacks shown in figure 8.2 (b), the distance between each green leaf layer is 3 mm. These green leaves were fixed by spacers made out of Al alloy with a structure shown in figure 8.2 (b), and the exposed area of the green leaves without contacting the Al spacer was 25 × 25 mm^2. We used various plasma treatment times, i.e. 0.5 min, 1 min, 3 min, 5 min and 7 min, on the targets – the exact treatment time for each experiment will be mentioned in the results section.

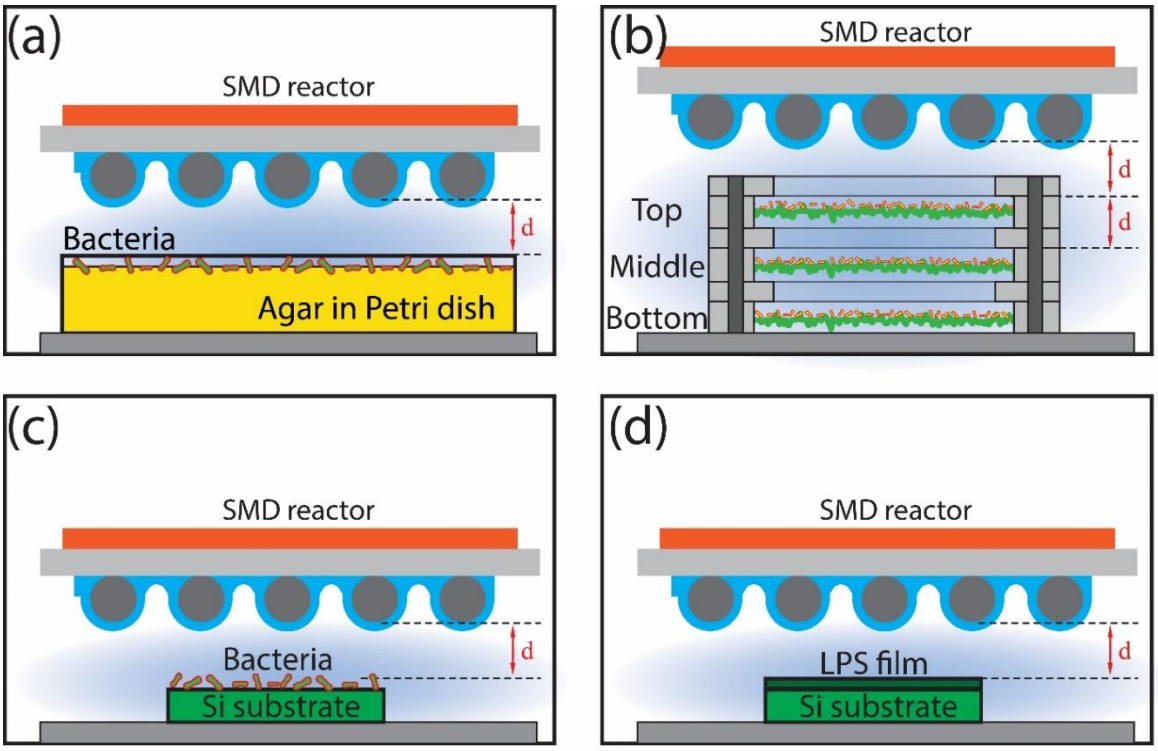

Figure 8.2 The schematic diagram of SMD treatment of: (a) *E. coli* O157:H7 inoculated PCA plates, (b) 3-layer stack of *E. coli* O157:H7 inoculated spinach leaves, (c) *E. coli* O157;H7 inoculated Si chips, and (d) LPS spin-coated on Si chips.

8.2.6 Post plasma treatment microbiological analysis

After plasma treatment, the *E. coli* O157:H7 inoculated PCA samples were aseptically removed from their corresponding Petri dishes. The spinach leaves were removed from the 3-layer stack shown in figure 8.2 (b). Subsequently the 25 × 25 mm^2 exposed region (not in direct contact with the Al spacer) was aseptically cut out of the spinach samples with sterile scissors and subjected to microbiological analysis.

The PCA samples and spinach leaves samples were individually transferred into Whirl-Pak sampling bags (Fisher Scientific Inc., Pittsburgh PA, USA) with peptone water (PW, Oxoid, Thermo Fisher Scientific, Waltham, MA) to obtain a 10% dilution of each

type of sample. The stomacher bags with the samples were processed for 5 min in a Seward 40 Circulator Stomacher (Seward Limited, UK), and additional 10% serial dilutions were prepared with PW from the resulting PCA and spinach leaves suspensions in PW. A volume of 100 μL of each dilution was inoculated onto Eosin Methylene Blue Agar, Levine (EMB, Becton Dickinson, Sparks, MD) for 48 h at 37 °C. The number of *E. coli* O157:H7 survivors was determined after incubation through plate counts and interpreted as log(CFU/g). The bacterial inactivation efficiency was calculated using the following equation:

$$log_{10}(N_R) = log_{10}(N_0) - log_{10}(N_S) \quad (8.1)$$

where N_R is the number of reduced cells, N_0 is the initial bacterial population, and N_S is the number of surviving cells after plasma treatment (N_R, N_0, and N_S are expressed as CFU/g). Each treatment was performed in 3 replicates and the error bar was given by standard deviation.

8.2.7 Cell morphology: optical image and scanning electron microscopy

The optical image of *E. coli* O157:H7 on Si substrate was acquired using Olympus BX60 microscope with 50x optical lens and Infinity 2 CCD sensor. We chose the *E. coli* O157:H7 inoculated on spinach leaves for bacterial cell morphology analysis. After SMD treatment, the treated spinach leaves along with the untreated leaf were fixed with glutaraldehyde and ethanol.[281] The fixed samples of spinach leaves and bacteria were then dried in 100% ethanol using an Autosamdri-815B critical point dryer (Tousimis, Rockville MD). Subsequently a layer of 80% Au and 20% Pd was sputter coated on the dried samples using Hummer X sputter system (Anatech USA, Hayward CA) with 1.6 kV voltage for 90 s. The SEM images were taken using a TESCAN GAIA FIB/SEM (Brno -

Kohoutovice, Czech Republic).

8.2.8 Surface characterization: ATR-FTIR and XPS

The FTIR characterization of *E. coli* O157:H7 and LPS (coated on Si chips) were performed on a Shimadzu IRTracer-100 equipped with liquid nitrogen-cooled HgCdTe (MCT) detector. A variable angle single reflection ATR accessory (VeeMaxIII, PIKE Technologies) along with a Ge crystal were used to measure the ATR-FTIR spectrum. To maintain consistent contact status between the samples and the Ge crystal, a pressure clamp with constant torque setting was also used along with the ATR accessory. The incident IR light angle was fixed at 60°, and the optical path of IR light was constantly purged with pure N_2 gas. For enhancing the signal to noise ratio of the ATR-FTIR spectrum of the ultra-thin LPS films, a ZnSe polarizer was installed at the optical inlet of the ATR accessory to eliminate the s-polarization of the IR light.[282] However, we did not use polarized IR light when measuring the ATR-FTIR of *E. coli* O157:H7. For both the bacteria and LPS, the IR spectra were acquired between 4000 cm^{-1} to 600 cm^{-1} with 4 cm^{-1} resolution averaged over 20 scans. The referencing backgrounds were obtained with no sample coupled to the Ge prism. Multiple-point baseline correction was consistently applied to all acquired ATR-FTIR spectrum.

The XPS of LPS films was acquired by a Vacuum Generators ESCALAB MK II system with non-monochromatic Al K_α radiation ($h\nu$ = 1486.6 eV). Both survey and the high-resolution C 1s, N 1s, O 1s and P 2p spectra were obtained with electron take-off angles of 20° (probing depth ~2 nm).[246] For C 1s spectrum, peaks corresponding to C-C/H (285 eV), C-O (286.5 eV), O-C-O/C=O (287.9 eV), O-C=O (289.1 eV), O-CO-O (290.2 eV) were fitted. For the N 1s spectrum, peaks corresponding to organic nitrate (R-

ONO_2, 408 eV) and N-C bond (400.1 eV) were fitted separately.[93] For O1s spectra, we fitted peaks corresponding to C=O and O*-CO-O (532.3 eV), C-O (532.6 eV), O-C-O (533.1 eV), O*-C=O (533.6 eV), O-CO*-O and O*-NO_2 (533.9 eV), O-NO_2* (534.7 eV).[196] All spectra were calibrated to the C-C/H peak at 285 eV. The elemental composition of the LPS films was calculated by integrating peak areas of C 1s, N 1s, O 1s and P 2p spectra with Scofield's sensitivity factor of 1, 2.85, 1.77 and 1.25, respectively.[179] All peak fitting and elemental composition analysis were performed using CasaXPS software.

8.2.9 Statistical analysis

When appropriate, statistical significance between treatments was determined through Analysis of Variance (ANOVA), followed by Tukey's pairwise comparisons (α = 0.05) with the software Minitab® version 18 (Minitab Inc., State College, PA).

8.3 Results and discussion

8.3.1Bacterial inactivation efficacy of SMD in N_2/O_2 mixture: effect of working gas composition

To evaluate the bacterial inactivation efficacy of the SMD reactor, we performed *E. coli* O157:H7 inactivation treatment in controlled environment with various N_2/O_2 mixtures as working gas. As shown in figure 8.3 (a), *E. coli* O157:H7 inoculated PCA samples were used as a model system to reduce the issues of bacterial coating typically associated with raw produce, e.g. uniformity and reproducibility. With 1 minute of treatment time, we observed > 2 logarithmic reductions from working gases with more than 20% of O_2, as illustrated in figure 8.3 (a). When comparing the efficiency of SMD treatment using different working gas compositions, we found that the bacterial

inactivation efficacy plateaus when the environmental O_2 composition is higher than 50%, and there is no significant difference ($P > 0.05$) between the treatments with O_2 concentrations higher than 20%. For SMD treatment in pure N_2 environment, marginal bacterial inactivation was observed, which was not significantly different from the control treatment ($P > 0.05$). This indicates that the oxygen containing reactive species generated by the SMD are essential for inactivating the bacteria.

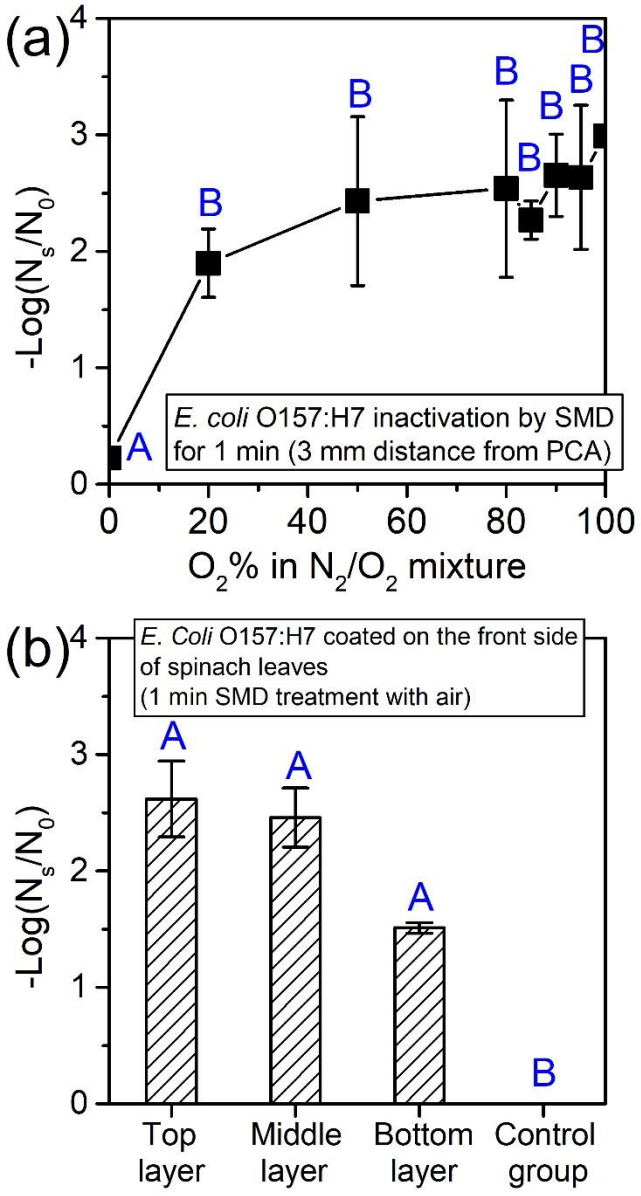

Figure 8.3 (a) Bacterial inactivation efficiency of the SMD reactor in various

working gas compositions evaluated by *E. coli* O157:H7 inoculated on PCA plates. The treatment distance and time is 3 mm and 1 min, respectively. (b) Bacterial inactivation efficiency of SMD reactor on green leaves evaluated by *E. coli* O157:H7 inoculated on the front side of spinach leaves. A three-layer green leaf stack shown in figure 8.2 (b) was used. Treatments that share the same label (A or B) are not significantly different ($P > 0.05$).

We expect higher bacterial inactivation efficacy of SMD with more O_2 concentration in the working gas. The plateau observed in the bacterial inactivation efficacy in figure 8.3 (a) with high O_2 composition might be mainly due to the surface property of the PCA samples rather than the effectiveness of SMD treatment. Bacteria may be hidden under the top layers of PCA caused by smearing during bacterial inoculation. Previously we measured the gas phase species generated by the SMD reactor with different working gas compositions and we found that the O_3 density showed a maximum with 95% O_2 and then decreased quickly with lower O_2 percentage in the O_2/N_2 mixture.[140],[261] We also found that the density of nitrogen containing reactive gas phase species changed dramatically with working gas composition and peaked at 50% O_2 in the O_2/N_2 gas mixture.[261] Because plasma generated reactive species are delivered to the target from the gas-solid interface, the bacteria hiding under PCA might not be inactivated even though the treatment is sufficient to kill all bacteria exposed, which leads to the observed leveling off in figure 8.3 (a). Due to its practical interest and the small difference of inactivation efficacy between 20% O_2 and higher O_2 percentage, ambient air was chosen as the working gas in the rest of this report.

8.3.2 Raw produce disinfection by SMD treatment

To demonstrate the effectiveness of SMD treatment on disinfecting bacterial contaminated raw produce, we evaluated the bacterial inactivation efficacy of SMD treatment with *E. coli* O157:H7 inoculated spinach leaves. To mimic the piles of green leaves found in industrial processing environment, a three-layer green leaf stack with constant distance of separation (3 mm, figure 8.2 b) was used as the processing target. As shown in figure 8.3 (b), after 1 min of SMD treatment in ambient air environment, we observed 2.6 ± 0.3 and 2.5 ± 0.3 logarithmic reductions from the top and middle layers of the green leaf stack, respectively. The SMD treatment is less effective on the bottom layer of the stack, for which $\sim 1.5 \pm 0.0$ logarithmic reductions was seen. However, no significant difference ($P > 0.05$) was observed between the antimicrobial effect found in each layer.

A possible explanation of the decrease of bacterial inactivation efficiency on the lower levels of the green leaf stack may be the inefficient transport of reactive species through the top layer. Due to the electrode configuration of the SMD reactor, the gaseous discharge is confined within a thin layer around the ground metal mesh. The lack of gas convection of the SMD reactor also limits the transport of reactive species, and thus the majority of species reaching target materials are long-lived reactive neutrals, e.g. O_3, N_2O_5, N_2O and HNO_3.[191] The green leaf at the upper level not only hinders the diffusion of these reactive neutrals but also serves as a sink where the reactive neutrals may be heavily consumed. The grater than 1.5 logarithmic cycles of bacterial reduction for the entire green leaf stack indicates that the SMD treatment might be a viable option for fast raw produce processing in an industrial setting.[260]

8.3.3 Oxidation of bacteria by SMD treatment

To directly evaluate the oxidation of the bacterial cells and provide information on the mechanism of bacterial inactivation by SMD treatment, the ATR-FTIR spectra of the untreated and treated *E. coli* O157:H7 cells as a function of processing time were measured and are shown in figure 8.4 (a). The ATR-FTIR spectrum of the untreated *E. coli* O157:H7 cells shows characteristic vibrational modes of Gram-negative bacteria.[283, 284] The two IR peaks at 1652 cm^{-1} (amide I) and 1543 cm^{-1} (amide II) come from the vibrations of chemical bonds in cellular proteins: the former peak belongs to the C=O stretching and the latter peak is a result of N-H bending and C–N stretching from the peptide group. The IR bands at 1458 cm^{-1} and 1396 cm^{-1} arise mainly from asymmetric and symmetric CH_3 bending of the methyl groups of proteins, respectively.[285] The IR band around 1232 cm^{-1} is mainly from the asymmetric PO_2^- stretching in phospholipids, phosphodiesters (nucleic acids) and phosphates (LPS). The symmetric stretching of PO_2^- also contributes to the band around 1083 cm^{-1}, however the IR peak at this position mainly comes from the C-O stretching modes of polysaccharides in LPS, peptidoglycan, etc..[284, 285]

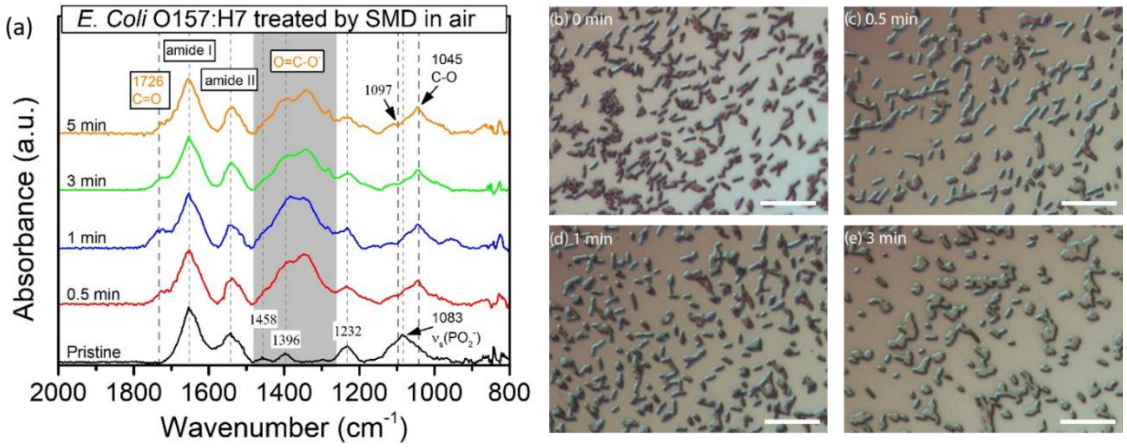

Figure 8.4 (a) The ATR-FTIR spectra of pristine, 0.5, 1, 3 and 5 min treated *E. coli*

O157:H7 cells. The optical image of *E. coli* on Si wafers after (b) 0 min (c) 0.5 min (d) 1 min and (e) 3 min of treatment by SMD. The scale bars in (b) – (e) indicate 10 μm.

After SMD treatment, the oxidation of *E. coli* O157:H7 was directly observed from the ATR-FTIR spectra. First, a new peak at 1726 cm^{-1} was detected and can be assigned to the C=O stretching vibration in carboxylic acid groups (COOH). Second, the rise of bands in the range of 1480 - 1260 cm^{-1} comes from the appearance of symmetric stretching vibration of carboxylate ($O=C-O^-$). At last, we also observed significant changes in the profile of the IR band in the region of 1150 – 950 cm^{-1} which indicates the modification of phosphor containing groups and polysaccharides. The increase of the IR peak near 1045 cm^{-1} might result from the formation of additional C-O bonds caused by plasma induced oxidation, whereas the decrease of the IR peak near 1100 cm^{-1} suggests the destruction of glycosidic bond in polysaccharides.[284] The reduction of the IR peak at 1083 cm^{-1} might be related to the destruction of either phospholipids from the cell membrane or polysaccharides in many cellular components. When comparing the spectra in figure 8.4 (a), we did not find significant differences as a result of increasing processing time from 0.5 min to 5 min.

In figures 8.4 (b) through (e), we show the optical images of both the untreated and 0.5, 1, 3 min treated *E. coli* O157:H7 cells. The untreated *E. coli* O157:H7 cells in figure 8.4 (b) have the typical rod-shaped morphology with a cell size of about 2.0 – 4.0 μm long and 0.25–1.0 μm in diameter. After 0.5 min of SMD treatment, the bacterial cells have expanded and a small portion of the bacteria showed cell lysis. When further increasing the plasma treatment time, we find that higher percentage of cell lysis occurs. Since the bacteria

in figure 8.4 are inoculated on dry Si wafers, results from figure 8.4 indicate that the SMD treatment is able to damage the structural integrity of the bacterial cell membrane which results in the lysis of the bacteria.

8.3.4 Bacteria cell morphology: SEM

The effect of SMD treatment on the structural integrity of the bacteria was further evaluated using scanning electron microscopy (SEM) of *E. coli* O157:H7 inoculated on spinach leaves. As shown in figure 8.5 (a), a healthy, untreated cell of *E. coli* O157:H7 is rod-shaped with a characteristic surface morphology.[286, 287] The SMD treatment is able to alter the cell morphology dramatically, especially after longer treatment time. First, with 1 min of treatment (figure 8.5 b) the surface of the bacterium inoculated on spinach leaf becomes more corrugated which suggests the damage of cell membrane by the reactive species generated by SMD. When increasing the treatment time to 3 min, we find that the cell expands especially in the radical direction and the surface of the cell loses its intrinsic texture possibly due to the stretching of the membrane. For the 5 min treated bacterium, even greater cell expansion and possible local rupture was observed. We also noticed that it becomes harder to locate bacterial cells on the dried green leaves after SMD treatment, especially for the 3 and 5 minutes treated samples. This might be due to the SMD induced lysis of the bacteria or modification of cell surfaces causing the bacteria to slough off more easily during the fixing process.

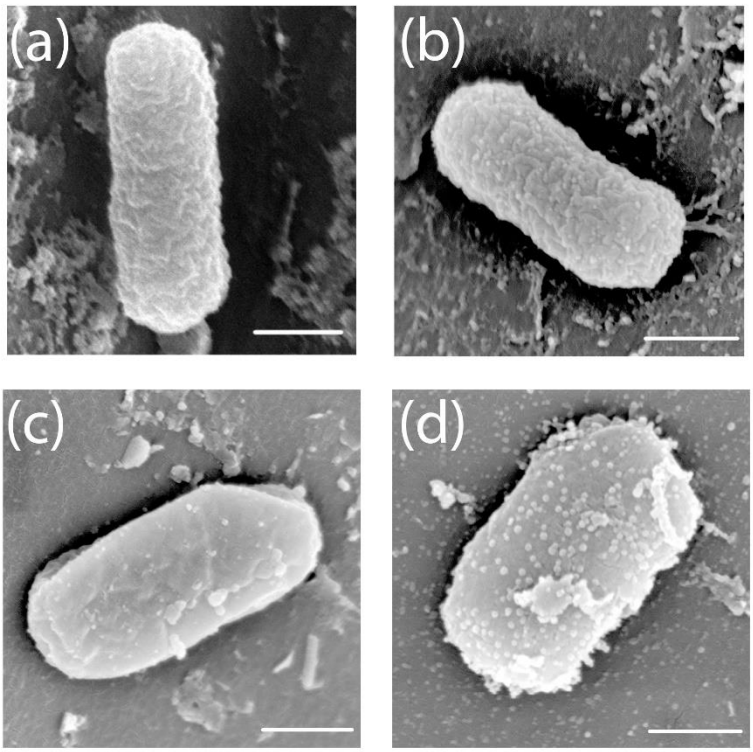

Figure 8.5 The SEM image of *E. coli* O157:H7 cell: (a) untreated, and SMD treated in air for (b) 1 minute, (c) 3 minutes and (d) 5 minutes. The scale bars indicate 500 nm.

When comparing the SEM of bacteria inoculated on spinach leaf (figure 8.5) to the optical images of bacteria inoculated on Si wafers (figures 8.4 b through e), we find that the bacteria located on Si wafers experience more damage than those inoculated on spinach leaves after SMD treatment, which suggests that the intrinsic surface property of targets can influence the efficiency of plasma disinfection. This may be caused by both the inefficient transport and the consumption of reactive species by the substrate surface. First, bacteria inoculated on green leaves could hide in microstructural features of spinach surfaces and avoid being directly exposed under plasma treatment. In contrast, the Si wafer has a flat surface where bacteria are evenly treated by SMD. Second, the Si wafer has a

thin (~1.7 nm) SiO_2 layer which is inert and deactivates few reactive species as compared to the organic substances on spinach leaves which serve as a sink of the oxidizing plasma species. For these reasons, the SMD treatment appears to be less effective on real food surfaces than on the surrogate Si wafers. Similar findings on the influence of food surface morphology on the inactivation efficacy of plasma treatment have also been reported in previous works.[288-290]

8.3.5 Damage to the cell membrane component: LPS

Since the outer leaflet of Gram-negative bacteria has a layer of LPS (schematic shown in figure 8.6 a) exposed to the environment, it is one of the first cell membrane components that reactive species attack during plasma treatment. To evaluate the effect of SMD treatment on the cell membrane components, we performed the ATR-FTIR analysis of ultra-thin (~ 13 nm) LPS films spin-coated on Si substrates. Because the Si substrate has a ~ 1.7 nm native SiO_2 layer on its surface, the ATR-FTIR spectra in figure 8.6 (b) show an O-Si-O stretching peak (labeled as F) at 1230 cm^{-1}. Due to the stability of this native SiO_2 layer under plasma treatment,[245] the O-Si-O stretching peak F can be used as a reference peak for calibrating the contact status between the sample and the Ge crystal.

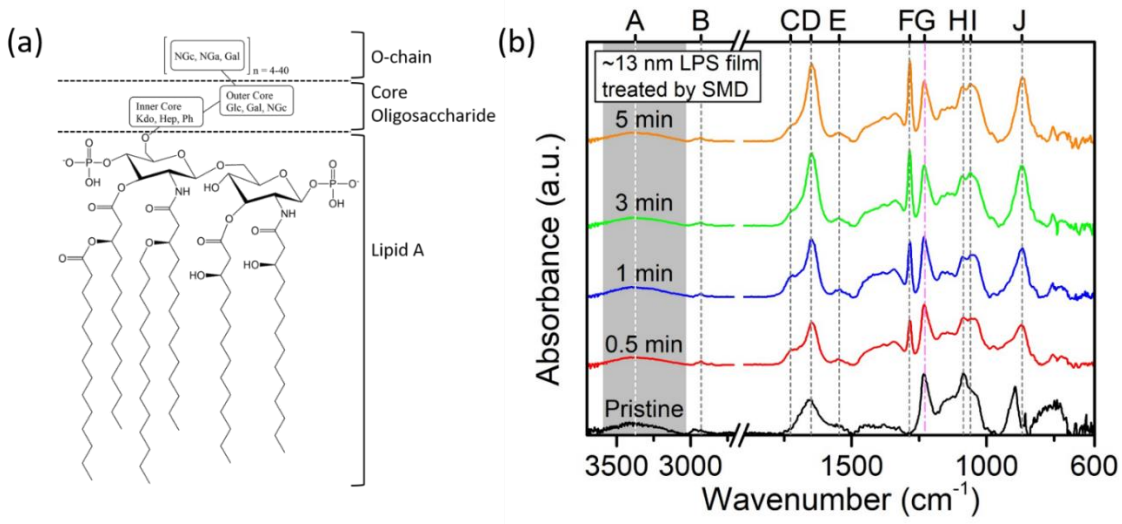

Figure 8.6 (a) The chemical structure of lipopolysaccharide (LPS) highlighting lipid A. NGc: N-acetyl-glucosamine, NGa: N-acetyl-galactosamine, Gal: galactose, Glc: glucose, Kdo: 3-deoxy-D-manno-oct-2-ulosonic acid, Hep: heptose, Ph: phosphate/pyrophosphate. (b) The ATR-FTIR spectra of pristine, 0.5 min, 1 min, 3 min and 5 min treated LPS.

First for the pristine LPS, its IR spectrum in figure 8.6 (b) shows similar peaks as that of the *E. coli* O157:H7 cells illustrated in figure 8.4 (e). The major features in the pristine LPS spectrum can be assigned to:[291-293] (1) peak A (3600 - 3100 cm^{-1}), amide A, (2) peak B (2990 - 2820 cm^{-1}), the stretching vibration of CH_2 and CH_3 bonds mainly from lipid A, (3) peak D (1651 cm^{-1}) and E (1500 cm^{-1}), the amide I and amide II from core-polysaccharide, (4) peak H (1085 cm^{-1} - 10), the C-O stretching of polysaccharides and the symmetric PO_2^- stretching of phosphates. After SMD treatment, we observed the rise of several new IR bands, including (1) peak C (1726 cm^{-1}), the C=O stretching vibration of carboxylic acid groups (COOH), (2) peak F (1284 cm^{-1}), the symmetric stretching vibration of carboxylate ($O=C-O^-$) group, (3) peak I (1061 cm^{-1}) and J (867 cm^{-1}), the asymmetric and symmetric stretching of C-C-OH. The emergence of these new O containing IR bands indicates that the LPS molecules experience oxidation during the SMD treatment. Compared to the ATR-FTIR of SMD treated *E. coli* O157:H7 cells, the IR spectra of SMD treated LPS also show IR peaks from C=O and $O=C-O^-$ groups.

To further evaluate the oxidation of LPS by SMD treatment, we performed XPS characterization of LPS films coated on Si substrate. Figure 8.7 shows the C 1s, N 1s and O 1s spectra of both pristine and SMD treated LPS in artificial air with 50% relative

humidity (RH, 20.5 ± 1 °C). Elemental composition analysis indicates that the percentage of C, O, N and P elements in the XPS spectra is 78.3 %, 18.6 %, 2.2 % and 0.9 %, respectively. The ratio between O and C composition can be then estimated as O/C = 0.238 which is comparable to that of lipid A structure (O/C = 0.255).[294] Since O-chain and core-polysaccharide has higher O/C ratio, we speculate that XPS measurements (probing depth ~ 2 nm) mainly characterize the lipid A structure of the LPS molecules which has long aliphatic chains and is responsible for the reduction of O/C ratio. Previous reports [294, 295] indicate that the lipid A layer is known to be formed at the air–water interface after spin-coating due to the amphiphile property of LPS. Out of all the C 1s electrons detected in figure 8.7 (a), 82.4 % of them is from the C-C/H bonds which leaves a small portion of C 1s electrons comes from oxygen containing moieties: C-O (14.2 %), C=O/O-C-O (3.0 %), O-C=O (0.3 %). In figure 8.7 (c) the O 1s spectrum of pristine LPS is shown, and we also observed these O containing functional groups.

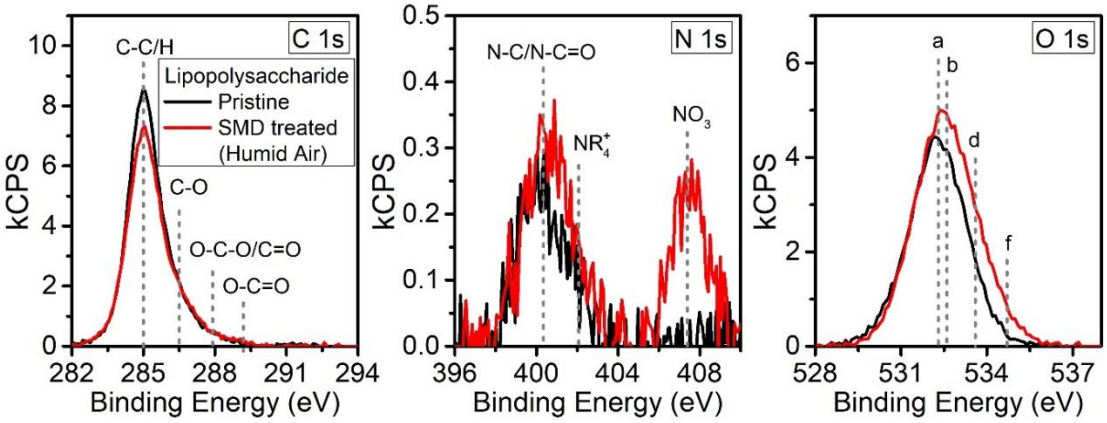

Figure 8.7 High resolution (a) C 1s, (b) N 1s, (c) O 1s spectrum of pristine and SMD treated LPS. Label a (532.3 eV): C=O, O-C=O*, O*-CO-O; b (532.6 eV) aliphatic C-O; c (533.1 eV): aromatic C-O, O-C-O; d (533.6 eV): O*-C=O; e (533.9 eV): O-CO*-O, O*-NO_2; f (534.7 eV): O-NO_2*.

After SMD treatment in 50% RH air environment, we observed the formation of organic nitrate (R-ONO_2) and the weak surface oxidation of the spin-coated LPS film, presumably the oxidation of lipid A structure. As shown in figure 8.7 (a), the SMD treatment causes the C-C/H content to drop from 82.4 % to 80.0 % accompanied by the slight rise of C-O, C=O/O-C-O and O-C=O moieties. Moreover, a new peak at 408 eV emerged in the N 1s spectrum can be assigned to R-ONO_2 which we have discussed previously.[93, 94] The small difference between the pristine and the SMD treated LPS films shown in figure 8.7 suggests that the lipid A part of the LPS molecule is relatively inert to SMD treatment. Combined with the ATR-FTIR results shown in figure 8.6 (b), we conclude that the SMD induced oxidation of the LPS molecules mainly occurs at the O-chain and core-polysaccharide parts.

The oxidation of bacterial cell and cellular components, as observed in figures 8.4 (a), 8.6 (b) and 8.7, can be attributed to the effect of reactive species generated by the SMD reactor, especially the long-lived neutrals. Previously we characterized the dominant reactive species in the afterglow of the SMD reactor, and we found that O_3, N_2O_5, N_2O and HNO_3 are the most abundant ones ($> 10^{15} cm^{-3}$).[261] Our surface and sub-surface characterization results of vinyl polymers treated by the SMD reactor show that these long-lived species could not only oxidize the material surface but also penetrate into the material bulk and cause bulk oxidation.[95, 242] Compared to vinyl polymers, the cellular components of bacteria are easier to be oxidized and permeated by these reactive species – hence the high bacterial inactivation efficiency with short treatment time.

8.4 Conclusion

In the present work we evaluated SMD as a disinfection technique for fresh produce. With ambient air as working gas and 1 min of treatment, effective bacterial inactivation with > 2 logarithmic cycles of *E. coli* O157:H7 reduction was observed. Since the SMD reactor can be easily scaled up and integrated in existing production lines, this makes the SMD suitable for large-scale raw food processing in centralized facilities. In addition, Since this disinfection approach only requires air and electricity, it also appears promising for the applications in remote locations.

We also characterized the effect of SMD generated reactive species on the bacterial cell morphology of *E. coli* O157:H7. We found that SMD treatment damages the structural integrity of the bacterial cell membrane and cause the swelling of the bacteria which eventually results in cell lysis. The ATR-FTIR spectra of *E. coli* O157:H7 coated on Si substrates suggest that SMD treatments can result in the oxidation of the bacterial cell components which is observed by (1) the formation of carboxylic acid (COOH) and carboxylate (COO^-) groups and (2) the modification of the phosphor containing groups (phospholipids and DNA) and polysaccharides. In contrast, the cellular proteins remained mostly unaffected after SMD treatment. To further explore the effect of SMD on bacteria cell membrane, we chose LPS which is the outermost component of Gram-negative bacteria as a model material. The ATR-FTIR and XPS analyses of SMD treated LPS suggest that the lipid A structure is relatively inert to SMD treatment and it is the O-chain and core-polysaccharide that are oxidized.

Acknowledgement

The authors gratefully acknowledge the financial support by the National Science

Foundation (PHY-1415353) and the US Department of Energy (DE-SC0001939). We thank C. Tous, A. J. Knoll and E. A. J. Bartis for helpful discussions and collaborations.

Chapter 9: Conclusions and Future work

The major contribution of this work is the establishment of an approach for studying plasma-surface interaction (PSI) at atmospheric pressure by correlating the plasma/gas phase measurements of well-controlled plasma source-environment systems with the surface and near-surface characterization results of model materials. In this approach, we emphasize on the controlled generation of reactive species from the plasma source, the regulated transport of reactive species to the target surfaces, as well as the simplified material structure subjected to plasma treatment. To isolate and identify the role of certain reactive species on materials, a plasma source is selected with its operating conditions carefully tuned for the generation of such species. Plasma-induced changes to materials were characterized and then quantitatively correlated to the gas phase species. Using this method, we were able to evaluate the effect of both short- and long-lived reactive neutrals on many types of functional groups.

In Chapter 2 we investigated the surface interaction of a well-characterized time modulated radio frequency (RF) plasma jet with three vinyl polymers, i.e. polystyrene (PS), poly(methyl methacrylate) (PMMA) and poly(vinyl alcohol) (PVA). With various feed gas compositions, such as Ar/1% O_2, Ar/1% air, Ar/1% H_2O, etc., we observed the generic fast polymer etching but mild chemical modification with characteristic carbonate ester and NO formation on the etched surface. We also found that adding O_2 and H_2O simultaneously into Ar feed gas lead to the reduction of polymer etch rate compared to adding them separately which suggests the reduction of O and OH density in Ar/O_2/H_2O plasma.

In Chapter 3, we focused on the effect of atomic O on polymers by using the same RF jet-PS model system as in Chapter 2. The surface response of PS to a number of plasma

processing parameters, namely treatment distance, environmental gas composition, as well as substrate temperature, were characterized by evaluating both the thickness and surface chemical composition change after treatment. We found that the etching efficiency of Ar/O_2 plasma dropped exponentially with nozzle-surface distance. The correlation of the etching depth profile of PS with the density profile of atomic O measured/simulated in the gas phase indicates that atomic O can be the dominant etchant species. The etching reaction coefficient of atomic O (number of C atoms removed per incident O atom) is estimated to be in the range of 2×10^{-4} - 4×10^{-4}. Different from the etching depth profile, we showed that surface oxygen composition of PS reached a maximum and then fell with treatment distance. The difference between etching and surface oxygen composition profiles along treatment distance implies that surface etching and modification can be controlled by different interfacial processes involving multiple plasma species. We also measured the substrate temperature dependence of PS etch rate and found that the apparent activation energy (E_a) of the PS etching reaction was in the range of 0.10 – 0.13 eV. This relatively low E_a value suggests the involvement of additional energetic plasma species in the etching reactions.

In Chapter 4, we evaluated the interaction mechanism of remote plasma oxidation (RPO) by studying the evolution of polymer film properties, including thickness, refractive index, surface moieties and bulk chemical composition. Using surface micro-discharge (SMD) and PS as model plasma-polymer system, we found that the polymer film underwent three distinct transformation stages during RPO, i.e. surface adsorption/oxidation, bulk expansion and etching. Further analysis of the chemical composition of the treated polymers indicates that the long-lived species generated by

remote plasma are able to (1) form surface nitrate adsorption and oxidation layer, (2) diffuse into the polymer and oxidize the polymer bulk (3) cause etching of the polymer surface. Our results suggest that long-lived reactive species may be responsible for the transformation stages.

In Chapter 5, we evaluate the effect of water vapor on the plasma processing of the PS model system using the RF jet. We identified the dominant etchant species generated in Ar/H_2O plasma as OH radicals, and by correlating the amount of OH radicals arriving at the polymer surface with the etched C atoms leaving the polymer surface, we estimated the etching reaction coefficient of OH radicals (number of C atoms removed per incident OH radical) to be of the order of 10^{-2}. When changing the treatment distance of Ar/H_2O plasma, we find that the polymer etch rate drops exponentially whereas the surface oxidation rate evaluated by the surface O composition shows a maximum at an intermediate treatment distance, which is similar to the behavior of Ar/O_2 plasma generated by the same RF jet. This difference between etching and surface modification again confirms that etching and surface modification may be controlled by different surface processes. We also evaluated the effect of substrate temperature on the polymer etch rate of Ar/H_2O plasma. The polymer etch rate decreases with increasing substrate temperature from 4 °C – 70 °C. A possible explanation is the increase of the etchant (OH) sticking coefficient or the enhancement of H_2O adsorption on polymer surfaces for lower substrate temperature.

In Chapter 6, we characterized the reactive species generated in the effluent of the SMD reactor using IR and UV absorption. With N_2 and O_2 mixture as working gas, the dominant reactive species were identified as O_3, N_2O_5, N_2O and HNO_3. We also quantified the density of these reactive species which changed with the ratio between N_2 and O_2 in

the feed gas. To study the effect of these long-lived reactive species on polymers, we exposed ultra-thin (~10 nm) PS films to the effluent of the SMD with various feed gas compositions. By correlating the thickness expansion rate of the PS film with the flux of the plasma generated reactive species, we found a linear relationship between the expansion rate and the flux of O_3, which suggests that O_3 is an essential reactant involved in causing the expansion of the PS film. When relating the quantified chemical composition of the treated PS films with the dose of the reactive species, we found that (1) the O elemental composition of the PS surface (~ 2 nm), (2) the aromatic ring content inside the ~ 10 nm film, and (3) the carbonyl groups inside the film all show exponential decrease or increase with the dose of O_3 delivered to the PS films. This indicates that O_3 might participate in the chemical modification of the PS structure, such as cleaving the aromatic rings and oxidizing them into carbonyls both on surface and in the polymer bulk.

In chapter 7, we studied the interaction between long-lived reactive neutrals generated by APP source and six different types of vinyl polymers, i.e. PS, P4MS, PαMS, PMMA, PVA and PP. We found structural dependence of polymer modification on these long-lived reactive species: for methyl, alcohol, ether based polymers, we found material removal caused by prolonged treatment; whereas for styrene-based polymers, we saw that the film thickness increased to a maximum and then decreased. The XPS and ATR-FTIR characterization of the treated PS films showed the destruction of aromatic rings and the formation of ether, ester and surface organic nitrate groups. The thickness expansion of the styrene-based polymers may be related to the oxidation of the tightly packed styrene rings to various moieties containing oxygen which occupy more volume. We also investigated the reaction mechanism of styrene-based polymers with long-lived species by comparing

PS with its derivatives namely P4MS and PαMS. We find that the reactive species generated by SMD primarily attack the C-H bond on the carbon site where the aromatic rings connect. We also performed the back-etching of PS films treated by long-lived reactive neutrals to examine their effect on the polymer subsurface and bulk. Compared to pristine PS films, the top 10 nm – 40 nm of the treated PS films (depending on treatment time) is greatly oxidized after long-lived reactive neutral treatment. We also found proof that organic nitrates only formed on the top few nm of the polymer surface. At last, we evaluated the apparent activation energy of SMD etching reactions with PMMA which we estimated as 0.84 eV.

In Chapter 8, we evaluated SMD as a disinfection technique for fresh produce. With ambient air as working gas and 1 min of treatment, effective bacterial inactivation with > 2 logarithmic cycles of *E. coli* O157:H7 reduction was observed. We found that SMD treatment damages the structural integrity of the bacterial cell membrane and cause the swelling of the bacteria which eventually results in cell lysis. The ATR-FTIR spectra of *E. coli* O157:H7 coated on Si substrates suggest that SMD treatments can result in the oxidation of the bacterial cell components which is observed by (1) the formation of carboxylic acid (COOH) and carboxylate (COO^-) groups and (2) the modification of the phosphor containing groups (phospholipids and DNA) and polysaccharides. The ATR-FTIR and XPS analyses of SMD treated cell membrane component lipopolysaccharide (LPS) suggest that the lipid A structure is relatively inert to SMD treatment and it is the O-chain and core-polysaccharide that are oxidized. Since the SMD reactor can be easily scaled up and integrated in existing production lines, this makes it suitable for large-scale raw food processing in centralized facilities.

In summary, the method of studying PSI presented in this work, i.e. controlled generation and regulated transport of reactive species, simplified target material structure, and correlating plasma-induced changes on materials to the gas phase reactive species, is a fruitful basis for the investigation of many plasma induced effects on materials, including the application field of surface modification, wetting and adhesion improvement, plasma medicine, bacterial inactivation, plasma catalysis, etc. This approach of studying PSI can be used for many different plasma-material systems and is not limited to the APPJ/SMD-PS system.

We found that the short- and long-lived reactive species generated by the APP have very different effects on organic substances. For the short-lived reactive species, they mainly react with the material surface which leads to two types surface effects: etching and modification. For the long-lived reactive species, we find that they not only react with the polymer surface but also diffuse into the polymer bulk and cause bulk modification. The recognition and separation of different roles of reactive species on materials can help improve our understanding on certain application mechanisms.

Many observations in this work show the complex nature of PSI under atmospheric pressure. For example, we found that the etching and surface modification of polymers might not be independent from each other: the etching process might impede the accumulation of surface modification by removing oxidized sites, whereas the excessive modification of material surfaces could eventually lead to etching. We also observed multiple reaction stages for polymers interacting with long-lived reactive neutrals. Therefore care must be taken when interpreting plasma-induced effects on materials. Comprehensive characterization techniques on the APP treated surface is strongly desired.

We applied the knowledge learned from APP treatment of polymers to explaining the mechanisms of APP interaction with biomolecules and bacterial cell membranes. Due to the complexity of bio-systems, we think this approach might be critical to the advance of the emerging field of plasma medicine and bacterial inactivation. We also demonstrated the effective bacterial inactivation by the SMD source and its potential to be integrated in industrial processing environments.

There are also many drawbacks for the approach used in this work. First and foremost, only a few types of reactive species generated by APP were quantified in our work and all the surface characterization results were correlated to one of these quantified species. Due to the complexity of APP, there might be other reactive species or even more than one species that result in the observed effect on materials. Based on the current procedure, it is difficult for us to exclude those possibilities. One potential solution to this issue could be introducing a control sample with scavengers on material surface that consumes certain known plasma species.

Another key missing piece in this work is evaluating the role of energetic species, such as ions, electrons and UV photons, on materials at atmospheric pressure. We suspect that these energetic species can play a key role on the noble gas containing APPs such as the Ar/H_2O and Ar/O_2 plasma jet. One further step of this work is to evaluate the charge particles generated by the RF jet using mass spectroscopy (MS) and then compare the role of these charged particles on polymers with short-lived reactive neutrals such as atomic O and OH radicals.

Related to the questions on the role of energetic species is: how does the momentum transfer from ions to neutral gas in the discharge region change the transport of reactive

species in the afterglow region? This is particularly interesting for the planar SMD reactor since the targets are usually placed few mm away from the discharge region. It is interesting to examine whether the short-lived neutrals or even the charge particles generated in the discharge region could be transported to the material surface.

Last, although we showed correlation between plasma induced effect on live bacteria and that on bacterial cell membrane components, it is unreasonable to assume that the bacterial inactivation directly comes from cell membrane damage. Many inactivation mechanisms involving reactive species generated by APP have been proposed before.[259] However, we think our results on the interaction between APP and model polymers might shine light on studying the more complex plasma-target system including live bacteria. Many future works focused on the effect of APP on the bacterial cellular components or their simpler surrogate materials could be helpful for improving our understanding of plasma induced bacterial inactivation.

References

[1]P. Luan, A. J. Knoll, P. J. Bruggeman, G. S. Oehrlein, *Journal of Vacuum Science & Technology A: Vacuum, Surfaces, and Films* **35**, 05C315 (2017).

[2]P. Luan, G. S. Oehrlein, *In preparation*, (2018).

[3]H. F. Winters, J. W. Coburn, *Surf. Sci. Rep.* **14**, 162-269 (1992).

[4]R. P. Wayne, I. Barnes, P. Biggs, J. P. Burrows, C. E. Canosa-Mas, J. Hjorth, G. Le Bras, G. K. Moortgat, D. Perner, G. Poulet, G. Restelli, H. Sidebottom, *Atmospheric Environment. Part A. General Topics* **25**, 1-203 (1991).

[5]R. L. Bruce, F. Weilnboeck, T. Lin, R. J. Phaneuf, G. S. Oehrlein, B. K. Long, C. G. Willson, A. Alizadeh, *May* **29**, (2011).

[6]A. J. Knoll, P. Luan, E. a. J. Bartis, V. S. S. K. Kondeti, P. J. Bruggeman, G. S. Oehrlein, *Plasma Processes and Polymers* **13**, 1069-1079 (2016).

[7]B. Vollmert, *Polymer chemistry*. (Springer Science & Business Media, 2012).

[8]S. J. Moss, A. M. Jolly, B. J. Tighe, *Plasma Chem. Plasma Process.* **6**, 401-416 (1986).

[9]A. N. Bhoj, M. J. Kushner, *Journal of Physics D-Applied Physics* **40**, 6953-6968 (2007).

[10]R. Dorai, M. J. Kushner, *Journal of Physics D-Applied Physics* **36**, 666-685 (2003).

[11]S. J. Blanksby, G. B. Ellison, *Acc. Chem. Res.* **36**, 255-263 (2003).

[12]E. T. Denisov, T. Denisova, *Handbook of antioxidants: bond dissociation energies, rate constants, activation energies, and enthalpies of reactions*. (CRC press, 1999), vol. 100.

[13]Y. Yamashita, K. Katayose, H. Toyoda, H. Sugai, *J. Appl. Phys.* **68**, 3735-3737 (1990).

[14]A. Ravve, *Principles of polymer chemistry*. (Springer Science & Business Media, 2013).

[15]C. Walling, A. Padwa, *J. Am. Chem. Soc.* **85**, 1593-1597 (1963).

[16]A. C. Fozza, J. E. Klemberg-Sapieha, M. R. Wertheimer, *Plasmas Polym.* **4**, 183-206 (1999).

[17]D. Hegemann, H. Brunner, C. Oehr, *Nuclear Instruments and Methods in Physics Research Section B: Beam Interactions with Materials and Atoms* **208**, 281-286 (2003).

[18]E. M. Liston, L. Martinu, M. R. Wertheimer, *J. Adhes. Sci. Technol.* **7**, 1091-1127 (1993).

[19]F. Poncin-Epaillard, S. Vallon, B. Drévillon, *Macromol. Chem. Phys.* **198**, 2439-2456 (1997).

[20]D. B. Graves, *Plasma Processes and Polymers* **11**, 1120-1127 (2014).

[21]X. Lu, S. Wu, *Ieee Transactions on Plasma Science* **41**, 2313-2326 (2013).

[22]K. Niemi, V. Schulz-Von Der Gathen, H. F. Dobele, *Plasma Sources Science & Technology* **14**, 375-386 (2005).

[23]J. S. Sousa, K. Niemi, L. J. Cox, Q. T. Algwari, T. Gans, D. O'connell, *J. Appl. Phys.* **109**, (2011).

[24]S. Zhang, W. Van Gaens, B. Van Gessel, S. Hofmann, E. Van Veldhuizen, A. Bogaerts, P. Bruggeman, *Journal of Physics D-Applied Physics* **46**, (2013).

[25]S. Bekeschus, S. Iseni, S. Reuter, K. Masur, K.-D. Weltmann, *Apr* **43**, 776-781 (2015).

[26]A. Schmidt-Bleker, J. Winter, S. Iseni, M. Duennbier, K. D. Weltmann, S. Reuter, *Journal of Physics D-Applied Physics* **47**, (2014).

[27]Y. Sakiyama, D. B. Graves, H.-W. Chang, T. Shimizu, G. E. Morfill, *Journal of Physics D-Applied Physics* **45**, 19 (2012).

[28]C. A. Vasko, D. X. Liu, E. M. Van Veldhuizen, F. Iza, P. J. Bruggeman, *Plasma Chemistry and Plasma Processing* **34**, 1081-1099 (2014).

[29]K. H. Kurniawan, T. J. Lie, M. M. Suliyanti, R. Hedwig, S. N. Abdulmadjid, M. Pardede, N. Idris, T. Kobayashi, Y. Kusumoto, K. Kagawa, M. O. Tjia, *Journal of Applied Physics* **98**, (2005).

[30]B. T. J. Van Ham, S. Hofmann, R. Brandenburg, P. J. Bruggeman, *Journal of Physics D-Applied Physics* **47**, (2014).

[31]S. Iseni, S. Reuter, K.-D. Weltmann, *Journal of Physics D-Applied Physics* **47**, (2014).

[32]G. Dilecce, P. F. Ambrico, M. Simek, S. De Benedictis, *Chemical Physics* **398**, 142-147 (2012).
[33]S. Schneider, J. W. Lackmann, F. Narberhaus, J. E. Bandow, B. Denis, J. Benedikt, *Journal of Physics D-Applied Physics* **44**, (2011).
[34]G. D. Stancu, F. Kaddouri, D. A. Lacoste, C. O. Laux, *Journal of Physics D-Applied Physics* **43**, 10 (2010).
[35]A. F. H. V. Gessel, S. C. V. Grootel, P. J. Bruggeman, *Plasma Science and Technology* **22**, (2013).
[36]A. F. H. Van Gessel, S. C. Van Grootel, P. J. Bruggeman, *Plasma Sources Science & Technology* **22**, (2013).
[37]K. Niemi, D. O'connell, N. De Oliveira, D. Joyeux, L. Nahon, J. P. Booth, T. Gans, *Applied Physics Letters* **103**, (2013).
[38]D. Schroeder, H. Bahre, N. Knake, J. Winter, T. De Los Arcos, V. Schulz-Von Der Gathen, *Plasma Sources Science & Technology* **21**, 024007 (2012).
[39] T. Batakliev, V. Georgiev, M. Anachkov, S. Rakovsky, S. Rakovsky, in *Interdisciplinary Toxicology*. (2014), vol. 7, pp. 47.
[40]Y. Matsumi, M. Kawasaki, *Chem. Rev.* **103**, 4767-4782 (2003).
[41]W. Van Gaens, A. Bogaerts, *Plasma Sources Science & Technology* **23**, 27 (2014).
[42]W. Van Gaens, A. Bogaerts, *Journal of Physics D-Applied Physics* **46**, 53 (2013).
[43]W. V. Gaens, P. J. Bruggeman, A. Bogaerts, *New Journal of Physics* **16**, 063054 (2014).
[44]R. Ono, T. Oda, *J. Appl. Phys.* **93**, 5876-5882 (2003).
[45]R. H. Hansen, J. V. Pascale, T. De Benedictis, P. M. Rentzepis, *Journal of Polymer Science Part A: General Papers* **3**, 2205-2214 (1965).
[46]H. Schonhorn, R. H. Hansen, *Journal of Applied Polymer Science* **11**, 1461-1474 (1967).
[47]J. F. Battey, *IEEE Trans. Electron Devices* **24**, 140-146 (1977).
[48]J. Cook, B. W. Benson, *J. Electrochem. Soc.* **130**, 2459-2464 (1983).
[49]F. D. Egitto, *Pure and applied Chemistry* **62**, 1699-1708 (1990).
[50]H. Suhr, *Plasma Chem. Plasma Process.* **3**, 1-61 (1983).
[51]S. J. Arnold, M. Kubo, E. A. Ogryzlo, in *Oxidation of Organic Compounds*. (AMERICAN CHEMICAL SOCIETY, 1968), vol. 77, chap. 70, pp. 133-142.
[52]P. B. Merkel, D. R. Kearns, *J. Am. Chem. Soc.* **94**, 1029-1030 (1972).
[53]M. Bodesheim, R. Schmidt, *The Journal of Physical Chemistry A* **101**, 5672-5677 (1997).
[54]R. D. Scurlock, B. Wang, P. R. Ogilby, *J. Am. Chem. Soc.* **118**, 388-392 (1996).
[55]A. A. Ionin, I. V. Kochetov, A. P. Napartovich, N. N. Yuryshev, *Deactivation of lipopolysaccharide by Ar and H 2 inductively coupled low-pressure plasma* **40**, R25 (2007).
[56]M. C. Derosa, R. J. Crutchley, *Coord. Chem. Rev.* **233–234**, 351-371 (2002).
[57]P. R. Ogilby, *Chem. Soc. Rev.* **39**, 3181-3209 (2010).
[58]I. Kruk, *Environmental toxicology and chemistry of oxygen species*. (Springer, 2013), vol. 2.
[59]N. Gaurav, S. João Santos, J. B. Peter, *Deactivation of lipopolysaccharide by Ar and H 2 inductively coupled low-pressure plasma* **50**, 105205 (2017).
[60]B. G. Rånby, J. F. Rabek, *Singlet oxygen reactions with organic compounds and polymers*. (John Wiley & Sons, 1978).
[61]E. L. Clennan, *Tetrahcdron* **56**, 9151-9179 (2000).
[62]J. R. Maccallum, C. T. Rankin, *Die Makromolekulare Chemie* **175**, 2477-2482 (1974).
[63]P. Bruggeman, D. C. Schram, *Plasma Sources Science & Technology* **19**, 045025 (2010).
[64]J. T. Herron, D. S. Green, *Plasma Chem. Plasma Process.* **21**, 459-481 (2001).
[65]P. Bruggeman, D. C. Schram, *Plasma Sources Science & Technology* **19**, 9 (2010).
[66]P. Bruggeman, F. Iza, D. Lauwers, Y. A. Gonzalvo, *Journal of Physics D-Applied Physics* **43**, (2010).
[67]T. Verreycken, P. J. Bruggeman, *Plasma Chem. Plasma Process.* **34**, 605-619 (2014).

[68]P. Luan, A. J. Knoll, H. Wang, V. S. S. K. Kondeti, P. J. Bruggeman, G. S. Oehrlein, *J. Phys. D: Appl. Phys.* **50**, 03LT02 (2017).
[69]C. J. Hall, P. J. Murphy, H. J. Griesser, *Plasma Processes and Polymers* **9**, 398-405 (2012).
[70]S. Huang, L. Dai, *The Journal of Physical Chemistry B* **106**, 3543-3545 (2002).
[71]P. Neta, L. M. Dorfman, in *Radiation Chemistry*. (AMERICAN CHEMICAL SOCIETY, 1968), vol. 81, chap. 15, pp. 222-230.
[72]R. Atkinson, W. P. L. Carter, A. M. Winer, *The Journal of Physical Chemistry* **87**, 1605-1610 (1983).
[73]W. Siemens, *Annalen der Physik* **178**, 66-122 (1857).
[74]U. Kogelschatz, *Plasma Chemistry and Plasma Processing* **23**, 1-46 (2003).
[75]R. Criegee, *Angewandte Chemie International Edition in English* **14**, 745-752 (1975).
[76]E. Erickson, R. Berntsen, E. Hill, P. Kusy, *Rubber Chem. Technol.* **32**, 1062-1079 (1959).
[77]E. H. Andrews, M. Braden, *J. Polym. Sci.* **55**, 787-798 (1961).
[78]L. Macmanus, M. Walzak, N. Mcintyre, *Journal of Polymer Science-A-Polymer Chemistry Edition* **37**, 2489-2502 (1999).
[79]H. Y. Nie, M. J. Walzak, B. Berno, N. S. Mcintyre, *Appl. Surf. Sci.* **144–145**, 627-632 (1999).
[80]M. J. Walzak, S. Flynn, R. Foerch, J. M. Hill, E. Karbashewski, A. Lin, M. Strobel, *J. Adhes. Sci. Technol.* **9**, 1229-1248 (1995).
[81]R. J. Klein, D. A. Fischer, J. L. Lenhart, *Langmuir* **24**, 8187-8197 (2008).
[82]D. B. Graves, *Journal of Physics D-Applied Physics* **45**, (2012).
[83]Y. Dingkun, W. Zhihua, D. Can, H. Yong, W. Ronald, C. Kefa, *J. Phys. D: Appl. Phys.* **49**, 455203 (2016).
[84]B. G. David, *Deactivation of lipopolysaccharide by Ar and H 2 inductively coupled low-pressure plasma* **45**, 263001 (2012).
[85]B. T. J. V. Ham, S. Hofmann, R. Brandenburg, P. J. Bruggeman, *J. Phys. D: Appl. Phys.* **47**, 224013 (2014).
[86]E. G. Janzen, A. L. Wilcox, V. Manoharan, *The Journal of Organic Chemistry* **58**, 3597-3599 (1993).
[87]V. B. O'donnell, B. A. Freeman, *Circulation Research* **88**, 12-21 (2001).
[88]R. Atkinson, *J. Phys. Chem. Ref. Data* **20**, 459-507 (1991).
[89]L. V. Phillips, D. M. Coyne, *The Journal of Organic Chemistry* **29**, 1937-1942 (1964).
[90]R. Atkinson, W. P. L. Carter, C. N. Plum, A. M. Winer, J. N. Pitts, *Int. J. Chem. Kinet.* **16**, 887-898 (1984).
[91]D. A. Knopf, J. Mak, S. Gross, A. K. Bertram, *Geophys. Res. Lett.* **33**, n/a-n/a (2006).
[92]S. Gross, A. K. Bertram, *Journal of Geophysical Research: Atmospheres* **114**, n/a-n/a (2009).
[93]E. a. J. Bartis, P. Luan, A. J. Knoll, D. B. Graves, J. Seog, G. S. Oehrlein, *Plasma Processes and Polymers* **13**, 410-418 (2016).
[94]E. a. J. Bartis, P. Luan, A. J. Knoll, D. B. Graves, J. Seog, G. S. Oehrlein, *Eur. Phys. J. D* **70**, 1-19 (2016).
[95]P. Luan, G. S. Oehrlein, *J. Phys. D: Appl. Phys.* **51**, 135201 (2018).
[96]K. U. Riemann, *J. Phys. D: Appl. Phys.* **24**, 493 (1991).
[97]B. N. Chapman, *Glow discharge processes: sputtering and plasma etching*. (Wiley, 1980).
[98]A. A. Kulikovsky, *Physical Review E* **57**, 7066-7074 (1998).
[99]B. Natalia Yu, J. K. Mark, *Plasma Sources Sci. Technol.* **20**, 035017 (2011).
[100]B. Natalia Yu, J. K. Mark, *J. Phys. D: Appl. Phys.* **46**, 125201 (2013).
[101]N. Y. Babaeva, N. Ning, D. B. Graves, M. J. Kushner, *J. Phys. D: Appl. Phys.* **45**, 115203 (2012).
[102]L. Stollenwerk, *New Journal of Physics* **11**, 103034 (2009).

[103]J. F. Ziegler, M. D. Ziegler, J. P. Biersack, *Nuclear Instruments and Methods in Physics Research Section B: Beam Interactions with Materials and Atoms* **268**, 1818-1823 (2010).
[104]H. Gokan, S. Esho, Y. Ohnishi, *Journal of the electrochemical Society* **130**, 143-146 (1983).
[105]K. C. Gopal, J. V. Joseph, B. G. David, *J. Phys. D: Appl. Phys.* **42**, 242001 (2009).
[106]R. L. Bruce, S. Engelmann, T. Lin, T. Kwon, R. J. Phaneuf, G. S. Oehrlein, B. K. Long, C. G. Willson, J. J. Végh, D. Nest, D. B. Graves, A. Alizadeh, *Journal of Vacuum Science & Technology B: Microelectronics and Nanometer Structures Processing, Measurement, and Phenomena* **27**, 1142-1155 (2009).
[107]M. R. Wertheimer, A. C. Fozza, A. Holländer, *Nuclear Instruments and Methods in Physics Research Section B: Beam Interactions with Materials and Atoms* **151**, 65-75 (1999).
[108]J. Brandrup, E. H. Immergut, E. A. Grulke, A. Abe, D. R. Bloch, *Polymer handbook*. (Wiley New York etc, 1989), vol. 7.
[109]P. Cheremisinoff, *Handbook of Engineering Polymeric Materials*. (Taylor & Francis, 1997).
[110]A. L. Andrady, *Physical properties of polymers handbook*, 857-866 (2007).
[111]E. Yousif, R. Haddad, *SpringerPlus* **2**, 398 (2013).
[112]V. E. Skurat, Y. I. Dorofeev, *Die Angewandte Makromolekulare Chemie* **216**, 205-224 (1994).
[113]F. Weilnboeck, R. L. Bruce, S. Engelmann, G. S. Oehrlein, D. Nest, T. Y. Chung, D. Graves, M. Li, D. Wang, C. Andes, E. A. Hudson, *Journal of Vacuum Science & Technology B* **28**, 993-1004 (2010).
[114]S. Reuter, J. Winter, A. Schmidt-Bleker, D. Schroeder, H. Lange, N. Knake, V. Schulz-Von Der Gathen, K. D. Weltmann, *Plasma Sources Science & Technology* **21**, (2012).
[115]S. Schneider, J. W. Lackmann, F. Narberhaus, J. E. Bandow, B. Denis, J. Benedikt, *Deactivation of lipopolysaccharide by Ar and H 2 inductively coupled low-pressure plasma* **44**, 295201 (2011).
[116]M. A. Hartney, D. W. Hess, D. S. Soane, *Journal of Vacuum Science & Technology B: Microelectronics Processing and Phenomena* **7**, 1-13 (1989).
[117]F. D. Egitto, V. Vukanovic, G. N. Taylor, in *Plasma deposition, treatment, and etching of polymers. Academic Press, San Diego,* R. D'Agostino, Ed. (1990), pp. 321-422.
[118]A. J. Knoll, P. Luan, A. Pranda, R. L. Bruce, G. S. Oehrlein, *Plasma Processes and Polymers*, e1700217-n/a (2018
).
[119]G. N. Taylor, T. M. Wolf, *Polymer Engineering & Science* **20**, 1087-1092 (1980).
[120]R. M. France, R. D. Short, *Langmuir* **14**, 4827-4835 (1998).
[121]T. Okuno, T. Yasuda, H. Yasuda, *Textile Research Journal* **62**, 474-480 (1992).
[122]M. B. Olde Riekerink, J. G. A. Terlingen, G. H. M. Engbers, J. Feijen, *Langmuir* **15**, 4847-4856 (1999).
[123]I. Junkar, U. Cvelbar, A. Vesel, N. Hauptman, M. Mozetič, *Plasma Processes and Polymers* **6**, 667-675 (2009).
[124]A. Holländer, R. Wilken, J. Behnisch, *Surf. Coat. Technol.* **116–119**, 788-791 (1999).
[125]O.-J. Kwon, S.-W. Myung, C.-S. Lee, H.-S. Choi, *J. Colloid Interface Sci.* **295**, 409-416 (2006).
[126]M. Morra, E. Occhiello, R. Marola, F. Garbassi, P. Humphrey, D. Johnson, *J. Colloid Interface Sci.* **137**, 11-24 (1990).
[127]M. R. Sanchis, V. Blanes, M. Blanes, D. Garcia, R. Balart, *Eur. Polym. J.* **42**, 1558-1568 (2006).
[128]M. R. Sanchis, O. Calvo, O. Fenollar, D. Garcia, R. Balart, *Polym. Test.* **27**, 75-83 (2008).
[129]T. Murakami, S.-I. Kuroda, Z. Osawa, *J. Colloid Interface Sci.* **202**, 37-44 (1998).
[130]S. Große-Kreul, C. Corbella, A. Von Keudell, B. Ozkaya, G. Grundmeier, *Plasma Processes and Polymers* **10**, 1110-1119 (2013).

[131]J. P. Chang, H. H. Sawin, *Journal of Vacuum Science & Technology B: Microelectronics and Nanometer Structures Processing, Measurement, and Phenomena* **19**, 1319-1327 (2001).
[132]S. G. Jennings, *J. Aerosol Sci* **19**, 159-166 (1988).
[133]J. M. Grace, L. J. Gerenser, *J. Dispersion Sci. Technol.* **24**, 305-341 (2003).
[134]S. Hofmann, A. F. H. Van Gessel, T. Verreycken, P. Bruggeman, *Plasma Sources Science & Technology* **20**, 065010 (2011).
[135]S. Zhang, A. Sobota, E. M. V. Veldhuizen, P. J. Bruggeman, *J. Phys. D: Appl. Phys.* **48**, 015203 (2015).
[136]S. Iseni, S. Zhang, A. F. H. V. Gessel, S. Hofmann, B. T. J. V. Ham, S. Reuter, K. D. Weltmann, P. J. Bruggeman, *New Journal of Physics* **16**, 123011 (2014).
[137]S. Zhang, A. Sobota, E. M. Van Veldhuizen, P. J. Bruggeman, *Plasma Sources Science & Technology* **24**, 045015 (2015).
[138]W. V. Gaens, A. Bogaerts, *Plasma Sources Science and Technology* **23**, 035015 (2014).
[139]S. Masuda, K. Akutsu, M. Kuroda, Y. Awatsu, Y. Shibuya, *IEEE Transactions on Industry Applications* **24**, 223-231 (1988).
[140]E. a. J. Bartis, A. J. Knoll, P. Luan, J. Seog, G. S. Oehrlein, *Plasma Chem. Plasma Process.* **36**, 121-149 (2016).
[141]E. a. J. Bartis, P. Luan, A. J. Knoll, C. Hart, J. Seog, G. S. Oehrlein, *Biointerphases* **10**, 029512 (2015).
[142]X. H. Yuan, L. L. Raja, *Appl. Phys. Lett.* **81**, 814-816 (2002).
[143]S. Reuter, J. Winter, S. Iseni, A. Schmidt-Bleker, M. Dunnbier, K. Masur, K. Wende, K. D. Weltmann, *Plasma Science, IEEE Transactions on* **PP**, 1-1 (2014).
[144]T. Shimizu, J. L. Zimmermann, G. E. Morfill, *New Journal of Physics* **13**, 023026 (2011).
[145]S. Reuter, J. Winter, A. Schmidt-Bleker, H. Tresp, M. U. Hammer, K. D. Weltmann, *Apr* **40**, 2788-2794 (2012).
[146]C. Tendero, C. Tixier, P. Tristant, J. Desmaison, P. Leprince, *Spectrochimica Acta Part B: Atomic Spectroscopy* **61**, 2-30 (2006).
[147]N. Vandencasteele, F. Reniers, *J. Electron. Spectrosc. Relat. Phenom.* **178**, 394-408 (2010).
[148]M. G. Kong, G. Kroesen, G. Morfill, T. Nosenko, T. Shimizu, J. Van Dijk, J. L. Zimmermann, *New Journal of Physics* **11**, 115012 (2009).
[149]S. Samukawa, M. Hori, S. Rauf, K. Tachibana, P. Bruggeman, G. Kroesen, J. C. Whitehead, A. B. Murphy, A. F. Gutsol, S. Starikovskaia, U. Kortshagen, J.-P. Boeuf, T. J. Sommerer, M. J. Kushner, U. Czarnetzki, N. Mason, *Journal of Physics D-Applied Physics* **45**, 253001 (2012).
[150]P. Bruggeman, R. Brandenburg, *Journal of Physics D-Applied Physics* **46**, 464001 (2013).
[151]J. L. Walsh, F. Iza, N. B. Janson, V. J. Law, M. G. Kong, *J. Phys. D: Appl. Phys.* **43**, 075201 (2010).
[152]G. B. Sretenović, I. B. Krstić, V. V. Kovačević, B. M. Obradović, M. M. Kuraica, *Appl. Phys. Lett.* **99**, 161502 (2011).
[153]O. Jun-Seok, A.-G. Yolanda, W. B. James, *J. Phys. D: Appl. Phys.* **44**, 365202 (2011).
[154]S. Arndt, E. Wacker, Y. F. Li, T. Shimizu, H. M. Thomas, G. E. Morfill, S. Karrer, J. L. Zimmermann, A. K. Bosserhoff, *Apr* **22**, 284-289 (2013).
[155]G. Fridman, G. Friedman, A. Gutsol, A. B. Shekhter, V. N. Vasilets, A. Fridman, *Plasma Processes and Polymers* **5**, 503-533 (2008).
[156]G. Isbary, G. Morfill, H. U. Schmidt, M. Georgi, K. Ramrath, J. Heinlin, S. Karrer, M. Landthaler, T. Shimizu, B. Steffes, W. Bunk, R. Monetti, J. L. Zimmermann, R. Pompl, W. Stolz, *British Journal of Dermatology* **163**, 78-82 (2010).
[157]R. Wild, T. Gerling, R. Bussiahn, K. D. Weltmann, L. Stollenwerk, *J. Phys. D: Appl. Phys.* **47**, 042001 (2014).
[158]E. a. J. Bartis, D. B. Graves, J. Seog, G. S. Oehrlein, *J. Phys. D: Appl. Phys.* **46**, 312002 (2013).

[159]A. J. Knoll, P. Luan, E. a. J. Bartis, C. Hart, Y. Raitses, G. S. Oehrlein, *Appl. Phys. Lett.* **105**, 171601 (2014).
[160]S. Hofmann, K. Van Gils, S. Van Der Linden, S. Iseni, P. Bruggeman, *Eur. Phys. J. D* **68**, 1-14 (2014).
[161]B. Van Gessel, R. Brandenburg, P. Bruggeman, *Appl. Phys. Lett.* **103**, 064103 (2013).
[162]A. F. H. Van Gessel, K. M. J. Alards, P. J. Bruggeman, *Journal of Physics D-Applied Physics* **46**, 265202 (2013).
[163]H. A. Aboubakr, P. Williams, U. Gangal, M. M. Youssef, S. a. A. El-Sohaimy, P. J. Bruggeman, S. M. Goyal, *Applied and Environmental Microbiology* **81**, 3612-3622 (2015).
[164]S. Zhang, Ph.D. Thesis, Eindhoven University of Technology, (2015).
[165]S. Zhang, A. F. H. V. Gessel, S. C. V. Grootel, P. J. Bruggeman, *Plasma Sources Sci. Technol.* **23**, 025012 (2014).
[166]V. Alenka, M. Miran, *J. Phys. D: Appl. Phys.* **50**, 293001 (2017).
[167]G. E. Morfill, T. Shimizu, B. Steffes, H.-U. Schmidt, *New Journal of Physics* **11**, 115019 (2009).
[168]R. Thirumdas, C. Sarangapani, U. S. Annapure, *Food Biophysics* **10**, 1-11 (2015).
[169]M. Keidar, *Plasma Sources Sci. Technol.* **24**, 033001 (2015).
[170]C. Tendero, C. Tixier, P. Tristant, J. Desmaison, P. Leprince, *Spectrochimica Acta Part B-Atomic Spectroscopy* **61**, 2-30 (2006).
[171]P. Bruggeman, R. Brandenburg, *Journal of Physics D-Applied Physics* **46**, (2013).
[172]A. Schutze, J. Y. Jeong, S. E. Babayan, J. Park, G. S. Selwyn, R. F. Hicks, *Ieee Transactions on Plasma Science* **26**, 1685-1694 (1998).
[173]Y. F. Li, J. L. Zimmermann, G. E. Morfill, *New Journal of Physics* **14**, 023058 (2012).
[174]A. Shashurin, M. Keidar, S. Bronnikov, R. A. Jurjus, M. A. Stepp, *Appl. Phys. Lett.* **93**, 181501 (2008).
[175]A. Bogaerts, E. Neyts, R. Gijbels, J. Van Der Mullen, *Spectrochimica Acta Part B: Atomic Spectroscopy* **57**, 609-658 (2002).
[176]S. Reuter, J. Winter, A. Schmidt-Bleker, H. Tresp, M. U. Hammer, K.-D. Weltmann, *Ieee Transactions on Plasma Science* **40**, 2788-2794 (2012).
[177]J. Y. Jeong, S. E. Babayan, V. J. Tu, J. Park, I. Henins, R. F. Hicks, G. S. Selwyn, *Plasma Sources Sci. Technol.* **7**, 282 (1998).
[178]K. Fricke, H. Steffen, T. Von Woedtke, K. Schröder, K.-D. Weltmann, *Plasma Processes and Polymers* **8**, 51-58 (2011).
[179]J. H. Scofield, *J. Electron. Spectrosc. Relat. Phenom.* **8**, 129-137 (1976).
[180]H. P. Li, X. Chen, *Thin Solid Films* **390**, 175-180 (2001).
[181]K. Wende, P. Williams, J. Dalluge, W. V. Gaens, H. Aboubakr, J. Bischof, T. V. Woedtke, S. M. Goyal, K.-D. Weltmann, A. Bogaerts, K. Masur, P. J. Bruggeman, *Biointerphases* **10**, 029518 (2015).
[182]S. Q. Zhang, W. Van Gaens, B. Van Gessel, S. Hofmann, E. Van Veldhuizen, A. Bogaerts, P. Bruggeman, *Journal of Physics D-Applied Physics* **46**, 205202 (2013).
[183]T. N. Murakami, Y. Fukushima, Y. Hirano, Y. Tokuoka, M. Takahashi, N. Kawashima, *Colloids and Surfaces B: Biointerfaces* **29**, 171-179 (2003).
[184]T. M. Mayer, R. A. Barker, *Journal of Vacuum Science and Technology* **21**, 757-763 (1982).
[185]A. Bogaerts, *Spectrochimica Acta Part B: Atomic Spectroscopy* **64**, 1266-1279 (2009).
[186]A. Bogaerts, M. Yusupov, J. Van Der Paal, C. C. W. Verlackt, E. C. Neyts, *Plasma Processes and Polymers* **11**, 1156-1168 (2014).
[187]M. Yusupov, A. Bogaerts, S. Huygh, R. Snoeckx, A. C. T. Van Duin, E. C. Neyts, *The Journal of Physical Chemistry C* **117**, 5993-5998 (2013).

[188]R. Atkinson, D. L. Baulch, R. A. Cox, J. N. Crowley, R. F. Hampson, R. G. Hynes, M. E. Jenkin, M. J. Rossi, J. Troe, *Atmos. Chem. Phys.* **4**, 1461-1738 (2004).
[189]X. Lu, G. V. Naidis, M. Laroussi, S. Reuter, D. B. Graves, K. Ostrikov, *Physics Reports* **630**, 1-84 (2016).
[190]A. J. Knoll, P. Luan, A. Pranda, R. L. Bruce, G. S. Oehrlein, *Submitted to Plasma Processes and Polymers*, (2017).
[191]Y. Sakiyama, D. B. Graves, H. W. Chang, T. Shimizu, G. E. Morfill, *Journal of Physics D-Applied Physics* **45**, 19 (2012).
[192]H. Tompkins, E. A. Irene, *Handbook of ellipsometry*. (William Andrew, 2005).
[193]R. Wilken, A. Holländer, J. Behnisch, *Macromolecules* **31**, 7613-7617 (1998).
[194]J. R. Pels, F. Kapteijn, J. A. Moulijn, Q. Zhu, K. M. Thomas, *Carbon* **33**, 1641-1653 (1995).
[195]J. Meichsner, M. Zeuner, B. Krames, M. Nitschke, R. Rochotzki, K. Barucki, *Surf. Coat. Technol.* **98**, 1565-1571 (1998).
[196]D. Briggs, *Surface analysis of polymers by XPS and static SIMS*. (Cambridge University Press, 1998).
[197]A. Pranda, S. a. G. Razo, Z. Tomova, J. T. Fourkas, G. S. Oehrlein, *Journal of Vacuum Science & Technology A: Vacuum, Surfaces, and Films* **36**, 021304 (2018).
[198]S. G. Kazarian, K. L. A. Chan, *Analyst* **138**, 1940-1951 (2013).
[199]G. Socrates, *Infrared and Raman characteristic group frequencies: tables and charts*. (John Wiley & Sons, 2001).
[200]W. Groh, A. Zimmermann, *Macromolecules* **24**, 6660-6663 (1991).
[201]Y. Liu, P. H. Daum, *J. Aerosol Sci* **39**, 974-986 (2008).
[202]J. Herron, D. Green, *Plasma Chem. Plasma Process.* **21**, 459-481 (2001).
[203]C. Cheng, J. Shen, D. Z. Xiao, H. B. Xie, Y. Lan, S. D. Fang, Y. D. Meng, K. C. Paul, *Chinese Physics B* **23**, 7 (2014).
[204]Q. Xiong, A. Y. Nikiforov, L. Li, P. Vanraes, N. Britun, R. Snyders, X. P. Lu, C. Leys, *European Physical Journal D* **66**, 8 (2012).
[205]N. Srivastava, C. J. Wang, *J. Appl. Phys.* **110**, 9 (2011).
[206]J. Winter, K. Wende, K. Masur, S. Iseni, M. Dunnbier, M. U. Hammer, H. Tresp, K. D. Weltmann, S. Reuter, *Journal of Physics D-Applied Physics* **46**, 11 (2013).
[207]S. Teodoru, Y. Kusano, A. Bogaerts, *Plasma Processes and Polymers* **9**, 652-689 (2012).
[208]D. X. Liu, P. Bruggeman, F. Iza, M. Z. Rong, M. G. Kong, *Plasma Sources Science & Technology* **19**, 22 (2010).
[209]K. Ding, M. A. Lieberman, *J. Phys. D: Appl. Phys.* **48**, 035401 (2015).
[210]T. Verreycken, P. J. Bruggeman, *Plasma Chem. Plasma Process.* **34**, 605-619 (2014).
[211]X. Y. Liu, X. K. Pei, K. Ostrikov, X. P. Lu, D. W. Liu, *Physics of Plasmas* **21**, 6 (2014).
[212]A. Schmidt-Bleker, J. Winter, S. Iseni, M. Dunnbier, K. D. Weltmann, S. Reuter, *Journal of Physics D-Applied Physics* **47**, 12 (2014).
[213]Y. Ippei, O. Ryo, O. Tetsuji, T. Koichi, *Plasma Sources Sci. Technol.* **24**, 015002 (2015).
[214]Z. Abd-Allah, D. a. G. Sawtell, K. Mckay, G. T. West, P. J. Kelly, J. W. Bradley, *J. Phys. D: Appl. Phys.* **48**, 085202 (2015).
[215]A. N. Bhoj, M. J. Kushner, *Plasma Sources Science & Technology* **17**, 11 (2008).
[216]D. Dobrynin, G. Friedman, A. Fridman, A. Starikovskiy, *New Journal of Physics* **13**, 13 (2011).
[217]M. Hahnel, T. Von Woedtke, K. D. Weltmann, *Plasma Processes and Polymers* **7**, 244-249 (2010).
[218]J. Jeon, T. M. Rosentreter, Y. Li, G. Isbary, H. M. Thomas, J. L. Zimmermann, G. E. Morfill, T. Shimizu, *Plasma Processes and Polymers* **11**, 426-436 (2014).

[219]B. D. Tompkins, J. M. Dennison, E. R. Fisher, *Plasma Processes and Polymers* **11**, 850-863 (2014).
[220]L. Bárdos, H. Baránková, *Thin Solid Films* **518**, 6705-6713 (2010).
[221]V. M. Donnelly, A. Kornblit, *Journal of Vacuum Science & Technology A* **31**, 050825 (2013).
[222]T. Verreycken, R. M. Van Der Horst, A. Baede, E. M. Van Veldhuizen, P. J. Bruggeman, *Journal of Physics D-Applied Physics* **45**, 045205 (2012).
[223]T. Verreycken, R. Mensink, R. Van Der Horst, N. Sadeghi, P. J. Bruggeman, *Plasma Sources Science & Technology* **22**, 11 (2013).
[224]L. M. Martini, N. Gatti, G. Dilecce, M. Scotoni, P. Tosi, *J. Phys. D: Appl. Phys.* **50**, 114003 (2017).
[225]G. Ketteler, S. Yamamoto, H. Bluhm, K. Andersson, D. E. Starr, D. F. Ogletree, H. Ogasawara, A. Nilsson, M. Salmeron, *The Journal of Physical Chemistry C* **111**, 8278-8282 (2007).
[226]N. Fox-Lyon, G. S. Oehrlein, N. Ning, D. B. Graves, *J. Appl. Phys.* **110**, 104314 (2011).
[227]V. S. S. K. Kondeti, U. Gangal, S. Yatom, P. J. Bruggeman, *Journal of Vacuum Science & Technology A* **35**, 061302 (2017).
[228]K. Wende, P. Williams, J. Dalluge, W. Van Gaens, H. Aboubakr, J. Bischof, T. Von Woedtke, S. M. Goyal, K.-D. Weltmann, A. Bogaerts, K. Masur, P. J. Bruggeman, *Biointerphases* **10**, 029518 (2015).
[229]R. Zellner, W. Steinert, *Int. J. Chem. Kinet.* **8**, 397-409 (1976).
[230]N. Cohen, K. R. Westberg, *J. Phys. Chem. Ref. Data* **20**, 1211-1311 (1991).
[231]S. Gomez, P. G. Steen, W. G. Graham, *Appl. Phys. Lett.* **81**, 19-21 (2002).
[232]W. G. Mallard, F. Westley, J. Herron, R. F. Hampson, D. Frizzell, *Version 2Q98, National Institute of Standards and Technology, Gaithersburg, MD*, (1998).
[233]D. X. Liu, F. Iza, X. H. Wang, M. G. Kong, M. Z. Rong, *Appl. Phys. Lett.* **98**, 221501 (2011).
[234]T. Verreycken, R. M. Van Der Horst, N. Sadeghi, P. J. Bruggeman, *Journal of Physics D-Applied Physics* **46**, (2013).
[235]J. Ehlbeck, U. Schnabel, M. Polak, J. Winter, W. Th Von, R. Brandenburg, T. V. D. Hagen, K. D. Weltmann, *J. Phys. D: Appl. Phys.* **44**, 013002 (2011).
[236]M. Baier, M. Görgen, J. Ehlbeck, D. Knorr, W. B. Herppich, O. Schlüter, *Innovative Food Science & Emerging Technologies* **22**, 147-157 (2014).
[237]T. Von Woedtke, S. Reuter, K. Masur, K. D. Weltmann, *Physics Reports* **530**, 291-320 (2013).
[238]P. Babington, K. Rajjoub, J. Canady, A. Siu, M. Keidar, J. H. Sherman, *Biointerphases* **10**, 029403 (2015).
[239]H. L. Chen, H. M. Lee, S. H. Chen, Y. Chao, M. B. Chang, *Applied Catalysis B: Environmental* **85**, 1-9 (2008).
[240]J. Van Durme, J. Dewulf, C. Leys, H. Van Langenhove, *Applied Catalysis B: Environmental* **78**, 324-333 (2008).
[241]W. V. Gaens, S. Iseni, A. Schmidt-Bleker, K. D. Weltmann, S. Reuter, A. Bogaerts, *New Journal of Physics* **17**, 033003 (2015).
[242]P. Luan, G. S. Oehrlein, *To be submitted*, (2018).
[243]P. Luan, V. S. S. K. Kondeti, A. J. Knoll, P. J. Bruggeman, G. S. Oehrlein, *To be submitted*, (2018).
[244]K. A. J., L. Pingshan, P. Adam, B. R. L., O. G. S., *Plasma Processes and Polymers* **15**, 1700217 (2018).
[245]P. Luan, G. Oehrlein, S., *To be submitted*, (2018).
[246]H. Hillborg, U. W. Gedde, *Polymer* **39**, 1991-1998 (1998).

[247]C. A. Cantrell, J. A. Davidson, A. H. Mcdaniel, R. E. Shetter, J. G. Calvert, *Chem. Phys. Lett.* **148**, 358-363 (1988).
[248]C. Chackerian, S. W. Sharpe, T. A. Blake, *J. Quant. Spectrosc. Radiat. Transfer* **82**, 429-441 (2003).
[249]S. W. Sharpe, T. J. Johnson, R. L. Sams, P. M. Chu, G. C. Rhoderick, P. A. Johnson, *Appl. Spectmsc.* **58**, 1452-1461 (2004).
[250]D. W. Griffith, *Appl. Spectmsc.* **50**, 59-70 (1996).
[251]N. J. Harrick, F. K. Du Pré, *Appl. Opt.* **5**, 1739-1743 (1966).
[252]E. A. Bruns, V. R. Perraud, A. Zelenyuk, M. J. Ezell, S. N. Johnson, Y. Yu, D. Imre, B. J. Finlayson-Pitts, M. L. Alexander, *Mar* **44**, 1056-1061 (2010).
[253]T. Saito, E. Niki, T. Shiono, Y. Kamiya, *Bull. Chem. Soc. Jpn.* **51**, 1153-1157 (1978).
[254] P. S. Bailey. (Elsevier Science, Burlington :, 1982).
[255]A. Pranda, S. a. G. Razo, Z. Tomova, J. T. Fourkas, G. S. Oehrlein, *Journal of Vacuum Science & Technology A* **36**, 021304 (2018).
[256]C. D. T., D. A., *Journal of Polymer Science: Polymer Chemistry Edition* **15**, 2321-2345 (1977).
[257]T. Y. Chung, D. B. Graves, F. Weilnboeck, R. L. Bruce, G. S. Oehrlein, M. Q. Li, E. A. Hudson, *Plasma Processes and Polymers* **8**, 1068-1079 (2011).
[258]R. M. France, R. D. Short, *J. Chem. Soc., Faraday Trans.* **93**, 3173-3178 (1997).
[259]X. Liao, D. Liu, Q. Xiang, J. Ahn, S. Chen, X. Ye, T. Ding, *Food Control* **75**, 83-91 (2017).
[260]N. N. Misra, C. Jo, *Trends in Food Science & Technology* **64**, 74-86 (2017).
[261]P. Luan, G. S. Oehrlein, *To be submitted*, (2018).
[262]G. K. Simon, C. Carles, V. K. Achim, O. Berkem, G. Guido, *Plasma Processes and Polymers* **10**, 1110-1119 (2013).
[263]D. Metzler, C. Li, S. Engelmann, R. L. Bruce, E. A. Joseph, G. S. Oehrlein, *Journal of Vacuum Science & Technology A* **34**, 01B101 (2016).
[264]J. H. Scofield, *J. Electron. Spectrosc. Relat. Phenom.* **8**, 129-137 (1976).
[265]M. B. Esler, D. W. Griffith, S. R. Wilson, L. P. Steele, *Anal. Chem.* **72**, 206-215 (2000).
[266]N. Stojilovic, *J. Chem. Educ.* **89**, 1331-1332 (2012).
[267]D. T. Clark, A. Dilks, *Journal of Polymer Science: Polymer Chemistry Edition* **15**, 15-30 (1977).
[268]R. A. Graham, H. S. Johnston, *The Journal of Physical Chemistry* **82**, 254-268 (1978).
[269]P. Grindrod, *The theory and applications of reaction-diffusion equations: patterns and waves*. (Clarendon Press, 1996).
[270]B. Ramos, F. A. Miller, T. R. S. Brandão, P. Teixeira, C. L. M. Silva, *Innovative Food Science & Emerging Technologies* **20**, 1-15 (2013).
[271]B. A. Niemira, *Annual review of food science and technology* **3**, 125-142 (2012).
[272]S. L. Burnett, L. R. Beuchat, *J. Ind. Microbiol. Biotechnol.* **25**, 281-287 (2000).
[273]V. H. Tournas, *International Journal of Food Microbiology* **99**, 71-77 (2005).
[274]B. Surowsky, O. Schlüter, D. Knorr, *Food Engineering Reviews* **7**, 82-108 (2015).
[275]C. Pignata, D. D'angelo, E. Fea, G. Gilli, *Journal of Applied Microbiology* **122**, 1438-1455 (2017).
[276]C. Hertwig, N. Meneses, A. Mathys, *Trends in Food Science & Technology* **77**, 131-142 (2018).
[277]M. Ito, J.-S. Oh, T. Ohta, M. Shiratani, M. Hori, *Plasma Processes and Polymers* **15**, 1700073 (2018).
[278]C. Sarangapani, A. Patange, P. Bourke, K. Keener, P. J. Cullen, *Annual Review of Food Science and Technology* **9**, 609-629 (2018).
[279]F. Fanelli, F. Fracassi, *Surf. Coat. Technol.* **322**, 174-201 (2017).
[280]Y. Changho, Y. Sung-Young, E. Sangheum, P. Seungil, K. Seong Bong, R. Seungmin, Y. Suk Jae, *Plasma Sources Sci. Technol.* **26**, 105007 (2017).

[281]L. Wasala, J. L. Talley, U. Desilva, J. Fletcher, A. Wayadande, *Phytopathology* **103**, 373-380 (2013).
[282]T. Lummerstorfer, J. Kattner, H. Hoffmann, *Analytical and Bioanalytical Chemistry* **388**, 55-64 (2007).
[283]E. J. Elzinga, J.-H. Huang, J. Chorover, R. Kretzschmar, *Mar* **46**, 12848-12855 (2012).
[284]V. A. Nadtochenko, A. G. Rincon, S. E. Stanca, J. Kiwi, *Journal of Photochemistry and Photobiology A: Chemistry* **169**, 131-137 (2005).
[285]W. Zeroual, C. Choisy, S. M. Doglia, H. Bobichon, J.-F. Angiboust, M. Manfait, *Biochimica et Biophysica Acta (BBA) - Molecular Cell Research* **1222**, 171-178 (1994).
[286]C. Timmons, K. Pai, J. Jacob, G. Zhang, L. M. Ma, *Food Control* **84**, 455-462 (2018).
[287]Y. Sun, Z. Zhang, S. Wang, *Molecules* **23**, 975 (2018).
[288]E. Noriega, G. Shama, A. Laca, M. Díaz, M. G. Kong, *Food Microbiology* **28**, 1293-1300 (2011).
[289]A. Fernández, E. Noriega, A. Thompson, *Food Microbiology* **33**, 24-29 (2013).
[290]C. Smet, E. Noriega, F. Rosier, J. L. Walsh, V. P. Valdramidis, J. F. Van Impe, *International Journal of Food Microbiology* **240**, 47-56 (2017).
[291]S. J. Parikh, J. Chorover, *Colloids and Surfaces B: Biointerfaces* **55**, 241-250 (2007).
[292]S. J. Parikh, J. Chorover, *Colloids and Surfaces B: Biointerfaces* **62**, 188-198 (2008).
[293]J. Kiwi, V. Nadtochenko, *Langmuir* **21**, 4631-4641 (2005).
[294]E. a. J. Bartis, C. Barrett, T.-Y. Chung, N. Ning, J.-W. Chu, D. B. Graves, J. Seog, G. S. Oehrlein, *J. Phys. D: Appl. Phys.* **47**, 045202 (2014).
[295]S. Roes, U. Seydel, T. Gutsmann, *Langmuir* **21**, 6970-6978 (2005).